Abstract

Unveiling the Structure of the Perfect Superfluid Using Correlation Functions

Ananya Rai

2025

The sequential clustering of particles into jets provides an algorithmic link between final-state hadrons and the partons from which they originated. Jet substructure techniques allow us to trace the radiation history of jets, offering a powerful framework to probe Quantum Chromodynamics (QCD) across different energy scales. Projected $N$-point Energy Correlators (ENCs) are a novel class of observables that explore the energy flow within hadronic jets. This thesis presents the first measurements of the two-point (EEC) and projected three-point correlators (E3C) as well as their ratio (E3C/EEC) at $\sqrt{s} = 13$ TeV using Run 2 data from the ALICE experiment. The ENCs demonstrate characteristic scaling behavior, while their ratios reveal sensitivity to the running of the strong coupling constant, $\alpha_s$. Corresponding first measurements of E3C and E3C/EEC at $\sqrt{s} = 5.02$ TeV are also presented, showing consistent features across center of mass energies. At extreme temperatures and densities, strongly interacting matter undergoes a phase transition into a deconfined state known as the Quark Gluon Plasma (QGP), which is created in heavy-ion collisions at the LHC. This thesis presents both the first application of and the techniques to measure higher-point Energy Correlators in heavy-ion collisions, thereby expanding the set of substructure tools available to probe the microscopic properties of the QGP.

# Unveiling the Structure of the Perfect Superfluid Using Correlation Functions

A Dissertation
Presented to the Faculty of the Graduate School
of
Yale University
in Candidacy for the Degree of
Doctor of Philosophy

by
Ananya Rai

Dissertation Director: Prof. Helen Caines

December 2025

Copyright © 2025 by Ananya Rai

All rights reserved.

# Unveiling the Structure of the Perfect Superfluid Using Correlation Functions

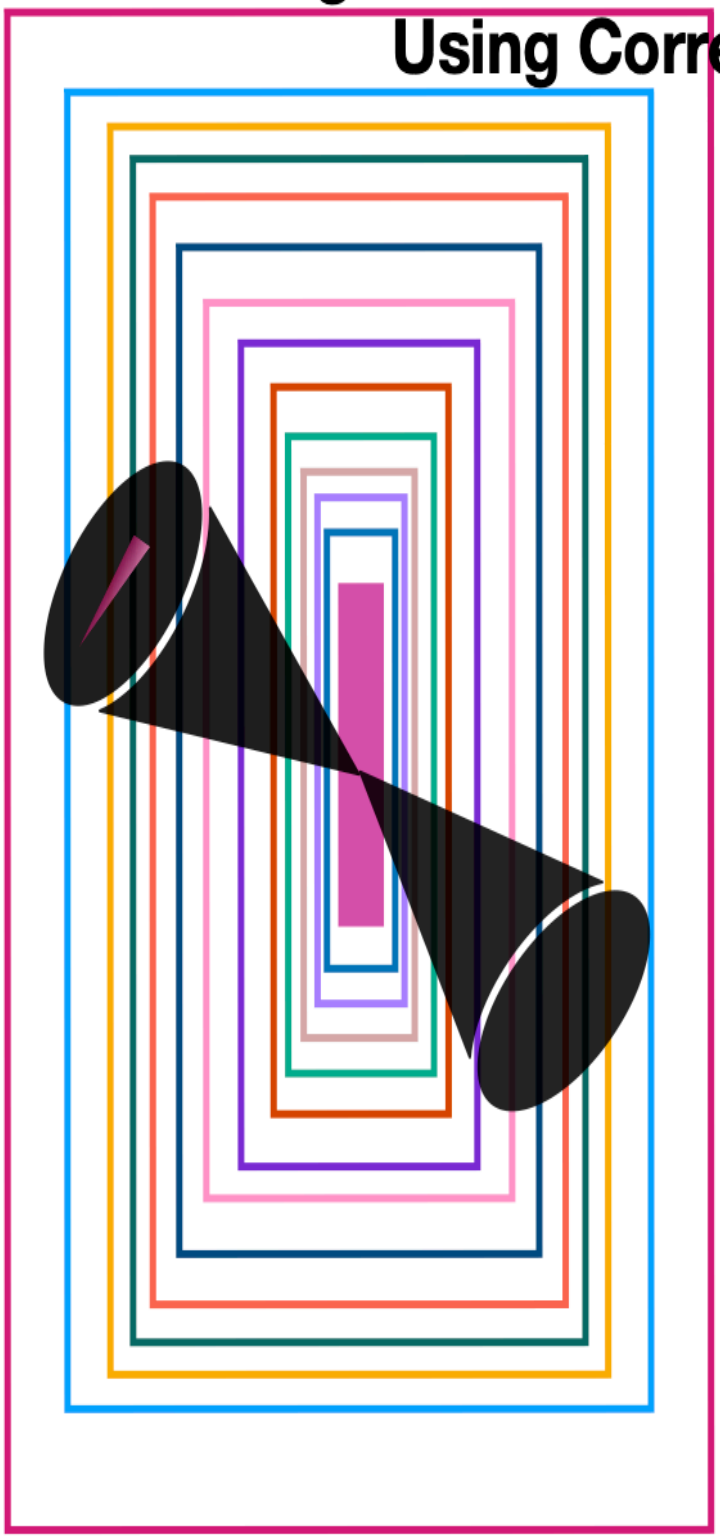

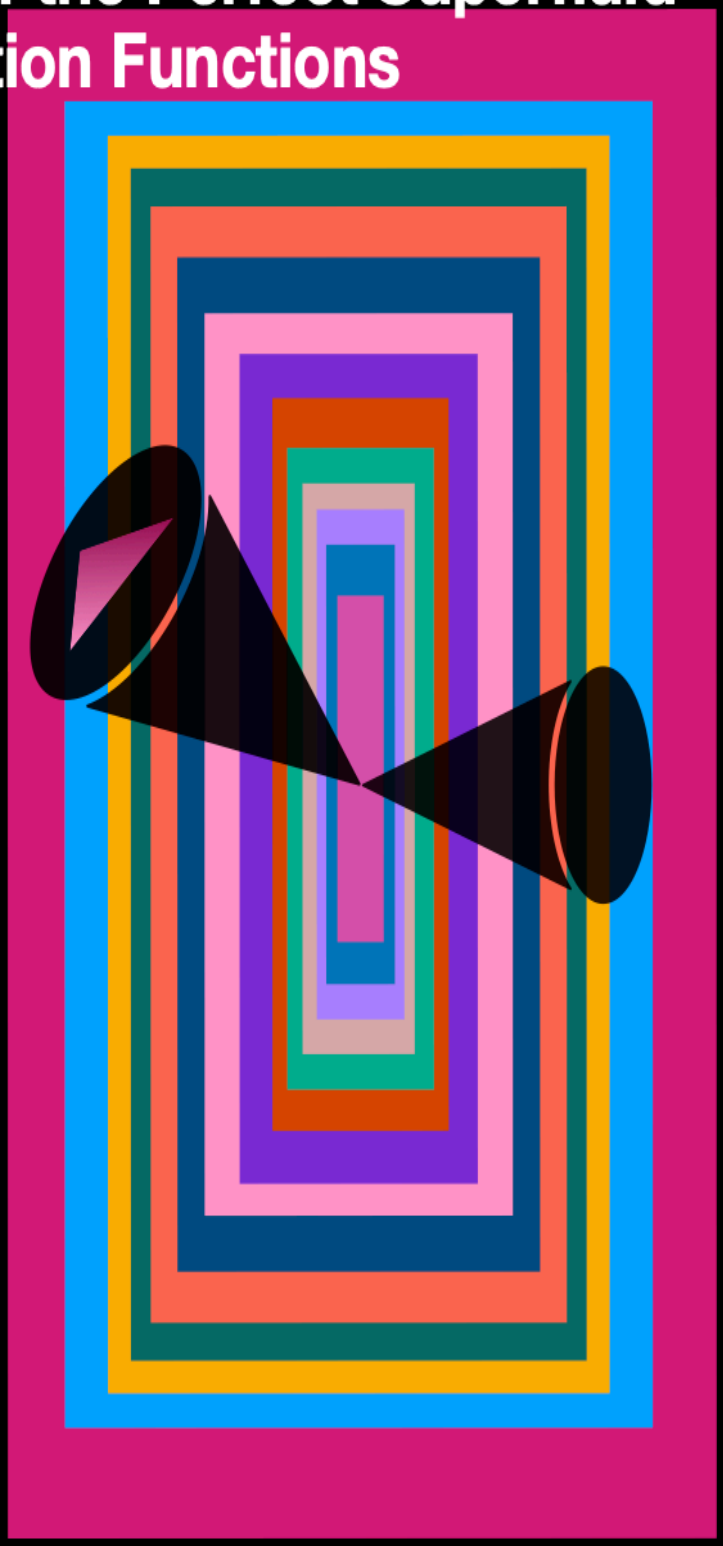

Ananya Rai

# Contents

# Acknowledgements

This thesis contains both my joys and frustrations of doing a PhD, carefully balanced into one experience. I want to acknowledge all the people who have helped me maintain this fine balance by bringing a lot of joy to my life.

I would be amiss to think that any of this would be possible without the support of my family. My parents and Mausi, who have always had unshakable faith in me and viewed me as more capable than I have ever viewed myself. Being away from you has always been the hardest part. Thank you for always reminding me that it would be worth it. Nani and Amma, you are a driving force in my life, keeping me motivated and inspired in spite of all the ups and downs in life. My brother, Adil, for always reminding me to chill out. Thank you for picking up every call and showing up whenever I needed you. My partner, Peter, for being there for me as we navigate life, careers, and distances. Thank you for making me laugh through all the uncertainty in life and for always pushing me to grow. Everything in life seems possible when I am with you.

While we now live far apart, I want to thank my childhood friends for being there consistently and unconditionally – Simmie, Ishi, Anushka, Shivani, Mayank, and Sahil. Because of you, I have felt so loved and supported across some 13000 km that separate us. I also want to thank my high school Math teacher, Dhirendra sir, and my Chemistry teacher, Satish sir, for ingraining in me a deep love of science and math and for teaching me how to take failure in my stride.

My college friends have been a constant source of comfort in my life, even as we have been spread out across the country. Avianne, Carla, Ana, Maya, Janki, Ayush, Nishil, Kaustubh, Tobias, Akanksha, Niana, and the rest of my physics 4 cohort. My San Diego friends whom I met through my partner – Jacob, Derek, William, and Rachael. Life was truly better because I got to spend so many days, evenings, and nights just hanging around you and laughing with you.

Life looked pretty bleak when I moved across the country in 2020 with no friends and only online classes. That turned around when I met my friends – Persky (Kirsty), Sean, Marc (Mark), Erase (Iris), Katharine, Sierra, Ally, Liam, Kaitlyn, Neel, Asheesh. I could write paragraphs about how each of you has added to my time in New Haven, but for the sake of keeping this short, I will just say – thank you for the endless laughter, commiseration, date nights, theme parties, and ragers. For listening to me rant about all things silly and significant. I have learned so much from you. It has only now dawned on me how much time has passed and how lucky I have been to pass it with you.

I want to thank my CERN friends for always making me feel welcome when I travel. Florian, Tony, Emma, Joshua, Nico, Georgios, Christian, Sebastian. Thank you for taking time out of your days and evenings to spend time with me – I love being at CERN, and a big part of that is getting to spend time with you. Arjun, thank you for coming into my life by chance and for bringing so much excitement with your love of physics and your humor. All through my PhD, I have come across many people who have mentored me in some capacity or another – Rithya, Ian, Dani, Nima, Raymond, Krishna, Jussi, Carlota, Jack, Markus, Freidi, Valentina, and Sami. It has been a joy to learn from you both about physics and life.

Any success I have had in grad school is because of the consistent support and inspiration I have felt while at RHIG. John, Paula, Nikolai, Prakhar, Ryan, Emily, Youqi, Isaac, Zoltan, Fernando, Mesut, Andrew, Sierra, Morgan. John, thank you for

your support and for always offering advice when I needed it, but most importantly, thank you for introducing me to Alfie. Paula, for always making sure I got where I needed to be and feeding me chocolate as I got through it. Fernando and Prakhar for the impromptu dinners and all the life advice (solicited or not). Isaac, for teaching me how to snowboard, for making me laugh consistently, and for going on walks with me to talk about life. Zoltan and Mesut for spending many hours with me, either in the office or outside. Andrew, for being a founding member of the Center of Excellence and for being an excellent friend and scientist. Sierra, for being the other founding member of the Center of Excellence, an excellent scientist, the older sibling (even though technically I'm older), and for letting me force my extrovertedness on you on our trips together. Hannah, I'm sad our time together in RHIG was short, but I'm glad we continued working together. Thanks for being an inspiration, a mentor, and a friend. All the jokes, work nights, and familiar looks have added joy to my life. From the laughter across the corridors to the frantic conference approvals, I have felt so much joy in doing physics with you all. I am fortunate to have found my way to RHIG.

Finally, I want to thank the two people who have impacted me most in grad school - my advisor, Helen, and my mentor, friend, Laura. Helen, thank you for taking a chance on me when I showed up at your office near the end of my second year of grad school, very confused about life and research. There is so much that I have learned from you that it is impossible to articulate it all. So I will write the two most important things that I know I will carry with me – how to do good science and how to be compassionate, and how those two things don't have to be mutually exclusive. Thank you for giving me the independence to follow my curiosities and for always meeting me where I was. I have consistently been mesmerized by your intellect and aspire to one day be as good a teacher for someone as you have been for me. I will miss walking into your office to tell you about yet another simple task that

did not go as planned. Laura, my experience at Yale is synonymous with you. I came to you knowing absolutely nothing, not sure if research was really for me, and now I'm writing a thesis. The fact that this exists is a testament to everything you have taught me. It is as much yours as it is mine. Thank you for being so selfless with your time, for pushing me to be a better scientist, and for supporting me through many stressful days and nights. Your insights and friendship have educated me in ways I could not have anticipated. I will miss spending my days in your office having two-minute conversations that were really three-hour long. Thank you for being my role model and friend.

मम्मा और पापा के लिए,
जिन्होंने प्यार से एक ज़िद्दी बेटी को बड़ा किया।

# List of Figures

# List of Tables

# Chapter 1

# Introduction

*"The best that most of us can hope to achieve in physics is simply to misunderstand at a deeper level." - Wolfgang Pauli*

The fundamental goal of particle and nuclear physics is to understand what the universe is composed of and how it has evolved to its current state.[1] To this end, we have created extensive theories about the smallest particles in nature. However, it was not until recently (in the last 150 years) that we began to test these theories.[2] Among all collaborations of physicists in particle and nuclear physics, the Conseil Européen pour la Recherche Nucléaire (CERN) is the largest, dedicated to uncovering the secrets of the universe through the study of particle and nuclear collisions at the Large Hadron Collider (LHC). One of CERN's four major experiments, A Large Ion Collider Experiment (ALICE), focuses on exploring Quantum Chromodynamics (QCD), the fundamental theory describing the strong interaction between quarks and gluons. In particular, ALICE investigates the Quark Gluon Plasma (QGP)—a hot, dense state of matter where quarks and gluons exist freely, resembling the conditions of the early

1. While it may be corny, I love the idea of the universe observing itself via the pursuit of physics.

2. An excellent narration of the history of these developments is captured in [30].

universe. This thesis presents the first measurements of the two-point (EEC) and the projected three-point correlator (E3C), as well as their ratio (E3C/EEC) at $\sqrt{s} = 13$ TeV using Run 2 data from the ALICE experiment. It also introduces the first application of higher-point energy correlators in heavy-ion collisions, along with the development of novel techniques for their measurement. Chapter 2 provides a brief overview of QCD and the emergent phenomena of the QGP. Chapter 3 introduces jets, a primary focus of this thesis. Jets are collimated sprays of particles produced in high-energy collisions, and studying them and their internal structure serves as a powerful probe of quark and gluon interactions. I also discuss how jets are a useful probe of the QGP. In Chapter 4, I introduce Energy Correlators, the central measurements of this thesis. Chapter 5 details the ALICE detector, highlighting the sub-detectors essential for jet measurements. Chapter 6 presents the measurement of $N$-point energy correlators in proton-proton collisions using ALICE, while Chapter 7 explores the phenomenological motivation for extending these measurements to heavy-ion collisions. Chapter 8 describes ongoing efforts to extend the measurement of energy correlators in the quark gluon plasma. Finally, Chapter 9 outlines future research directions and potential advancements based on the findings of this thesis.

# Chapter 2

# A Brief Overview of QCD

## 2.1 The Standard Model

The Standard Model of particle physics is one of the most successful and well-tested theories in science, having led to 50 Nobel Prizes to date. It describes three of the four fundamental forces of nature—electromagnetic, weak, and strong forces—while the fourth, gravity, remains outside its scope.

The Standard Model classifies particles into two broad categories: fermions and bosons. Fermions, which include quarks and leptons, obey Fermi-Dirac statistics and have half-integer spin. Quarks, which come in six flavors (up, down, charm, strange, top, and bottom), combine in groups to form composite particles like baryons and mesons. Leptons, such as electrons, muons, and tau particles, along with their corresponding neutrinos, are elementary particles that do not participate in strong interaction and are found either independently (like electrons) or in specific decay processes (like neutrinos).

Bosons, on the other hand, have integer spin and obey Bose-Einstein statistics. These particles are force carriers, mediating the fundamental interactions between fermions. The photon mediates electromagnetic interactions, the W and Z bosons

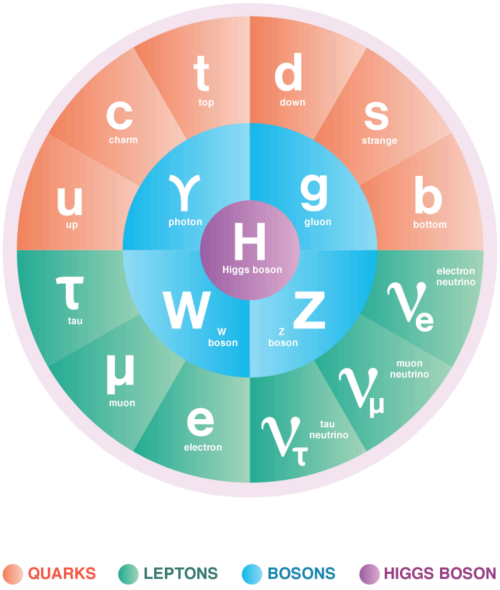


Figure 2.1: Summary of the particles in the Standard Model. Image courtesy of Symmetry Magazine.

mediate the weak force, and gluons mediate the strong force, which binds quarks together inside hadrons. The Higgs boson, discovered in 2012, is responsible for giving mass to other particles via the Higgs field, which permeates the universe. A summary of the particles in the Standard Model is depicted in Fig. 2.1. The Standard Model has been tested to extraordinary precision, with no violations found up to a level of $10^{-16}$, and many of its predictions have been confirmed by experiments. However, despite its successes, the Standard Model is not a complete theory of the universe. It does not include gravity, nor does it account for phenomena such as dark matter, dark energy, or the matter-antimatter asymmetry observed in the cosmos.

In this thesis, I will focus on the particles that carry color charge and interact via the strong force. These particles, which include quarks and gluons, are essential to understanding the intricate dynamics of nuclear interactions and remain an area of active research in the pursuit of a more complete theory of fundamental physics.

## 2.2 Quantum Field Theories (QFTs)

*This section provides a brief overview of the modern perspective on quantum field theories (QFTs). A more detailed pedagogical discussion can be found in standard textbooks, such as [31].*

Quantum Field Theories combine classical field theories, special relativity, and quantum mechanics [31]. They provide a theoretical framework to study particles (in particle and nuclear physics) and quasiparticles (in condensed matter physics). The main ingredient in the field theory formalism is the Lagrangian, $\mathcal{L}$ (or equivalently, the action $S = \int dx^4 \mathcal{L}$), which encodes the interactions of particles and quasiparticles. Modern QFTs are formulated in terms of *Fermi's Golden Rule* [32], which states that the S-matrix [33] element encodes the probability of the initial state transforming into a final state, i.e., a cross-section. In Sec. 2.3.1, I will discuss how this is applied to measure observables of interest to nuclear physics.

### 2.2.1 The Renormalization Group (RG) and Effective Field Theories (EFTs)

As one progresses in their journey through physics, it becomes clear that the fundamental question is one of scales. This idea is akin to using a camera with limited resolving power: to capture a hummingbird's wing in motion, one requires a faster shutter speed. Likewise, to observe finer physical details, we must develop more refined tools—"better cameras"—to probe smaller distances and higher energies. This perspective is central to both the renormalization group (RG) and effective field theory (EFT) frameworks, which are deeply interconnected. The renormalization group, developed by Wilson [34], Migdal [35, 36], and Kadanoff [37], provides a systematic approach for understanding how physical theories evolve across scales. It enables us to perform perturbative computations by regulating divergences and encapsulates

the "running" of coupling constants via the $\beta$-function, as discussed in Sec. 2.3 for Quantum Chromodynamics (QCD). RG flow equations allow us to evolve theories from one energy scale to another by progressively integrating out high-energy degrees of freedom, leaving behind an effective description at lower energies.

This naturally leads to the framework of Effective Field Theories, which have become the standard language of modern theoretical physics. EFTs implement the idea that multi-scale problems can be simplified by separating physics according to energy scales. One constructs an EFT by retaining only the degrees of freedom relevant to the scale of interest and organizing interactions accordingly in the Lagrangian. This approach not only simplifies calculations but also provides a controlled expansion in powers of the energy scale ratio. EFTs are used extensively in both perturbative and non-perturbative contexts. Prominent examples include heavy quark effective theory (HQET) [38], chiral perturbation theory [39], and soft-collinear effective theory (SCET) [40]. Even the Standard Model itself is widely believed to be an EFT of a more fundamental high-energy theory that remains experimentally inaccessible. For a comprehensive review, see [41].

## 2.3 Quantum Chromodynamics (QCD)

Quantum chromodynamics is the underlying quantum field theory that describes the strong nuclear force. QCD is a non-abelian SU(3) gauge theory composed of six flavors of spin 1/2 quarks that interact via the exchange of a spin 1 massless gauge boson called the gluon. These quarks and gluons exchange what is called color charge, hence, the name "chromo". The QCD Lagrangian [31] is given by

$$\mathcal{L}_{\text{QCD}} = -\frac{1}{4} G^a_{\mu\nu} G^{a\mu\nu} + \bar{\psi}_i \left( i\gamma^\mu (D_\mu)_{ij} - m\delta_{ij} \right) \psi_j \tag{2.1}$$

where $\psi_i$ is the quark field, with index $i$ running over different quark flavors, $m$ refers to the quark mass, $D_\mu$ is the gauge covariant derivative,[1] $G^a_{\mu\nu}$ the gluon field strength and $a$ the color index. The $G^a_{\mu\nu}$ term is given by

$$G^a_{\mu\nu} \equiv \partial_\mu A^a_\nu - \partial_\nu A^a_\mu + g f^{abc} A^b_\mu A^c_\nu \tag{2.3}$$

where, $A^a_\mu$ represents the gluon field, $f^{abc}$ the SU(3) structure constants and $g$ the dimensionless coupling constant. It is the final term in $G^a_{\mu\nu}$ that leads to the peculiarities of QCD. This term is a result of the fact that gluons carry color charge and hence can self-interact (in contrast, photon-photon interaction is not allowed at tree level in quantum electrodynamics (QED)). The tree-level Feynman diagrams of QCD are shown in Fig. 2.2.

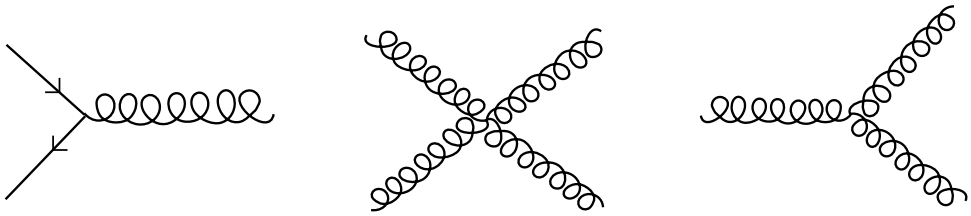

Figure 2.2: Feynman diagrams representing tree-level QCD interactions with lines representing quarks and wiggles representing gluons.

There are two defining features of QCD:

- Asymptotic freedom: QCD has a peculiar property that when two colored objects move farther apart, the force between them increases. Whereas, when

1. Herein, the gauge covariant derivative is defined as

$$(D_\mu)_{ij} = \partial_\mu \delta_{ij} - ig\,(T_a)_{ij}\,A^a_\mu, \tag{2.2}$$

which couples the quark field to the gluon fields $A^a_\mu$ with coupling strength $g$ via the infinitesimal SU(3) generators $T_a$ in the fundamental representation. For details, see Ref. [31].

they are close to each other, the strong force is weaker. This is encapsulated in a potential of the form

$$V(r) = -\frac{A_{eff}}{r} + \alpha r \tag{2.4}$$

This phenomenon was discovered in 1973 by Gross and Wilczek [42] and led to the emergence of QCD as the prevailing theory for strong interactions. This results from the fact that gluons themselves carry color charge. While quark anti-quark ($q\bar{q}$) pairs cause screening of color charge,[2] gluons lead to an anti-screening. Thus, the gluons offset the screening effects from the $q\bar{q}$ pairs. When we have a sufficiently low number of flavor of quarks,[3] as is the case in QCD, then asymptotic freedom is valid.

- Color confinement: This is the property that color singlet states cannot exist which means that we can never directly probe quarks and gluons. Instead, these partons combine to form color-neutral objects called hadrons. Phenomenologically, this is understood to be due to the gluon. A formal proof of confinement is an open problem in QCD.

Thus, we see that the strength of the strong force changes with distance (or energy). More formally, the running of the coupling is a result of the RG evolution of the coupling constant encoded in the $\beta$ function given by

$$\beta(\alpha_s) = -\left(11 - \frac{n_s}{6} - \frac{2n_f}{3}\right)\frac{\alpha_s^2}{2\pi} \tag{2.5}$$

A nonzero $\beta$ function indicates that the coupling constant runs with energy. In this context, $n_s$ denotes the number of scalar bosons (which is zero in our case), and $n_f$ represents the number of quark flavors. The $\beta$ function remains negative

2. This screening of charge is similar to how electric charges are screened in a dielectric medium.

3. The $\beta$ function, as shown in Equation 2.5 is negative as long as the number of flavors is $\leq 16$, which implies that coupling constant decreases at high energies.

as long as $n_f \leq 16$, ensuring that the theory exhibits asymptotic freedom within this range. Therefore, with six quark flavors, QCD remains asymptotically free. The experimental evidence for this "running" of the coupling strength is shown in Fig. 2.3.

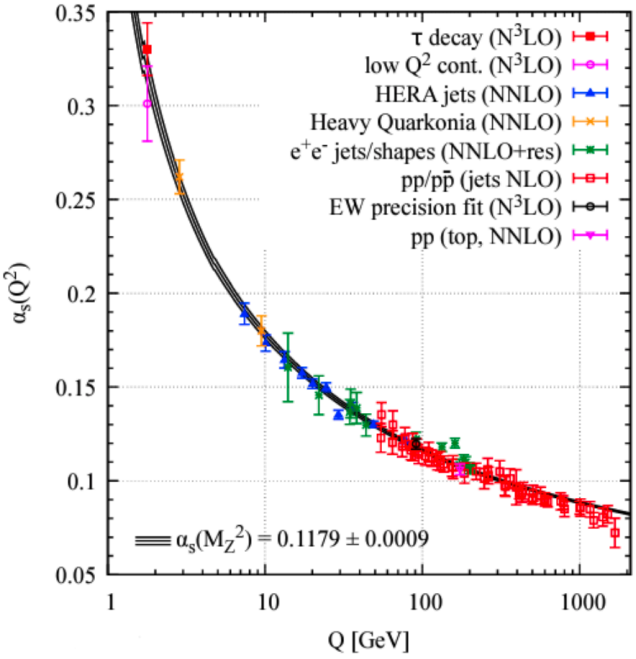


Figure 2.3: Experimental evidence for the running of the strong coupling constant, $\alpha_s$ as a function of energy (Q). Figure taken from [1].

### 2.3.1 Perturbative QCD (pQCD)

At very high energies Q (small $r$), we are in the regime of asymptotically free QCD (meaning that the strong force is weak), and we can use techniques from perturbation theory [43] to perform analytic calculations. In pQCD, we compute scattering cross-sections, i.e., the probability of two partons interacting with each other. Any cross-section in pQCD can be written as

$$\sigma(v) = \sum_{i=0}^{\infty} \alpha_s^i \sigma_i \tag{2.6}$$

where $v$ is a generic observable. $\sigma_0$ represents the Born-level (tree-level) or leading order (LO) cross-section for the scattering process of interest. Subsequent contributions in the perturbative expansion $\sigma_i$ constitute the next-to$^i$-leading (N$^i$LO) corrections. These subsequent corrections (encoded in powers of $\alpha_s$) come from emissions of QCD partons or virtual corrections. Due to the complexity of computation, calculations in pQCD are often performed up to a fixed order in $\alpha_s$ (these are called *fixed-order calculations*). However, fixed-order calculations may suffer from phase space limitations where singularities might exist. To get around these issues, techniques such as *resummation* [44] are applied. Additionally, *all-order calculations* can be performed under certain assumptions on emission kinematics. The most accurate theoretical description involves matching the two approaches [45].

In reality, what we really want to compute are differential cross-sections, which give us the probability of something happening with a particular measured value. These are written as

$$\frac{d\sigma}{d\mathcal{O}} = \int d\Phi \, |\mathcal{M}|^2 \, \delta\left(\mathcal{O} - \hat{\mathcal{O}}(\Phi)\right) \tag{2.7}$$

where, $\mathcal{O}$ is the observable of interest, $d\Phi$ is the differential phase space and $\delta(\mathcal{O} - \hat{\mathcal{O}}(\Phi))$ is the measurement constraint with $\mathcal{O}$ representing the measured value and $\hat{\mathcal{O}}(\Phi)$ representing the functional form of the observable in phase space coordinates. In experiments, we generally measure probability distributions of the form

$$p = \frac{1}{\sigma}\frac{d\sigma}{d\mathcal{O}} \tag{2.8}$$

Now that we understand that we can get differential partonic cross-sections, we are left with one final puzzle which is that partons are contained in composite objects called hadrons. Thus, simple parton scattering cannot capture the scattering of hadrons. However, there exist *factorization theorems*[4] [46] which allow us to factorize

4. Strictly speaking, factorization is assumed for hadron-hadron scattering but rigorously proven for lepton-hadron scattering [46, 47].

the high energy (UV)/short distance physics (partons) from low energy (IR)/large distance physics (hadrons). This allows a pQCD cross-section to be decomposed into a partonic cross-section which is convoluted with non-perturbative functions [48]. We can write this as

$$\frac{d\sigma}{d\mathcal{O}} = \sum_{i,j} \int_0^1 dx_i\, dx_j \sum_f \int d\Phi_f\, f_i/h_1(x_i, \mu_F^2) f_j/h_2(x_j, \mu_F^2)\, \frac{d\hat{\sigma}_{ij\to f}}{d\hat{\mathcal{O}}} D_f(O \to \hat{O}, \mu_F^2) \tag{2.9}$$

where, $d\hat{\sigma}$ is the partonic cross-section, $f_{i/h}$ are the non-perturbative *parton density functions* (PDFs) which parametrize the distribution of partons inside the target hadron, $h$ [49], $\mu_F$ is the factorization scale that separates the PDFs from the partonic cross-section, $D_f$ are *fragmentation functions* (FFs) [50] which are universal[5] and represent the probability density of a final state parton fragmenting into a hadrons. Both PDFs and FFs are obtained from fits to experimental data.[6]

### 2.3.2 Non-perturbatve QCD (npQCD)

Perturbative methods offer excellent insight into QCD dynamics at high energies, where we have asymptotic freedom. However, as we get to lower energies and $\alpha_s \sim 1$, this approach breaks down since the strong force is no longer weak. This means that we now need different tools to study QCD interactions. Here, I summarize two main approaches that are relevant for this thesis:

- Lattice QCD (LQCD): Wilson [55] developed the lattice QCD formulation to study low-energy QCD phenomena by discretizing Euclidean gauge theories. In lattice QCD, quarks are placed on lattice sites and gluon fields connect neighboring sites, with the lattice spacing, $a$, controlling the continuum limit. The

5. The universality of fragmentation functions has been challenged by a recent measurement by the ALICE collaboration [51].

6. Once the PDFs are obtained from data, they can be evolved from one perturbative scale to another using Dokshitzer-Gribov-Lipatov-Altarelli-Parisi (DGLAP) equations [52–54].

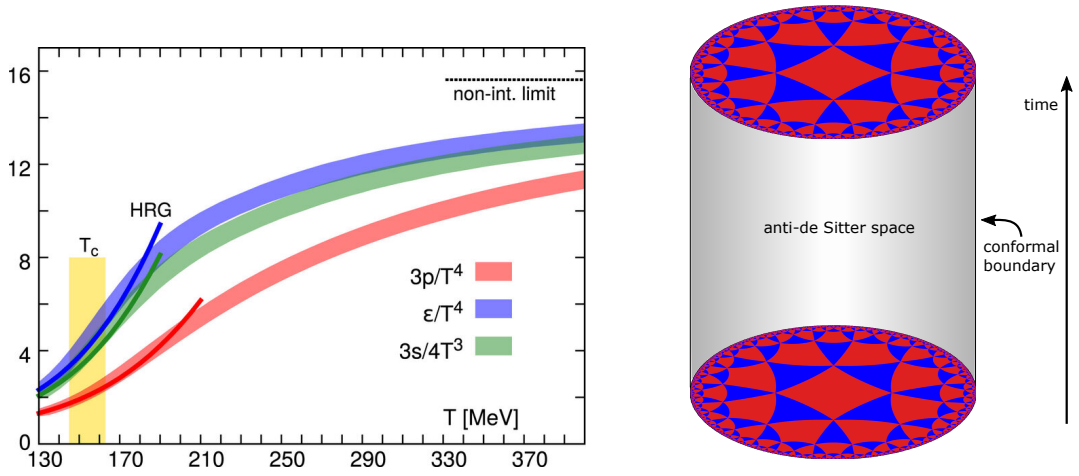


Figure 2.4: Left: Plot depicting the variation of various thermodynamic quantities with temperature as predicted via lattice QCD [2]. Right: AdS/CFT correspondence, where 3-D AdS space is represented by a stack of hyperbolic disks. The CFT sits on the boundary of this cylinder. Figure taken from [3].

two key parameters are the bare quark masses and the strong coupling constant, $\alpha_s$. Since Euclidean and Minkowski field theories are analytically connected and can be mapped to statistical mechanics, lattice QCD allows QCD to be treated as a statistical mechanics problem.[7] An example of LQCD predictions is shown in the left panel of Fig. 2.4, where calculations of various thermodynamic properties are compared to predictions from the hadron resonance gas model.[8] For more details, see [57].

- Gauge-gravity duality (AdS/CFT correspondence): In 1997, Maldacena [58] conjectured that the boundary of Anti-de Sitter space is the usual Minkowski spacetime for a conformal field theory. Thus, there exists a mapping between the two theories, and computations that might be easier to perform in one theory can give insight into the physics of the other. An illustration of this

7. Statistical mechanics and quantum field theories, while presented very differently, are intimately connected. Note, however, that LQCD does not allow dynamics. A great introduction to this connection can be found in [56].

8. The hadron resonance gas model will be discussed in Sec. 2.4.3.

correspondence is shown in the right panel of Fig. 2.4. For more information on AdS/CFT correspondence, the reader is referred to [59].

These npQCD techniques have been successful in predicting various aspects of QCD physics, as will be illustrated throughout this thesis.

## 2.4 Quark Gluon Plasma (QGP)

To understand the strong force completely, we want to understand how it behaves in different regimes—these different regimes can be the number of spacetime dimensions, many-body interactions, etc. To motivate this, I will digress a little bit and draw some parallels with the field of condensed matter physics. In condensed matter physics, we typically deal with systems of many interacting particles (atoms, electrons, etc.), and the emergent phenomena that arise from these interactions, which can include things like superconductivity, magnetism, and topological phases. These phenomena are often not straightforward consequences of the underlying microscopic laws but are instead collective effects that arise from the interactions of large numbers of particles and depend critically on the dimensions of physical spacetime. This idea of collective behavior extends to QCD as well. For example, confinement is an emergent phenomenon of low-energy QCD. Similarly, if we go to high-energy QCD, another emergent phenomenon exists—a state of matter called the Quark Gluon Plasma, where the relevant degrees of freedom are the quarks and gluons, not hadrons. The study of this state of matter is one of the central goals of the high-energy nuclear physics program.

### 2.4.1 The QCD Phase Diagram

After the Big Bang, as the universe expanded and cooled, partons combined to form color-singlet hadrons and the nuclear matter that we now see all around us. However,

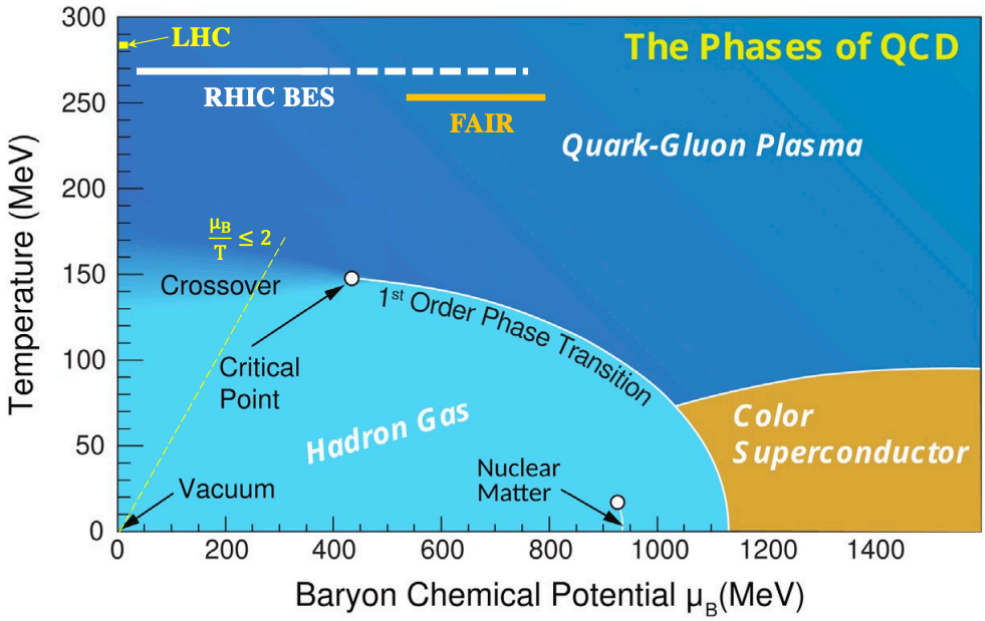


Figure 2.5: The QCD phase diagram as a function of baryon chemical potential ($\mu_B$) and temperature (T). Figure taken from [4].

at very high energy densities, hadronic matter undergoes a phase transition (computed using lattice QCD techniques) to a color deconfined state of a strongly-coupled fluid called the Quark Gluon Plasma (QGP) whose existence was proposed in 1975 [60] and subsequently confirmed at the Relativistic Heavy Ion Collider (RHIC) [61–65]. Our current understanding of the QCD phase diagram as a function of of temperature $T$ and baryon chemical potential ($\mu_B$, which describes the excess of quarks over anti-quarks) is shown in Fig. 2.5. We see that the QGP can exist at very high temperatures ($2 \times 10^{12}$ K) and low $\mu_B$ as well as lower temperatures but finite $\mu_B$. When $\mu_B$ is 0, the transition from hadrons to QGP is a smooth cross-over and is well understood by lattice QCD [57]. At higher $\mu_B$, the transition might be a first-order phase transition with a Critical Point in between [26].

We cannot go back in time to study the Big Bang, but we can recreate the conditions of the primordial universe by colliding relativistic heavy-ions to attain temperatures of $\sim 10^{12}$ K at collider experiments such as the LHC and RHIC.

### 2.4.2 QGP Signatures

To confirm the existence of a QGP, various signatures of this state of matter have been proposed and subsequently verified experimentally:

- Strangeness Enhancement: It was predicted that in a hot, dense QCD medium, strangeness (which is not present in the initial colliding nuclei) would be produced due to flavor creation, flavor excitation, and via gluon splitting during partonic evolution [66]. This prediction has been confirmed via several measurements, which indicate that production of multi-strange hadrons is saturated in the QGP.[9]

- Sequential Quarkonium Suppression: Quarkonium (bound states of heavy quark-anti-quark pairs) suppression, especially the suppression of $J/\psi$ ($c\bar{c}$), due to color screening in the deconfined QGP, was initially proposed as a signature of QGP [68]. Various experimental measurements have since confirmed the sequential suppression of the quarkonium states in the QGP, with weakly bound states showing higher suppression than more tightly bound states.[10]

- Jet Quenching: Another QGP signature, initially predicted by Bjorken [69], is the attenuation of the spray of hadrons (jets) produced from a fragmenting parton that undergoes energy loss as it traverses the QGP. Jet quenching has been confirmed via various measurements across experiments. Jet quenching will be discussed extensively in Sec. 3.6.2.

There exist other signatures that are not listed here, which include chiral symmetry restoration, high-momentum hadron suppression, etc. A comprehensive review of our current understanding can be found in [70].

9. This enhancement has since been observed for various multi-strange hadrons in high multiplicity pp collisions as well [67], opening the question of small system QGP formation.

10. Non-QGP effects (such as Cold Nuclear Matter (CNM) effects due to gluon shadowing) also contribute to this suppression and have been studied extensively [27].

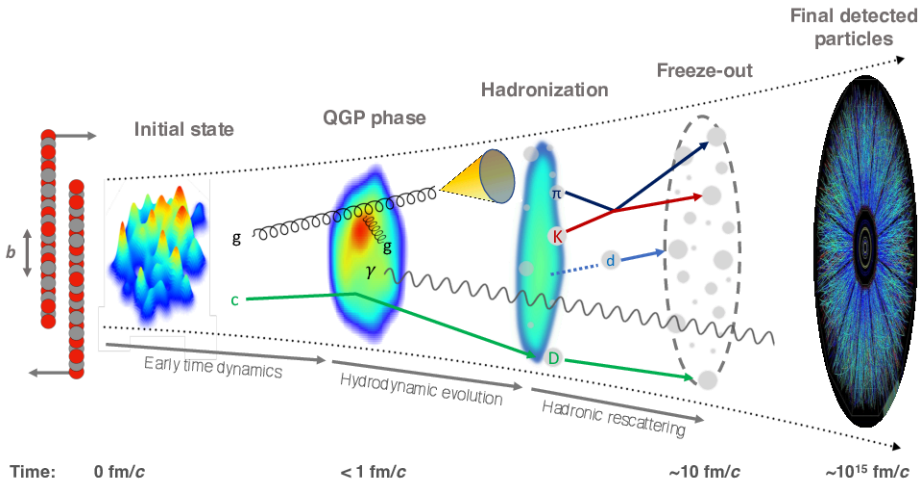


Figure 2.6: The evolution of a heavy-ion collision. Figure taken from [4].

### 2.4.3 Relativistic Heavy-Ion Collisions

Heavy-ion collisions allow us to go back in time and re-create the conditions of the early universe. The evolution of a heavy-ion collision can be described by the following "standard model" (as depicted in Fig. 2.6):

#### Initial Condition

In heavy-ion collisions, the nuclei behave as Lorentz-contracted pancakes at $t = 0$, creating a high energy density in a small volume. Thus, modeling the initial energy density distribution is crucial. Despite the lack of a first-principles QCD evolution of the initial state there are two widely used models that attempt to describe this—the Monte-Carlo Glauber model[11] [72] and the Color Glass Condensate model (CGC) [73]. The Glauber model is a Monte-Carlo method which implements the initial conditions via a probabilistic geometrical nuclear overlap approach and models the nuclei via *thickness functions* ($\hat{T}_A(\vec{s})$, where $\vec{s}$ is the transverse position with respect to the center

11. There also exists the *optical* limit of the Glauber model [71] which does not consider the local density fluctuations of nucleons and instead treats colliding nucleons as flux tubes with smooth density.

of mass of the nucleus). In contrast, the CGC model describes nuclear collisions in terms of the partonic content of the nuclei. The main assumption is that the energy density produced by colliding nuclei is dominated by gluons. Due to its reliance on partonic degrees of freedom, this model is reliable only at very high energies.

### Pre-equililbrium Phase

The matter produced from the initial scatterings is highly inhomogeneous and far from equilibrium. During this transition phase, the medium expands longitudinally close to the speed of light as well as radially. This phase is under active investigation [74, 75]. No generally accepted approach exists.

### QGP Phase

After the pre-equilibrium phase, relativistic viscous hydrodynamics[12] kicks in. The inputs to hydrodynamics are the initial conditions (from the models described above) and the equation of state (from lattice calculations). Viscous hydrodynamics contains a shear ($\eta$) and bulk ($\zeta$) viscosity term, which manifests as *anisotropic* and *radial flow* respectively. Measurements of *anisotropic flow* also offer the greatest evidence for the applicability of this framework and will be discussed in Sec. 2.5.2. Various hydrodynamical models that employ this are MUSIC [79], iEBE-VISHNU [80], CLVisc [81], or transport models such as AMPT [82]. However, it is worth noting that alternative approaches to hydrodynamics that rely on microscopic non-equilibrium calculations with partonic degrees of freedom also exist [83–85].

12. Recent studies question the existence of an equilibrated QGP phase and the applicability of fluid dynamics far from local equilibrium [76–78].

### Hadronization

*The discussion in this section is restricted to hadronization in nuclear collisions, while hadronization models for proton-proton collisions are addressed separately in Sec. 3.2.1.*

As the fluid cools down, it breaks up into hadrons via the Cooper-Frye prescription [86]. This is most commonly modeled using the Hadron Resonance Gas/Statistical Hadronization Model (HRG/SHM) [87], which relies on ideas first proposed by Fermi [88], Landau [89], and Hagedorn [90]. The crucial assumption is that all localized multi-hadronic states with the correct quantum numbers are equally probable, since at the phase boundary between the QGP and hadronic phase, the fireball is almost at thermal equilibrium. In the hadronic phase, the HRG constitutes the resonance contribution. The underlying assumption is that resonances are the dominant contribution to hadronic interactions, and thus, this system can be treated as an ideal gas of known resonances and hadrons.

### Freezeout

Two freezeout stages occur towards the end of a heavy-ion collision. After hadronization, the hadrons can scatter inelastically and elastically. The inelastic scattering lasts until the chemical freezeout ($T_{ch}$), while the elastic scattering lasts until the kinetic freezeout ($T_{kin}$). The temperature for the chemical freezeout[13] is estimated via taking ratios of yields of different hadron species and performing thermal fits by fixing values of $T$ and $\mu_B$. $T_{ch} \sim 156.5 \pm 1.5$ MeV at the LHC ($\mu_B = 0$). To estimate the kinetic freezeout temperature, "effective" temperatures are estimated for hadron species of different masses by using their transverse momenta ($p_{\mathrm{T}}$) spectra. These effective temperatures are then extrapolated to the 0 mass limit to get an estimate of the final temperature of the hadrons.

13. Flavor-dependent multiple temperature freezeout schemes are also under investigation [91].

These are the stages we measure in an experiment and then try to understand the dynamics of earlier stages.

## 2.5 Probing QCD

Due to the phenomenon of color confinement, quarks and gluons—being colored objects—cannot be observed in isolation. As a result, direct probes of these fundamental constituents are not possible. Instead, we study QCD indirectly by examining the particles they form. One of the most powerful tools developed for this purpose is high-energy particle/nuclear collisions, giving rise to the field of collider physics, which allows us to explore QCD dynamics by recreating conditions where quarks and gluons are momentarily liberated before hadronizing.

### 2.5.1 Collider Physics

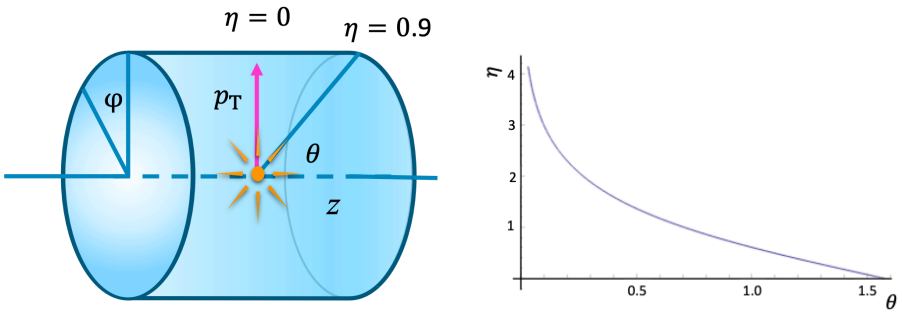


Figure 2.7: Left: Illustration of frequently used collider coordinates. The $\eta = 0.9$ depicts the range of the ALICE detector, which is used for measurements performed in this thesis. Right: Relationship between $\eta$ and $\theta$. Figure taken from [5].

Particle colliders offer us a wealth of knowledge and are employed to probe all fundamental interactions except gravity. The high energies at particle colliders are beneficial as they enable us to exploit the asymptotic freedom of QCD. Indeed, this is important from a field theory standpoint because it allows us to use first principles to answer questions, providing us with some of the most stringent tests of our

understanding of the strong interaction.[14] When particles are accelerated to such high velocities at colliders, their 4-momentum changes are described by the theory of special relativity (as defined in Equation 2.10).

$$4 - Momentum : p^{\mu} = (m_{\mathrm{T}} \cosh y, p_{\mathrm{T}} \sin \phi, p_{\mathrm{T}} \cos \phi, m_{\mathrm{T}} \sinh y) \tag{2.10}$$

where $p_{\mathrm{T}}$ is the momentum transverse to the beam direction (which is assumed to be along $z$, without loss of generality) and $m_{\mathrm{T}} = \sqrt{p_{\mathrm{T}}^2 + m^2}$ is the transverse mass. Thus, using coordinates with simple transformations under these longitudinal boosts is useful. These coordinates are defined below and are illustrated in Fig. 2.7.

$$Rapidity : y = \frac{1}{2} \ln \left( \frac{E + p_z}{E - p_z} \right) \tag{2.11}$$

For massless particles, the rapidity is simplified to

$$Pseudorapidity : \eta = -\ln \tan(\theta/2) \tag{2.12}$$

Additionally, these definitions lead to a metric-independent distance measure between two particles $i$ and $j$ via

$$\Delta R_{ij}^2 = (y_i - y_j)^2 + (\phi_i - \phi_j)^2 \tag{2.13}$$

There are two main collider facilities in the world. The Large Hadron Collider (LHC) is located at CERN, Geneva, Switzerland. The second collider facility is the Relativistic Heavy Ion Collider (RHIC) at Brookhaven National Lab (BNL) located on Long Island, New York. More details about these facilities will be discussed in Chapter 5, with a special focus on the LHC, which houses the ALICE experiment,

14. For a detailed overview, see [9].

which is the focus of this thesis.

### 2.5.2 Experimental Probes of QCD and QGP

We employ a variety of probes to study QCD over the entirety of its phase space, to understand how equilibrium is achieved in gauge theories, and to understand if the fluid picture of QGP is applicable. These are generally categorized into soft, electroweak, and hard probes.

#### Soft Probes

In the context of the QGP, "soft probes" refer to low-momentum particles ($p_{\mathrm{T}} \lesssim 2$ GeV/$c$) that dominate the particle production in heavy-ion collisions. These particles provide valuable insights into the temperature, chemical composition, and dynamics of the QGP. Specifically, these measurements allow us to understand the *collective* behavior of the QGP, where we can describe collectivity via

$$P(\vec{p_1}, \vec{p_2}) \neq P(\vec{p_1})P(\vec{p_2}) \tag{2.14}$$

where, $P(\vec{p_1})$ is the probability of producing a particle with momentum $\vec{p_1}$ in the collision. By measuring the spectra of identified particles, one can extract information about both the temperature of the system and the baryonic chemical potential [92].

As the QGP expands and undergoes freeze-out, the expansion dynamics are captured in the transverse momentum spectra of the produced hadrons. Measurements of the mean $p_{\mathrm{T}}$ of identified hadrons investigate the *radial* flow, which is linked to the bulk viscosity ($\zeta$) of the QGP. Radial flow causes the $p_{\mathrm{T}}$ spectra of heavier hadrons to become flatter at low $p_{\mathrm{T}}$ since they receive a greater boost. The initial spatial anisotropy of the colliding nuclei is manifested in the momentum anisotropy of the final state hadrons [93]. Measurements of momentum anisotropy, as defined in Equa-

tion 2.15, provide insight into the expansion and hadronization of the QGP.

$$\frac{dN}{d\phi} = \frac{1}{2\pi}\left[1 + 2\sum_{n=1}^{\infty} v_n \cos(n(\phi - \psi_n))\right] \tag{2.15}$$

where $\nu_2$ measures the *elliptic* flow,[15] which is connected to the shear viscosity ($\eta$) of the QGP [96]. Higher-order flow harmonics provide insight into fluctuating initial conditions. There are a variety of other soft probes. These include two-particle correlations where long-range correlations indicate collective behavior [97], event-by-event fluctuations of conserved charges can help characterize the QCD critical point [98].

In pp collisions, the goal is often to study the hard scattering. However, any collision produces both hard and soft particles. Since soft dynamics cannot be computed via pQCD techniques, the measurements of the soft particles, called the underlying event (UE), are necessary. Such studies with respect to a hard particle are useful to characterize the soft structure of the event when hard scatterings are present [99,100].

### Electroweak Probes

Electroweak probes of the QGP are constituted by particles that interact via the electroweak force, such as photons, dileptons, and $Z^0/W^+$ bosons. These probes do not interact strongly with the QGP since their mean-free path is larger than the size of the QGP. Thus, they offer insight into the conditions that existed during their production. There are a few different types of photons created from hadronic collisions—*decay* photons (from hadronic decays), *prompt* photons (produced via hard parton interactions), and *thermal* photons (produced during QGP expansion).[16] Thermal

15. Elliptic flow is regarded as one of the most prominent signatures of the QGP. Nonetheless, measurements have indicated collective behavior in smaller systems as well [94,95]. This complicates the picture more than previously believed.

16. Photons not coming from hadronic decays are also called *direct* photons.

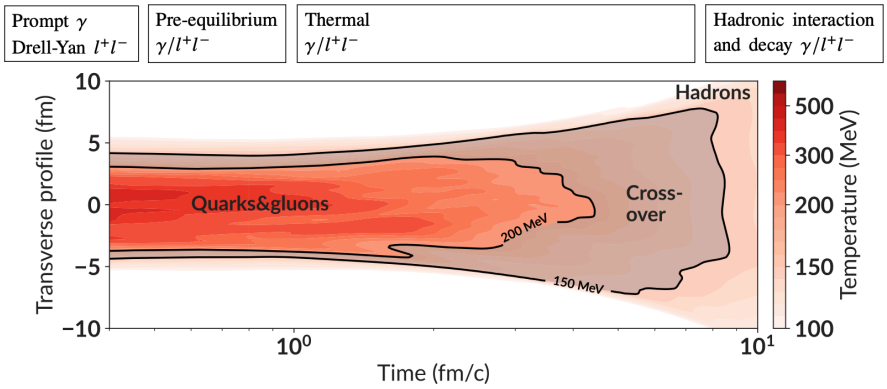


Figure 2.8: Figure depicting the various sources of photon and dilepton production at $\sqrt{s_{\rm NN}} = 200$ GeV. Figure taken from [6].

photon measurements provide constraints on the initial temperature and evolution of the QGP. Similarly, studying dilepton pair production allows us to probe the temperature of the QGP [101]. High $p_{\rm T}$ bosons (especially, W) can also help constrain nuclear PDFs (nPDFs) [102]. Additionally, studying boson-tagged hard probes (see Sec. 2.5.2) offers enhanced control over measurements of hard probes, allowing for a clearer distinction of underlying effects that can otherwise become convoluted.

Electro-weak probes are not generally utilized in this manner to study vacuum QCD.

### Hard Probes

Hard probes of the QGP, such as jets, heavy quarks, and quarkonia (heavy-flavor bound states of $q\bar{q}$ such as $J/\psi$ ($c\bar{c}$), $\Upsilon$(1S) ($b\bar{b}$) etc.),[17] originate from high-momentum transfer scatterings between partons. They are referred to as "hard" because they result from perturbative processes involving large momentum exchanges and hence, can be calculated via pQCD techniques. Formed during the initial scattering, before the formation of the QGP medium, these probes traverse and interact with the evolving

17. Note that heavy quarks are not produced thermally in the QGP since their masses are larger than the QGP temperature.

QGP.[18] As colored objects propagating through a colored medium, they experience energy loss due to interactions with the QGP. This energy loss is characterized by the transport coefficient $\hat{q} = d\langle k_\perp^2 \rangle / dL$, which quantifies the average transverse momentum broadening per unit path length induced by the medium [29]. Jets are collimated sprays of hadrons formed due to the iterative $1 \to 2$ splittings of a high-energy parton.[19] Their interaction with the medium leads to modifications in their spectra and internal structure, providing insights into the microscopic structure of the QGP. Jets will be discussed in detail in Chapter 3. Heavy quarks and quarkonia fall into what are called "'open heavy-flavor" and "hidden heavy-flavor" measurements, respectively. Open heavy flavor measurements, such as those of heavy-flavor mesons ($D$ meson, $B$ meson), probe the spatial diffusion coefficient, $D_S$,[20] which characterizes the long-wavelength properties of heavy-flavor transport in the QGP [105]. Sequential quarkonium suppression, as described in Sec. 2.4.2, probes the temperature evolution of the QGP [106, 107]. A detailed review of hard probes as tools to study the QGP can be found in [108].

In vacuum, jets form the background of many particle searches. This means that understanding them is crucial for enabling such measurements. Studies of heavy quarks help constrain heavy-flavor fragmentation [51] as well as their dynamics.

## 2.6 Goals of This Thesis

The goal of this thesis is to leverage hard probes, specifically jets, and a novel jet substructure observable known as the $N$-point Energy Correlator, to gain deeper

18. One can think of this as performing a scattering experiment, where the hard probes scatter through the QGP and their modification reveals information about the medium.

19. This includes jets initiated by heavy-flavor quarks as well. Also called heavy-flavor jets.

20. In the QGP, heavy quarks undergo Brownian motion. The diffusion coefficient encodes their interaction with the QGP [103, 104].

insights into the internal structure of QCD jets, both in vacuum and in the medium. The unique analytical framework of these observables, derived from first-principles quantum field theory, enables a direct connection to the strong coupling constant, $\alpha_s$. Additionally, this thesis aims to explore how the substructure of jets is modified in the presence of the QGP, using this observable to probe the effects of the medium on jet properties.

# Chapter 3

# Jets as Probes of QCD

## 3.1 Jet Physics

*Here, I give a brief overview of jet physics and an intuitive picture of why jets are useful in teaching us about QCD dynamics.*

With access to high energies via collisions at the LHC (i.e., when the strong force is weak), there has been rapid growth in the variety of questions that can be asked and how to ask them. This has led to the emergence of new subfields within the particle and nuclear physics community. One such subfield is jet substructure and is the focus of this thesis.

As mentioned in Chapter 2, quarks and gluons can never be observed directly due to color confinement. What is observed in collider experiments are color-singlet hadrons. Thus, to explore the dynamics of these quarks and gluons, we use high-energy collisions between protons or heavy-ions.[1] During these high-energy collisions, the partons inside the nucleons may participate in a high-momentum ($Q^2$) exchange scattering. The high momentum transfer in these "hard" scatterings causes the scattered quarks and gluons to undergo successive splittings and shed their "virtu-

1. Jets also appear in $e^+e^-$ collisions, where they provide a clean environment to study QCD through the process $e^+e^- \to q\bar{q}$, mediated by the production of virtual photons.

ality" until they reach the hadronization scale $\Lambda_{\text{QCD}}$ ($\mathcal{O}(1\text{ GeV})$) where confinement kicks in. This evolution is depicted in Fig. 3.1. Due to the collinear divergence[2] of

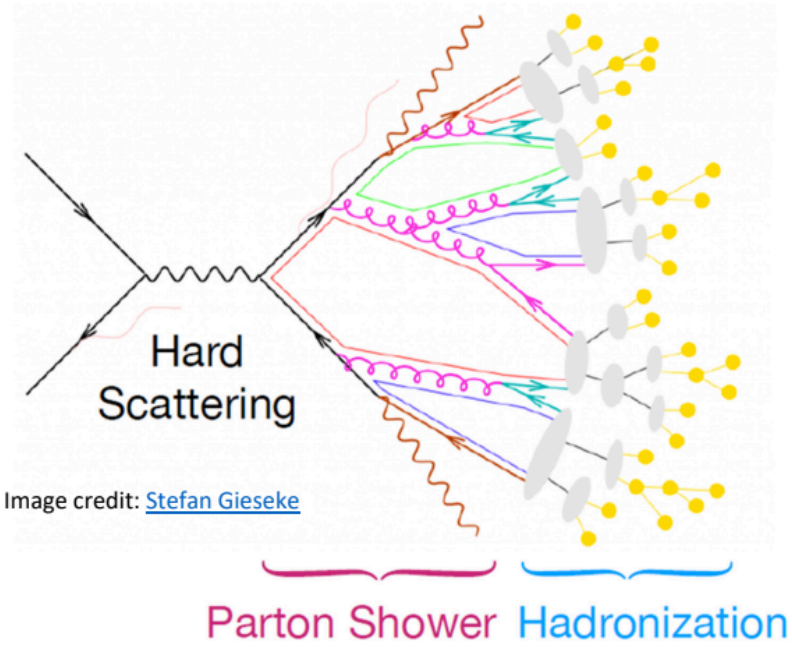


Figure 3.1: Jet evolution depicting how a final state quark from a hard scattering successively showers, leading to hadronic jet production.

QCD—meaning that splittings collinear to the parton are more probable—successive splittings tend to cluster around the initial quark or gluon that initiated the shower. Furthermore, because of momentum conservation, dijet events are most common. If instead, QCD were strongly coupled at high energies, the fragmentation pattern of the jet would be more isotropic, as shown in Fig. 3.2, due to a more even splitting where the momentum fractions of the daughters are roughly equal [7].

Jets have been observed at a wide range of energy scales, from orders of about ∼10 GeV (at DESY) [109] to ∼1 TeV (at the LHC) [110,111] and offer us an insight into the dynamics of quarks and gluons. They are a feature of weakly coupled gauge theories (in this case, QCD) that are dominated by collinear splittings at weak coupling (high energies). Thus, studying jets and their radiation pattern, i.e., jet substructure, can

2. This is discussed in more detail in Sec. 3.2.1.

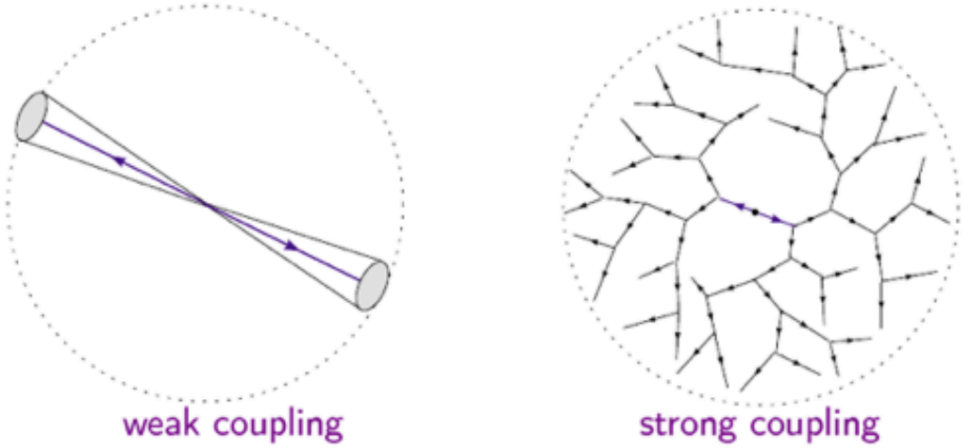


Figure 3.2: Jet evolution at weak vs strong coupling depicting how QCD jets are a feature of the partonic degrees of freedom. Figure taken from [7].

illuminate the dynamics of partons that we cannot observe directly. In a heavy-ion collision, jets serve as tools to study the properties of the medium. Their modification compared to vacuum QCD provides valuable insights into the microscopic properties of the QCD medium.

## 3.2 Jets in Vacuum QCD

### 3.2.1 Theoretical Overview

Jet measurements are often compared to two kinds of theoretical predictions—one coming from analytic calculations and the other coming from models that rely on Monte Carlo Event Generators. Although the implementation is slightly different, both of these techniques rely on QCD bremsstrahlung. The essential ingredients that enable such comparisons are briefly outlined here. A comprehensive review is provided in [112].

### Analytic Calculations

Theoretically, the key property that enables pQCD calculations of jets is known as the collinear factorization property of QCD [113]. Collinear factorization applies when the angle between two particles $(i, j)$ becomes smaller than any other angle between them and other particles. It enables the decomposition of an $N$-point calculation of an S-matrix element into a product of an $(N-1)$-point calculation and a collinear piece of the form

$$|\mathcal{M}(p_1, \ldots, p_i, p_j, \ldots, p_N)|^2_{i||j} \propto \alpha_s P_{(ij)\to ij}(z) |\mathcal{M}(p_1, \ldots, p_{(ij)}, \ldots, p_N)|^2 + \ldots \quad (3.1)$$

where $P_{(ij)\to ij}(z)$ are the $1 \to 2$ Dokshitzer-Gribov-Lipatov-Altarelli-Parisi (DGLAP) splitting functions [52–54].[3] In the matrix calculation, the momenta of particles $i, j$ are replaced by a single particle with the sum of their individual momenta $(i, j)$. This factorization is depicted in Fig. 3.3. The DGLAP splitting functions are universal functions that encode the splitting probability distribution of the energy fraction $z$ carried by the particle $i$ in the splitting. At leading order, they take the form shown in Equation 3.2 below

$$\begin{aligned}
P_{q\to qg}(z) &= C_F \left[\frac{1+(1-z)^2}{z}\right], \\
P_{q\to gq}(z) &= C_F \left[\frac{1+z^2}{(1-z)_+}\right], \\
P_{g\to q\bar{q}}(z) &= T_R \left[z^2 + (1-z)^2\right], \\
P_{g\to gg}(z) &= C_A \left[\frac{z}{(1-z)_+} + \frac{1-z}{z} + z(1-z\right] + \delta(1-z)\frac{(11C_A - 4n_f T_R)}{6}
\end{aligned} \quad (3.2)$$

3. In principle, $1 \to n$ splitting functions are also calculable and $1 \to 3$ splitting functions already exist in literature [114, 115].

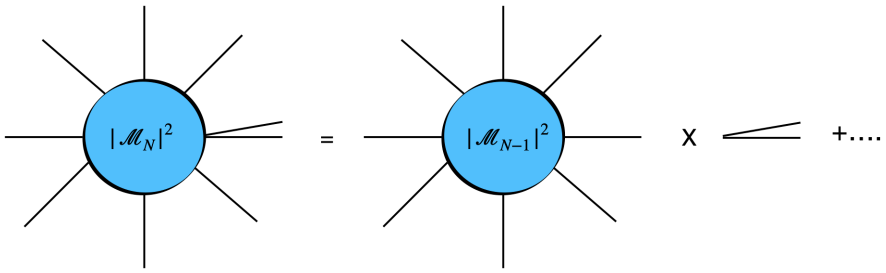


Figure 3.3: QCD factorization in the collinear limit depicting the decomposition of an $N$-point calculation of an S-matrix element into a product of an $(N-1)$-point calculation and a collinear piece.

The "+" is defined as $\int_0^1 \frac{f(x)}{(1-x)_+}\,dx = \int_0^1 \frac{f(x)-f(1)}{1-x}\,dx$, for a generic function $f(x)$. $n_f$ refers to the number of active[4] quark flavors, while $C_i$ are Casimir color factors which come from the color algebra associated with QCD. $C_F = \frac{4}{3}$ for quarks and $C_A = 3$ for gluons and $T_R = 1/2$ by convention. Thus, Equation 2.9 can be modified, at leading order, for jets as

$$\frac{d\sigma^{(0)}}{d\mathcal{O}} = \frac{\alpha_s}{\pi}\int \frac{d\theta}{\theta} dz\, P_{(ij)\to ij}(z)\,\delta\left(\mathcal{O} - \hat{\mathcal{O}}(z,\theta)\right) \tag{3.3}$$

These splitting probabilities (at leading order) are then as shown in Equation 3.4

$$p(z,\theta)dzd\theta \propto \frac{\alpha_s}{\pi} dz P_{(ij)\to ij}(z)\frac{d\theta}{\theta} \tag{3.4}$$

Furthermore, when $z$ tends to 0, the splitting functions take the form

$$p(z,\theta)dzd\theta \propto \frac{\alpha_s C_i}{\pi}\frac{dz}{z}\frac{d\theta}{\theta} \tag{3.5}$$

4. "Active" refers to the quark flavors whose masses are below the energy scale being probed.

where $C_i$ is a color factor of the parton $i$. This density becomes large under two conditions: i) $z \to 0$ (soft limit) and ii) $\theta \to 0$ (collinear limit). This is where *infrared and collinear safety* (IRC safety) [31] becomes a guiding principle for constructing jet observables. IRC safety ensures that emissions of infinitely soft or exactly collinear nature do not lead to divergences in analytic calculations, keeping the cross-sections finite. Thus, it is useful to construct jet observables that are IRC-safe and can be computed using pQCD techniques.

With the expression for the splitting probability in hand, it becomes natural to visualize the internal structure of a jet in terms of the logarithmic variables $(log(1/\theta), log(1/z))$. This representation is commonly known as the Lund Plane [116]. In experimental analyses, one typically constructs the Primary Lund Plane [117,118], which is populated by recursively following and recording the successive splittings along the harder prong at each branching step during the declustering of a jet. The "primary" designation refers specifically to this procedure of tracing the most energetic branch backward through the jet's fragmentation history. This method provides a powerful way to map out the phase space of QCD splittings, with different physical processes preferentially populating distinct regions of the plane. The characteristic features of such splittings are illustrated in the right panel of Fig. 3.4. Scanning along the $x$-axis takes us from wider to narrower splittings, while scanning along the y-axis takes us from uneven to even splittings. In this representation, diagonal lines with negative slope correspond to contours of constant transverse momentum $k_{\mathrm{T}}$ (since taking the logarithm of $1/k_{\mathrm{T}} \approx 1/z\theta$ gives $-\log k_{\mathrm{T}} \approx \log(1/z) + \log(1/\theta)$), revealing the interplay between angular and momentum scales in the jet. For example, the underlying event sits at the upper left corner while the hard collinear splittings sit at the bottom right. Additionally, at leading order, the density of emissions in the Lund Plane is proportional to the strong coupling constant $\alpha_s$ [116] as is shown in Equation 3.5. The Lund Plane has been experimentally measured at ALICE [119],

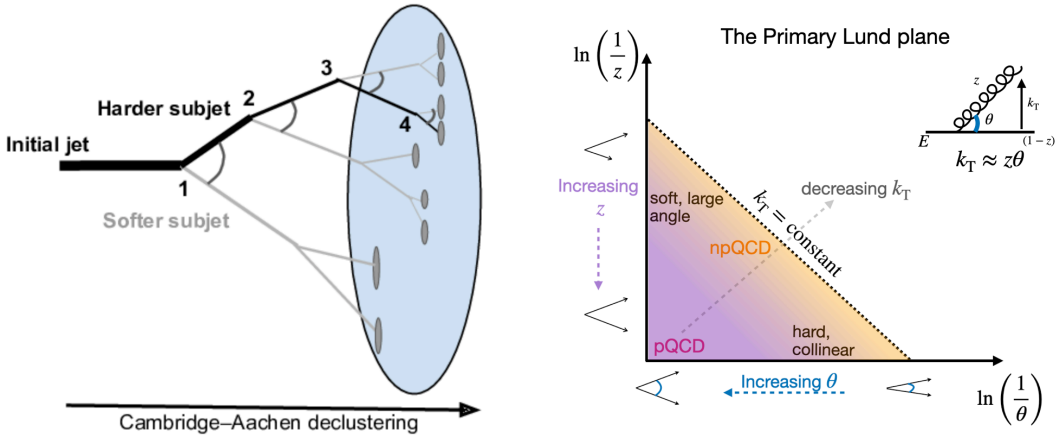


Figure 3.4: Left: Figure depicting how a jet is declustered to create the Primary Lund Plane. The darker prong is considered to be the core, while the grey prong is considered to be an emission at each step in the declustering process. Figure taken from [8]. Right: The Primary Lund Plane depicting the different emission regions in a jet. The figure on the top right depicts an example of a $q \to qg$ splitting.

ATLAS [120], and CMS [8]. Later in this thesis, I will discuss another observable, the $N$-point Energy Correlator (ENC), which offers us a new way to visualize jet evolution.

### Monte Carlo (MC) Event Generators

Jet measurements are often compared to simulations that use splitting function probabilities to describe the evolution of a parton from high virtuality down to the hadronization scale. The main ingredients of an event generator are described below:

- Hard Process: The hard process refers to the initial scattering between incoming partons. The kinematics of the particles produced from the hard scattering are calculated using perturbation theory.

- Parton Shower: Parton showers model how a hard scattering process is progressively dressed with additional emissions that are increasingly soft (lower energy) or collinear (smaller angle). This recursive process builds an approximate yet realistic picture of the partonic structure across all perturbative resolution scales,

starting from the hard scale and evolving down to a cutoff near the hadronization scale. At each step, the number of partons typically increases by one, occasionally by two. The parton shower encompasses both *Initial State Radiation* (ISR), which refers to radiation emitted by incoming partons prior to the hard scattering, and *Final State Radiation* (FSR), which describes radiation emitted by the outgoing partons following the hard interaction. For further details, see [121].

- Hadronization: Since final state partons need to hadronize, event generators need to employ hadronization models. Thus, one needs a general prescription to go from partonic degrees of freedom to hadronic degrees of freedom. Two commonly used models are the Lund-String model (implemented in a popularly used MC event generator called PYTHIA [122]) and the Cluster model (implemented in another popularly used MC event generator called HERWIG [123]). These are shown in Fig. 3.5. The Lund String models hadronization via a color string, akin to a stretched rubber band, that connects partons. As the string stretches and its energy increases, it "breaks," producing quark-antiquark pairs that form hadrons (e.g., mesons or baryons). This iterative process distributes the string's energy among the hadrons, constrained by kinematics. The model combines a Coulomb-like term for short-range forces with a linear term for string tension. In contrast, the Cluster Model describes hadronization as partons grouping into color-neutral clusters after high-energy collisions. These clusters, typically quark-antiquark pairs or three-quark systems, form due to a linearly growing potential. The clusters then decay into hadrons (mesons or baryons), preserving color-neutrality.

- Underlying Event (UE): This refers to the activity in a hadron collision that is not directly associated with the hard scattering process, often resulting from

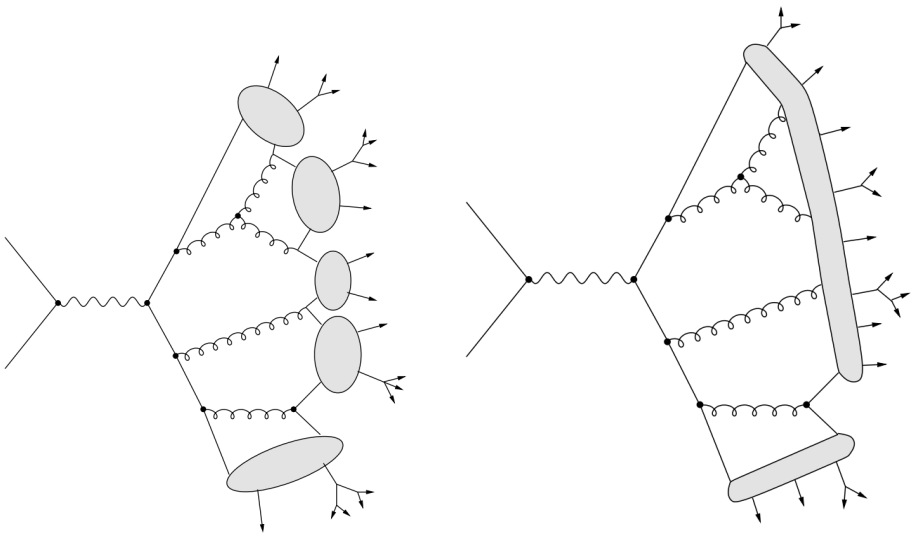

Figure 3.5: Left: Depiction of the Lund-String hadronization model. Right: Depiction of the Cluster hadronization. Figure taken from [9].

*multiple parton interactions* (MPI) [124] and beam remnants. The UE is composed of both soft and semi-hard physics.

- Hadronic Decays: After hadronization, all unstable hadrons undergo decay so that the final output of event generators is stable hadrons.

A diagrammatic sketch of the processes encoded in an event generator is shown in Fig. 3.6.

## 3.3 How to Find Jets?

There is some arbitrariness in how jets are defined. For example, there is no clear definition of what "collimated" means. From a theoretical point of view, there exists no inherent cut-off angle that determines whether a particle should belong to one jet or another. This makes it difficult to determine if a particle belongs to one jet or another. Additionally, the effects of all physical processes, perturbative (including FSR, ISR, and MPI), and non-perturbative (including UE and hadronization), need to be considered since they contribute to particles inside jets [44].

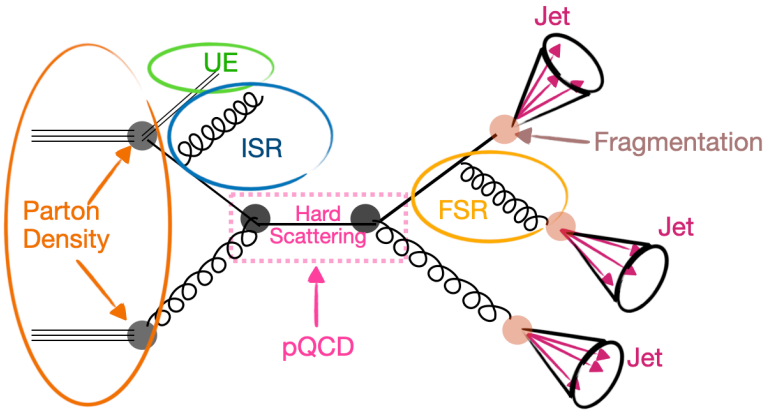


Figure 3.6: An illustration of some of the perturbative and non-perturbative processes modeled by MC Event Generators. Figure adapted from [10].

To overcome these challenges, considerable effort has been devoted to developing systematic definitions for jets [117]. These definitions, commonly known as *jet algorithms*, are designed with experimental viability in mind so that theoretical pQCD calculations can be accurately mapped onto experimental analyses. In constructing these algorithms, a key theoretical constraint is IRC safety.[5]

### 3.3.1 Jet Algorithms and Experimental Jets

Jet algorithms require two key ingredients to be defined:

- Jet Radius: The first ingredient of any jet clustering algorithm is the jet resolution parameter or jet radius, $R$. This parameter defines a distance in the $(y, \phi)$ plane such that if for two particles $(i, j)$, $R_{ij} > R$ then they do not belong to the same jet. This is how we practically define what we consider "collimated" or collinear.

5. More recently, there has been a shift toward track-based observables due to improved tracking resolution in experiments [125]. While these observables are IRC unsafe, they might offer more precise measurements of jet substructure. Even the observable measured in this thesis, although IRC safe theoretically, is constructed to be IRC unsafe experimentally for better measurement. See discussion in Sec. 6.2.2.

- Recombination Scheme: The second ingredient is a recombination scheme—which specifies how overall jet properties are determined from its constituents. The scheme used for jet reconstruction in this thesis is called the *E-scheme*, which determines jet properties by summing the components of the constituents' 4-momentum vectors.

Once these ingredients have been defined, jet reconstruction in experiments is achieved through the application of jet-finding algorithms. Over the past two decades, IRC safe jet algorithms have been extensively studied and developed [117, 126, 127]. In experiments, jets are reconstructed by applying these algorithms to the final state hadrons detected during a collision event. There are two kinds of jet algorithms—sequential clustering algorithms and cone algorithms [117]. Sequential clustering algorithms are generally employed in hadronic collisions [128], which are a focus of this thesis. There are three variables that are considered for jet reconstruction $d_{ij}$, $d_{iB}$, $\Delta R_{ij}$, and $R$

$$d_{ij} = min(p_{Ti}^{2p}, p_{Tj}^{2p}) \frac{\Delta R_{ij}^2}{R^2} \tag{3.6}$$

$$d_{iB} = p_{Ti}^{2p} \tag{3.7}$$

where $R$ is the radius of the jet, $d_{iB}$ is the distance from the beam, $p_{Ti}$ is the transverse momentum of the particle, and $\Delta R_{ij}$ is the distance between two particles in the $y$-$\phi$ plane, as described in Equation 2.13. For specific values of p, we get the $k_{\mathrm{T}}$ ($p = 1$), Cambridge/Aachen ($p = 0$), and anti-$k_{\mathrm{T}}$ ($p = -1$) jets [129]. The general procedure for finding jets follows the following workflow:

1. For each pair of particles $i$ and $j$, calculate $d_{ij}$ and $d_{iB}$.

2. Find min($d_{ij}$,$d_{iB}$). If the minimum value is $d_{ij}$, combine these "particles" into a composite one.[6] If the minimum value is $d_{iB}$, then this collection of particles

6. More information about recombination schemes can be found in [129].

forms a "jet" object and these particles are removed from the event particle list.

3. Steps 1 and 2 are repeated until the event particle list is exhausted.

The best jet definition is informed by the physics goals of the measurement. In the case of vacuum QCD measurements, anti-$k_{\mathrm{T}}$ jets are widely used because they identify the hardest prong first. In the case of Pb-Pb collisions, $k_{\mathrm{T}}$ jets are also used to estimate the soft underlying event and perform a pedestal subtraction, this will be discussed in more detail in Chapter 8. Additionally, experiments also use the terms "full" jet and "charged" jets. Full jets are reconstructed from all particles, both neutral and charged, whereas charged jets are reconstructed only from charged particles. This is generally due to experimental constraints such as detector resolution and statistics. The work in this thesis uses charged jets.[7]

## 3.4 Jets as Proxies for Partons

Since we use hadronic jets to investigate the dynamics of quarks and gluons, assessing how accurately a jet serves as a proxy for its initiating parton is important. To do so, we must identify the factors that shift the jet's transverse momentum relative to that of the original parton. The primary contributors to this discrepancy are FSR, hadronization, and the UE. While FSR and hadronization tend to remove energy from the jet (by removing particles out of the jet cone), the UE typically adds energy to the jet (by adding particles to the jet cone) [130, 131].[8] The average shift in $p_{\mathrm{T}}$ between the original parton and the reconstructed jet ($\langle \delta p_{\mathrm{T}} \rangle$) induced by these effects at leading order is tabulated in Table 3.1. The total shift in the jet transverse momentum can be approximated as an uncorrelated sum of three primary effects:

7. This is because ALICE tracking detectors offer great angular and momentum resolution as is discussed in Sec. 5.2.2. Additionally, the ALICE EMCal does not provide full azimuthal coverage, limiting the statistics available for jet substructure measurements.

8. Ref. [131] contains a pedagogical calculation of these effects.

hadronization, UE, and perturbative corrections. Notably, increasing the jet radius $R$ enhances the jet's sensitivity to contamination from the UE, leading to the inclusion of soft, wide-angle radiation that is unrelated to the hard scattering process associated with the initiating parton. On the other hand, a larger jet radius tends to suppress hadronization corrections, as more of the nonperturbative final-state radiation is captured within the jet. These effects also vary with flavor, where larger color factors, $C_i$ (such as for gluons), cause a larger impact on this shift. Finally, the parton $p_{\mathrm{T}}$ impacts this shift via its effect on FSR. These competing dependencies imply that careful consideration must be given to the choice of jet radius when comparing experimental jet measurements to pQCD predictions, as the balance between perturbative and nonperturbative contributions can significantly affect the interpretation of the observed jet properties [132].

| **Physical Effect** | **Parton $p_T$** | **Color Factor** | **Jet radius ($R$)** |
|---|---|---|---|
| FSR | $\sim \alpha_s(p_T)p_T$ | $C_i$ | $\ln R + \mathcal{O}(1)$ |
| Hadronization | – | $C_i$ | $-1/R + \mathcal{O}(R)$ |
| UE | – | – | $R^2/2 + \mathcal{O}(R^4)$ |

Table 3.1: Main physical effects contributing to a shift $\langle \delta p_T \rangle$ in the transverse momentum of a jet compared to its parent parton in $pp$ collisions at LO. Table taken from [29].

## 3.5 Jets in the QGP

Previously, I discussed how jets evolve in a vacuum and how their substructure reveals the dynamics of their constituent partons. The situation becomes more intricate in the presence of a colored medium such as the QGP. As a jet traverses the QGP, it loses momentum—a process known as jet quenching (originally proposed by Bjorken as a QGP signature in an unpublished 1989 paper [69]). Additionally, the medium itself responds to the jet—a phenomenon referred to as medium response [133, 134]. The interaction of the jet with the strongly coupled medium also leads to modifications in

their internal structure relative to jets in a vacuum. Because jets interact with and are modified by the QGP, they serve as powerful probes of the medium's properties [135, 136], providing insights into phenomena ranging from initial state effects to the hydrodynamization of the QGP. This approach is analogous to scattering experiments, where the modifications observed in the probe yield valuable information about the object being investigated.

### 3.5.1 Jet and Jet Substructure Modification in the QGP

Jet quenching reveals itself through a variety of observables. The modifications experienced by jets traversing the QGP can be broadly classified into two categories: changes at the jet level and alterations in jet substructure. At the jet level, phenomena such as jet suppression—arising from energy loss—and deflection of the jet axis due to scatterings in the QGP are observed. In the following discussion, I explore how jet quenching influences both the overall jet properties and its internal substructure. *While I have subdivided these effects into jet and substructure modification, it is understood that modification of one invariably affects the other.*

#### Jet Modification in the QGP

One of the first signatures of QGP formation was jet quenching, i.e., the suppression or disappearance of jets due to energy loss suffered by the initiating parton [69]. Thus, studying this energy loss can provide valuable information about the properties of the plasma. A jet loses energy in the QGP by two primary processes: *collisional energy loss* (elastic scatterings, dominate at low particle momentum) and *radiative energy loss* (inelastic scatterings, dominate at high particle momentum) [29]. From a theoretical point of view, it is assumed that pQCD factorization still holds in the QGP with the modification due to the presence of the medium being encoded in fragmentation functions. All jet quenching models rely on this assumption [7]. Jet

quenching models generally have a single parameter that is tuned to data. A summary of these models categorized based on what they calculate is shown in Table 3.2.

| **Category** | **Formalisms / Models** |
|---|---|
| Radiated gluon spectrum | BDMPS-Z (Baier-Dokshitzer-Mueller-Peigné-Schiff-Zakharov) [137, 138] |
| | DGLV (Gyulassy-Levai-Vitev) [139] |
| | ASW (Armesto-Salgado-Wiedemann) [140] |
| Change in final distribution of partons | AMY (Arnold-Moore-Yaffe) [141] |
| | HT (Higher Twist) [142] |
| Drag force | AdS/CFT (strong coupling limit) [143] |

Table 3.2: Classification of jet quenching models.

Experimentally, jet quenching has been confirmed both at RHIC [144] and at the LHC [145–149] by measuring the suppression of jets as compared to expectations from pp collisions. These measurements have also been extended to studying the jet radius dependence of jet energy loss [150]. Beyond energy loss, it has been proposed that the jet axis may undergo deflection due to either point-like Molière scattering [151] or multiple soft scatterings [152], depending on the thickness of the medium. Such effects have been investigated through jet acoplanarity measurements [153,154], which study the trigger-normalized distribution in $\Delta\phi$ of jets recoiling from a high-$p_{\mathrm{T}}$ trigger hadron.[9]

### Jet Substructure Modification in the QGP

Due to the interaction of the jet with the medium and the subsequent reaction of the medium to the jet, the internal structure of jets can also be modified. This may manifest itself in several ways, such as *momentum broadening* where, due to radiative and collisional interactions with the medium, higher momentum final state particles get shifted to lower momentum, causing a "broadening" of the jet [155]. Radiative energy loss due to inelastic collisions with particles in the medium may cause gluonstrahlung

9. Recent measurements [154], however, have attributed the observed broadening primarily to the effects of the medium wake rather than to point-like scatterings.

(gluon radiation), leading to *medium-induced splittings*. These splittings, modeled via modified DGLAP splitting functions to account for medium-induced emissions, would then modify the substructure of a jet. Effects coming from the medium's resolution length ($L_{\text{res}}$), i.e., the length at which it can resolve independent sources of color charge, would also modify substructure. If $L_{\text{res}}$ exceeds the typical size of the jet's substructure, the medium perceives the jet as a single, coherent object—a phenomenon known as color coherence. Conversely, if the medium can resolve the jet's internal structure, it will treat the jet as composed of multiple independent targets, leading to color decoherence [156]. Finally, the interaction of the jet with the medium can induce a *wake* of soft particles that may enter the jet cone and modify the substructure of the jet.[10] Wake effects are most prominent at large distances from the jet axis. Medium response effects are modeled via a Monte Carlo approach with different approximations in models such as JEWEL [157, 158] (includes a BDMPS based medium-induced gluon radiation in a medium with a Bjorken expansion i.e., longitudinal 1D expansion), JETSCAPE [159] (a modular framework which incorporates a medium-modified shower as well as medium response), LBT [160] (includes momentum broadening and medium-induced splitting). The Hybrid model [143] includes modified fragmentation and an AdS/CFT [58] based approach to incorporate hydrodynamic wake effects. This will be discussed in more detail in Chapter 7.

## 3.6 Jet and Jet Substructure Measurements

### 3.6.1 Measurements in vacuum

*The measurements listed here are not meant to be exhaustive. They help contextualize the plans for $\alpha_s$ extraction with the measurement in this thesis, which will be detailed in Chapter 6.*

10. Wake effects will be discussed in detail in Chapter 7.

### $\alpha_s$ Extraction from Jet Cross-Sections

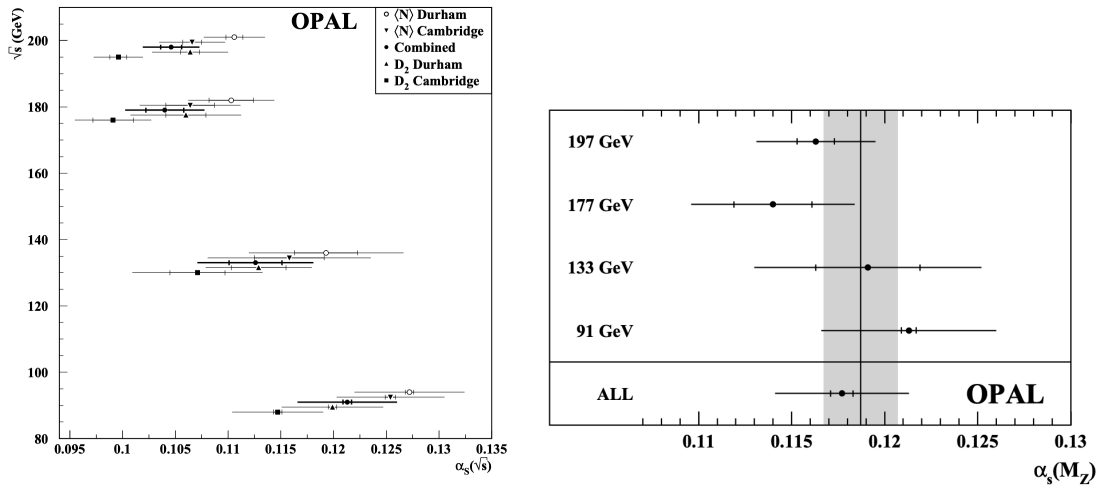


Figure 3.7: Left: $\alpha_s$ as a function of $\sqrt{s}$ using two-jet rate measurements ($D_2$) and average jet rate measurements ($\langle N \rangle$) with the OPAL detector. Right: $\alpha_s$ determination from the measurements shown in the left panel. Figures taken from [11].

The strong coupling constant, $\alpha_s$, governs the strength of the strong nuclear force. From the renormalization group, we know that $\alpha_s$ evolves with energy, as shown in Fig. 2.3. However, it cannot be measured directly in experiments. Instead, the common approach is to analyze observables known to depend on $\alpha_s$, compare theoretical predictions at different energy scales, and determine which best aligns with experimental data. Numerous measurements of $\alpha_s$ have been conducted, for a review see [1]. At $e^+e^-$ colliders, for example, jet rate measurements, $R_n$—the ratio of events with $n$ jets to the total number of events—have been a key method for extracting $\alpha_s$.[11] In the left panel of Fig. 3.7, the values of $\alpha_s$ as a function of $\sqrt{s}$ are plotted. The differential two-jet rate ($D_2$)[12] and the average jet rate ($\langle N \rangle$) were measured. The labels "Durham" and "Cambridge" refer to the different clustering algorithms used

11. This is because $R_n$ can be expanded as a power series in $\alpha_s$. For more details, see [161].

12. In this context, *differential* refers to analyzing the hadronic final state of each event by applying a jet clustering algorithm with a variable resolution parameter. The algorithm continues merging particles until only two jets remain. The key observable is then defined as the maximum value of the resolution parameter for which the event is still classified as having two resolved jets.

to find jets. The change in $\alpha_s$ as a function of $\sqrt{s}$ depicts the running of the coupling discussed in Sec. 2.3. An average value of $\alpha_s$ was computed from the measurement as shown in the right panel of Fig. 3.7.

### Track Functions for Substructure Precision

Track functions ($r_q$) are non-perturbative functions that quantify the fraction of energy carried by charged hadrons (or *tracks*) from quark or gluon fragmentation in a jet [162–164]. They are defined as the ratio of the sum of momenta of charged constituents to the jet $p_{\mathrm{T}}$ (the jets in this case are full jets, i.e., composed of both neutral and charged particles). This approach is appealing because tracks offer superior angular resolution, leading to more precise measurements. However, the challenge lies in that such measurements are not inclusive (since they do not include neutral particles) and, as a result, are not IR-safe. A measurement of this observable by the ATLAS collaboration [12] has demonstrated the potential of these techniques. The measurement in a jet $p_{\mathrm{T}}$ bin at central rapidity is shown in Fig. 3.8. The width of the distribution highlights the challenge of mapping charged jets to full jets, as charged

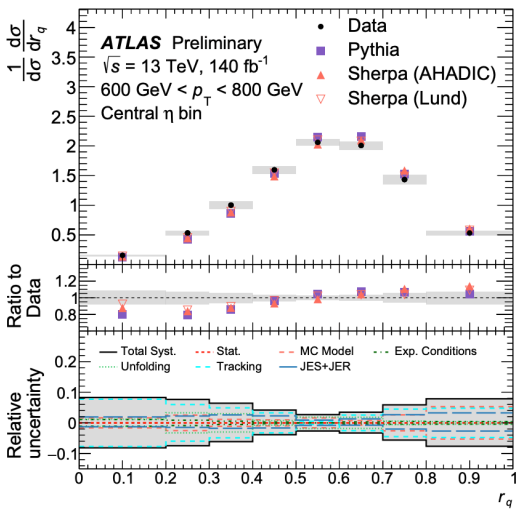


Figure 3.8: ATLAS track function measurement at mid-rapidity in pp collisions at $\sqrt{s} = 13$ TeV [12]. $r_q$ measures the momentum fraction of charged tracks in a full jet.

jets are more than just the charged particles within a full jet.[13] Theorists can use these measurements as input for pQCD calculations, thereby refining predictions for various processes.

### 3.6.2 Measurements in Heavy-Ion Collisions

*The measurements listed here are not meant to be exhaustive. Instead, they are described to contextualize the motivation for the phenomenological work detailed in Chapter 7 as well as the ongoing Pb-Pb measurement detailed in Chapter 8*

#### Jet Energy Loss

A major challenge in jet measurements in heavy-ion collisions is distinguishing between jet-medium interactions and *selection bias* [165, 166]. Selection bias favors narrower jets, which lose less energy in the QGP, complicating the interpretation of jet energy loss. As mentioned in Sec. 2.5.2, photon-tagged jet measurements help mitigate this issue, as the photon energy provides a reliable proxy for the energy of the quark initiating the jet. This also creates a quark-enriched sample, reducing ambiguities related to color factors. By studying the jet substructure as a function of momentum imbalance between the jet and photon, we can gain more insight into the underlying energy loss mechanisms. Such a measurement of the *groomed*[14] jet radius $R_{\mathrm{g}}$, which is defined as the angular distance between subjets (the two hardest prongs of a jet), was performed by the CMS collaboration [13]. $R_{\mathrm{g}}$ allows one to gain information about the resolution length of the medium as described in 3.5.1. Figure 3.9 shows the $R_{\mathrm{g}}$ distributions for two different jet selections. The left panel corresponds to a more inclusive sample, while the right panel focuses on jets that have experi-

13. For further discussion, see Sec. 6.6.2.

14. Grooming [167–169] is a technique that is used to access the perturbative hard parton splitting, which involves iteratively dropping the different components of a jet that do not satisfy certain "hardness" criteria.

enced less energy loss. The ratio to vacuum, shown in the bottom panels, reveals a clear narrowing of $R_g$ in the less quenched sample. This highlights the importance of selection bias in interpreting jet substructure modifications in heavy-ion collisions.

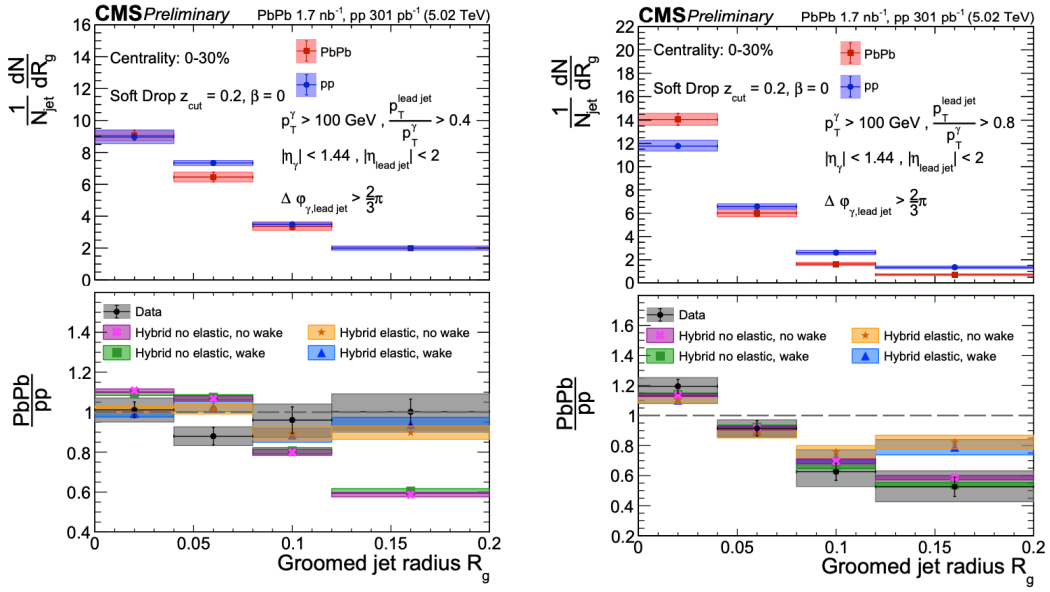


Figure 3.9: Measurement of the groomed jet radius, $R_g$ by the CMS collaboration [13]. Left: $R_g$ for both more and less quenched jets. The ratio in the bottom panel is largely consistent with unity. Right: $R_g$ for less quenched jets, depicting that a higher degree of quenching biases the jet sample to be narrower.

### Jet Induced Medium Response

In Sec. 3.5.1, the discussion focused on how jet-medium interactions can lead to medium-induced modifications of the jet structure. Specifically, such effects can manifest as an enhancement of particles in the direction of the jet, creating a wake of soft hadrons. In contrast, a depletion of particles in the direction opposite to the jet, known as the *diffusion wake*, may also occur. This diffusion wake signal would have an ($\eta$, $\phi$) structure as depicted by the depletion at $\Delta\eta = 0$ in the left plot of Fig. 3.10.

A recent ATLAS measurement [170] sought to detect the diffusion wake signal using jet-track correlations in photon-tagged jets. By tagging the photon, the analy-

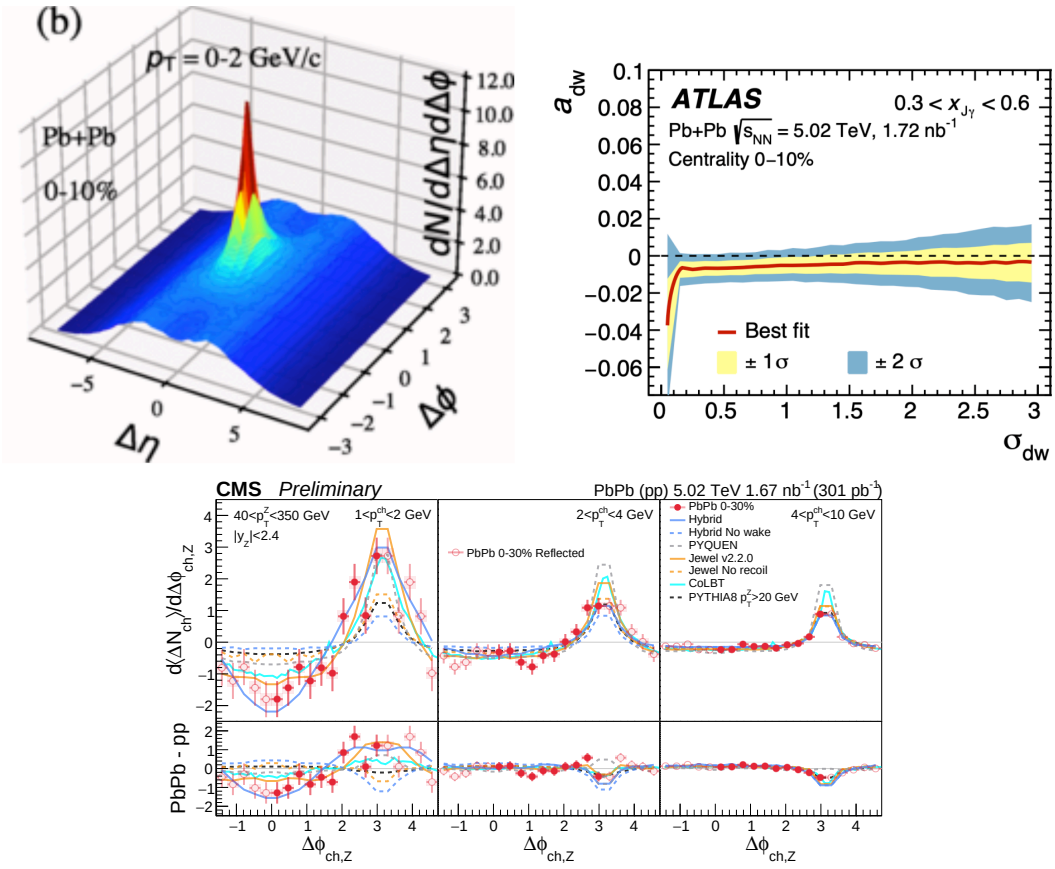


Figure 3.10: Top Left: Structure of jet-induced diffusion wake in the coLBT model [14]. Top Right: Measurement of the amplitude of the diffusion wake by ATLAS collaboration in Pb-Pb collisions at $\sqrt{s_{\rm NN}} = 5.02$ TeV. Bottom: Measurement of $Z^0$-tagged hadrons yields as a function of $\phi$ relative to the direction of the $Z^0$ boson by CMS collaboration in Pb-Pb collisions at $\sqrt{s_{\rm NN}} = 5.02$ TeV.

sis isolates the region opposite the jet, preventing overlap with the wake signal. The study measured the ratio of correlated to uncorrelated yields as a function of pseudo-rapidity distance from the jet but found no conclusive evidence, as the diffusion wake amplitude (see top right panel of Fig. 3.10) was consistent with zero. However, a similar CMS measurement using $Z^0$-tagged hadrons [171] did observe a signal corresponding to the diffusion wake (as shown by the depletion of soft hadrons around $\Delta\phi = 0$ in the left most plot of the bottom panel of Fig. 3.10), i.e., a depletion of particle yields along the direction of the $Z^0$ boson. This tension highlights the need for further investigation.

# Chapter 4

# Energy Correlators: A Revival Story

## 4.1 Correlation Functions in Physics

Correlation functions are fundamental tools studied across many areas of physics, as they provide insight into how different parts of a system are related or "correlated" with each other. In the most basic sense, a correlation function measures the statistical dependence between different degrees of freedom in a system, offering valuable information about the structure and behavior of the system as a whole. They are especially important in fields like statistical mechanics and condensed matter physics, where they are used to probe phase transitions and critical phenomena. A classic example is the 1-D Ising model, where spin-1/2 particles interact in a linear chain. At low temperatures, spins align, forming long-range correlations that signal a transition to the ferromagnetic phase. As the system approaches the critical temperature, the correlation length diverges, marking a phase transition from disorder to order. In cosmology, correlation functions help to understand large-scale structure and cosmic inflation. By analyzing cosmological correlators, which measure correlations in pri-

mordial density fluctuations, cosmologists test inflationary models and their impact on galaxy formation and the cosmic microwave background. Across disciplines, correlation functions provide deep insights into system evolution, from phase transitions in condensed matter to structure formation in the universe. In heavy-ion collisions, correlations allow us to study the collective behaviour of the QGP as described in Sec. 2.5.2. In the next section, I will explore how similar techniques are being applied to jet evolution from perturbative splittings to hadronization.

## 4.2 Energy Correlators: Theory

Energy correlators are a class of IRC-safe observables that measure the asymptotic energy flux. One can think of detectors that are on a celestial sphere (i.e., very far away from the collision) that read the energy deposited by particles after a high-energy collision. They are defined as correlation functions, $\langle\Psi|\mathcal{E}(\vec{n}_1)\mathcal{E}(\vec{n}_2)\cdots\mathcal{E}(\vec{n}_k)|\Psi\rangle$ of the energy flow operator [172–179]

$$\mathcal{E}(\vec{n}_1) = \lim_{r\to\infty}\int \mathrm{d}t\, r^2 n_1^i\, T_{0i}(t, r\vec{n}_1) \tag{4.1}$$

where $T_{ij}$ is the stress energy tensor. This detector, which is specified by a three-vector, $\vec{n}_1$, detects any particles whose momentum is along the direction specified by the unit vector $\vec{n}_1$, and measures their energy. Correlation functions of these operators are functions of the angles between the vectors $\vec{n}_i$ on the celestial sphere as shown in Fig. 4.1.

Energy correlator observables were first introduced to study the structure of the asymptotic energy flux in $e^+e^-$ colliders in Refs. [180–184]. These authors also computed the two-point correlator (also referred to as the Energy Energy Correlator or EEC or E2C) at leading order. Energy correlators have seen a revival for two major reasons:

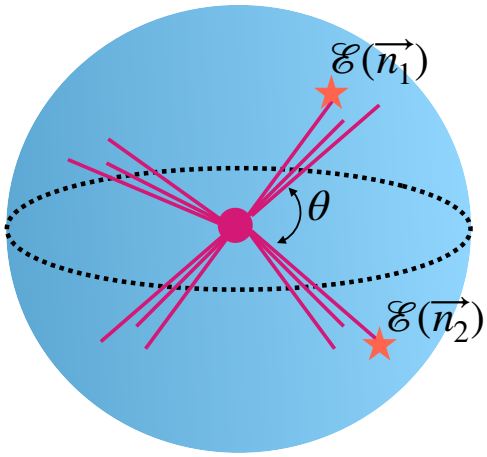


Figure 4.1: A visualization of detectors on the celestial sphere reading in the energy flux from a collision event. In this case, the angle $\theta$ represents $R_{\mathrm{L}}$ as discussed in the text, while $\mathcal{E}(\vec{n}_1)$ and $\mathcal{E}(\vec{n}_2)$ represent the energy flux, as defined in Equation 4.1, along directions $\vec{n}_1$ and $\vec{n}_2$, respectively.

- These observables are particularly appealing to theorists because they are accessible through multiple complementary approaches. On one hand, they are directly connected to correlation functions of local operators involving the theory's stress-energy tensor. On the other hand, they can be computed in the weak coupling regime using perturbative techniques such as form factors or scattering amplitudes. Moreover, in conformal field theories (as discussed in Sec. 4.2.1), they are amenable to non-perturbative analysis via the light-ray operator product expansion [179, 185].

- Experimentally disentangling perturbative from non-perturbative effects is a significant challenge in jet physics. Therefore, developing precise mappings of jet evolution is invaluable. This effort complements analyses of jet substructure, such as those utilizing the Lund Plane, as discussed in Sec. 3.2.1. Note that the Primary Lund Plane relies on declustering algorithms, whereas, as shall become clear over the next few chapters, the ENCs do not require any declustering. An additional advantage is that grooming, as described in Sec. 3.6.2, is also not

required for these observables.

Here, I want to describe some concepts that will be useful to understand the structure of these correlators in pQCD.

### 4.2.1 Operator Product Expansion (OPE)

In their seminal work, Maldacena and Hoffman [176] showed that one could relate the collider observables to objects in a conformal field theory (CFT). CFTs are quantum field theories that exhibit *conformal symmetry*, meaning they remain invariant under local angle-preserving (conformal) transformations. One can think of this as the theory in which the physics remains the same at every scale (scale invariant). A CFT is typically defined by a set of primary operators $\mathcal{O}_i(x)$ that transform under conformal transformations as

$$\mathcal{O}_i(x) \to \lambda^{-\Delta_i}\mathcal{O}_i(\lambda x) \tag{4.2}$$

where $\Delta_i$ is the scaling dimension of the operator. Correlation functions in a CFT are highly constrained by symmetry; for instance, the two-point function of a scalar primary operator in Euclidean space takes the form

$$\langle \mathcal{O}(x)\mathcal{O}(y)\rangle = \frac{C}{|x-y|^{2\Delta}} \tag{4.3}$$

Since QCD is approximately conformal at very high energies, we can use this language to discuss QCD phenomena. This forms the basis of the "scaling" behavior is discussed in the following sections.

### 4.2.2 Anomalous Dimensions

*A pedagogical discussion can be found in any standard QFT textbook such as [31].* Classical scaling dimensions describe how operators transform under spacetime rescaling, ensuring a dimensionless action in natural units ($\hbar = c = 1$). In a $d$-dimensional spacetime, the action takes the form

$$S = \int d^d x \, \mathcal{L} \tag{4.4}$$

where the Lagrangian density must have mass dimension $[\mathcal{L}] = d$. This determines the classical scaling dimensions of fields:

- Scalar field: $[\phi] = \frac{d-2}{2}$ from terms like $(\partial_\mu \phi)^2$.
- Fermionic field: $[\psi] = \frac{d-1}{2}$ from $\bar{\psi} i \gamma^\mu \partial_\mu \psi$.
- Gauge field: $[A_\mu] = \frac{d-2}{2}$ from $F_{\mu\nu} F^{\mu\nu}$.

These dimensions reflect naive power counting but are modified by quantum effects. Quantum interactions introduce *anomalous dimensions*, modifying classical scaling through renormalization. The anomalous dimension $\gamma$ of an operator $\mathcal{O}$ appears in its renormalization group evolution

$$\mu \frac{d}{d\mu} \mathcal{O} = \gamma \mathcal{O} \tag{4.5}$$

These corrections result from the scale dependence of coupling constants and fields. In QCD, anomalous dimensions govern scaling violations in deep inelastic scattering [186] and the running of parton distribution functions [187]. In CFTs, they determine deviations from naive scaling, affecting critical exponents and correlation functions. Anomalous dimensions also shape renormalization group flows, leading to non-trivial fixed points and insights into universality classes in statistical mechanics

and QFT.

### 4.2.3 Projected $N$-Point Energy Correlators

In the context of collider physics experiments, one can measure correlations in the energy flux $\langle \mathcal{E}(\vec{n}_1) \cdots \mathcal{E}(\vec{n}_k) \rangle$ as a function of the angles of the $\vec{n}$ vectors. These vectors are not required to be distinct (i.e., they could be collinear). The projected correlators were introduced in Ref. [188] for the purpose of focusing on the scaling behavior of the $N$-point correlators as a function of the overall angular scale set by $R_{\mathrm{L}}$ (the largest angle between any two out of $N$ particles). The projected $N$-point correlator, which is denoted as $\mathrm{ENC}(R_{\mathrm{L}})$, is defined by integrating out all the shape information of the correlator, keeping only $R_{\mathrm{L}}$ fixed

$$\mathrm{ENC}(R_{\mathrm{L}}) \equiv \left( \prod_{k=1}^{N} \int d\Omega_{\vec{n}_k} \right) \delta(R_{\mathrm{L}} - \Delta \hat{R}_{\mathrm{L}}) \cdot \frac{1}{(E_{\mathrm{jet}})^{(N)}} \langle \mathcal{E}(\vec{n}_1) \mathcal{E}(\vec{n}_2) \ldots \mathcal{E}(\vec{n}_N) \rangle \tag{4.6}$$

where $N$ represents the number of particles in the correlation. The two-point correlators have been computed at next-to-leading order (NLO) in QCD [189, 190], and NNLO in $\mathcal{N} = 4$ super Yang-Mills (SYM) [191, 192]. The three-point correlator has been computed in both the collinear limit [193], and at generic angles [194–196].

Crucial for the work contained in this thesis is the fact that ENCs exhibit a clear "scaling" behavior [15, 188] which can be written as

$$d\sigma^{[N]}/dR_{\mathrm{L}} \sim R_{\mathrm{L}}^{\gamma(N+1,\alpha_s)}/R_{\mathrm{L}} \tag{4.7}$$

where $N$ is the number of particles in the correlator and $\gamma$ is the anomalous dimension of the ENC operator. $1/R_{\mathrm{L}}$ is the classical scaling behavior of the ENC operators, while the quantum mechanical scaling behavior is encoded in the anomalous dimensions.

With this framework in mind, the left panel of Fig. 4.2 illustrates distinct scaling

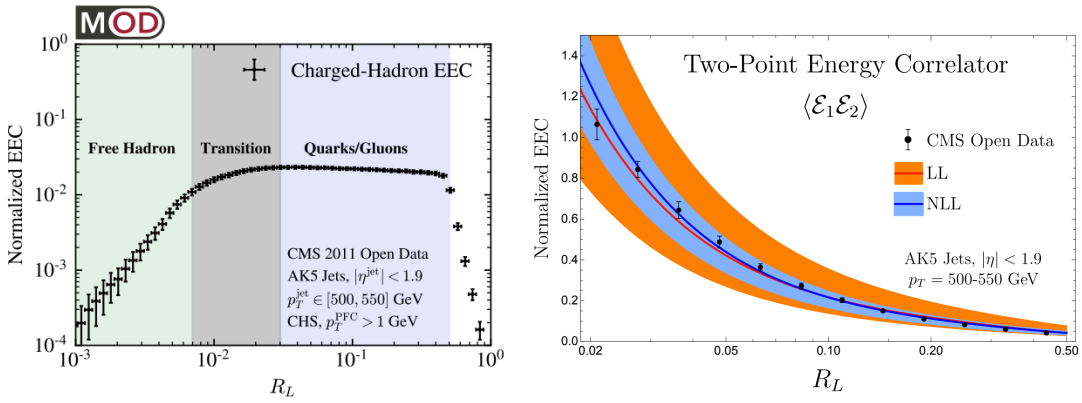


Figure 4.2: Left: The two-point energy correlator (EEC) computed with CMS Open Data. Figure taken from [15]. Right: Theoretical predictions for the EEC compared to CMS Open Data. The bands represent theoretical uncertainty. Figure taken from [16].

behavior consistent with theoretical predictions where the evolution of the jet as a function of $R_{\rm L}$ is imprinted in the slopes. At large values of $R_{\rm L}$, the distribution is dominated by perturbative partons. As $R_{\rm L}$ decreases, a transition region associated with hadronization emerges, eventually giving way to a regime of free-streaming, non-interacting hadrons. The characteristic slope observed in the free-streaming regime arises purely from geometric considerations. The right panel of Fig. 4.2 presents a comparison between leading-order (LO) and next-to-leading-logarithmic (NLL) theoretical predictions and the corresponding measurements obtained from CMS Open Data. This comparison is limited to the range of $R_{\rm L}$ where pQCD calculations are expected to provide a reliable description. Two predictions that are not obvious from the plot but will be discussed in Chapter 6 as part of this thesis work are:

- The transition region is roughly expected to scale with jet $p_{\rm T}$ as $p_{\rm T} R_{\rm L} \sim \Lambda$, where $\Lambda$ is a constant that is roughly related to the confinement scale [15].

- Consequently, at higher jet $p_{\rm T}$, the perturbative regime is anticipated to extend to smaller values of $R_{\rm L}$, reflecting the angular ordering[1] characteristic of QCD

1. Angular Ordering is a feature of vacuum QCD jets. This means that as the partons continue splitting, the iterative splitting will get smaller and smaller in angle with respect to the direction

jet evolution.

### Ratios of Higher Point Correlators to EEC

Since the ENC is dominated by classical scaling, the effects of quantum interactions can be enhanced by taking ratios of higher-point correlators to the two-point correlator. The ratio is given as

$$\frac{\frac{d\sigma^{[M]}}{dR_{\mathrm{L}}}}{\frac{d\sigma^{[N]}}{dR_{\mathrm{L}}}} \propto R_{\mathrm{L}}^{[\gamma(M+1,\alpha_{\mathrm{S}})-\gamma(N+1,\alpha_{\mathrm{S}})]} \tag{4.8}$$

The classical scaling behavior will cancel, leaving only the anomalous dimensions.[2] The shaded region in the left panel of Fig. 4.3 largely corresponds to the region where the NLL calculation is valid, as shown in the right panel. This distinct scaling behavior is a result of quantum mechanical interactions. These anomalous dimensions have a logarithmic dependence on $\alpha_s$, as shown in Equation 4.8, and the result is therefore directly proportional to $\alpha_s$ (plus higher-order corrections) [188,197]. This is analogous to two/three-jet ratios that are often used for measurements of the strong coupling as discussed in Sec. 3.6.1, but in the collinear limit within a jet. Note that fixing the overall normalization of these ratios is difficult from a theoretical perspective since it requires knowledge of the global phase space, while these observables are calculated in a limited kinematic region within a jet. Thus, the absolute $y$ values are not consequential. While the normalization can be arbitrary, the slopes or the "scaling" behavior encodes QCD dynamics.

There has been rapid growth on the theoretical front to extend these observables

of the parent parton. The angular ordering of QCD is a direct consequence of the partonic interactions [9]. This is a generic feature of any gauge theory (in the case of QED, this is called the *Chudakov effect* and leads to suppression of soft bremsstrahlung from electron-positron pairs).

2. The anomalous dimensions described here are not just numbers but $4 \times 4$ matrices of the QCD interactions.

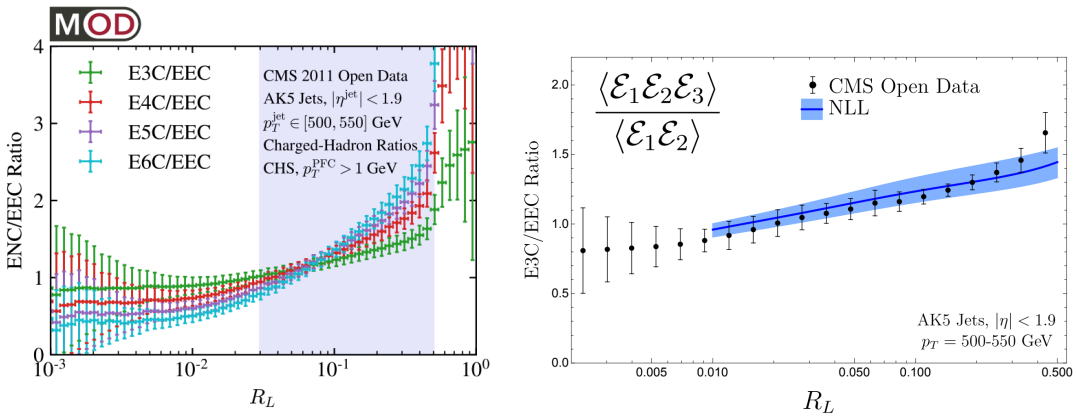


Figure 4.3: Left: Ratios of projected higher-point energy correlators to the EEC computed with CMS Open Data. Figure taken from [15]. Right: Theoretical predictions for the E3C/EEC ratio compared to CMS Open Data. The band represents theoretical uncertainty. Figure taken from [16].

to various collision systems[3] (p-A [198–201], A-A [24, 25, 202–204]), jet populations (heavy-flavor ENCs [205]) etc. Additionally, different types of energy correlators have been proposed to probe different effects—these include charged energy correlators [206], energy correlators for heavy-flavor jets [205], and IRC unsafe correlators[4] (where the energy weight is defined as $\langle \Psi | \mathcal{E}^m(\vec{n}_1)\mathcal{E}^m(\vec{n}_2)\cdots\mathcal{E}^m(\vec{n}_k)|\Psi\rangle$ with $m \neq 1$) which probe more of the soft or hard phenomena [17].

### 4.2.4 Full Shape Dependent Three Point Correlator: EEEC

In addition to the scaling behavior captured by projected energy correlators, higher-point correlators encode a wealth of structural information. The first correlator to exhibit non-trivial shape dependence is the three-point Energy-Energy-Energy Correlator (EEEC), originally computed in the context of elementary particle collisions [193] and then analyzed using CMS Open Data by authors in [15]. This correlator depends on three angular separations—$R_{\text{L}}$, $R_{\text{M}}$, and $R_{\text{S}}$—which correspond to the largest, in-

3. One such effort will be discussed in Chapter 7.

4. CMS has measured the two-point correlator with $m = 2$ in pp and Pb-Pb collisions [207].

termediate, and smallest pairwise angles among the three particles. In contrast, the projected three-point correlator considers only the largest angle, $R_{\mathrm{L}}$.

To disentangle overall scale from shape, it is helpful to factor out the dominant scaling, which is governed by the largest angle $R_{\mathrm{L}}$, and instead describe the geometry of the correlator using the triangle formed by the three angles. As outlined in Ref. [15], when analyzing jets that evolve purely in vacuum, it is natural to characterize the shape using the variables $(R_{\mathrm{L}}, \xi, \phi)$, where

$$\xi \equiv \frac{R_{\mathrm{S}}}{R_{\mathrm{M}}}, \qquad \phi \equiv \arcsin\left(\sqrt{1 - \frac{(R_{\mathrm{L}} - R_{\mathrm{M}})^2}{R_{\mathrm{S}}^2}}\right) \tag{4.9}$$

The main configurations created via these correlators are shown in Fig. 4.4. For example, the top left panel shows where the *equilateral* ($R_{\mathrm{L}} = R_{\mathrm{M}} = R_{\mathrm{S}}$) triangles are situated in this coordinate space. The *flattened* ($\phi \to 0$) and *squeezed* (described below) configurations are shown in the top right and bottom left panels, respectively. Due to the collinear singularity inherent in vacuum parton shower evolution, the correlator is typically dominated by small-$\xi$ configurations as shown in Fig. 4.5. Here, the authors analyzed high $p_{\mathrm{T}}$ ($500-550$ GeV/$c$) anti-$k_{\mathrm{T}}$ jets of radius 0.5 at a specific value of $R_{\mathrm{L}}$ ($\sim 0.25$) in the projected correlators. This figure shows that when two directions are fixed at an angular separation $R_{\mathrm{L}}$, the third is most likely to lie nearly collinear with one of them. We refer to such configurations—where $R_{\mathrm{S}} \ll R_{\mathrm{M}} \sim R_{\mathrm{L}}$—as *squeezed triangles*.[5] In vacuum jet evolution, the EEEC is largely populated by these squeezed triangular shapes.

The work described in Chapter 7 constitutes the first effort to extend the full three-point correlators to heavy-ion collisions as a probe of jet-medium interactions.

5. Note that $\phi$, as shown in the bottom panel of Fig. 4.4, can be thought of as an angular variable when $\xi$ is small. A discussion of the geometry of this coordinate mapping can be found in the supplemental material of Ref. [15].

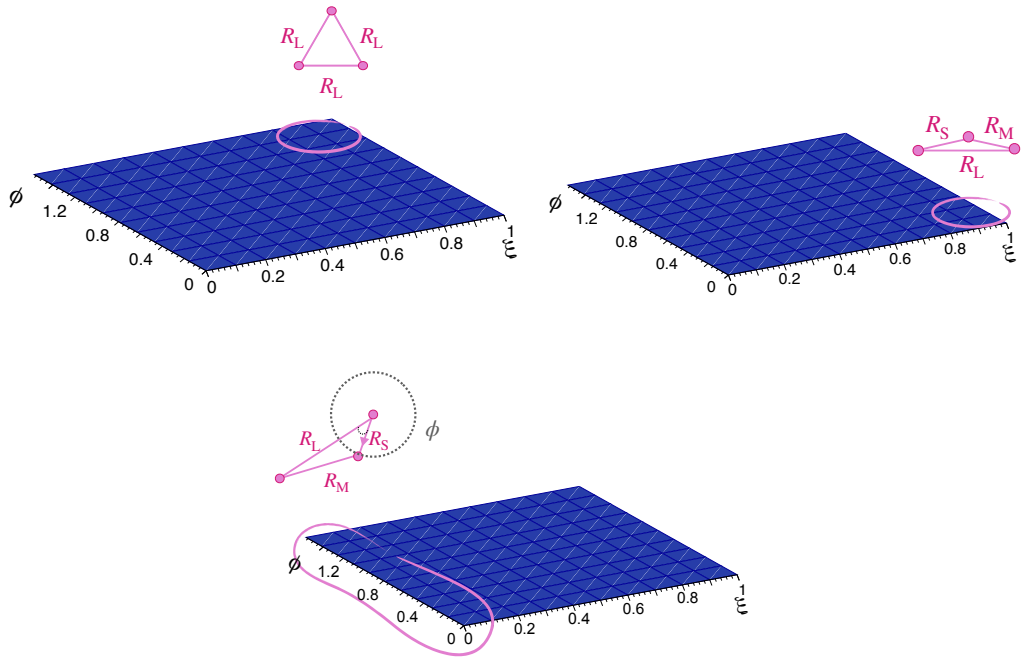


Figure 4.4: Three possible shapes of the three-point Energy-Energy-Energy Correlator: equilateral, flattened, and squeezed triangles. The collinear singularity of QCD guarantees that for jets in vacuum, the EEEC is dominated by the squeezed triangle region. Figure taken from [17].

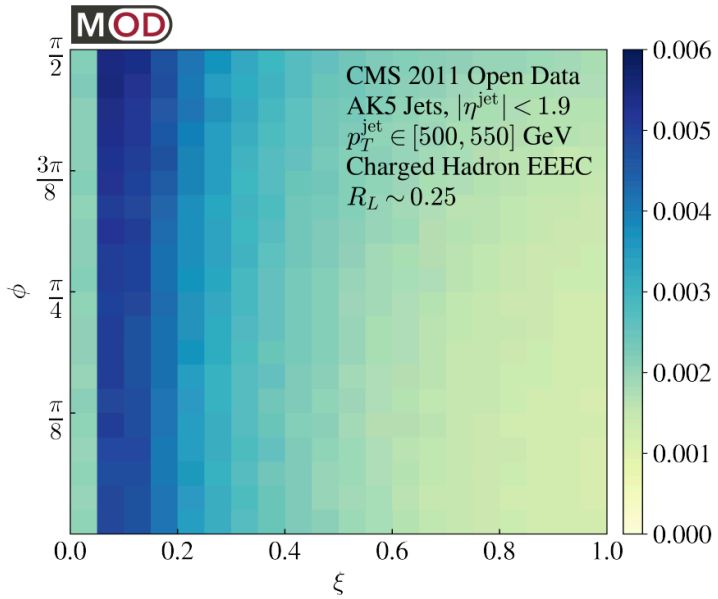


Figure 4.5: EEEC for vacuum jets with CMS Open Data. The enhancement at small values of $\xi$ is a result of the collinear singularity of vacuum QCD. Figure taken from [15].

# Chapter 5

# The ALICE Detector

## 5.1 Collider Facilities for Hadronic Collisions

To resolve the internal structure of hadrons, we accelerate them to very high velocities so that the hadrons become Lorentz-contracted pancakes, such that the internal degrees of freedom, the partons, become relevant.

There are two main collider facilities in the world. The Relativistic Heavy Ion Collider (RHIC) at Brookhaven National Lab (BNL) is located on Long Island, New York. The second collider facility is the Large Hadron Collider (LHC), which is located at CERN, Geneva, Switzerland.

#### Relativistic Heavy Ion Collider

RHIC began operations in 2000 and is the world's first dedicated heavy-ion collider. It consists of a 3.8 km ring and is highly versatile, capable of colliding various particle species, including gold (Au), uranium (U), deuterons (d), helium-3 ($^3$He), protons (p), isobaric nuclei, and, recently, oxygen (O). RHIC also accelerates polarized protons, making it unique for studying spin physics. It provides complementary information to the LHC by allowing the exploration of QGP at finite baryon chemical potential

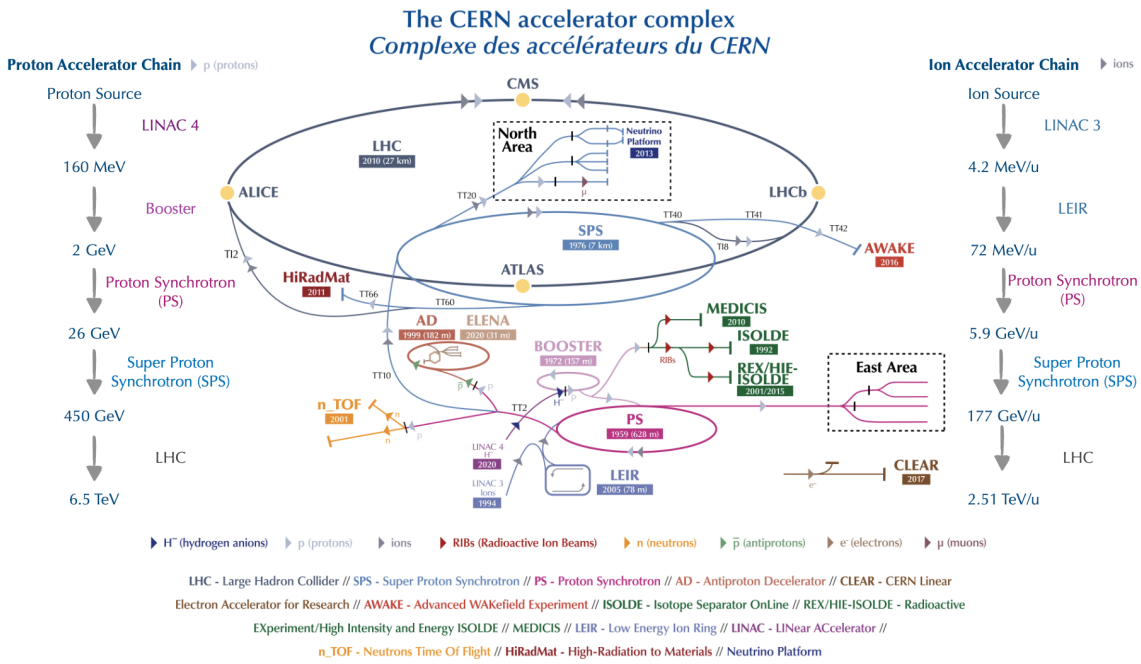


Figure 5.1: Figure (last updated in 2022) depicting the LHC accelerator complex and the experiments housed at CERN. A sequence of accelerators allows the LHC to reach top collision energies of 13.6 TeV. Figure taken from [18].

($\mu_B$). It has a maximum center-of-mass energy of $\sqrt{s_{\rm NN}} = 200$ GeV for heavy-ion collisions and $\sqrt{s} = 510$ GeV for proton-proton collisions. The Beam Energy Scan (BES) program probes phase transitions at lower energies down to $\sqrt{s_{\rm NN}} = 3.0$ GeV. Currently, RHIC hosts two major experiments: **STAR** (Solenoidal Tracker at RHIC), which studies QGP properties and hadronization, and **sPHENIX**, a next-generation detector focusing on jet quenching, heavy-quark interactions, and electromagnetic probes of the QGP. RHIC is expected to be replaced by the **Electron-Ion Collider (EIC)**, scheduled to begin data-taking in 2034.

### Large Hadron Collider

The Large Hadron Collider (LHC), the highest-energy particle accelerator ever constructed, became operational in 2008. It houses four major collider experiments: ALICE, ATLAS, CMS, and LHCb, as shown in Fig. 5.1. It is a 27 km ring that

is made up of eight arcs (where the magnets bend the beam) and eight insertions (the purpose of each insertion depends on its goal) as depicted in Fig. 5.2. The LHC collides protons along with heavier nuclei such as p-Pb, Pb-Pb, and Xe-Xe ions. In 2025, the LHC is scheduled to collide p-O, O-O and possibly Ne-Ne ions as well. Its first data-taking phase, Run 1, spanned from 2009 to 2013. The data analyzed in this thesis were recorded during Run 2, which took place between 2015 and 2018.[1] Before the beams enter the LHC, they are successively accelerated to higher and higher energies by a series of accelerators. The collision process can be summarized by the following steps:

- Protons or Pb ions are created by stripping electrons off them. In the case of protons, hydrogen atoms are ionized. In the case of Pb, Pb vapor is ionized by an electron current, creating many different charge states.

- From Linac (3 and 4 in Fig. 5.1), the protons are injected into the PS Booster (PSB), then to the Proton Synchrotron (PS), and then to the Super Proton Synchrotron (SPS). Finally, they are transferred to the LHC. In the case of Pb ions, a series of selections are made to create a Pb54+ beam that goes from the Low Energy Ion Ring (LEIR) to the PS, from where it goes to the SPS. At the SPS, Pb82+ is selected and transferred to the LHC.

- The beams arrive at the LHC in *bunches*, which results from using radio frequency (RF) cavities to accelerate the beams. The LHC further accelerates the protons to 6.5 TeV and Pb ions to 2.76 TeV. A bunch contains about $10^{11}$ protons with a typical spacing of 25 ns, or about 10 million heavy ions with a spacing of 150 ns.

1. The LHC is currently operating in Run 3. Following this phase, a long shutdown is planned beginning in 2026, during which significant upgrades will be implemented to prepare for the High Luminosity LHC (HL-LHC) era [208].

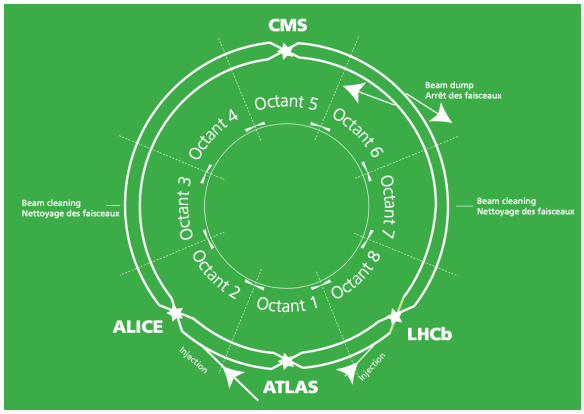


Figure 5.2: LHC ring is made up of octants. Figure taken from [19].

After reaching the LHC, the beams also go through several phases of tuning before they collide at the interaction point of each experiment. During Run 2, the LHC reached the highest beam energies of 13.6 TeV. This thesis focuses on proton-proton (pp) collisions at center-of-mass energies of 13 TeV and 5.02 TeV, as well as lead-lead (Pb–Pb) collisions at 5.02 TeV, all recorded during this data-taking period.

### 5.1.1 Collider Luminosity

To study rare physics phenomena, i.e., those processes that have a small production cross-section ($\sigma_P$, measured in units of barn, where 1 barn = $10^{-24}\,\mathrm{cm}^2$), resulting from high-energy collisions, we need a large number of collisions. The key ingredient that enables the study of physics processes at colliders is called *luminosity* ($L$, measured in units of $\mathrm{b}^{-1}\mathrm{s}^{-1}$), which is proportional to the number of collisions per second and is related to the cross-section by the equation

$$\frac{dR}{dt} = L \times \sigma_P \tag{5.1}$$

$dR/dt$ represents the rate at which the desired event occurs. Luminosity is a property of the machine, while cross-section is a property of the physics phenomena we are interested in. For hadronic collisions, luminosity is determined via a technique

called van der Meer scans/separation scans [209]. In this technique, the beams are separated in the transverse $(x, y)$ plane, and the change in luminosity is measured. During Run 2, the highest integrated LHC luminosities were about 166 $\text{fb}^{-1}$ for pp collisions [210].[2] For comparison, the integrated luminosity during Run 1 was $\sim$ 30 $\text{fb}^{-1}$ for pp collisions.

## 5.2 The ALICE Experiment

*This section describes the ALICE detector setup during the Run 2 data-taking period (2015–2018), as the analyses in this thesis utilize Run 2 data. Details about the Run 3 upgrade of the ALICE detector can be found in [211].*

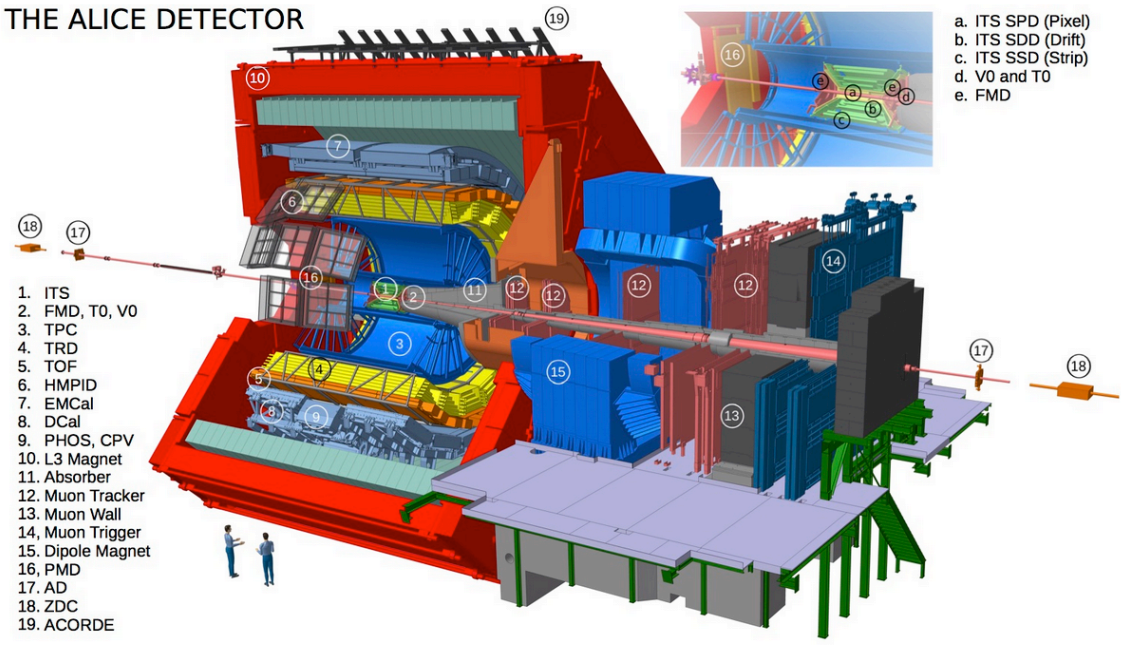


Figure 5.3: ALICE detector during the Run 2 period.

A Large Ion Collider Experiment (ALICE) at the LHC is its only dedicated heavy-ion experiment. Situated at Point 2 in St.Genis, France, it is designed for studying

2. 1 $\text{fb}^{-1}$ corresponds to approximately 100 million million collisions.

larger and more complex systems, i.e., collisions of ultra-relativistic heavy nuclei. It is composed of 17 sub-detector systems as shown in Fig. 5.3. A summary of each detector, its acceptance, and its purpose is presented in Table 5.1. ALICE has excellent tracking resolution, with the ability to track particles with $p_{\mathrm{T}}$ as low as 0.15 GeV/$c$ as well as excellent particle identification (PID) abilities up to 20 GeV/$c$. A complete description of the ALICE experimental setup and its performance can be found in [20, 212].

The ALICE central barrel detectors (shown in green in Table 5.1) are located within a solenoid magnet ($B = 0.5\ T$) in the mid-rapidity region and are used for particle tracking and identification. The main charged particle tracking detectors include the Inner Tracking System (ITS), the Time Projection Chamber (TPC), and the Time-Of-Flight detector (TOF). The V0 scintillating detector covers $-3.7 < \eta < -1.7$ and $2.8 < \eta < 5.1$ and is used for the online trigger and offline event selection. The ALICE detector also consists of an electromagnetic calorimeter (EMCal) to measure electromagnetic probes such as photons and uncharged jet constituents. In the following sections, I will limit the discussion to detector components that are critical for the analysis in this thesis.

### 5.2.1 ALICE Trigger Detectors for Event Selection

The V0 scintillating detector covers the ranges of $-3.7 < \eta < -1.7$ (V0C) and $2.8 < \eta < 5.1$ (V0A) and is used for a minimum-bias (MB) trigger to collect the data sample, by requiring a signal above a given threshold in both V0 counters. They are also used to determine centrality in Pb-Pb collisions as discussed in Chapter 8.

### 5.2.2 ALICE Tracking Detectors

To perform jet substructure measurements, we need to reconstruct jets and also the tracks that comprise that jet. The components of the ALICE detector relevant to our

| Detector | Acceptances | Main Purpose |
|---|---|---|
| SPD* | $\|\eta\| < 2.0$ | Vertex tracking |
| SDD | $\|\eta\| < 0.9$ | Tracking, PID |
| SSD | $\|\eta\| < 1.0$ | Tracking, PID |
| TPC | $\|\eta\| < 0.9$ | Tracking, PID |
| TRD* | $\|\eta\| < 0.8$ | Electron identification |
| TOF* | $\|\eta\| < 0.9$ | PID |
| PHOS* | $\|\eta\| < 0.12$, $220° < \phi < 320°$ | Photon detection |
| EMCal* | $\|\eta\| < 0.7$, $80° < \phi < 187°$ | Photon and jet detection |
| HMPID | $\|\eta\| < 0.6$, $1° < \phi < 59°$ | PID |
| ACORDE* | $\|\eta\| < 1.3$, $30° < \phi < 150°$ | Cosmic ray detection |
| PMD | $2.3 < \eta < 3.9$ | Photon detection |
| FMD | $3.6 < \eta < 5.0$ | Charged particle detection |
| | $1.7 < \eta < 3.7$ | Charged particle detection |
| | $-3.4 < \eta < -1.7$ | Charged particle detection |
| V0* | $2.8 < \eta < 5.1$ | Charged particle detection |
| | $-3.7 < \eta < -1.7$ | Charged particle detection |
| T0* | $4.6 < \eta < 4.9$ | Time, vertex measurement |
| | $-3.3 < \eta < -3.0$ | Time, vertex measurement |
| ZDC* | $\|\eta\| > 8.8$ | Forward neutron detection |
| | $6.5 < \|\eta\| < 7.5$, $\|\phi\| < 10°$ | Forward proton detection |
| | $4.8 < \eta < 5.7$, $\|2\phi\| < 32°$ | Forward photon detection |
| MCH | $-4.0 < \eta < -2.5$ | Muon tracking |
| MTR* | $-4.0 < \eta < -2.5$ | Muon trigger |

Table 5.1: ALICE detector components with their acceptance ranges and functions. Unless specified, detectors have full azimuthal ($\phi$) coverage. Central barrel detectors are shown in green; those marked with an asterisk ($*$) are used for triggering. Adapted from [20].

analysis are the ones that are used for the jet reconstruction of charged jets. These are the Inner Tracking System (ITS) and the Time Projection Chamber (TPC).

### Inner Tracking System (ITS)

The ALICE Inner Tracking System (ITS) consists of six concentric cylindrical layers of silicon detectors, optimized for precise particle tracking, vertex reconstruction, and

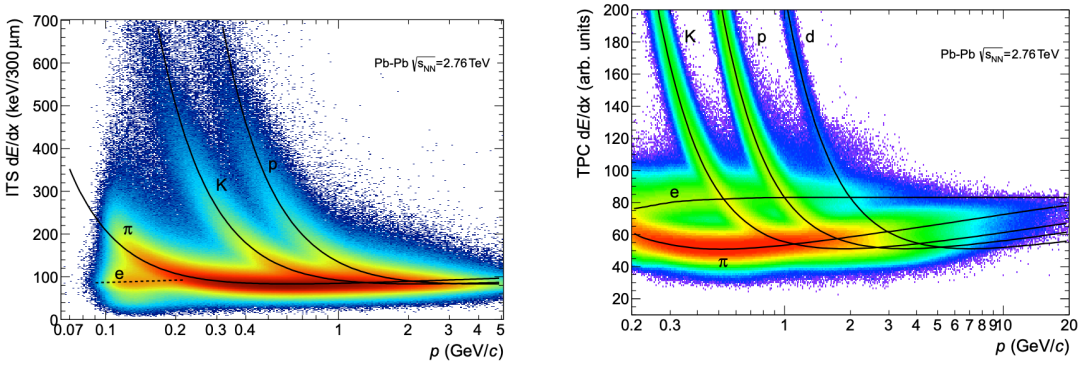


Figure 5.4: Figure depicting PID performance of ALICE detectors. Left: ITS. Right: TPC. Figures taken from [20].

particle identification. It enables measurements of particles with transverse momentum down to 150 MeV/$c$. The detector covers a pseudorapidity range of ($|\eta| < 0.9$) and has full azimuthal coverage. It is segmented into three distinct technologies: Silicon Pixel Detectors (SPD) form the two innermost layers and are closest to the beamline. These determine the position of the primary vertex as well as the position of decay vertices for strange, charm, and beauty particles that undergo weak decays. Silicon Drift Detectors (SDD) form the two middle layers, and Silicon Strip Detectors (SSD) form the two outermost layers. The ITS also plays a pivotal role in PID by measuring the specific ionization energy loss ($dE/dx$), as shown in the left panel of Fig. 5.4, in its silicon layers, complementing the information from the TPC and other ALICE subsystems.

### Time Projection Chamber (TPC)

The ALICE Time Projection Chamber (TPC) is a high-precision tracking detector designed to reconstruct charged particle trajectories and identify them. The TPC is a cylindrical drift chamber filled with a $Ne/CO_2/N_2$ gas mixture and operates within a uniform electric field created by a central high-voltage electrode (kept at -100kV). It has full azimuthal coverage and a pseudorapidity range of ($|\eta| < 0.9$). It enables PID for particles in the momenta in the range of 0.25-20 GeV/$c$. As charged particles

traverse the TPC, they bend in the magnetic field, enabling the measurement of their momentum and charge. Along their paths, they ionize the gas within the chamber, releasing free electrons. These electrons drift toward the readout planes located at both ends of the detector under the influence of a uniform electric field. The drift occurs at a well-calibrated velocity, ensuring precise timing and spatial resolution for track reconstruction.

The TPC measures the specific ionization energy loss ($dE/dx$) of charged particles as they propagate through the detector, which is shown in the right panel of Fig. 5.4. This energy loss follows the Bethe-Bloch formula [213] which describes the mean energy loss per unit path length of a charged particle traversing matter due to inelastic Coulomb interactions with atomic electrons. In the ALICE TPC, the collected $dE/dx$ values from multiple ionization clusters along the track are used to determine the most probable energy loss, which is then compared to theoretical Bethe-Bloch predictions to infer the particle species. This technique is particularly effective for separating electrons, pions, kaons, and protons in the low to intermediate momentum range, complementing other ALICE detectors like the Time-Of-Flight (TOF) system for comprehensive PID.

### 5.2.3 Track Reconstruction

In ALICE, track reconstruction combines information from the ITS and the TPC through a predefined procedure to ensure high precision and efficiency as summarized in Fig. 5.5. The process consists of several steps:

1. Clusterization: Each detector is treated independently, converting raw data into clusters based on position, signal amplitude, and other relevant parameters.

2. Preliminary Reconstruction: The primary interaction point (vertex) is reconstructed using only clusters from the SPD, the innermost part of the ITS.

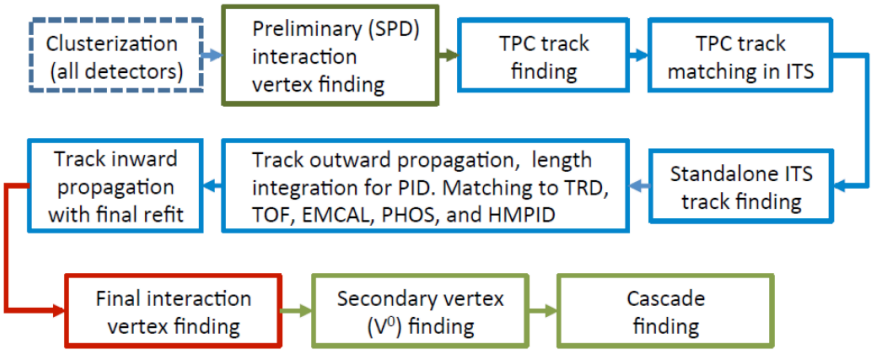


Figure 5.5: A schematic detailing the track reconstruction procedure employed during ALICE Runs 1 and 2. Figure taken from [21].

3. Track Reconstruction: A *Kalman-filter algorithm*[3] [214] is employed, starting from the outer radius of the TPC and propagating tracks inward to the ITS layers. This is then followed by a second reconstruction phase where the tracks are propagated outwards from the ITS to the outer TPC radius and beyond to the other detectors. Finally, the track is refitted inward from the outer detectors to the ITS. This procedure is shown in Fig. 5.5. Tracks that successfully combine TPC and ITS information are known as *global tracks*, providing high precision and momentum resolution. These tracks are further propagated to other detectors, associating them with corresponding clusters.

To ensure track uniformity in the azimuthal direction ($\phi$), which is critical for jet reconstruction, *hybrid tracks* are introduced by merging two reconstruction methods: *global tracks* and so-called *constrained global tracks*, which are TPC tracks that do not include an SPD hit or an ITS refit constraint. These tracks are, however, constrained to the primary vertex to improve their momentum resolution.

3. *Kalman filtering* is an iterative procedure that propagates a track's state from one step to the next, using the previous state to predict the next position and momentum while simultaneously accounting for uncertainties arising from processes such as energy loss that might occur at each step.

# Chapter 6

# Projected *N*-Point Correlator Measurement in pp Collisions

*This chapter details the measurement of the Projected N-point Correlators at two center of mass energies ($\sqrt{s} = 13$ TeV and $\sqrt{s} = 5.02$ TeV). The analysis methodology is the same in both cases unless otherwise specified in the text.*

## 6.1 Motivation

As discussed in Chapter 4, energy correlators offer us a new avenue to visualize jet evolution that is complementary to the Lund Plane.[1] The clean separation of scales makes them an appealing tool to study jet substructure. The analyses presented in this thesis constitute the first measurement of higher-point energy correlators at ALICE. The analysis at $\sqrt{s} = 5.02$ TeV was performed, as a part of this thesis study, to establish a baseline for the measurement discussed in Chapter 8. Although this chapter primarily features plots from the $\sqrt{s} = 13$ TeV analysis, corresponding results

1. A discussion on the Lund Plane can be found in Sec. 3.2.1.

for the $\sqrt{s} = 5.02$ TeV dataset are provided in Appendix A.4.

### Previous Measurements of Energy Correlators

*The discussion in this section is limited to measurements of Energy Correlators in pp collisions. Additional measurements in other systems (such as $e^+e^-$ and p-Pb) have also been performed. Measurements performed in heavy-ion collisions will be discussed in Chapter 8.*

The $N$-point Energy Correlators (ENCs) have been recently measured across a wide range of phase space at RHIC and the LHC. Throughout the literature, the two-point energy correlator is referred to interchangeably as the EEC or E2C. In this thesis, EEC is used to denote the two-point correlator. A summary of the CMS [23], ALICE [215][2], and STAR [22][3] measurements are tabulated below. Two[4] of these measurements are shown in Fig. 6.1. The left panel illustrates the common confinement scale probed through the relation $p_{\mathrm{T,jet}} R_{\mathrm{L}} \propto \Lambda$ in the EEC, while the right panel presents the E3C/EEC ratio as a probe of the strong coupling constant, $\alpha_s$. CMS

| Experiment | Center-of-Mass Energy ($\sqrt{s}$) | Observable | Jet $p_{\mathrm{T}}$ range |
|---|---|---|---|
| STAR | 200 GeV | EEC, E3C | $15 < p_{\mathrm{T,jet}}^{\mathrm{full}} < 50$ GeV/$c$ |
| ALICE | 5.02 TeV | EEC | $20 < p_{\mathrm{T,jet}}^{\mathrm{ch}} < 80$ GeV/$c$ |
| CMS | 13 TeV | EEC, E3C | $90 < p_{\mathrm{T,jet}}^{\mathrm{full}} < 1000$ GeV/$c$ |
| CMS | 5.02 TeV | EEC | $120 < p_{\mathrm{T,jet}}^{\mathrm{full}} < 200$ GeV/$c$ |

Table 6.1: Summary of jet ENC measurements at RHIC and the LHC. ALICE uses charged jets, while the measurements at STAR and CMS use full jets. Additionally, the CMS measurement at $\sqrt{s} = 13TeV$ is performed on dijets.

has also extracted $\alpha_s$ from the measured E3C/EEC ratio.[5]

2. ALICE has also measured the EEC for heavy-flavor tagged ($D^0$-tagged) jets [216] in pp collisions, which shows modified substructure compared to light quark initiated jets due to the presence of the dead cone (suppression of radiation around the region surrounding a massive quark).

3. STAR [22] and ALICE [217] have also measured Charged Energy Correlators in pp collisions, which may enable discrimination between different hadronization mechanisms [206].

4. A summary of ENC measurements in pp collisions is presented in Sec. 9.2.

5. The discussion on the dependence of the ratio on $\alpha_s$ can be found in Sec. 4.2.3.

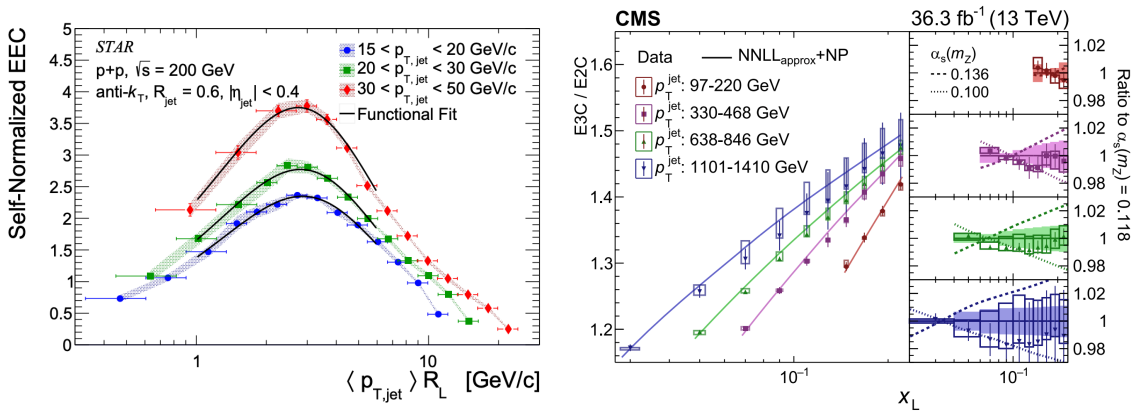


Figure 6.1: Left: Results from the STAR collaboration of the EEC measurement at $\sqrt{s} = 200$ GeV [22]. Right: E3C/EEC ratio measured by the CMS collaboration in pp collisions at $\sqrt{s} = 13$ TeV [23].

### Work in This Thesis

The work contained in this thesis pertains to measuring the EEC, E3C, and the E3C/EEC ratio in pp collisions to extract $\alpha_s$ at $\sqrt{s} = 13$ TeV and $\sqrt{s} = 5.02$ TeV with ALICE. This is interesting for a few reasons:

- Measuring the same observable at different center-of-mass energies allows us to assess its sensitivity to variations in the quark–gluon composition of the jet sample.

- ALICE sits at an intermediate kinematic range between STAR and other higher-energy LHC experiments, such as CMS and ATLAS, and overlaps with both, probing a unique phase space.

- Additionally, this range offers sensitivity to both perturbative and non-perturbative effects as it has recently been shown that ENCs might be sensitive to non-perturbative power corrections originating from large-angle soft gluon emissions [218].

- Finally, as discussed in Sec. 4.2.3, measuring the E3C/EEC ratio at ALICE will provide access to $\alpha_s$ in a kinematic regime distinct from that probed by the

existing CMS measurement.

## 6.2 Analysis Methodology

The data sets for both analyses are listed below:

- $\sqrt{s} = 13$ TeV: The analyzed data sample consists of about 1700 M minimum-bias events from pp collisions at $\sqrt{s} = 13$ TeV, corresponding to an integrated luminosity of $L_{int}$= 22.55 nb$^{-1}$ [219], collected during the years 2016, 2017, and 2018.

- $\sqrt{s} = 5.02$ TeV: The analyzed data sample consists of about 870 million minimum bias events from pp collisions at $\sqrt{s} = 5.02$ TeV, corresponding to an integrated luminosity of $L_{int} = 18.0 \pm 0.4$ nb$^{-1}$, collected during 2017 [220].

Only events with a primary vertex reconstructed within ±10cm from the center of the detector along the beamline were used for the analysis.

### 6.2.1 Jet and Track Selection

For this analysis, charged particle anti-$k_T$ jets of radius $R = 0.4$ with $|\eta_{jet}| < 0.5$ are reconstructed using the *E-scheme*.[6] The jet $p_T$ range used for the analyses is listed below:

- $\sqrt{s} = 13$ TeV: The jet $p_T$ range is from 20-80 GeV/$c$ to ensure high statistics.

- $\sqrt{s} = 5.02$ TeV: The jet $p_T$ range is from 70-120 GeV/$c$ to complement the measurement range for the Pb-Pb analysis described in Chapter 8.

Hybrid tracks, as described in Sec. 5.2.3, are used for selecting the jet constituents.

6. For details on jet reconstruction, see Sec. 3.3.1.

### 6.2.2 Constructing the Correlators

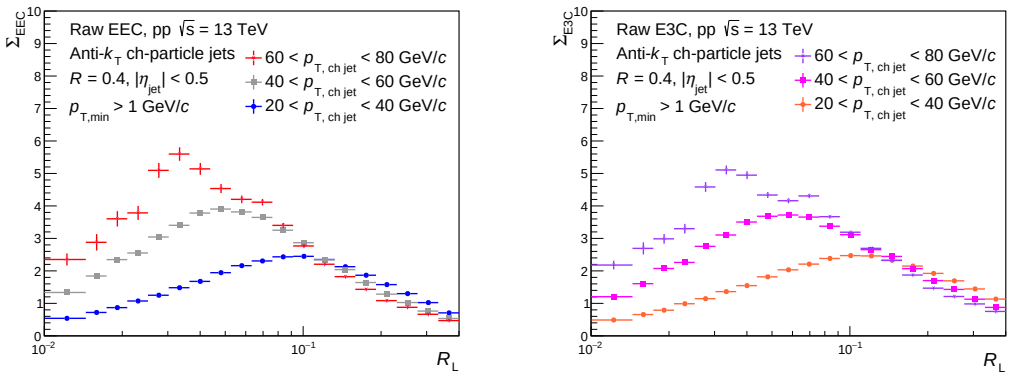


Figure 6.2: Raw distributions for $R = 0.4$ anti-$k_{\mathrm{T}}$ ch-particle jets normalized by the number of jets and bin-width. Left: EEC. Right: E3C.

Once jets are reconstructed, the jet constituents are iterated over to construct pairs (EEC) or triplets (E3C) from the constituent tracks. Only constituents with $p_{\mathrm{T}}$ greater than 1 GeV/$c$ are used to construct the ENC. This cut is applied to suppress contributions from the underlying event (UE),[7] which is approximately 1 GeV/$c$ in pp collisions at ALICE. However, it should be emphasized that applying this threshold, combined with the use of charged particles only, renders the experimental definition of the observable infrared and collinear (IRC) unsafe. Information about the largest angle between $N$ constituents, $R_{\mathrm{L}}$, and the corresponding weight (as defined in Equation 6.1) is stored. The distance between particles is computed using the track coordinates $(\eta, \phi)$ instead of $(y, \phi)$ since $\Delta R = \sqrt{\Delta\eta^2 + \Delta\phi^2}$ represents a purely angular variable, whereas rapidity $y$ depends on particle mass. The weight is defined as

$$ENC_{\mathrm{weight}} = \frac{p_T^i p_T^j .. p_T^N}{p_{T,jet}^N} \tag{6.1}$$

for $N$ particles. 3D histograms of ($R_{\mathrm{L}}$, $p_{\mathrm{T,ch\ jet}}$, $ENC_{\mathrm{weight}}$) are constructed. The 3D histograms are subsequently projected onto 1D weighted distributions, where the

7. For a discussion on the underlying event, see Sec. 3.2.1.

weights correspond to the sum of $ENC_{\text{weight}}$ in each $R_{\text{L}}$ bin (see Sec. 6.5.1 for a detailed discussion), within specific jet $p_{\text{T}}$ intervals. The raw distributions of these correlators are shown in Fig. 6.2. Once the raw distributions are constructed, they need to be corrected for detector effects. The detector effects most pertinent to this analysis are summarized in Sec. 6.2.3.

### 6.2.3 Detector Effects

Various detector effects can impact the ENC. These include the track momentum, angular resolution, and missed or merged tracks. To assess these effects, a high statistics a $p_{\text{T}}^{\text{hard}}$-binned[8] Monte Carlo (MC) production was employed using PYTHIA8 with the Monash 2013 tune [221], followed by a full GEANT3 [222] detector simulation of the ALICE detector. This simulation considers all the detector effects described above and thus is used to evaluate and perform these corrections. These effects are encapsulated in the *response matrix* $R$, which is constructed from MC simulations that map truth-level inputs to detector-level outputs. The matrix element $R_{ij}$ represents the probability that an event originating in true bin $j$ is observed in reconstructed bin $i$

$$R_{ij} = \text{Prob}(\text{observed in bin } i \mid \text{true in bin } j) \tag{6.2}$$

The detector effects impact the jet $p_{\text{T}}$ and the individual track pairs. These can contribute to migration in the jet $p_{\text{T}}$ bins, $R_{\text{L}}$, and the weight. Multiple response matrices are constructed in this analysis to evaluate how detector effects influence the observables under study.

8. MC simulations are created in $p_{\text{T}}^{\text{hard}}$ bins which set the scale of the hard scattering. This is done to ensure high statistics. These are then reweighted to obtain a physical distribution of the jet spectra and the observables under consideration.

### Jet Performance and Jet Momentum Migration

The jet performance measures how well the jet is reconstructed by comparing the jet at the truth level to the reconstructed jet at the detector level. The detector jets must be matched to the corresponding generator-level truth signal jet to evaluate the jet performance. This is done through a geometrical matching procedure. For the jet to be a match, the jets' axes[9] must be within $R = 0.4$ of each other and be a unique match. The response matrix for jet $p_{\mathrm{T}}$ is shown in Fig. 6.3. Two other quantities

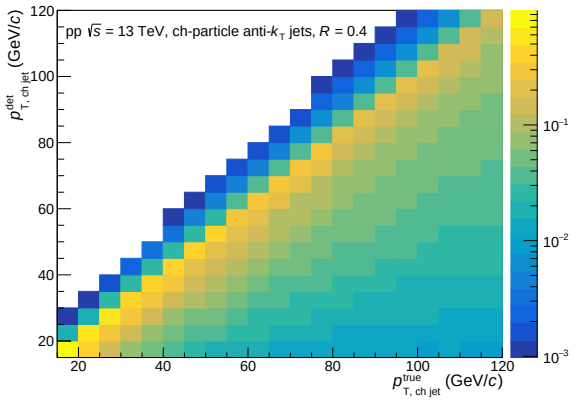


Figure 6.3: Response matrix for jet $p_{\mathrm{T}}$. The non-diagonal nature of the response matrix illustrates the smearing in jet $p_{\mathrm{T}}$ due to detector effects. The white spaces on the plot mean that there are no entries in that bin.

that help assess jet performance are the Jet Energy Scale (JES) and the Jet Energy Resolution (JER), described by Equations 6.3 and 6.4 respectively

$$\mathrm{JES} = \left\langle \frac{p_{\mathrm{T,det}} - p_{\mathrm{T,true}}}{p_{\mathrm{T,true}}} \right\rangle \tag{6.3}$$

$$\mathrm{JER} = \frac{\sigma(p_{\mathrm{T,det}})}{p_{\mathrm{T,true}}} \tag{6.4}$$

9. Jet axes are defined in $(\eta, \phi)$ by taking a sum of the four momenta of the jet constituents. This is typically done using the FASTJET package [129].

The JES and JER for the $R = 0.4$ jets at $\sqrt{s} = 13$ TeV are shown in the left and right panels of Fig. 6.4, respectively.[10] The ENC observables are also sensitive to

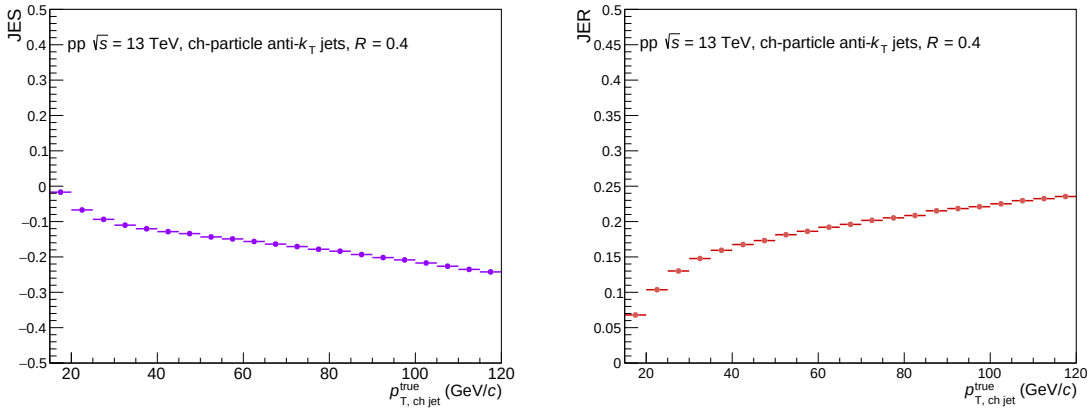


Figure 6.4: Left: Jet Energy Scale (JES). Right: Jet Energy Resolution (JER) for anti-$k_T$ jets with $R = 0.4$ in pp collisions at $\sqrt{s} = 13$ TeV.

changes in jet $p_T$. Thus, any migration in $p_T$ from the truth to the detector level will impact the shape of the curve. If the detector level jet $p_T$ is higher than the truth, the distribution will shift to the left, while if it is lower, the distribution will shift to the right, as shown in Fig. 6.5.

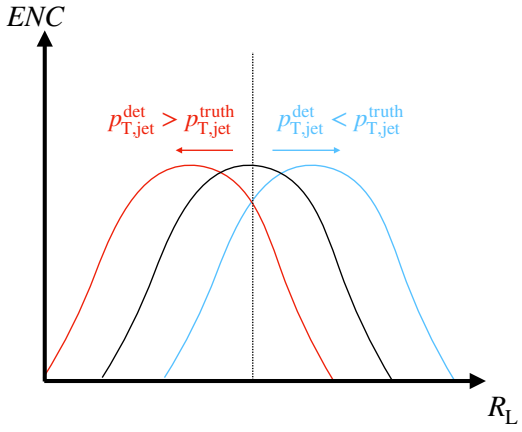


Figure 6.5: Illustration depicting how variations in reconstructed (detector-level) jet $p_T$ can cause shifts in the truth ENC curve (shown in black).

10. Note that the JES and JER depend on detector conditions and thus can be different at $\sqrt{s} = 13$ TeV and $\sqrt{s} = 5.02$ TeV.

### Track Resolution Effects

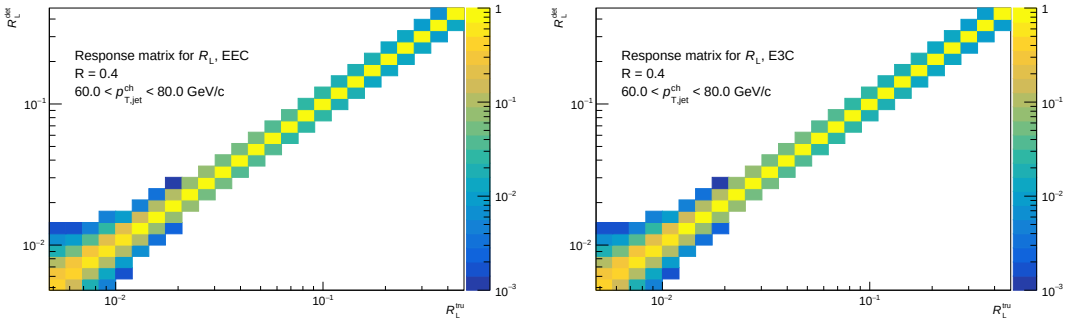


Figure 6.6: Response matrix for $R_{\mathrm{L}}$ in one jet $p_{\mathrm{T}}$ bin. Left: EEC. Right: E3C. The diagonal nature of the response matrix illustrates the great angular resolution from ALICE tracking detectors. Note that the measurement range in this analysis is from $0.01 < R_{\mathrm{L}} < 0.4$.

$R_{\mathrm{L}}$ **Migration**: A migration in $R_{\mathrm{L}}$ would change the observed shape of the ENC. We expect $R_{\mathrm{L}}$ migration to not be a significant effect due to the great excellent tracking resolution in ALICE which is $\sim 1$ mrad at $p_{\mathrm{T,track}} > 1$ GeV/$c$ [20, 223]. This is illustrated for one jet $p_{\mathrm{T}}$ bin in Fig. 6.6.

**Particle Tracking**: Particle tracking impacts the weights used in the ENC through two main factors:

- Single Particle Tracking: Single particle tracking efficiency will affect the ENC because it will determine how many tracks appear in the correlator.
- Pair Efficiency Effects: The ENCs are defined as an inclusive sum over pairs of all the charged particles in a jet. In the case of the EEC, these are two particle pairs ($ij$), and in the case of the E3C, these are triplets ($ijk$). The sum includes all permutations of the $ij$ indices in the case of the EEC and the $ijk$ indices in the three-point case. The two main effects that play a role in this are track merging and track splitting. The track merging effect has previously been analyzed in HBT [223,224] correlation measurements as well as the ALICE EEC measurement at $\sqrt{s} = 5.02$ TeV [215]. Track merging occurs when two tracks

are very close to each other in the TPC and get reconstructed as one track. To ensure that the pair efficiency remains relatively high, the measurement is constrained to a lower bound of $R_{\mathrm{L}} = 0.01$. Due to the hybrid track selection[11] employed to find jet constituents, split tracks are extremely rare.

### Effects of Track $p_{\mathrm{T}}$ Resolution on ENC Weights

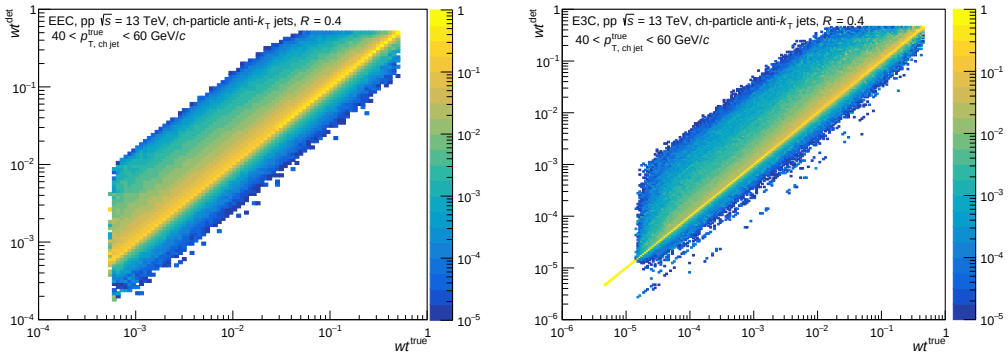


Figure 6.7: Response matrix for weight in one jet $p_{\mathrm{T}}$ bin. Left: EEC. Right: E3C.

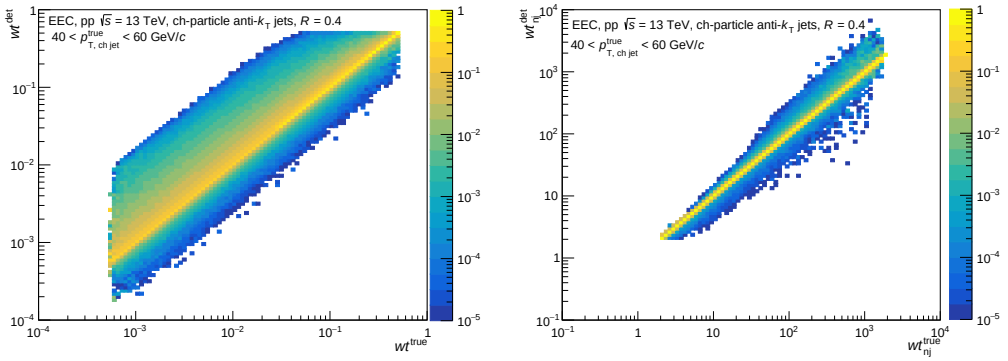


Figure 6.8: Response matrix for EEC weight in one jet $p_{\mathrm{T}}$ bin. Left: With weight definition including jet $p_{\mathrm{T}}$. Right: Without weight definition including jet $p_{\mathrm{T}}$.

The influence of track $p_{\mathrm{T}}$ resolution on the correlators enters primarily through the weight factors. However, the resolution of the weights reflects a convolution of both jet $p_{\mathrm{T}}$ smearing and track $p_{\mathrm{T}}$ smearing. The response matrices for weights for

11. For a discussion on the hybrid track selection employed in this analysis, see Sec. 5.2.3.

the EEC and E3C are shown in the left and right panels of Fig. 6.7, respectively. To isolate the contribution from jet $p_{\mathrm{T}}$ smearing, we examine the response matrices of the weights with $(wt)$ and without $(wt_{\mathrm{nj}})$ jet $p_{\mathrm{T}}$ dependence. These comparisons, shown for the EEC in Fig. 6.8, indicate that the dominant source of smearing in the weight distributions originates from the jet $p_{\mathrm{T}}$ resolution. The same reasoning applies to the E3C as well. Comparing the left and right panels of Fig. 6.7, it is clear that the E3C shows less smearing compared to the EEC. This is because the E3C is composed of triplets such as $(i, i, j)$ (apart from triplets $(i, j, k)$ where $i \neq j \neq k$), whereas in the EEC, we only consider $(i, j)$ pairs where $i \neq j$. Thus, the E3C weight response benefits from one particle being counted twice.

To further investigate this effect, we examine the JER as a function of the weight. A non-flat JER profile as a function of the weight indicates a correlation between the two quantities, motivating the use of a full three-dimensional unfolding procedure. Fig. 6.9 presents this dependence for the EEC (left panel) and the E3C (right panel) within a representative jet transverse momentum bin. A variation of approximately 10% across the weight axis confirms that the smearing is not independent of the weight. This observation motivates the use of an unfolding technique known as

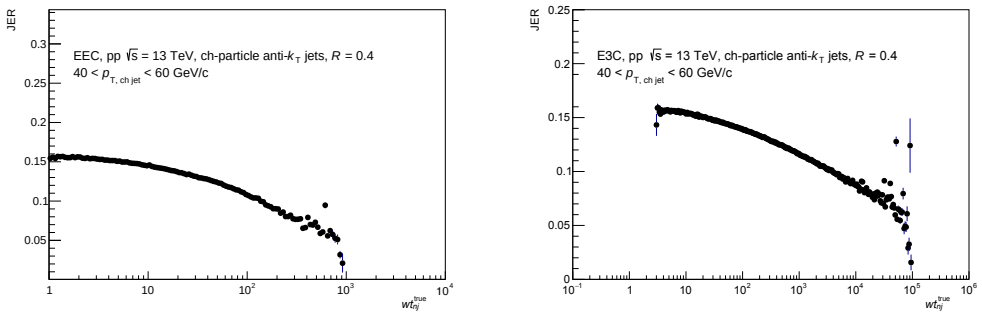


Figure 6.9: JER as a function of weight in one jet $p_{\mathrm{T}}$ bin. Left: EEC. Right: E3C.

Iterative Bayesian Unfolding,[12] which is described in detail in Sec. 6.3.

12. This is the primary justification for adopting iterative Bayesian unfolding over the simpler Bin-by-Bin correction method previously used in this measurement. Details can be found in Appendix A.1.

## 6.3 Correction Methodology

*This analysis employs two correction methods: bin-by-bin correction (applied to preliminary $\sqrt{s} = 13$ TeV results) and unfolding (used for both $\sqrt{s} = 5.02$ TeV, preliminary in 2025, and 13 TeV). This section focuses on the unfolding approach; bin-by-bin results for 13 TeV are provided in Appendix A.1.*

The raw distributions need to be evaluated and corrected for detector effects. The correction method generally applied in modern jet physics analyses is called *unfolding*. Unfolding is a statistical technique used to correct for detector effects and resolution limitations in experimental data. When measurements are taken, they often suffer from distortions due to the finite resolution of the detector or inefficiencies in data collection. Unfolding aims to reconstruct the true distribution of a measured variable by applying an inverse transformation that accounts for these distortions.

### 6.3.1 Iterative Bayesian Unfolding

Raw distributions in high-energy physics (HEP) experiments must be corrected for detector effects, including resolution smearing and inefficiencies. This correction is essential for comparing experimental measurements with theoretical predictions and is commonly performed using statistical techniques known as unfolding. Among the various unfolding approaches, *Iterative Bayesian Unfolding* [225] is one of the most widely adopted methods in modern jet physics analyses.[13]

Unfolding aims to reconstruct the true distribution of a physical quantity $\mathbf{x} = (x_1, x_2, \ldots, x_n)$ from a distorted observed distribution $\mathbf{y} = (y_1, y_2, \ldots, y_m)$, where the distortion arises from detector effects. In a Bayesian framework, one updates prior

13. Alternative methods include singular value decomposition (SVD) [226] and more recent machine-learning-based techniques such as Omnifold [227], which have also been successfully applied in experimental contexts [228].

knowledge of the true distribution based on observed data via Bayes' theorem

$$P(\mathbf{x}|\mathbf{y}) \propto P(\mathbf{y}|\mathbf{x})P(\mathbf{x}) \tag{6.5}$$

where $P(\mathbf{y}|\mathbf{x})$ is the likelihood given the detector response, and $P(\mathbf{x})$ is the prior. Iterative Bayesian unfolding begins with an initial prior (typically derived from the MC truth) and refines this estimate through successive iterations. After several iterations, the estimate converges toward the most probable true distribution given the measured data and prior assumptions.

In this analysis, a response matrix $R$ is constructed using high-statistics PYTHIA8 simulations (Monash 2013 tune [221]), which are propagated through a detailed GEANT3 [222] simulation of the ALICE detector. As an example, we can consider a 1D unfolding of the jet spectra. In this case, the response matrix effectively encodes the mapping from true jets to reconstructed jets and is formally inverted to apply the correction to real data

$$\vec{p}_{\text{true}} = R^{-1}\vec{p}_{\text{rec}} \tag{6.6}$$

This matrix inversion is nontrivial, especially when $R$ contains significant off-diagonal elements, which arise from migrations between bins due to poor resolution or limited acceptance. Moreover, direct inversion often leads to instabilities, as statistical fluctuations in the data can give rise to a large space of unphysical solutions. To address this issue, *regularization* is employed—typically by imposing a smoothness constraint—to stabilize the solution and suppress unphysical fluctuations or oscillations in the unfolded distribution. For the $\sqrt{s} = 13$ TeV and 5.02 TeV analyses presented in this thesis, the unfolding approach is applied to both datasets.

### 6.3.2 3D Unfolding for ENC: Performance

*The unfolding performance shown here is for illustrative purposes on the final observables of interest. For checks across the whole phase space as well as for the* $\sqrt{s} = 5.02$ *TeV analysis, see Appendix A.4.*

A 3D unfolding procedure is employed for the ENC measurement using the RooUnfold package [229], where the unfolding axes correspond to $R_{\mathrm{L}}$, jet $p_{\mathrm{T}}$, and weight. The response matrix is now a 6D response matrix. The bins for unfolding are optimized based on statistics available in the data -

- $\sqrt{s} = 13$ TeV: The unfolding is performed in 22 $R_{\mathrm{L}}$, 5 jet $p_{\mathrm{T}}$, and 20 weight bins (for both EEC and E3C).
- $\sqrt{s} = 5.02$ TeV: The unfolding is performed in 22 $R_{\mathrm{L}}$, 6 jet $p_{\mathrm{T}}$, and 15 weight bins for EEC and 23 weight bins for E3C.

The binning is described in Table 6.2 for the $\sqrt{s} = 13$ TeV analysis.

| Axis | Binning Description |
|---|---|
| $R_{\mathrm{L}}$ | Uniform log bins in the range $[0.01, 0.4]$, with additional edge bins |
| Jet $p_{\mathrm{T}}$ | Bin edges: [0, 20, 40, 60, 80, 120] GeV/$c$ |
| Weight | Uniform log bins in the range $[10^{-4}, 0.25]$ (EEC) and $[10^{-6}, 0.148]$ (E3C) |

Table 6.2: Binning definitions used for the 3D unfolding procedure at $\sqrt{s} = 13$ TeV.

Several checks are made to ensure that the unfolding is working correctly. The basic idea is to check for convergence (i.e., the stability of the result) while varying the regularization parameter, which corresponds to the number of unfolding iterations ($n_{\mathrm{iter}}$).

**Trivial MC Closure**: This test verifies the unfolding procedure by correcting the detector-level distribution using a response matrix constructed from both detector and truth-level simulations. The unfolded result must accurately reproduce the original truth distribution. The results of trivial unfolding are shown in Fig. 6.10.

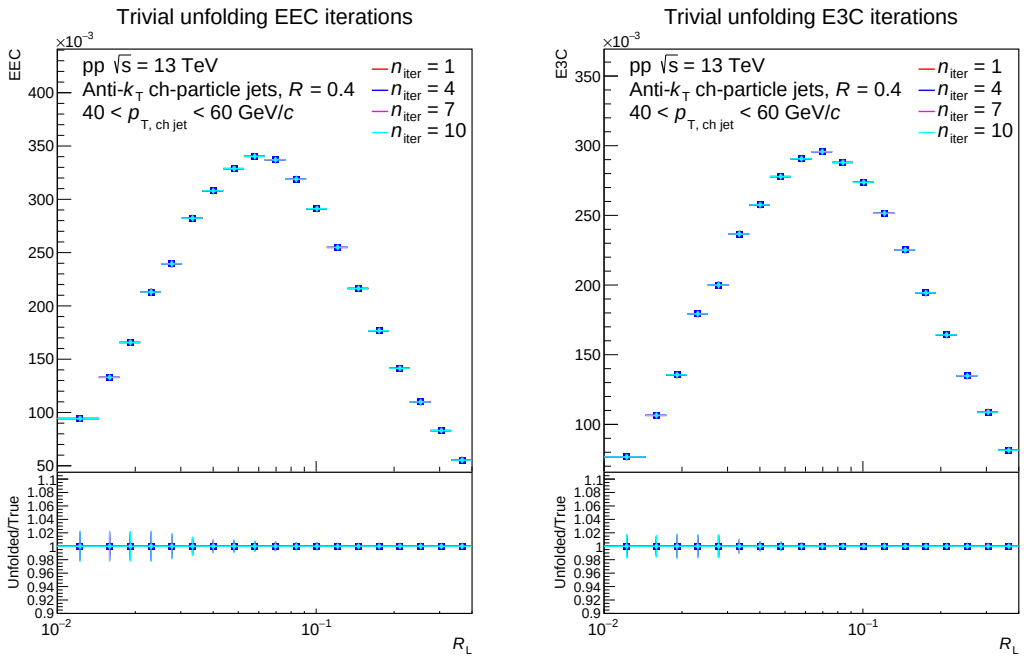


Figure 6.10: Trivial unfolding closure. Left: EEC. Right: E3C. The fact that the ratio to truth (bottom panel) is at unity confirms that trivial unfolding is working.

**Split MC Closure**: In this test, half the MC sample is used to construct the response while the other half forms the "pseudo-data". The pseudo-data is then unfolded and compared to the truth distribution. The results of split unfolding are shown in Fig. 6.11.

**Refolding Test**: This test validates the unfolding setup by "folding" the truth distribution with the response matrix. A correctly implemented procedure should reproduce the raw distribution. The results of folding closure are shown in Fig. 6.12. Once these checks are verified, the raw data can now be unfolded. This is detailed in the next section.

### 6.3.3 3D Unfolding for ENC: Data

After verifying these checks, the raw data is unfolded. A key validation step in this process is assessing the stability of the unfolding procedure against variations in the regularization parameter. If the procedure is stable, the final distribution should

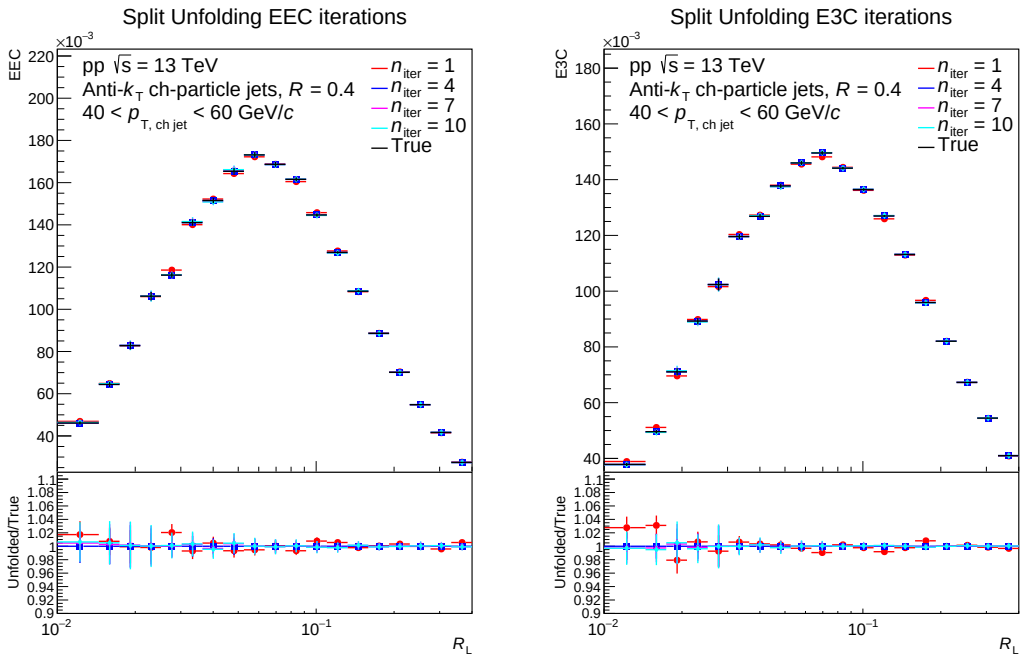


Figure 6.11: Split MC unfolding closure. Left: EEC. Right: E3C. The fact that the ratio to truth (bottom panel) is within 5% of unity indicates good closure.

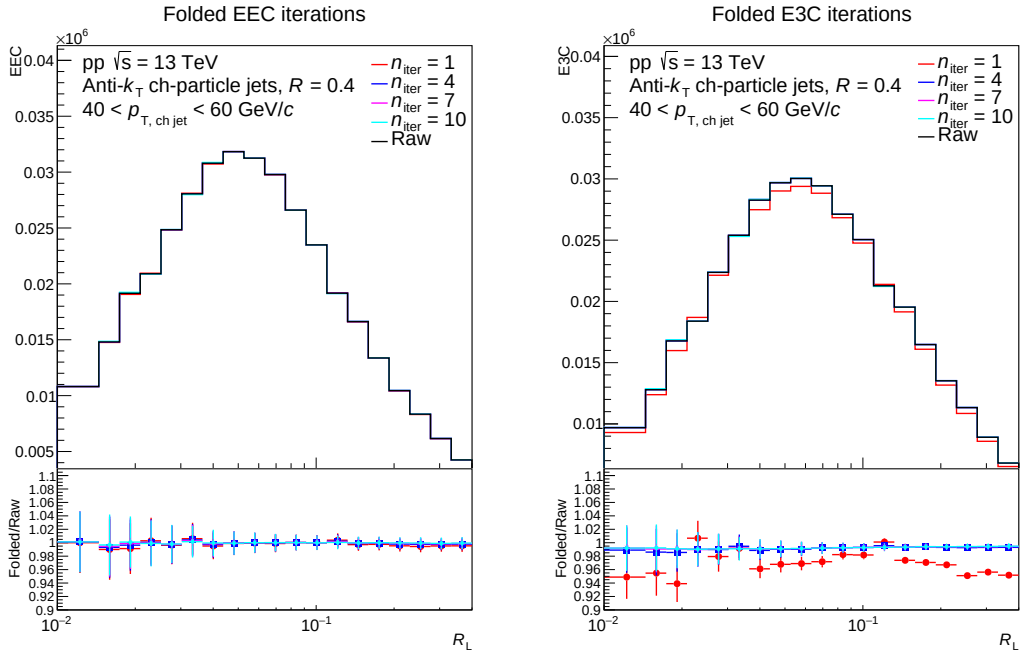


Figure 6.12: MC folding closure. Left: EEC. Right: E3C. The fact that the ratio to raw data (bottom panel) is within 5% of unity indicates good closure.

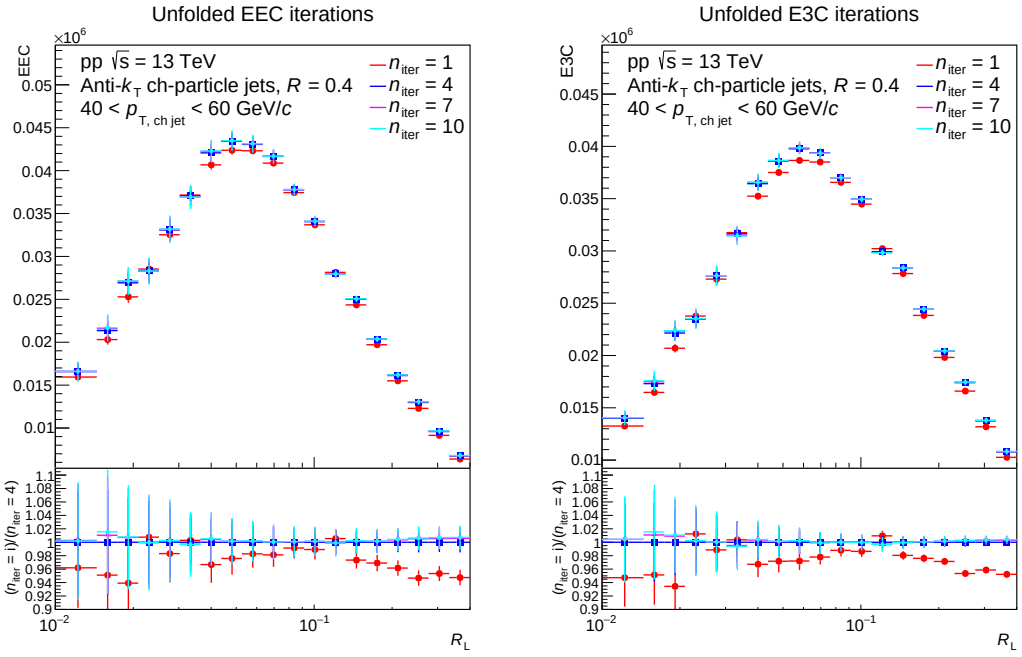


Figure 6.13: Unfolding convergence. Left: EEC. Right: E3C. The ratio to the fourth iteration (bottom panel) shows that after the first iteration, all iterations sit within 5%, indicating good stability.

remain unaffected by changes in regularization. For Bayesian unfolding, the regularization parameter corresponds to the number of iterations. Therefore, unfolding convergence is tested by varying the iteration count. The unfolding convergence for the EEC and E3C is illustrated in Fig. 6.13, where the ratio of different iterations is compared to the fourth iteration. Convergence is achieved by the fourth iteration for both the EEC and E3C. To reduce statistical uncertainties arising from the unfolding process, the fourth iteration is chosen as the nominal case. Note: a 1D unfolding is also performed separately to unfold the jet $p_{\mathrm{T}}$ so that these distributions can be normalized by the number of jets. Details can be found in Appendix A.2.

## 6.4 Statistical Uncertainties

*At the time of writing this thesis, the procedure described in this section is ongoing for both analyses.*

As mentioned in Sec. 6.2.2, the ENC observable is generated by projecting a 3D unfolded histogram into a 1D histogram across various jet $p_{\mathrm{T}}$ bins. The weight distribution within a jet is a correlated quantity. This can be illustrated with a jet containing two particles; for instance, if one particle accounts for half the fraction of the jet $p_{\mathrm{T}}$, then the other particle must account for the remaining half due to momentum conservation. Therefore, by knowing something about one particle, we can, in principle, determine the characteristics of the other particle. Another example involves a jet with three particles A, B, and C; if we know that AB and AC exist, we can determine what the $R_{\mathrm{L}}$ distance between BC should be. Similarly, since this distribution is filled numerous times per jet, it inherently has correlated bins. To address the correlated statistical uncertainties, 1000 replicas of the ENC observable are generated using the Bootstrap technique [230–232].

For this study, The ATLAS Bootstrap package [233, 234] was used to create 1000 replicas of jet events at the raw level. These can then be unfolded, and a correlation matrix can be derived across all bins. The statistical uncertainties in the projections can then be computed by considering the complete covariance matrix in 3D space. An illustration of this procedure is shown in Fig. 6.14. The 3D space is flattened to a 1D space using ROOT's global indexing. Each bin corresponds to a specific bin in ($R_{\mathrm{L}}$, jet $p_{\mathrm{T}}$ weight). The blue areas correspond to bins with no entries, while the boxes indicate correlations across bins. The diagonal stripes in the boxes represent the self-correlations. Moreover, the E3C/EEC ratio is measured on the same dataset, which implies that these observables are statistically correlated. This correlation can also be addressed via the Bootstrap technique. Note: This procedure is ongoing for the analyses presented in this thesis and will be finalized before publication.

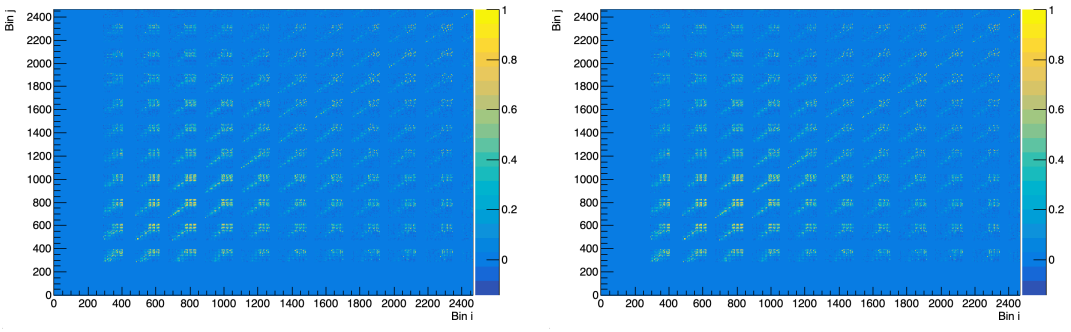


Figure 6.14: Correlation matrices across bins in 3D space. Left: EEC. Right: E3C.

## 6.5 Systematic Uncertainties

Several systematic uncertainties are considered for both the EEC and E3C measurements. They can be broadly categorized into uncertainties from binning choice, uncertainties from detector effects (tracking efficiency), and uncertainties from unfolding (regularization parameter, prior variation, generator dependence, measured jet $p_{\mathrm{T}}$ range).

### 6.5.1 Systematics from Choice of Binning

The preliminary measurement of the EEC and E3C, as discussed in Appendix A.1, initially utilized unbinned weights to populate 2D weighted histograms as a function of jet $p_{\mathrm{T}}$. However, to perform 3D unfolding, which typically requires binned histograms, the weights must now be discretized. The final measurement is obtained by projecting a 3D histogram onto a 1D distribution, where the third axis corresponds to the correlator weight. In this analysis, the weight axis is binned using uniformly spaced intervals on a logarithmic scale.

In the limit of infinite statistics and fine binning, discretized weights closely approximate the true unbinned values. However, with finite statistics, broader binning becomes necessary, and approximating the weight by a single characteristic value within each bin can introduce distortions. A study based on PYTHIA simulations,

shown in the top left panel of Fig. 6.15, illustrates that excessively coarse binning leads to significant shape distortions. To mitigate these effects, studies were performed to determine bin widths that minimize distortions while keeping reasonable statistics in each bin, and the ratio between the binned and unbinned distributions at the raw level is used to assign a systematic uncertainty associated with the binning procedure.

To further improve the accuracy of the binned representation for the $\sqrt{s} = 13$ TeV analysis, two prescriptions for evaluating the correlator weight in each $R_{\mathrm{L}}$ bin were studied: (1) computing the weight at the bin center, defined as

$$ENC_{\mathrm{weight}}(R_{\mathrm{L}}) = \sum_{i=1}^{n_{\mathrm{bins}}} wt_i(\text{bin center}) \times n_i^{\mathrm{counts}} \tag{6.7}$$

where $wt_i$ is the weight evaluated at the bin center and $n_i^{\mathrm{counts}}$ is the number of entries in the bin; and (2) computing the weight using the geometric mean of the bin edges, defined as

$$ENC_{\mathrm{weight}}(R_{\mathrm{L}}) = \sum_{i=1}^{n_{\mathrm{bins}}} \left( \sqrt{w_i^{\mathrm{low}} \times w_i^{\mathrm{high}}} \right) \times n_i^{\mathrm{counts}} \tag{6.8}$$

where $w_i^{\mathrm{low}}$ and $w_i^{\mathrm{high}}$ are the lower and upper edges of the $i$-th weight bin, respectively. A comparative study found that the geometric mean provides a more faithful representation[14] of the underlying unbinned distribution, as illustrated in the top right panel of Fig. 6.15. The geometric mean is used to compute binned weights. The ratio of unbinned to binned distribution at the raw level is used as a systematic uncertainty. This uncertainty is negligible except for the E3C in the 60-80 GeV/$c$ bin, as is shown in the bottom panel of Fig. 6.15. Additional plots can be found in

14. The geometric mean of $n$ numbers is defined as the $n$th root of their product (as opposed to the arithmetic mean, which is defined as the sum of numbers divided by $n$). It better preserves the logarithmic scaling properties of the correlator weights. Since the weights span several orders of magnitude and are distributed approximately log-uniformly within each bin, the geometric mean more accurately captures the typical scale of entries within a bin compared to the arithmetic bin center, which tends to bias toward higher values.

Appendix A.2.2.

Note: For the $\sqrt{s} = 5.02$ TeV analysis, the arithmetic mean was used to compute bin weights, with systematic uncertainties assigned to account for the resulting bias. This will be improved prior to publication to reduce systematic errors.

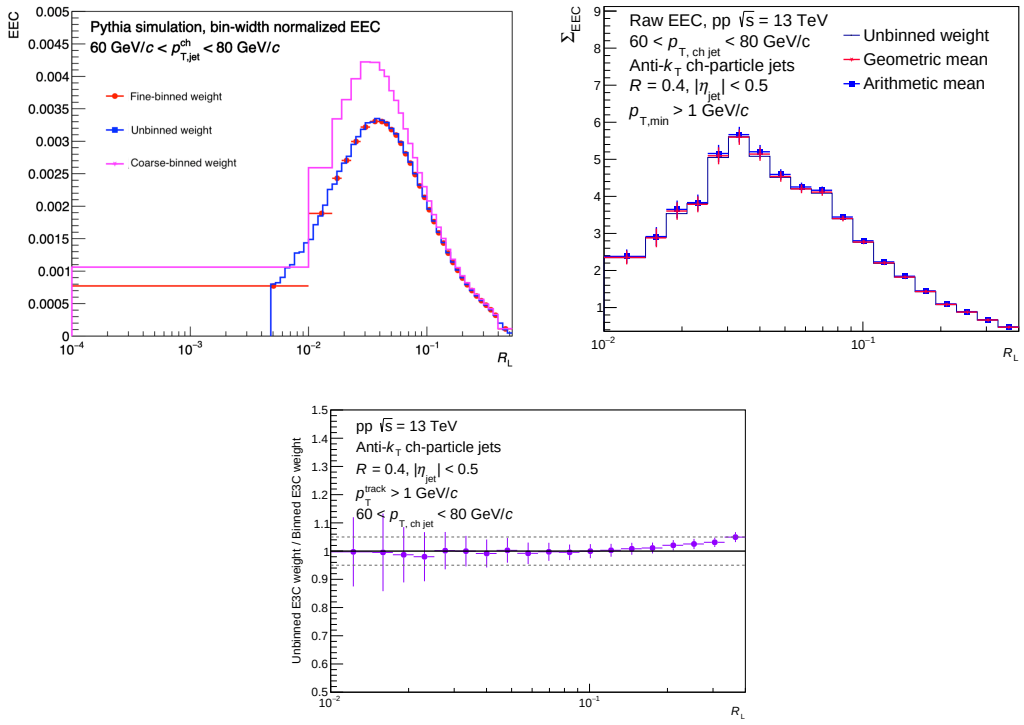


Figure 6.15: Top Left: Comparison of the EEC distribution obtained using different weight binning strategies. Top Right: Comparison of different weight evaluation methods applied to raw data. Evaluating the weight using the geometric mean yields a more faithful representation of the underlying distribution. Bottom: The maximum difference between unbinned and binned weights is in the 60-80 GeV/$c$ bin for the raw E3C distribution.

### 6.5.2 Systematics from Detector Effects

**Tracking Efficiency**: The effects of tracking efficiency on the ENC are described in Sec. 6.2.3. Thus, it is important to characterize the effect of tracking inefficiency on the observables. The tracking efficiency at ALICE for pp collisions is at 84% for tracks $p_{\mathrm{T,track}} = 1$ GeV/$c$ and stays above 75% for higher $p_{\mathrm{T,track}}$ [235]. This systematic is

implemented by reducing the efficiency by 3% in the MC and then unfolding raw data with the corresponding response matrix.

### 6.5.3 Systematics from Unfolding

Unfolding systematics mainly come from the following sources:

**Regularization Parameter**: The unfolding procedure includes a regularization parameter, whose variation is treated as a systematic uncertainty. Since this parameter corresponds to the number of iterations, it is varied by $\pm 1$, and the resulting difference from the nominal case is taken as a systematic uncertainty.

**Prior Variation**: Since the unfolding procedure relies on a prior, it is important to assess the prior dependence on the final result. Prior variation is performed via reweighting the MC sample by the ratio of detector-level MC to raw data. The difference in the unfolded result from the nominal case is then taken as a systematic.

**Generator Dependence**: The truth and detector-level distributions used to construct the response matrix for the nominal results are obtained from PYTHIA8 and PYTHIA8+GEANT3 simulations, respectively. To account for potential generator bias, a HERWIG fast simulation[15] is used to generate an alternative set of truth and detector-level distributions. For consistency, a PYTHIA8 fast simulation is also performed. The raw data is unfolded using both generators, and the difference in the final results from these fast simulations is taken as a systematic uncertainty.

**Bin Truncation**: To quantify the effects of our jet $p_{\mathrm{T}}$ cuts on our unfolded result, we vary the lower jet $p_{\mathrm{T}}$ bin of our detector level distribution by 5 GeV/$c$, allowing only detector level jets above 20 GeV/$c$, (instead of our nominal 15 GeV/c), to enter into our response matrices. The raw data is unfolded using the modified response,

15. To replicate the full simulation, the fast simulation incorporates both tracking efficiency and pair efficiency effects present in the ALICE full simulation. The code for the fast simulation can be found at: https://github.com/anabananana98/ENC-analysis/blob/main/ALICE_ENC_fsTrackMatching.cc

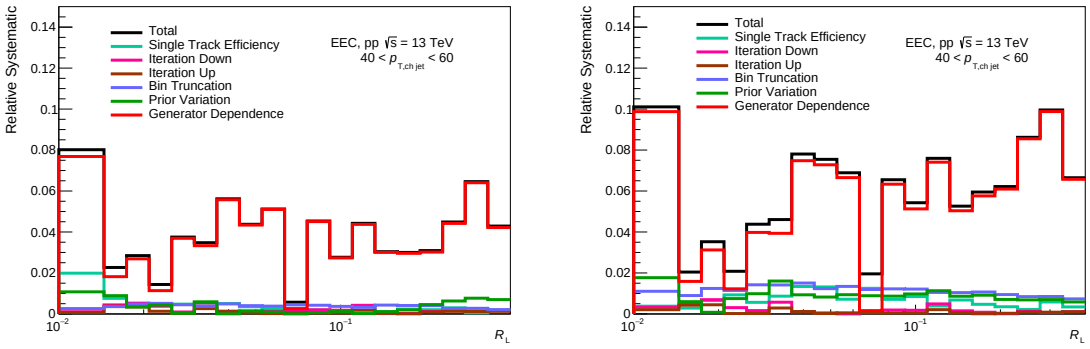


Figure 6.16: Relative systematics in one jet $p_{\mathrm{T}}$ bin for the measurement at $\sqrt{s} = 13$ TeV. Left: EEC. Right: E3C.

and the difference in the final results is taken as a systematic uncertainty. For the $\sqrt{s} = 5.02$ TeV analysis, the nominal value is 40 GeV/$c$ and is raised to 45 Gev/$c$.

Figure 6.16 presents a summary of the relative systematic uncertainties for a representative jet $p_{\mathrm{T}}$ bin. Among the sources considered, generator dependence emerges as the dominant contributor to the total uncertainty for both the EEC and E3C measurements. Additional plots illustrating the relative systematic uncertainties across other jet $p_{\mathrm{T}}$ bins are provided in Appendix A for both analyses.

## 6.6 Results and Discussion

*This section presents results from the updated measurement at $\sqrt{s} = 13$ TeV as well as results from the measurement at $\sqrt{s} = 5.02$ TeV. Preliminary results for $\sqrt{s} = 13$ TeV analysis can be found in Appendix A.1 including a discussion on comparison with MC generators.*

### 6.6.1 EEC and E3C

**Results at $\sqrt{s} = 13$ TeV**

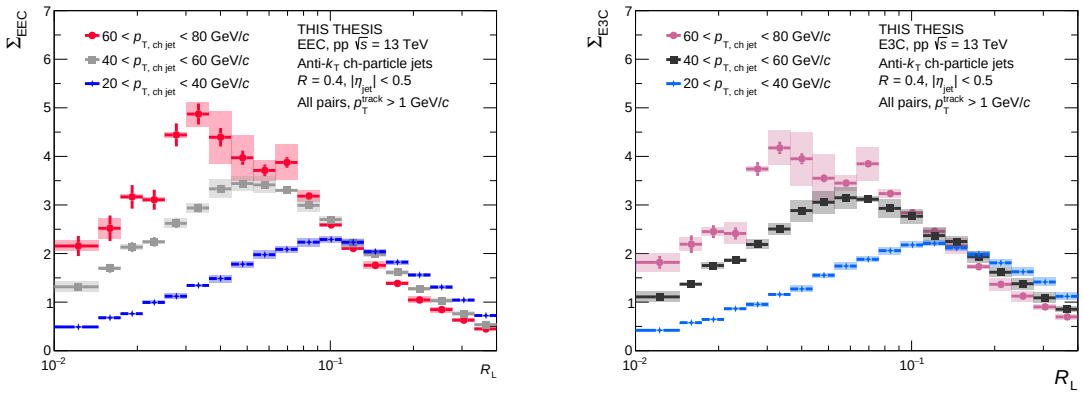


Figure 6.17: Fully corrected distribution for charged anti-$k_T$ jets of $R = 0.4$ in pp collisions at $\sqrt{s} = 13$ TeV with the ALICE detector. Left: EEC. Right: E3C.

Fig. 6.17 presents the fully corrected EEC and E3C distributions, each normalized by the number of jets (and bin-width), for pp collisions at a center-of-mass energy of $\sqrt{s} = 13$ TeV. These observables reveal distinct scaling behavior that reflects the underlying dynamics of jet formation, as discussed in Chapter 4. In particular, the distributions exhibit two clearly separated regimes as a function of their angular separation, $R_L$: at large $R_L$, the correlators are dominated by partonic contributions, while the small $R_L$ region is governed by free-streaming hadrons. This separation reflects the angular-ordered nature of QCD jets, consistent with theoretical expectations outlined in Sec. 4.2.3.

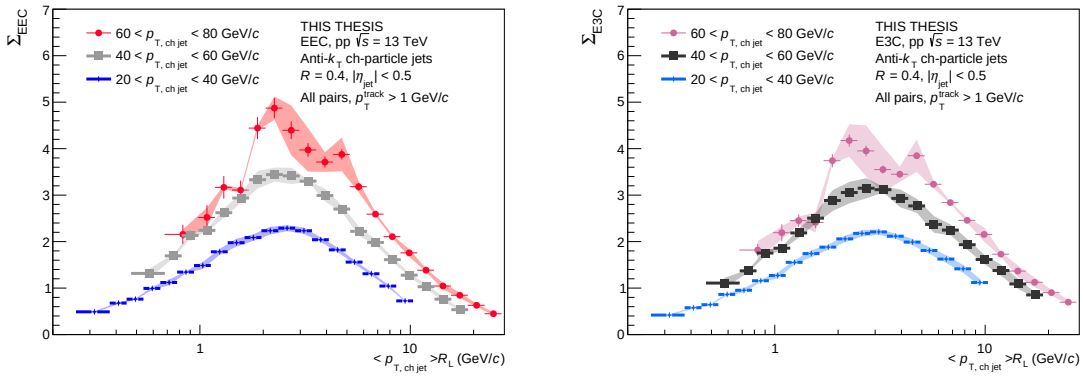


Figure 6.18: Normalized EEC and E3C distributions as a function of $\langle p_{\mathrm{T,\ ch\ jet}} \rangle\, R_{\mathrm{L}}$

As the jet $p_{\mathrm{T}}$ increases, the peak of the EEC and E3C distributions shifts consistently toward smaller values of $R_{\mathrm{L}}$. This trend reflects the empirical scaling behavior observed in previous studies, where the peak location follows the relation $R_{\mathrm{L,peak}} \propto \Lambda / p_{\mathrm{T,jet}}$ [15], as discussed in Sec. 4.2.3. This relationship is also highlighted in Fig. 6.18 where the $\langle p_{\mathrm{T}} \rangle$ scaled distributions are shown for the EEC (left panel) and the E3C (right panel). In this case, the scaling by average $p_{\mathrm{T}}$ is performed after unfolding. The average $p_{\mathrm{T}}$ in a bin is computed using a fine-binned distribution of jet cross-section in PYTHIA. Similar behavior has been documented in other experimental measurements of the EEC [22,23,215], reinforcing the interpretation that this scaling captures key features of perturbative QCD dynamics.

This phenomenon illustrates the angular-ordered nature of QCD parton showers: as a high-energy parton radiates, each successive splitting occurs at a smaller angle relative to its parent. Reading the distribution from left to right in $R_{\mathrm{L}}$ thus corresponds to probing progressively earlier stages of the shower evolution,[16] moving from free-streaming hadrons to perturbative dynamics. The sharp rise in the distri-

16. This process can be understood through the concept of *formation time* ($\tau_f$), which characterizes the timescale over which the two partons produced in a $1 \to 2$ QCD splitting decohere and begin to act as independent emitters of radiation [236]. In the soft and collinear limit, the formation time is approximately $\tau_{\mathrm{form}} \approx 1/R_{\mathrm{L}}^2$ [236], implying that splittings at larger angles (larger $R_{\mathrm{L}}$) occur earlier in time.

bution at small $R_{\mathrm{L}}$ is a manifestation of the collinear singularity inherent in QCD splitting functions. However, this rise is eventually tempered by non-perturbative hadronization effects, which cause the distribution to turn over at the smallest angular scales. As mentioned in Sec. 4.2.3, this regime is dominated by geometrical correlations arising from uniformly distributed hadrons.

**Results at $\sqrt{s} = 5.02$ TeV**

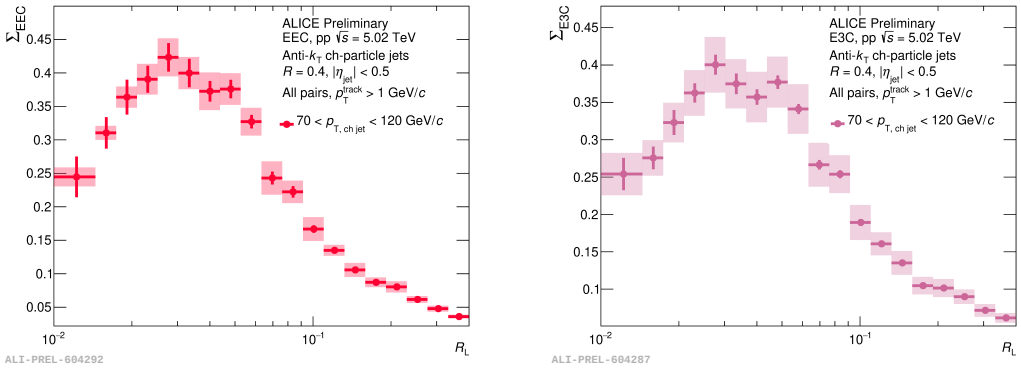


Figure 6.19: Fully corrected distribution for charged anti-$k_{\mathrm{T}}$ jets of $R = 0.4$ in pp collisions at $\sqrt{s} = 5.02$ TeV with the ALICE detector. Left: EEC. Right: E3C.

Fig. 6.19 shows the fully corrected EEC and E3C distributions, normalized by the number of jets, for proton-proton collisions at a center-of-mass energy of $\sqrt{s} = 5.02$ TeV. The overall structure and scaling behavior of the distributions remain consistent with those observed at $\sqrt{s} = 13$ TeV, indicating the robustness of the underlying QCD dynamics across different energies. While some variation in the perturbative regime is theoretically expected, primarily due to changes in the relative quark and gluon jet fractions at different collision energies, these differences are not significant with the current systematic uncertainties.

### 6.6.2 E3C/EEC Ratio

It is expected from pQCD that the E3C and EEC should scale with the anomalous dimensions ($\gamma$) of these operators in the perturbative regime, as discussed in Sec. 4.2. However, this behavior is suppressed by the leading behavior, which goes like $\sim 1/R_{\mathrm{L}}$. To access these scalings that arise due to quantum mechanical interactions, one can take a ratio of the measured EEC and E3C distributions which approximately scales as $R_{\mathrm{L}}^{\gamma_3-\gamma_2}$, as discussed in Sec. 4.2.3.

**Results at $\sqrt{s} = 13$ TeV**

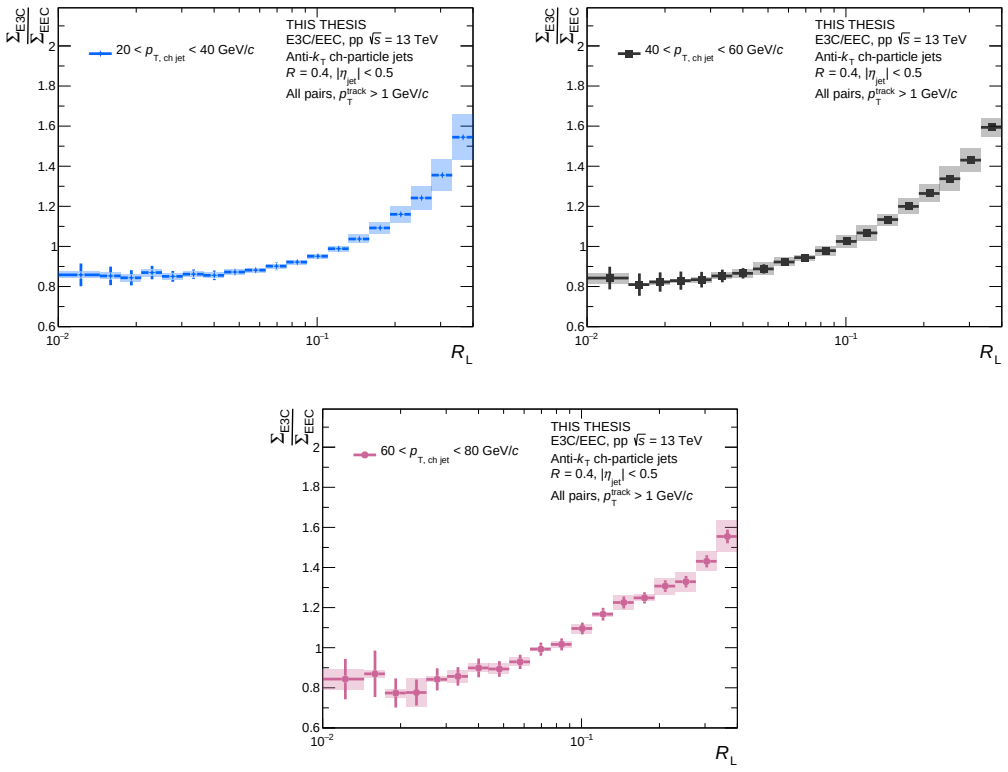


Figure 6.20: Fully corrected E3C/EEC ratio for or charged anti-$k_{\mathrm{T}}$ jets of $R = 0.4$ in pp collisions at $\sqrt{s} = 13$ TeV with the ALICE detector.

These are shown in Fig. 6.20 and in the right panel of Fig. 6.21. A few notable features can be seen from these plots. First, from formal theoretical considerations, it is known that $\gamma_{N+1} > \gamma_N$ [237], which is reflected in the data (since the slope here

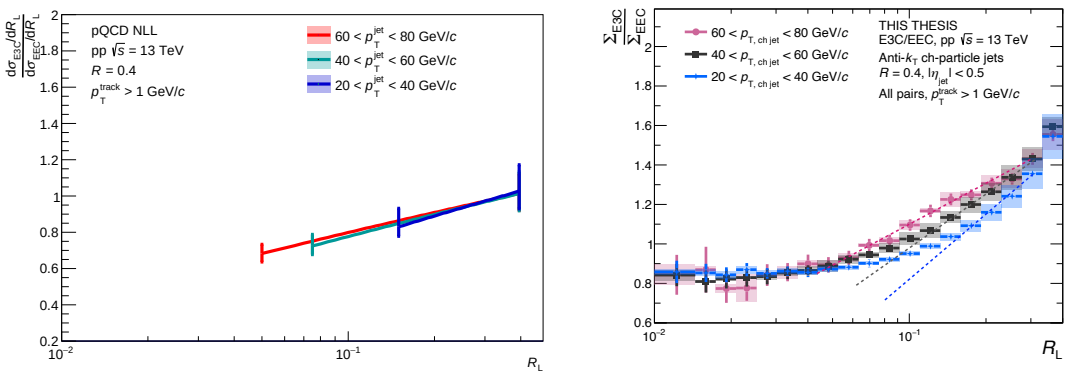


Figure 6.21: Left: pQCD calculation at NLL for charged tracks in full anti-$k_{\mathrm{T}}$ jets of $R = 0.4$. Right: E3C/EEC measurement at $\sqrt{s} = 13$ TeV for charged jets. The dotted lines are hand-drawn and meant to guide the eye.

is proportional to $(\gamma_3 - \gamma_2)$, where 3 and 2 correspond to E3C and EEC respectively, as discussed in Sec. 4.2.3) by the positive slope of the E3C/EEC ratio at large $R_{\mathrm{L}}$. Second, if one looks at the right panel of Fig. 6.21—at low $R_{\mathrm{L}}$, in the non-perturbative regime, the slope is flat for all jet $p_{\mathrm{T}}$ bins, confirming that the trivial correlation at low $R_{\mathrm{L}}$ arises due to free-streaming hadrons (since the slope in this region is proportional to $R_{\mathrm{L}}$). Third, and most significant, is that as one goes to higher jet $p_{\mathrm{T}}$, the curve becomes flatter in the perturbative regime, as can be seen in Fig. 6.20. Since the slope of the E3C/EEC ratio is proportional to $\alpha_s$ [188], this flatness with rising jet $p_{\mathrm{T}}$ is indicative of the running of $\alpha_s$ (which, as shown in Fig. 2.3, becomes smaller at higher energies). This is also shown by the dotted lines in the right panel of Fig. 6.21.

This behavior is compared to pQCD predictions[17] at next-to-leading logarithmic (NLL) accuracy in Fig. 6.21, based on calculations from Ref. [16]. The pQCD calculation is performed for charged tracks clustered into full jets, whereas the measurement presented here is based on charged jets. Since charged jets and full jets do not correspond one-to-one, as illustrated in Fig. 6.22—which presents the response matrix for charged jets matched to full jets in ALICE kinematics using a PYTHIA [221]

17. Note that, as discussed in Sec. 4.2, since the y-values are arbitrary, these curves have been normalized to be equal to 1 in the highest $R_{\mathrm{L}}$ bin.

generator-level simulation—a direct comparison is not valid. The highly non-diagonal structure of the matrix highlights the significant differences between the two jet types. Therefore, only qualitative comparisons between the measurement and theory are currently meaningful, with the primary observation being that the overall trends are consistent.

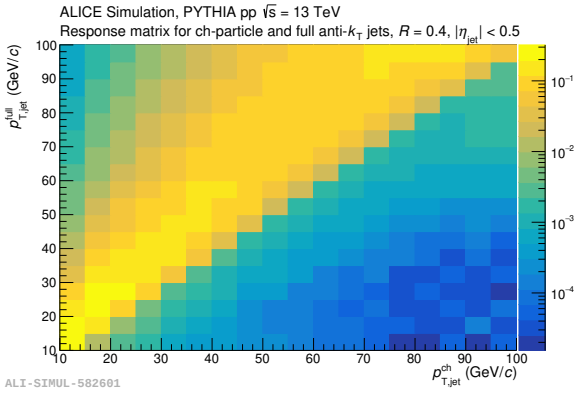


Figure 6.22: Response matrix for charged vs full jets anti-$k_{\mathrm{T}}$ jets of $R = 0.4$ in ALICE kinematics at $\sqrt{s} = 13$ TeV.

### Results at $\sqrt{s} = 5.02$ TeV

The E3C/EEC ratio at $\sqrt{s} = 5.02$ TeV is shown in Fig. 6.23. The same characteristic features described in the previous section are observed: the ratio remains approximately flat in the non-perturbative regime and exhibits a positive slope in the perturbative regime. This slope is again attributed to the anomalous dimensions of the ENC operators, which scale proportionally with $\alpha_s$. Although differences in the quark/gluon composition of the jet population at different center-of-mass energies could, in principle, affect the observed slopes [15], the current experimental uncertainties preclude drawing definitive conclusions.

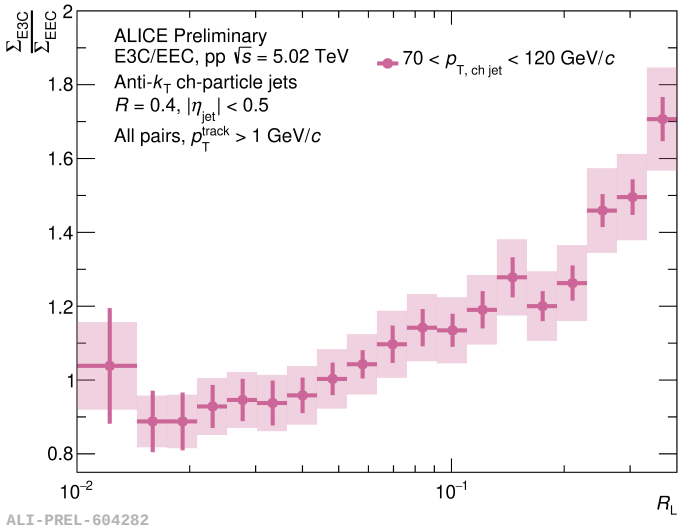


Figure 6.23: Fully corrected E3C/EEC ratio for charged anti-$k_{\mathrm{T}}$ jets of $R = 0.4$ in pp collisions at $\sqrt{s} = 5.02$ TeV with the ALICE detector.

# Chapter 7

# Probing the QGP with Energy Correlators

*The work detailed in this chapter focuses on the projected N-point correlators and shape-dependent higher-point correlators in heavy-ion collisions. Further checks of the conclusions in this work are detailed in Appendix B.*

## 7.1 Energy Correlators in Heavy-Ion Collisions

Energy correlators have emerged as a powerful tool for probing jet substructure in vacuum, inspiring their application to studying jet-medium interactions. An active research program is already underway to explore their relevance in heavy-ion collisions [24, 25, 202–204, 238–241]. The plots in Fig. 7.1 present two studies demonstrating that interactions with the medium can lead to a large-angle enhancement of the two-point energy correlator. In both cases, $L$ denotes the length of the QGP brick and $E$ represents the energy of the quark. In the left panel, the observed enhancement is attributed to color decoherence effects [24]. The variable $\hat{q}$ is the quenching parameter characterizing the medium's transport properties. Increasing $\hat{q}$ values correspond to stronger jet-medium interactions, resulting in greater energy loss. In this

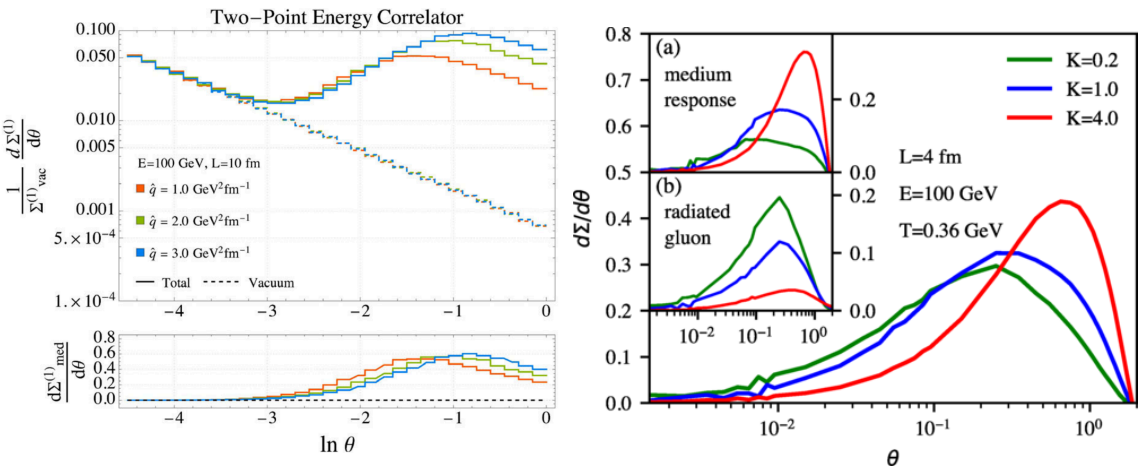


Figure 7.1: Left: Large angle enhancement for the EEC due to color decoherence effects [24]. Right: Medium response effects in the LBT framework [25].

regime, the medium resolves the jet's substructure, leading to enhanced medium-induced radiation at large angles, which manifests as an increased EEC signal in the wide-angle region. The right panel of Fig. 7.1 presents the EEC as computed within the LBT framework [25]. In this case, $T$ represents the medium temperature and $K$ is related to the Debye screening mass, setting the characteristic momentum and angular scales of parton-medium interactions.[1] Increasing $K$ enhances both the energy transferred to the medium, reflected by the larger medium response contribution in inset (a), and the elastic energy loss of the leading parton, which reduces its contribution as seen in inset (b). Overall, the EEC is dominated by medium response effects, while medium-induced radiation provides a subleading contribution; both mechanisms manifest as enhancements at large angles. A recent measurement from the CMS collaboration revealed modifications consistent with expectations from modification due to jet-medium interactions [207]. However, previous studies have primarily focused on the two-point correlator. Given that ratios of projected correlators in vacuum are sensitive to the anomalous dimensions of energy flow operators, it is compelling to investigate whether these ratios undergo modification in the QGP.

1. Note that this figure is for a single quark interacting with the medium. The authors make similar conclusions for a full quark-initiated jet shower. For details, see Ref. [25].

This chapter contributes to this effort by extending the analysis to higher-point correlators to assess their sensitivity to medium response effects. These studies were conducted using the Hybrid Weak/Strong Coupling Model (hereafter referred to as the Hybrid Model) and published as a few-author paper in JHEP [17].

## 7.2 Hybrid Model Overview

A full review of the Hybrid Model and its implementation can be found in [143]. Here, I mention some noteworthy features of the model:

- Vacuum splitting probabilities (without MPIs but including ISR), modification of PDFs is implemented.
- Quenching calculated via $\mathcal{N} = 4$ super Yang-Mills (SYM) via an AdS/CFT [58] approach with one parameter that is tuned to data.
- Temperature profile of an expanding medium at every space-time point derived from 3+1D VISHNU [80].
- No implementation of medium-induced radiation.

Essentially, the jets produced from PYTHIA propagate unperturbed until hydrodynamization kicks in at $\tau_{hydro}$, which is about 0.2 fm/c. The jets now interact with a hydrodynamically evolving QGP and suffer energy loss. Since this happens in the strong coupling regime, from the energy and momentum conservation with the medium, the energy deposited in the medium hydrodynamizes at distances $\approx 1/T$, exciting a wake.[2] The wake continues to evolve hydrodynamically until the temperature cools to the freezeout temperature. Then this wake turns into many soft hadrons with a momentum distribution described via the Cooper-Frye freezeout prescription. This is then hadronized using the PYTHIA Lund-String hadronization model [122].

2. It is important to note that no conclusive measurement of the wake has appeared to date.

## 7.3 Expectations for Modification of Projected *N*-Point Energy Correlators

Since jets lose energy in the QGP, one expectation for the ENCs is that the distribution will change solely due to effects from jet quenching. This may manifest as a narrowing of the distribution.

Since the wake is produced in all directions, some of it inevitably enters the jet, introducing soft hadrons that alter its substructure. While the wake is a correlated response to the presence of the jet, the correlations between jet and wake particles within the jet should differ from those arising purely from the jet's fragmentation. Energy correlators, which are sensitive both to the jet's fragmentation pattern and the characteristic scale of the QGP, provide a means to distinguish these effects.

Computing particle pairs as a function of $R_{\mathrm{L}}$ for a uniform distribution results in a distribution that is peaked at large $R_{\mathrm{L}}$. Because the wake is uniformly distributed within the jet cone, its influence should manifest as a large-angle modification due to correlations between jet and wake particles (hard-soft correlations). In contrast, correlations between wake particles alone will be predominantly soft, as the wake consists of low-$p_{\mathrm{T}}$ hadrons. As a result, one expects energy correlators to reveal significant large-angle modifications, capturing the interplay between jet fragmentation and medium response.

## 7.4 New Coordinates for Energy-Energy-Energy Correlators in Heavy-Ion Collisions

As mentioned in Sec. 4.2.4, the EEEC is sensitive to the shape of energy flow. The $(\xi, \phi)$ coordinates introduced in that section are well-suited for visualizing the EEEC in vacuum QCD, as they emphasize the theory's collinear singularity. However, out-

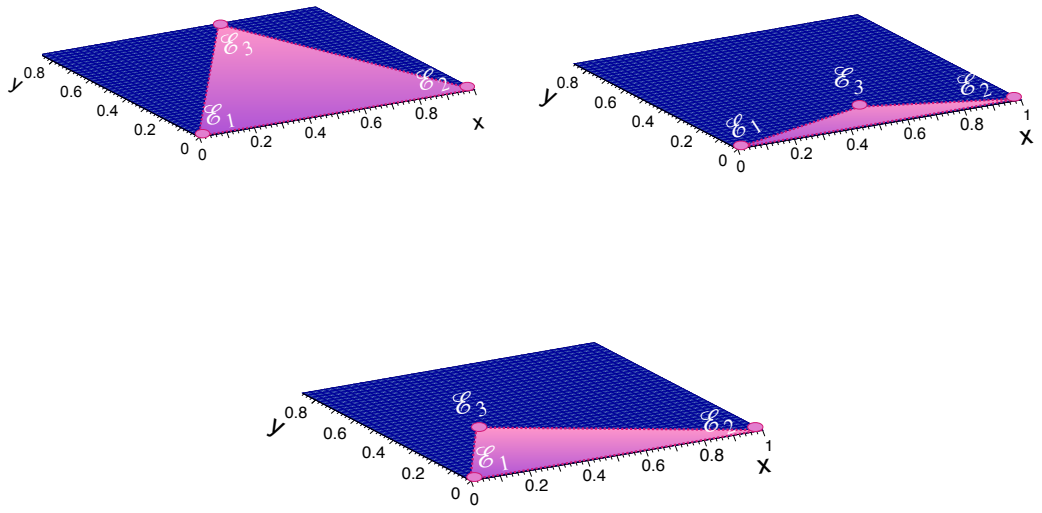


Figure 7.2: Three possible shapes of the three-point Energy-Energy-Energy Correlator triangles in $x$-$y$ coordinate system. Top Left: Equilateral. Top Right: Flattened. Bottom: Squeezed. These can be contrasted with the $\xi - \phi$ coordinates in Fig. 4.4.

side the squeezed limit (i.e., at larger $\xi$), the Jacobian of this coordinate system is not flat. As shown explicitly in Appendix B, the Jacobian develops a sharp peak at the equilateral triangle configuration ($\xi = 1$, $\phi = \pi/2$). This non-uniformity becomes problematic when the EEEC receives significant contributions near the equilateral region—such as from soft hadrons emitted in jet wakes—since the Jacobian can obscure physical effects. To address this, one can either plot ratios in which the Jacobian cancels or adopt a new coordinate system with a flat Jacobian across the relevant phase space. Given that the equilateral regime is populated in such scenarios, we adopt the latter approach to ensure accurate visualization of the underlying physics. We detail the flat-Jacobian coordinate system and its transformation to $(\xi, \phi)$ in Appendix B. To characterize the shape of the EEEC triangle, we employ Cartesian coordinates $(x, y)$ in the plane. The triangle is first rescaled such that its longest side, of length $R_{\mathrm{L}}$, becomes 1. This side is placed along the $x$-axis between $(0, 0)$ and $(1, 0)$, and the third vertex is located at $(x, y)$, which fully determines the

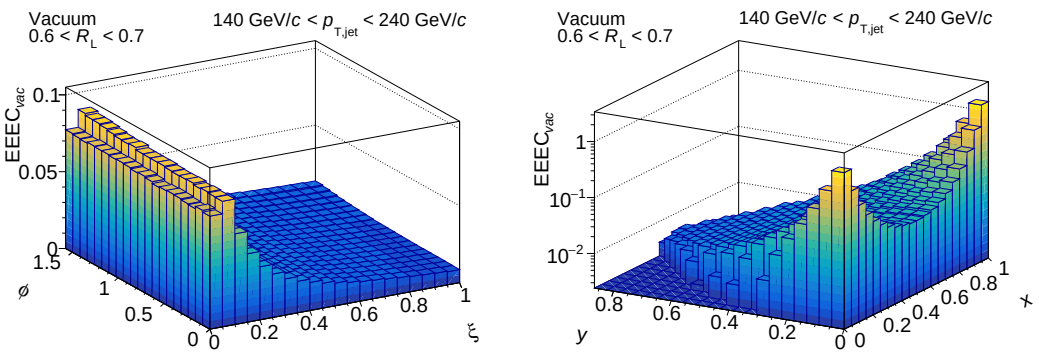


Figure 7.3: EEEC for anti-$k_T$ jets with $R = 0.8$ in vacuum (i.e., from proton-proton collisions). Left: Plotted in $(\xi, \phi)$ coordinates. Right: Plotted in $(x, y)$ coordinates. The collinear enhancement, arising from the singular behavior of the splitting function that governs vacuum parton shower development, is clearly visible—either in the small-$\xi$ region or near the points $(0, 0)$ and $(1, 0)$ in the $(x, y)$ plane.

triangle's geometry. By symmetry, we restrict to $y > 0$, since flipping $y$ would yield an equivalent triangle. The mapping into $(x, y)$ coordinates for squeezed, flattened, and equilateral triangles is illustrated in Fig. 7.2. Because this coordinate system is Cartesian, the Jacobian is flat. The domain of valid triangles is bounded by two arcs and the $y = 0$ line. The $(x, y)$ coordinates shown in Fig. 7.2 can be compared to the $(\xi, \phi)$ coordinates shown in Fig. 4.4 in Chapter 4. For reference and orientation, we show in Fig. 7.3 the EEEC for jets in vacuum, plotted in $(x, y)$ coordinates. The collinear enhancement observed at small $\xi$ in the left plot appears in $(x, y)$ space near the points $(0, 0)$ and $(1, 0)$, which correspond to collinear configurations. Put differently, if two particles in the jet are fixed at the ends of the longest side of the triangle, the third particle is most likely to be found nearly collinear with one of them—a manifestation of the dominance of collinear splittings in vacuum jet evolution.

## 7.5 Simulation Details

Each sample contains ∼1 million events, all for collisions with a center of mass energy of $\sqrt{s_{NN}} = 5.02$ TeV. The heavy-ion events simulated correspond to the 0–5% most

central[3] (head-on) collisions. In the inclusive jet samples, $\widehat{p}_{\mathrm{T,min}}$ is set to 100 GeV/$c$ in PYTHIA; this corresponds to the minimum $p_{\mathrm{T}}$ of the initial hard scattering from which the parton showers that PYTHIA then describes originate. Inclusive jets with $p_{\mathrm{T,jet}} > 140$ GeV/$c$ are reconstructed. For this study, inclusive hadron-level anti-$k_{\mathrm{T}}$ jets of $R = 0.8$ were reconstructed. Jets are required to have $|\eta_{\mathrm{jet}}| < 2.0$. To identify a $\gamma$-jet event, a set of selection criteria is designed to closely replicate those used in experimental analyses [242]. First, the photon must be well-separated from the jet in azimuth, satisfying $\Delta\phi > 2\pi/3$. Additionally, the photon must be isolated, which is defined as having less than 5 GeV/$c$ of transverse energy within a cone of radius $R = 0.4$ centered on the photon direction. For $\gamma$-tagged jets, the photon's transverse momentum, $p_{\mathrm{T}}^{\gamma}$, is taken as a proxy for the jet's initial transverse momentum when constructing the correlators.

Three scenarios are examined to explore the effects of jet-medium interactions:

- *Vacuum:* Simulations of proton-proton collisions with jets evolving entirely in vacuum. In the Hybrid Model, vacuum samples are simply PYTHIA simulations with the specified settings described earlier. These vacuum samples serve as baseline references. Any differences between observables in a vacuum sample and those in Hybrid Model samples can be attributed to the effects of the parton shower interacting with the QGP.

- *Medium with Wake:* Hybrid Model simulations of Pb-Pb collisions capture parton showers interacting with the QGP, losing energy and momentum to the medium. This energy deposition forms a wake in the hydrodynamic QGP, which after freezeout, manifests as soft hadrons. These simulations account for all contributions to the final hadron distributions in Pb-Pb jet events.

3. "Centrality" is an experimental term that is used to characterize how head-on a collision is. Details about this definition can be found in Chapter 8.

- *Medium without Wake:* These Pb-Pb collision simulations are identical to the previous case, except that hadrons from the wake are excluded. Jets in this sample consist only of hadrons from the medium-modified parton shower, as modeled in the Hybrid Model. While this scenario is unphysical—since omitting the wake violates energy and momentum conservation—it serves as a valuable tool. Comparing observables from this sample with those from the full "medium with wake" simulation isolates the wake's impact on any given observable.

## 7.6 Results and Discussion

### 7.6.1 Projected *N*-Point Energy Correlators

The top panel of Fig. 7.4 presents the E2C for inclusive jets in vacuum, in medium with wake, and in medium without wake, revealing three key features.

First, in both medium cases, the E2C peak shifts leftward, indicating a smaller characteristic angle compared to vacuum. In vacuum, this peak marks the transition between hadron-dominated small-angle scaling and parton shower-driven large-angle scaling, following $R_{\mathrm{L}} \sim \Lambda/p_{\mathrm{T,jet}}$ [15] as discussed in Chapter 6. In heavy-ion collisions, this shift directly reflects parton energy loss as jets traverse the QGP. Since selected Pb-Pb jets (with $p_{\mathrm{T,jet}} > 140$ GeV/$c$) have already lost energy, their vacuum-equivalent $p_{\mathrm{T}}$ would be higher. The percentage shift in the E2C peak relative to pp collisions encodes this energy loss, allowing substructure techniques to quantify it [243].

Second, in the medium without wake case, a modest modification appears beyond the peak to the right, where parton shower dynamics dominate, alongside a slight peak height increase. These effects arise from parton energy loss, which modifies the shower and biases jet selection toward narrower jets.

Third, the most significant effect occurs at large angles ($R_{\mathrm{L}}$). In the wake-free

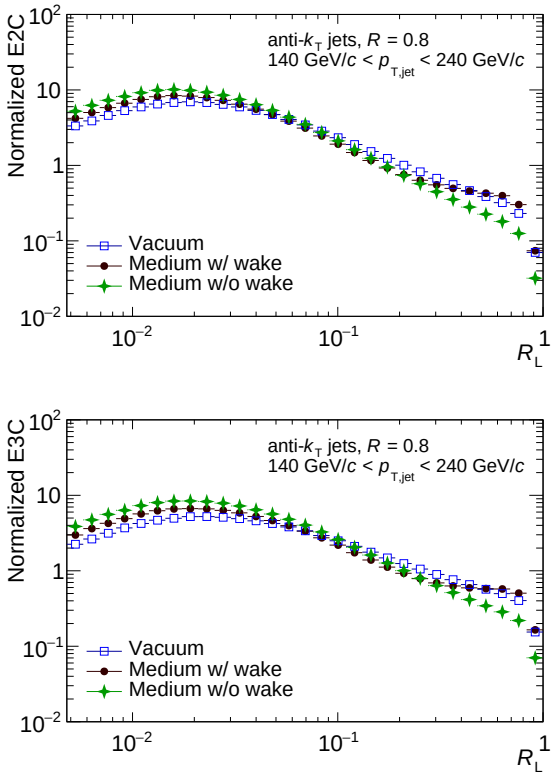


Figure 7.4: ENC distributions as a function of $R_{\mathrm{L}}$ for inclusive jets with $R = 0.8$ and $140 < p_{\mathrm{T,jet}} < 240$ GeV/$c$ in vacuum, medium with wake, and medium without wake. These distributions are per-jet and bin-width normalized. Top: E2C (or EEC). Bottom: E3C.

case, parton shower modifications alter the E2C scaling, as expected. However, in the medium with wake, a substantial enhancement at large $R_{\mathrm{L}}$ disrupts vacuum-like scaling due to hadrons originating from the wake. In the Hybrid Model, this effect is directly attributed to the wake, whereas other models of jet-medium interactions [24, 25, 202–204, 238–241] also exhibit large-angle modifications but with stronger parton shower alterations.

The bottom panel of Fig. 7.4 extends this analysis to the E3C, where the same three effects appear. The E3C/E2C ratio is presented in Fig. 7.5, which in vacuum follows a power-law scaling governed by twist-2 anomalous dimensions and is proportional to the QCD coupling $\alpha_s$, as described in Sec. 4.2.3. In Pb-Pb collisions, the ratio deviates from vacuum scaling, consistent with wake-induced modifications to

E2C and E3C. At very small angles, the ratio remains unchanged, as hadronization scaling dominates and the wake has no contribution. Focusing on medium effects,

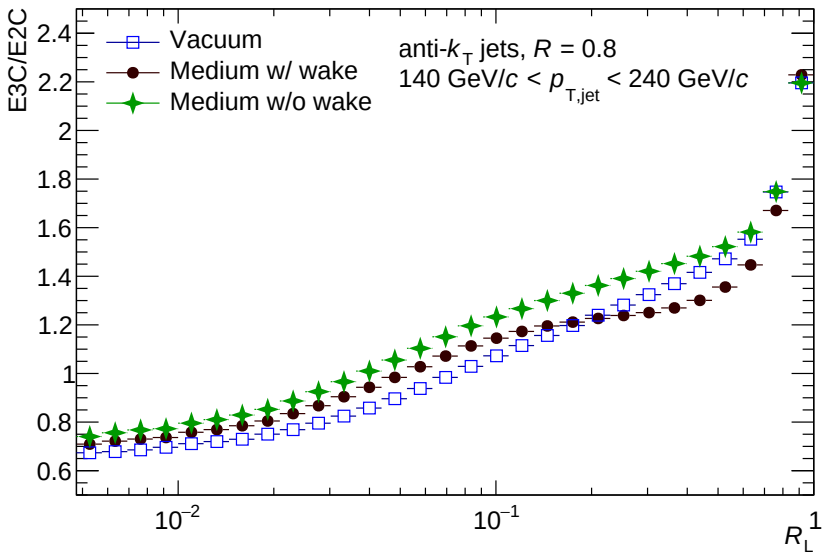


Figure 7.5: Ratio of E3C to the E2C as a function of $R_{\mathrm{L}}$ for inclusive jets with $R = 0.8$ and $140 < p_{\mathrm{T,jet}} < 240$ GeV/$c$ in vacuum, medium with wake, and medium without wake. These distributions are per-jet and bin-width normalized.

the wake-free case shows a mild scaling deviation at large angles due to parton energy loss. When the wake is included, scaling breaks down further, with an almost flat E3C/E2C ratio at large angles. This flat dependence of the E3C/E2C ratio on $R_{\mathrm{L}}$ over a range of large angles suggests that hadrons from the wake are distributed nearly uniformly in angular scale.[4] It would be interesting to extend this study to other models to investigate if the projected correlators can exhibit unique sensitivity to various medium effects.

4. While this does not imply that the wake has a uniform overall shape, it indicates that the angular distribution of its hadrons is relatively featureless, lacking spikiness or fine substructure. See, for example, [244] for further discussion.

### 7.6.2 Full Shape Dependent Energy-Energy-Energy Correlators

While the shape of the three-point correlator for jets in vacuum has been extensively studied using perturbative QCD, heavy-ion collisions provide a particularly compelling application. In this context, the EEEC offers a means to disentangle medium-induced modifications to the parton shower from jet-induced perturbations to the QGP. To isolate the impact of hadrons produced in the wake, we analyze three scenarios: jets in vacuum, jets in-medium without the wake, and jets in-medium with the wake. These are shown in Fig. 7.6.

Before comparing the two upper panels in Fig. 7.6, it is instructive to contrast the upper right panel (jets in-medium without wake) with the lower panel (jets in vacuum). In the Hybrid Model, each parton in the shower loses energy and momentum to the medium, resulting in a uniform suppression of the EEEC across the entire $(x, y)$ plane. This includes the collinear, squeezed-triangle regions near $(x, y) = (0, 0)$ and $(1, 0)$ that dominate in vacuum. The effect of the wake can then be isolated by comparing the upper left and upper right panels, revealing how the presence of wake-induced hadrons further modifies the EEEC structure beyond the suppression caused by parton energy loss alone.

To more clearly illustrate the effects discussed above, we can examine the ratio of the EEEC in heavy-ion collisions (with and without the wake) to the EEEC in vacuum, shown in Fig. 7.7 in $(x, y)$ coordinates. In the right panel, where wake-induced hadrons are excluded, the ratio remains relatively flat and consistently below unity across the phase space. This suppression reflects the energy loss experienced by partons in the Hybrid Model. Interestingly, the suppression is least pronounced in the collinear regions near $(x, y) = (0, 0)$ and $(1, 0)$, where the most energetic particles are located. This behavior is consistent with the energy loss of high-energy partons in a strongly coupled medium [143].

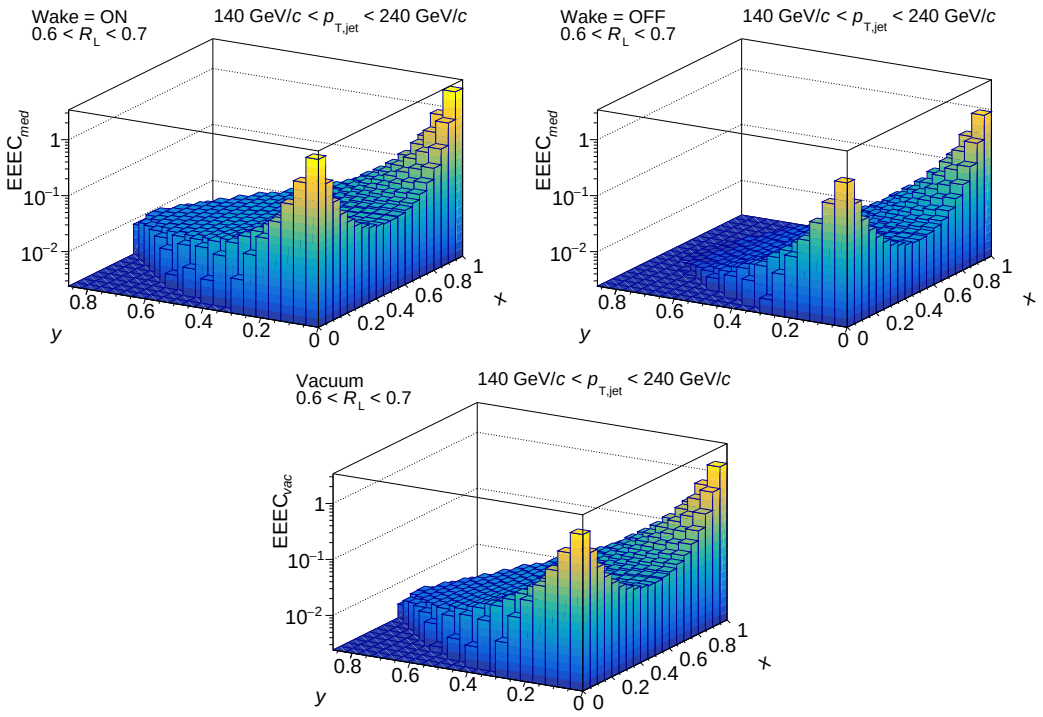


Figure 7.6: Shape-dependent EEEC distributions. Top Left: In-medium EEEC with wake effects. Top Right: In-medium EEEC without the wake. The presence of the wake leads to a pronounced enhancement in the equilateral region, where hadrons from the wake dominate the correlator. Bottom: Vacuum EEEC for comparison.

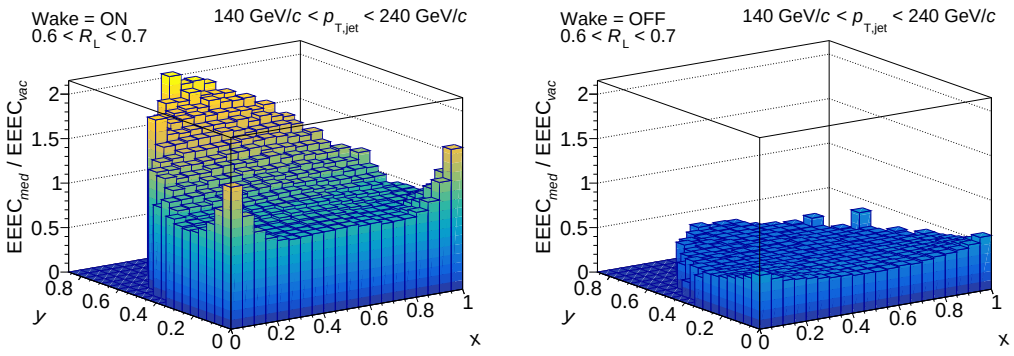


Figure 7.7: The ratio of the shape-dependent EEEC in medium to that in vacuum. Left: With wake. Right: Without wake. A clear enhancement in the equilateral region is visible in the left plot, indicating a significant contribution from wake-induced hadrons. Each distribution is normalized by the number of jets in the corresponding sample prior to computing the ratios.

By contrast, the left panel—where hadrons from the wake are included—shows a pronounced enhancement in the equilateral region of the correlator, with the in-medium to vacuum EEEC ratio reaching values close to 2. This demonstrates a significant contribution from soft hadrons emitted by the jet wake. The stark contrast between the two panels of Fig. 7.7 provides compelling evidence that, in Pb-Pb collisions, the EEEC is dominated in the equilateral region by energy flow sourced from jet-induced wakes, corresponding to three well-separated angular directions.

Comparison of jets produced in association with a high-$p_{\mathrm{T}}$ photon ($140 < p_{\mathrm{T}}^{\gamma} < 240$ GeV/$c$)—referred to as $\gamma$-tagged jets—to inclusive jets within the same $p_{\mathrm{T}}$ range ($140 < p_{\mathrm{T}}^{\mathrm{jet}} < 240$ GeV/$c$) is shown in Fig. 7.8. The procedure for selecting $\gamma$-tagged jets is described in Sec. 7.5. As can be seen in Fig. 7.8, $\gamma$-tagged jets exhibit a more pronounced enhancement in the equilateral region of the EEEC compared to inclusive jets. This difference can be attributed to two primary factors. First, $\gamma$-tagged jets offer a more precise estimate of the unquenched jet $p_{\mathrm{T}}$ (as discussed in Sec. 2.5.2 and 3.6.2), thereby providing a clearer view of medium-induced effects. Second, inclusive jet samples are subject to contamination from overlapping wake contributions. As discussed in Appendix B, inclusive events often contain an away-

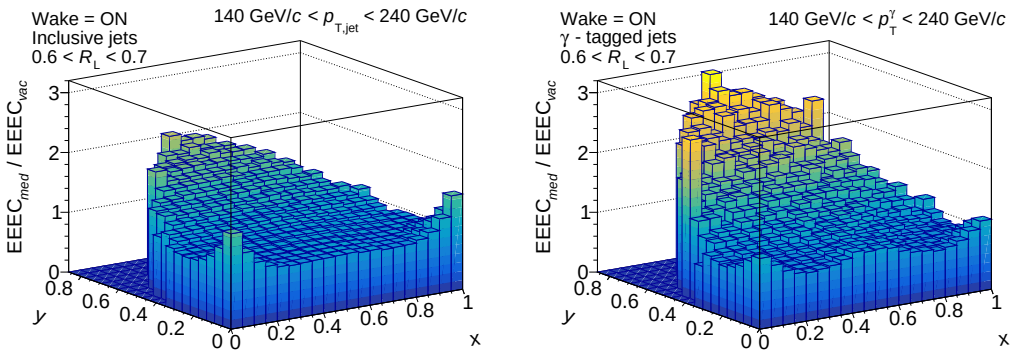


Figure 7.8: Ratio of the shape-dependent EEEC in medium with wake to that in vacuum. Left: For inclusive jets. Right: For $\gamma$-tagged jets. The enhancement observed in the equilateral region is more pronounced for $\gamma$-tagged jets, indicating a greater relative contribution from hadrons originating in the wake.

side jet roughly opposite in azimuth to the selected jet. The wake from this away-side jet can partially cancel the wake associated with the selected jet,[5] leading to a reduced EEEC enhancement in the equilateral region. While the evidence is somewhat indirect, the comparison in Fig. 7.8 strengthens the interpretation that the equilateral region of the EEEC is populated predominantly by hadrons originating from jet-induced wakes.

This chapter presents the first study of higher-point correlators in a heavy-ion environment. The results for the EEC reveal a large-angle enhancement, consistent with previous observations discussed in Sec. 7.1. Furthermore, the modification observed in the E3C/EEC ratio has been independently confirmed by other studies [245]. This work also provides the first full analysis of the shape-dependent EEEC, which exhibits unique signatures attributable to wake effects. Extending this analysis to other theoretical models could further elucidate the sensitivity of these observables to different aspects of medium response arising from jet–medium interactions.

5. Also known as "negative wake" or "diffusion wake" in the literature. These correspond to a depletion of particles on the opposite side of a jet. See discussion in Sec. 3.6.2 and Appendix B.

# Chapter 8

# Projected $N$-Point Correlator Measurement in Pb-Pb Collisions

*The analysis in this chapter extends the pp measurement of energy correlators to Pb-Pb collisions. Thus, only methodologies explicitly different from the pp case are discussed here. Anything not discussed can be assumed to follow the same procedure as in Chapter 6. Additional checks for the analysis methodology are shown in Appendix C.*

## 8.1 Geometry of Heavy-Ion Collisions

The question of geometry becomes essential in the context of heavy-ion collisions, as nuclei are spatially extended objects relative to the characteristic energy scales of the interaction. The geometric configuration of a collision is typically characterized by the impact parameter, $b$, which denotes the transverse distance between the centers of the two colliding nuclei at the time of impact. A smaller value of $b$ corresponds to a more head-on, or "central," collision, whereas larger values indicate "peripheral" collisions. This distinction is illustrated schematically in the right panel of the cartoon in Fig. 8.1. However, the impact parameter itself is not directly accessible

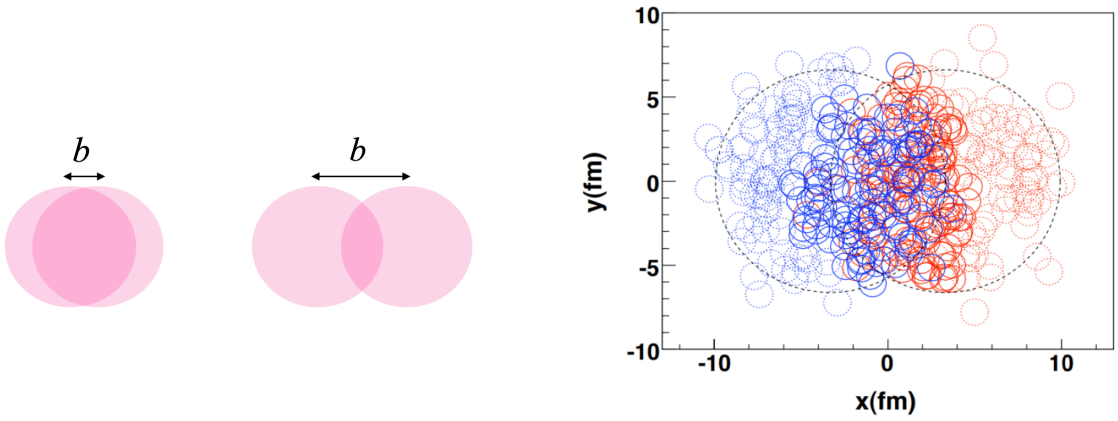


Figure 8.1: Left: Side view of colliding nuclei for central and peripheral collisions. $b$ represents the impact parameter of the colliding nuclei. Right: Pb-Pb collision depicting spectator nucleons (dashed), participant nucleons (solid), and binary collisions (overlapped circles). Figure taken from [26].

in experiments. Instead, experimental analyses rely on the concept of *centrality* to estimate the degree of overlap between the two nuclei. Centrality is typically inferred from final-state observables such as charged-particle multiplicity or total transverse energy, under the assumption that more central collisions produce a greater number of final-state particles due to the higher energy density of the collision.[1] When two nuclei collide, not all nucleons participate in the collision. The nucleons are categorized as *spectators*, *participants*, and *participants in a binary collision*. The number of nucleons of each category helps determine the collision geometry:

- Number of Spectators ($N_{\text{spec}}$) nucleons are nucleons that are outside the interaction region.

- Number of Participant nucleons ($N_{\text{part}}$) are nucleons that interact with at least one nucleon of the opposite nucleus.[2] $N_{\text{part}}$ is driven by the collision geometry,

1. It is worth noting that different experiments may employ distinct methodologies for centrality determination. This complexity is further amplified in asymmetric systems, such as p–Pb collisions, where the geometrical interpretation becomes less straightforward. Thus, it is now conventional to use the term "event activity" in lieu of centrality. Recent efforts have focused on systematically investigating the dependence of centrality definitions on experimental observables [246–248].

2. Ultraperipheral collisions (UPCs) form a special case where two nuclei only interact via an

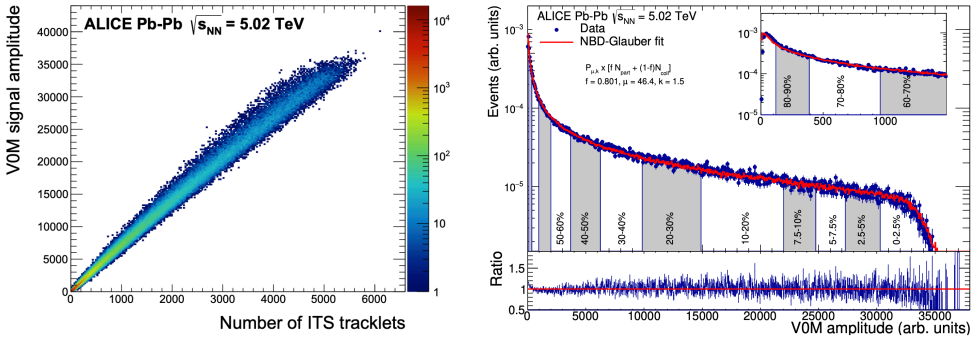


Figure 8.2: Left: Correlation between V0M amplitude and reconstructed track segments in the ITS at midrapidity. Figure taken from [27]. Right: V0M signal amplitude with a Glauber+NBD fit. The inset shows a zoomed-in version of the most peripheral region. Figure taken from [28].

which is quantified by the impact parameter.

- Number of binary collisions ($N_{\text{coll}}$) encapsulates the total number of nucleon pairs that collide.

These are depicted in Fig. 8.1. At ALICE, centrality[3] is determined by the V0 detector.[4] The signal in the V0 detector is correlated with the charged particle multiplicity at midrapidity, as shown in the left panel of Fig. 8.2. This distribution is then fit with Glauber [72] coupled to a particle production model to determine the average values of these geometrical quantities [28], as shown in the right panel of Fig. 8.2. The centralities are then reported in percentiles with smaller values, such as 0-10% referring to central collisions, while larger values, 60-80% referring to peripheral collisions.

exchange of photons created due the large electromagnetic fields of the ions [249].

3. An alternative method employed at ALICE relies on measuring the energy deposited in the Zero-Degree Calorimeter (ZDC) by particles close to the beam direction, which can be related to $N_{\text{spec}}$.

4. See Chapter 5 for details about the V0 detector.

## 8.2 Methodology

Here I outline the analysis methodology of measurement of the EEC and E3C in Pb-Pb collisions in 0-10% centrality at $\sqrt{s_{\mathrm{NN}}} = 5.02$ TeV.[5] The analysis workflow is as follows:

- Construct ENCs from raw data (as described in Sec. 6.2.2).
- Perform background subtraction using perpendicular cones (described in Sec. 8.2.5).
- Perform 3D-unfolding on the observable along three axes to get the final corrected result (as described for pp collisions in Sec. 6.3).

### 8.2.1 Data Selection

This analysis uses the Pb-Pb collision data taken in 2018 during Run 2 of the LHC at $\sqrt{s_{\mathrm{NN}}} = 5.02$ TeV. For event selection, a reconstructed primary vertex with -10 cm $< V_z <$ 10 cm of the interaction point is required. Moreover, only events in the 0–10% centrality class are considered. After all event selection cuts, about 56 million events are analyzed.

### 8.2.2 Track Selection and Jet Reconstruction

Track selection for this analysis closely follows the procedure described in Sec. 5.2.3. Charged particle anti-$k_{\mathrm{T}}$ jets of radius $R = 0.4$ are reconstructed using the *E-scheme*. A jet area[6] cut of $A_{\mathrm{jet}} > 0.6\pi R^2$ is applied to remove contamination from unphysical jets [250]. Additionally, the measurement parameters also need to be optimized so that the rate of "fake" or purely "combinatorial" jets[7] is minimized. With these

5. *NN* refers to the energy per nucleon inside the colliding nucleus.

6. Jet area is determined by using the active area method in FastJet [129].

7. Fake/combinatorial/unmatched jets result from an upward fluctuation of the background. Thus, larger radii jets at lower $p_{\mathrm{T}}$ are more susceptible to having fake jet contamination.

constraints in mind, anti-$k_{\mathrm{T}}$, $R = 0.4$ jets are reconstructed and measured in jet $p_{\mathrm{T}}$ intervals of 70-90 GeV/$c$ and 90-120 GeV/$c$. However, there is an additional step that is required in the presence of a heavy-ion background that is not present in pp collisions. This is detailed in Sec. 8.2.3.

### 8.2.3 Background Subtraction at the Jet Level

Heavy-ion collisions come with the added complexity of having a large fluctuating underlying event density (UE). At the LHC, in Pb-Pb 0-10% central collisions, the UE density is $\approx 138$ GeV/$c$ [251]. This large UE background needs to be subtracted to get a correct estimate of the jet $p_{\mathrm{T}}$. This step is commonly referred to as *pedestal-subtraction* and helps correct the $p_{\mathrm{T}}$ of the reconstructed jet. This method involves estimating the UE density ($\rho$) event by event and subtracting it from the raw jet $p_{\mathrm{T}}$. To obtain $\rho$, we cluster all particles in the event into background jets using the $k_{\mathrm{T}}$ algorithm (excluding the two leading jets in the event since these might be signal jets). The background jets have the same selections as signal jets, except there is no area cut. $\rho$ is then calculated via

$$\rho = \text{median}\left(\frac{p_{\mathrm{T}}^{\mathrm{rec}}}{A^{\mathrm{rec}}}\right) \tag{8.1}$$

where $p_{\mathrm{T}}^{\mathrm{rec}}$ is the $p_{\mathrm{T}}$ of the reconstructed cluster and $A^{\mathrm{rec}}$ is the area[8] of the reconstructed cluster. Finally, a pedestal subtraction is performed as shown in Equation 8.2

$$p_{\mathrm{T,\,sub}} = p_{\mathrm{T,\,raw}} - A_{\mathrm{jet}}\rho \tag{8.2}$$

Note that unfolding is still needed to fully correct the jet $p_{\mathrm{T}}$ since pedestal subtraction only performs an average correction and does not account for fluctuations or any

8. $A^{\mathrm{rec}}$ is the area of the reconstructed cluster in the $(\eta, \phi)$-plane calculated by the active ghost area method of FastJet [129], with a ghost area of 0.005.

missed energy due to tracking inefficiencies.

### 8.2.4 Raw Data

After performing the pedestal subtraction, we can take a look at the raw data for the EEC, E3C, and E3C/EEC ratio. These are shown in Fig. 8.3 and Fig. 8.4. Note that these distributions are still contaminated by the uncorrelated background, i.e., fake tracks. While the pedestal subtraction described in Sec. 8.2.3 roughly corrects the jet $p_{\mathrm{T}}$ on average, it still needs to be unfolded. Furthermore, it does not remove the contribution from background tracks. Since ENCs are correlations between tracks in a jet, one also needs to perform a track-level subtraction. These fake tracks are composed of the uncorrelated particles from the bulk of the QGP.

### 8.2.5 Background Subtraction for ENCs

*Here I outline the subtraction procedure developed for this analysis. Various studies to validate this procedure are detailed in Appendix C.*

As discussed in Chapter 6, ENCs, as defined in this thesis, are track-level observables. Consequently, raw distributions—such as those shown in Fig. 8.3 and Fig. 8.4—are contaminated by correlations arising from uncorrelated background sources, namely the bulk of the QGP unrelated to jet fragmentation or medium response induced by the jet. To isolate effects associated with a correlated medium response to the jet, it is necessary to subtract these uncorrelated background contributions. To estimate the contribution from uncorrelated background, we employ the method of perpendicular or random cones [251] and make use of the ALICE embedding framework described in Sec. 8.2.5. This technique involves placing a cone either randomly or at a location perpendicular to the jet axis. Given that most events are dijet events, these cones typically contain only background particles, effectively decoupled from the hard jet. Subtraction is then performed at the ensemble level. The core idea

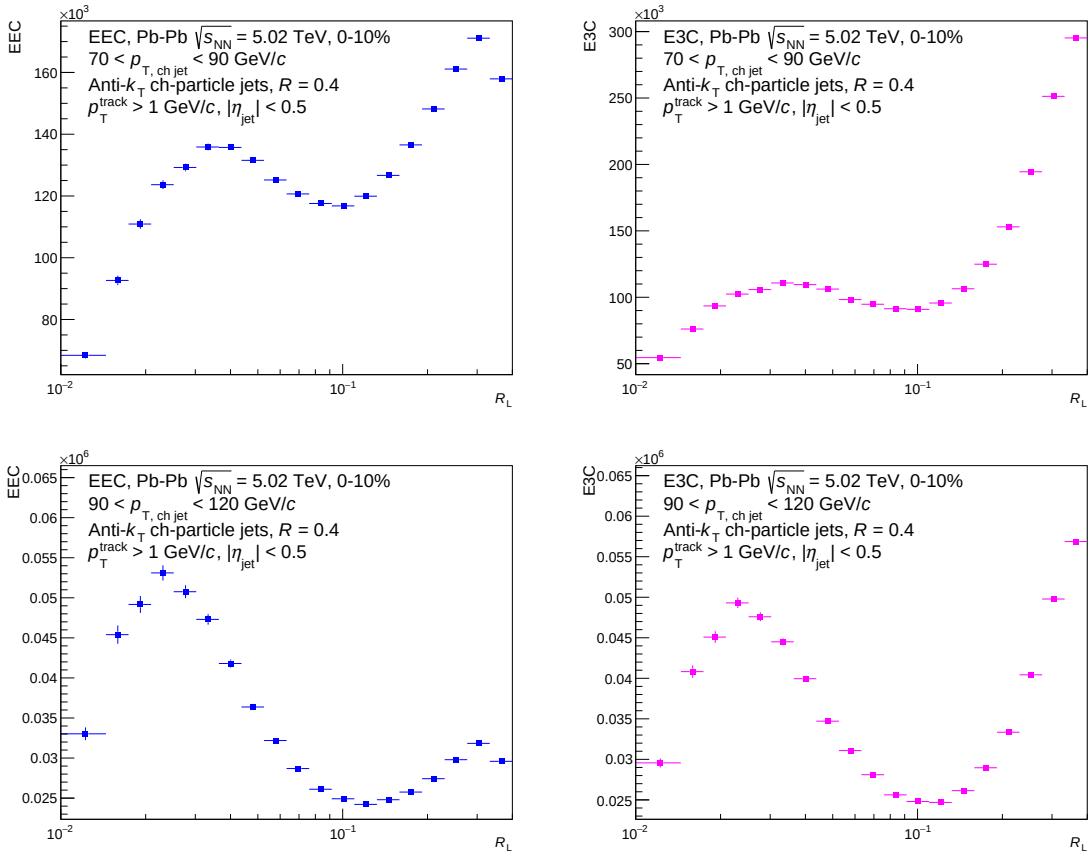


Figure 8.3: Raw distributions of energy correlators (ENCs). Left: EEC. Right: E3C. Each row corresponds to a different jet $p_{\mathrm{T}}$ bin: 70–90 GeV/$c$ (Top) and 90–120 GeV/$c$ (Bottom).

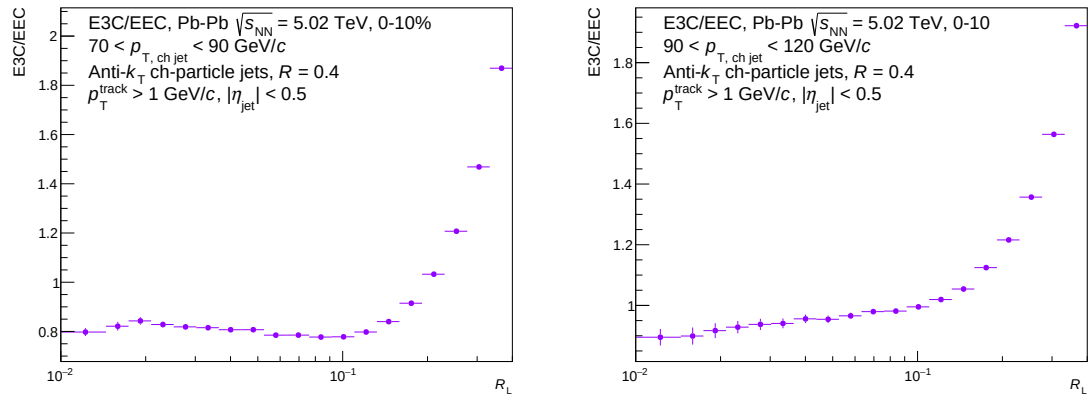


Figure 8.4: Raw distribution of E3C/EEC ratio in two jet $p_{\mathrm{T}}$ bins. Left: 70-90 GeV/$c$. Right: 90-120 GeV/$c$.

is that signal–background and background–background correlations can be approximated by constructing ENCs using particles within these cones.[9]

**EEC: Background Subtraction**

Our objective is to isolate the EEC contribution from the signal particles ($S$) in the raw measurement obtained from the signal-containing jet ($J$), which includes both signal and background contributions ($B$), as expressed in Equation 8.3

$$J = S + B \Rightarrow J^2 = S^2 + B^2 + 2SB \tag{8.3}$$

Therefore, we need to remove the contribution from $B^2$ and $SB$. To do this, we can create cones of $R = 0.4$ perpendicular to the jet. These cones are composed of background particles only, thus, the $B^2$ correlation will be captured by the correlations in this cone. To get the $SB$ correlations, we form pairs from the reconstructed jet, $J$, and a perpendicular cone, $B'$, to determine $JB'$

$$JB' = (S + B)B' = SB' + BB' \tag{8.4}$$

Now, with some algebra, we can see that

$$J^2 - B'^2 - 2JB' = S^2 + (B^2 - B'^2) + (2SB - 2SB') - 2BB' = S^2 - 2BB' \tag{8.5}$$

This extra correlation $BB'$ can be labeled as the "mis-modeled" background. If we do not remove this, we will over-subtract our signal correlations. To account for this we need a second cone of $R = 0.4$. This cone is a $B''$ cone, and we can create correlations of the form

$$S^2 - 2BB' + 2B'B'' = S^2 - (2BB' - 2B'B'') = S^2 \tag{8.6}$$

9. This technique is inspired by the CMS measurement of the EEC in Pb-Pb collisions [252]. However, the methodologies developed in this section are novel and have not been employed before.

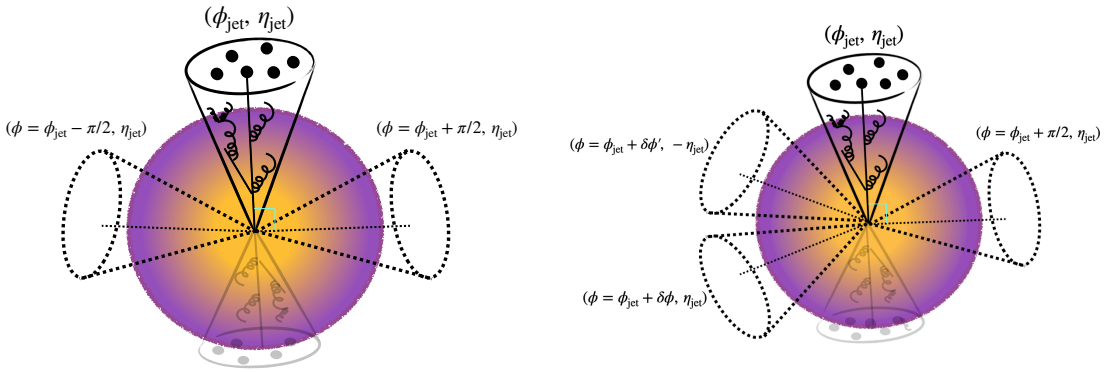


Figure 8.5: Left: Cones for EEC. Right: Cones for E3C.

Thus, we can write our subtraction for the EEC in one compact formula

$$S^2 = J^2 - B'^2 - 2JB' + 2B'B'' \tag{8.7}$$

**E3C: Background Subtraction**

A similar argument follows for the E3C, except now we have extra correlations of the type $SBB$, $SSB$. These correlations require an additional cone to account for $B'B''\tilde{B}$ correlations. To construct these three cones, one cone is constructed at $(\Delta\phi = \pi/2, \eta_{\text{jet}})$, another at $(\Delta\phi = -\pi/2, \eta_{\text{jet}})$, and the final cone is at an angle $(\Delta\phi = \pi/2 \pm 0.2, , -\eta_{\text{jet}})$ to avoid any overlap with the jet. A cartoon of this construction is shown in the right panel of Fig. 8.5.

The subtraction formula for E3C can be written as

$$S^3 = J^3 - B'^3 - 3J^2B' - 3JB'^2 + 3B'B''^2 + 6JB'B'' - 6B'B''\tilde{B} \tag{8.8}$$

This subtraction is shown in Fig. 8.6.

Note: The idea is to correct ENCs by constructing jet-background correlations using extra cones. This method allows us to find the signal correlations without prior knowledge of correlations due to signal and background particles. This subtraction

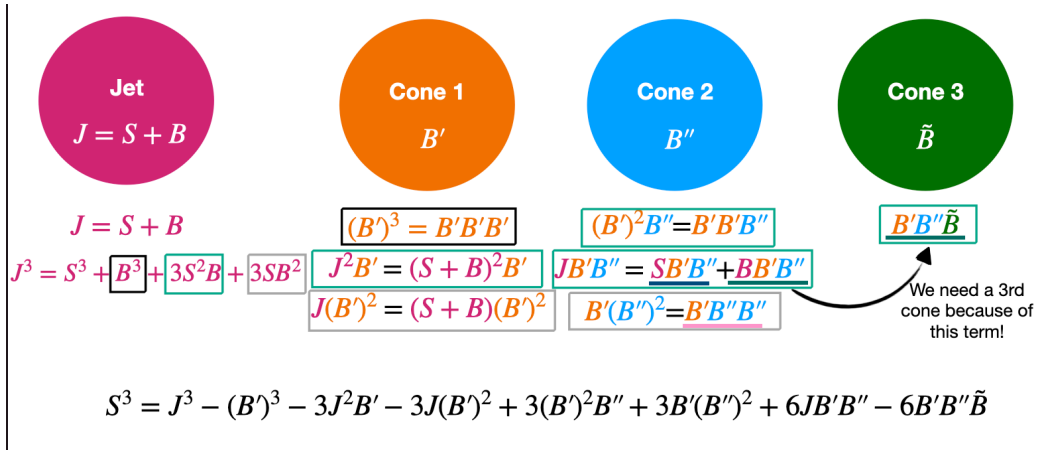


Figure 8.6: Figure depicting the background subtraction method we use for correcting the E3C distribution. The procedure is the same, except we need an additional cone to remove the $B'B''\tilde{B}$ correlation. The cones will be oriented as described in the right panel of Fig. 8.5.

is performed on the ensemble level.

### Accounting for Different UE Density: c-factors

The number of background tracks in our jet cone vs random cone will not necessarily be the same because our jet finding condition imposes an explicit jet $p_{\mathrm{T}}$ cut. This is confirmed by studies in Appendix C, where the closure of the subtraction procedure is shown to worsen when there is a mismatch in the UE density under our jet cone and perpendicular cone.

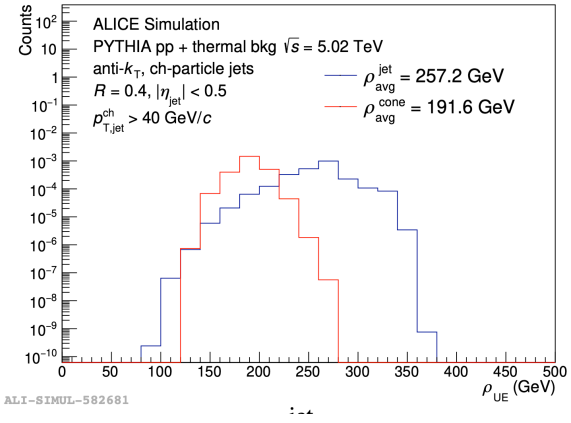


Figure 8.7: Difference in UE density arising from having a jet $p_{\mathrm{T}}$ threshold.

This mismatch will naturally lead to an underestimation of the background in our jet and therefore, an underestimation of the background correlations. This is shown for a more realistic case where we re-find jets after adding thermal background in Fig. 8.7. The difference in $\langle\rho\rangle$ between the cone and the jet highlights this effect.

We use various c-factors to correct our mismatched background correlations due to the difference in UE density. These are tabulated in 8.1. It is important to note that the c-factor will be *different* for contributions coming from combinatorial jets. This is expected since combinatorial jets that pass the jet $p_{\mathrm{T}}$ threshold have to sit on a much larger background fluctuation.

| **c-factor** | **Matched Jets** | **Unmatched Jets** |
|---|---|---|
| $c_{B^2}$ | $c_{B^2_m} = (B')^2_m/B^2$ | $c_{B^2_{um}} = (B')^2_{um}/B^2$ |
| $c_{BB'}$ | $c_{BB'_m} = (B'\tilde{B})_m/BB'$ | $c_{BB'_{um}} = (B'\tilde{B})_{um}/BB'$ |
| $c_{SB}$ | $c_{SB_m} = (SB')_m/SB$ | - |

Table 8.1: Table depicting the construction of c-factors for the EEC observable. The ratios represent the division of 3D histograms filled with respective contributions. The denominators represent the sum of matched and unmatched jet contributions. The subscripts "$m$" and "$um$" denote matched and unmatched (combinatorial/fake) jets, respectively.

Once we have determined these c-factors, we can correct each contribution from the background as shown

$$B^2 = B'^2 \left(1/c_{B^2_m} + 1/c_{B^2_{um}}\right) \tag{8.9}$$

$$BB' = B'\tilde{B} \left(1/c_{BB'_m} + 1/c_{BB'_{um}}\right) \tag{8.10}$$

$$SB = SB' \left(1/c_{SB'_m}\right) \tag{8.11}$$

It is important to note that, although a distinction is initially made between matched jets and unmatched (combinatorial/fake) jets, as discussed in Sec. 8.2.2, the kinematic selections applied in this analysis effectively suppress the contribution from

| c-factor | Matched Jets | Unmatched Jets |
|---|---|---|
| $c_{B^3}$ | $c_{B^3_m} = (B')^3_m / B^3$ | $c_{B^3_{um}} = (B')^3_{um} / B^3$ |
| $c_{BBB'}$ | $c_{BBB'_m} = (B'B'B'')_m / BBB'$ | $c_{BBB'_{um}} = (B'B'B'')_{um} / BBB'$ |
| $c_{BB'B'}$ | $c_{BB'B'_m} = (B'B''B'')_m / BB'B'$ | $c_{BB'B'_{um}} = (B'B''B'')_{um} / BB'B'$ |
| $c_{SBB}$ | $c_{SBB_m} = (SB'B')_m / SBB$ | - |
| $c_{SSB}$ | $c_{SSB_m} = (SSB')_m / SSB$ | - |
| $c_{SBB'}$ | $c_{SBB'_m} = (SB'B'')_m / SBB'$ | - |
| $c_{BB'\tilde{B}}$ | $c_{BB'\tilde{B}_m} = (B'B''\tilde{B})_m / BB'B''$ | $c_{BB'\tilde{B}_{um}} = (B'B''\tilde{B})_{um} / BB'B''$ |

Table 8.2: Table depicting the construction of c-factors for the E3C observable. The ratios represent the division of 3D histograms filled with respective contributions. The denominators represent the sum of matched and unmatched jet contributions. The subscripts "$m$" and "$um$" denote matched and unmatched (combinatorial/fake) jets, respectively.

purely combinatorial jets. As a result, the correction factors employed are derived exclusively from matched jets. Accordingly, the influence of combinatorial jets is considered negligible and is not discussed further in the remainder of this analysis.

### 3D Version of Background Subtraction

In practice, a three-dimensional background subtraction must be implemented to align with the three-dimensional unfolding procedure. This requires performing the subtraction on the raw data using a 3D histogram with axes corresponding to $R_{\mathrm{L}}$, jet $p_{\mathrm{T}}$, and the observable weight. Similarly, the c-factors used for correction are constructed as three-dimensional histograms defined over the same axes.

### Testing Subtraction Closure

To check the validity of the subtraction procedure, this procedure is tested using the ALICE embedding framework, which combines a known signal from simulation with real Pb–Pb minimum bias events. This embedding process enables the evaluation of background effects in a controlled setting where the true signal is known. To ensure

high statistical precision, a $p_{\mathrm{T}}^{\mathrm{hard}}$-binned Monte Carlo (MC) production was employed using PYTHIA8 with the Monash 2013 tune [221], followed by a full GEANT3 [222] detector simulation. Each of the 20 $p_{\mathrm{T}}^{\mathrm{hard}}$ bins—defined by the edges [5, 7, 9, 12, 16, 21, 28, 36, 45, 57, 70, 85, 99, 115, 132, 150, 169, 190, 212, 235, 1000] GeV/$c$—contains approximately 1,000,000 events. After generating signal events and applying detector simulation, these events are overlaid with Pb–Pb minimum bias background at the detector level to create hybrid events. To account for the degraded tracking efficiency in Pb–Pb collisions compared to pp, an additional 2% of tracks in the PYTHIA events are randomly removed during the embedding process.[10] Since each track has an unambiguous association with a single particle, tracks in the hybrid event represent a straightforward combination of the signal and background tracks–which is exactly what is needed to construct ENCs for various combinations of signal and background tracks. Furthermore, the embedding is also needed to construct the ingredients for unfolding, such as the response matrices. See Sec. 8.3 for further discussion on unfolding. A two-step matching procedure is employed to identify Hybrid jets, which consist of a combination of PYTHIA-generated particles and real data. First, the detector-level jet is geometrically matched to a PYTHIA-level jet. Subsequently, the same detector-level jet is matched to a corresponding Hybrid-level jet. In both steps, a geometric matching criterion of $R < 0.3$ is applied. Additionally, a transverse momentum threshold of 40 GeV/$c$, applied after pedestal subtraction, is used to ensure jet quality and suppress background contributions.

The EEC and E3C distributions obtained from embedding with the different contributions, where $s$ stands for signal particles (i.e., PYTHIA particles) and $b$ for background, to the total curves are shown in Fig. 8.8. The contribution of the uncorrelated background dominates at large $R_{\mathrm{L}}$, which is again a feature of geometry.

In this analysis, the subtraction is first performed without applying the $c$-factor

10. This track rejection is performed uniformly to emulate the observed tracking inefficiency.

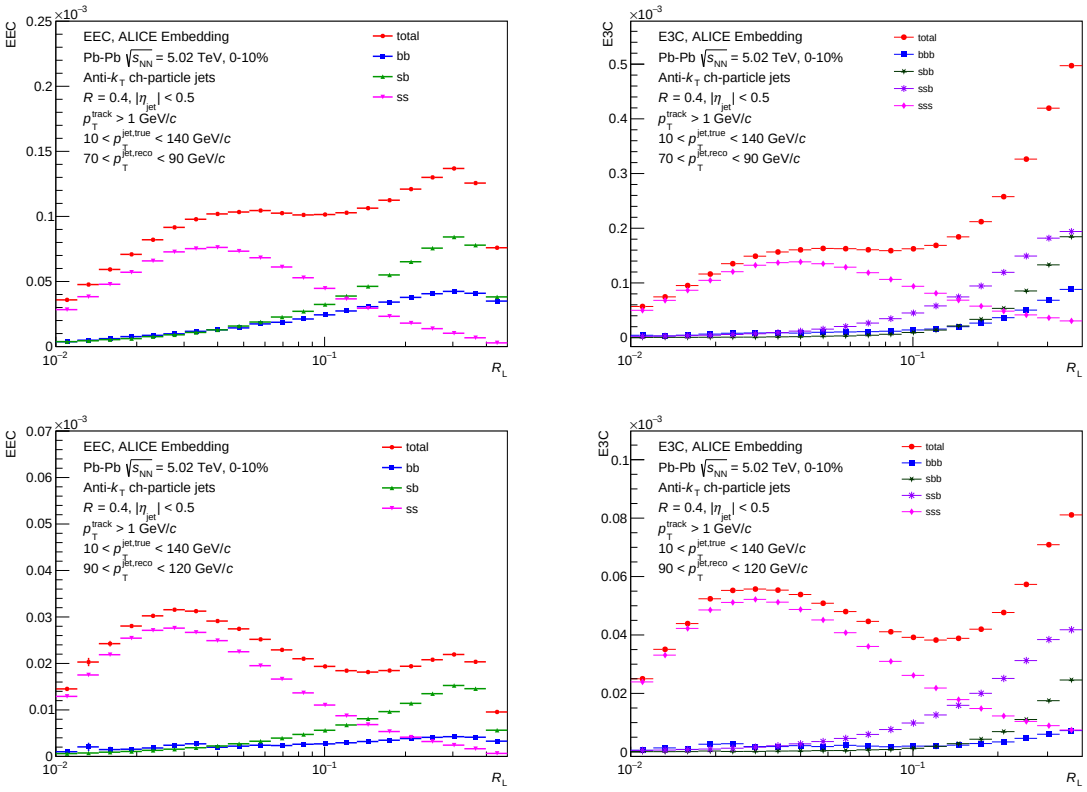


Figure 8.8: Left: EEC and Right: E3C distributions from embedding, shown for two jet $p_{\mathrm{T}}$ bins: 70–90 GeV/$c$ (Top) and 90–120 GeV/$c$ (Bottom), illustrating contributions from different particle types.

correction. In this case, the UE density in the cones does not match that of the jets, leading to an imperfect subtraction. As a result, background contributions—particularly in the large $R_{\mathrm{L}}$ region—are expected to remain. This behavior is observed in Fig. 8.9. To validate the effectiveness of the c-factor correction, a split test is performed. Specifically, the c-factors are computed using one subset of events and then applied to correct jets from an independent subset. As this correction is statistical, the expectation is that the split test will yield convergence similar to the behavior observed in the toy model, as shown in Appendix C. However, additional effects from the embedding procedure may lead to a less precise closure. The results, shown in Fig. 8.10, indicate that closure is achieved to within 10% across most bins, with deviations increasing to approximately 25% in the largest $R_{\mathrm{L}}$ bins.

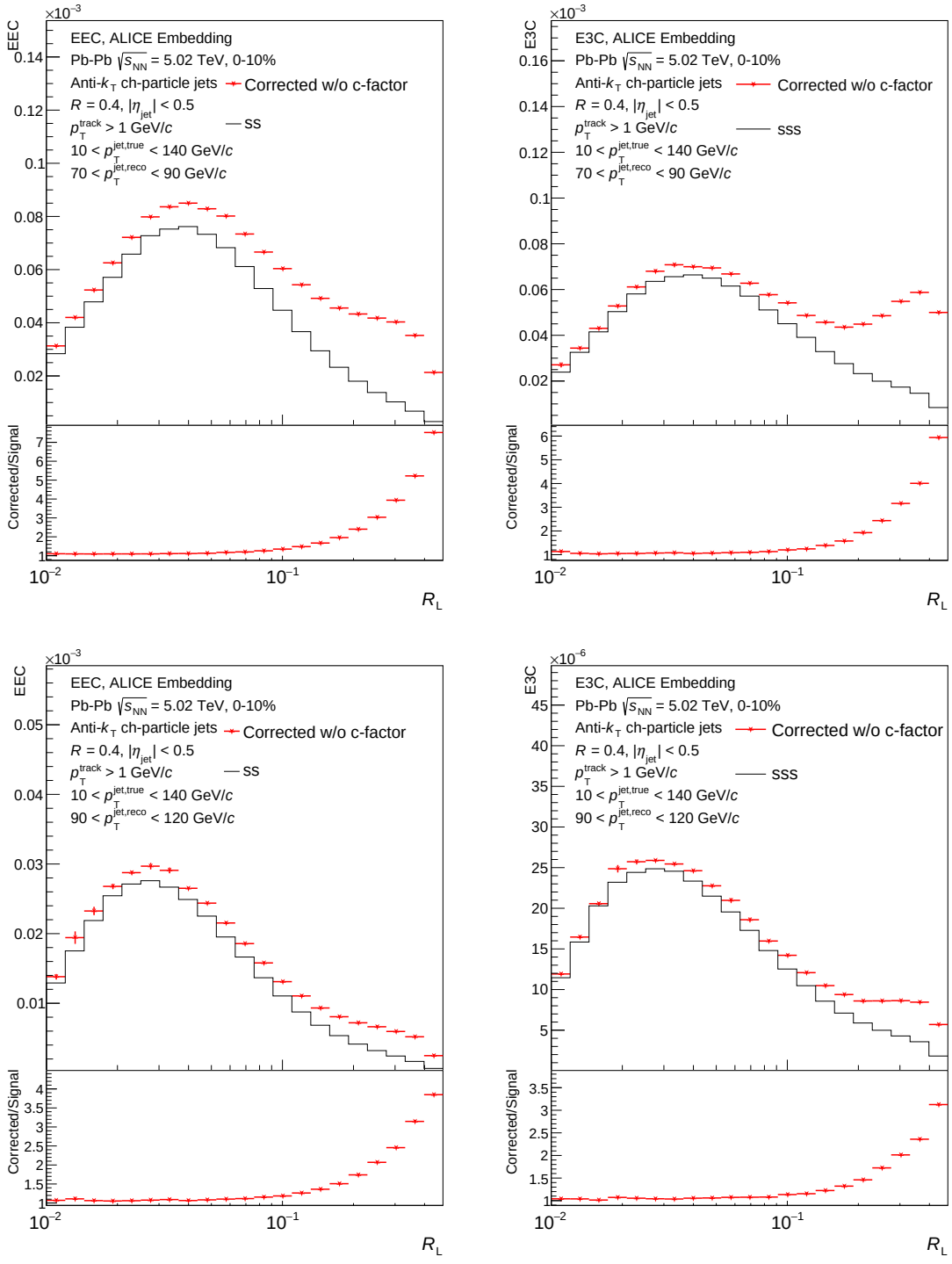


Figure 8.9: Performing background subtraction without applying c-factor in two jet $p_T$ bins: 70-90 GeV/$c$ (Top) and 90-120 GeV/$c$ (Bottom). Left: EEC. Right: E3C.

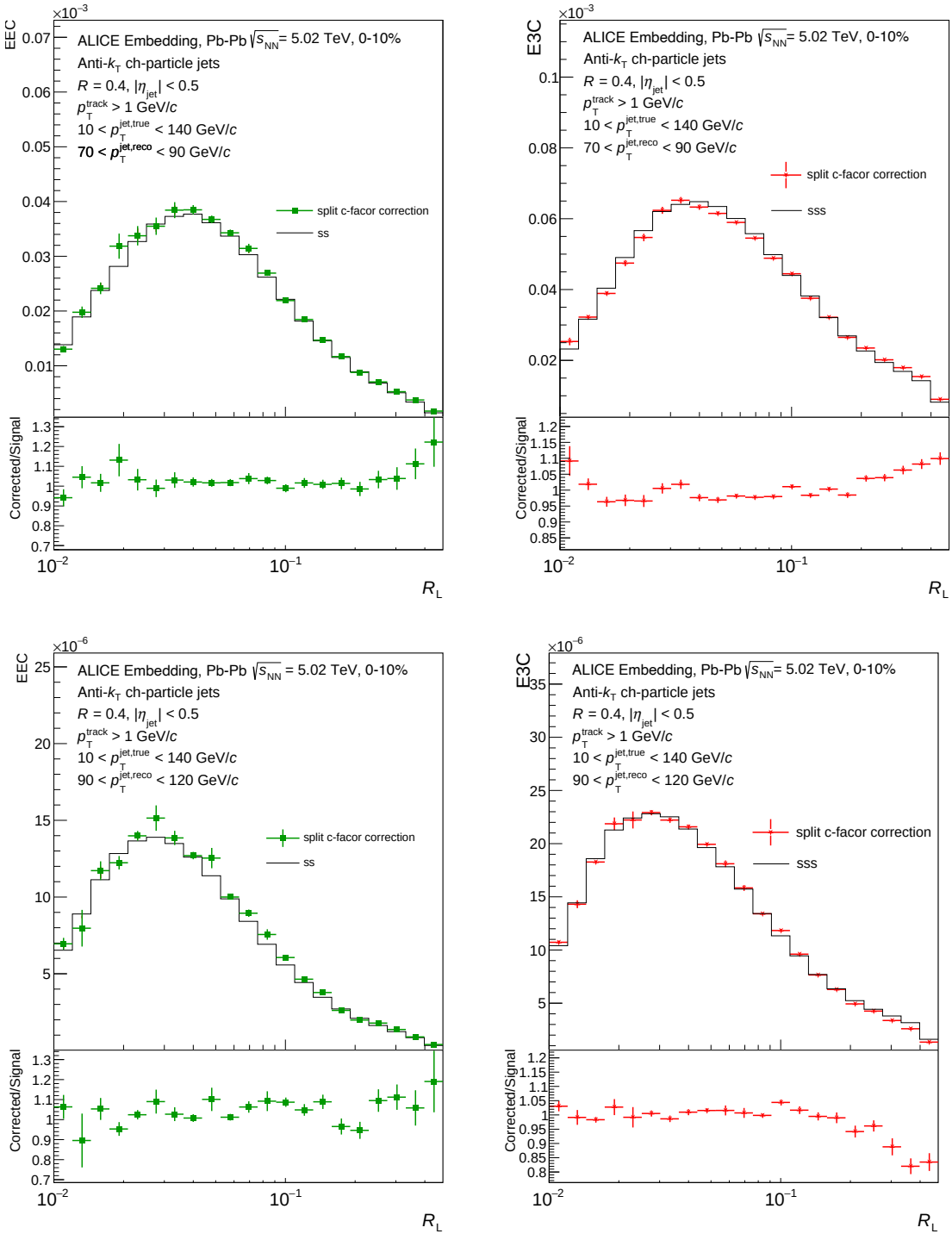


Figure 8.10: Performing background subtraction with c-factor in two jet $p_T$ bins: 70-90 GeV/$c$ (Top) and 90-120 GeV/$c$ (Bottom). Left: EEC. Right: E3C.

## 8.3 Next Steps

A key challenge in using the embedding framework arises from the possibility that the underlying Pb–Pb data into which the simulated signal is embedded may already contain real jets. This introduces the potential for overlap between embedded PYTHIA jets and genuine jets from the data, resulting in "overlapped" jets that can contaminate the correction factors (c-factors) derived from the embedding procedure at a higher rate than occurs in Pb-Pb events themselves. To mitigate this issue, an additional matching criterion is introduced, requiring that at least 50% of the energy in the hybrid jet originates from the embedded PYTHIA jet. This stricter condition enhances the purity of the matched jet sample by reducing contamination from background data jets. The analysis steps described above can then be repeated with this improved matching requirement, ensuring that the resulting c-factors more accurately reflect the embedded signal.[11] Following this correction, the next step involves performing iterative three-dimensional Bayesian unfolding, consistent with the methodology outlined in Sec. 6.3. A preliminary validation of the full procedure, including 3D unfolding in a toy model for the EEC, is presented in Appendix C.

In this thesis, a novel background subtraction procedure has been developed for the ENCs to specifically address the challenges associated with performing track-level corrections for this observable in heavy-ion collisions. This new methodology provides a systematic framework for mitigating the effects of background contamination, which is particularly important given the complex environment of Pb–Pb events. The full implementation of this procedure is ongoing, and final results applying this technique to experimental data are expected to be presented soon.

11. This work is currently ongoing at the time of writing this thesis.

# Chapter 9

# Looking to the Future

## 9.1 Conclusions

This thesis presents a detailed investigation of a novel class of jet substructure observables known as the $N$-point Energy Correlators (ENCs), with an emphasis on their potential to probe the internal structure of jets. It includes the first measurement of higher-point energy correlators in proton-proton (pp) collisions at the ALICE experiment, as discussed in Chapter 6.

In addition to their application in vacuum-like environments, Chapter 7 extends the use of ENCs to heavy-ion collisions, where jets propagate through a hot, dense, and strongly interacting medium, the Quark Gluon Plasma (QGP). In such environments, the evolution of the jet is significantly altered by interactions with the medium. This study, published in JHEP [17], demonstrates that the ENCs, their ratios, and their full shape-dependent extension, the Energy Energy Energy Correlator (EEEC), are sensitive to jet–medium interaction mechanisms. The establishment of this sensitivity opens up a promising new avenue for characterizing jet quenching phenomena and probing the microscopic properties of the QGP.

To enable these measurements in the complex environment of heavy-ion collisions,

this thesis introduces a suite of novel analysis techniques in Chapter 8. These methods are specifically designed to address the challenges posed by high background activity and the requirement for precise track-level corrections. These methods are now being applied to Run 2 ALICE data, with preliminary measurements currently underway.

In conclusion, this work establishes $N$-point Energy Correlators and their ratios as powerful and versatile observables for studying QCD dynamics across a range of environments. In proton-proton collisions, they offer a precise probe of the angular structure of jets and the underlying parton shower evolution. In heavy-ion collisions, they provide a new framework for investigating medium-induced modifications to jets and for isolating the signatures of different medium response mechanisms. Together, these developments significantly broaden the toolkit available for jet substructure studies at the LHC and beyond.

## 9.2 Future Extensions of the Work in This Thesis

### Opportunities for the ENC Measurement: pp Collisions

Recent years have seen a surge of measurements of $N$-point Energy Correlators (ENCs) across a broad kinematic range, as illustrated in Fig. 9.1.[1] As discussed in Sec. 4.2.3, ratios of projected correlators are sensitive to the running of the strong coupling constant, $\alpha_s$. The measurement presented in this thesis provides a complementary opportunity to measure $\alpha_s$ in a kinematic regime distinct from that explored by the CMS collaboration [23]. Importantly, recent studies indicate that the phase space accessible at ALICE may be particularly sensitive to non-perturbative effects [218], suggesting that an extraction of $\alpha_s$ in this environment could provide novel constraints on non-perturbative corrections that were previously assumed to be negligible [15].

1. In this plot, each curve has been scaled such that the peak position sits at 1 on the $y$-axis.

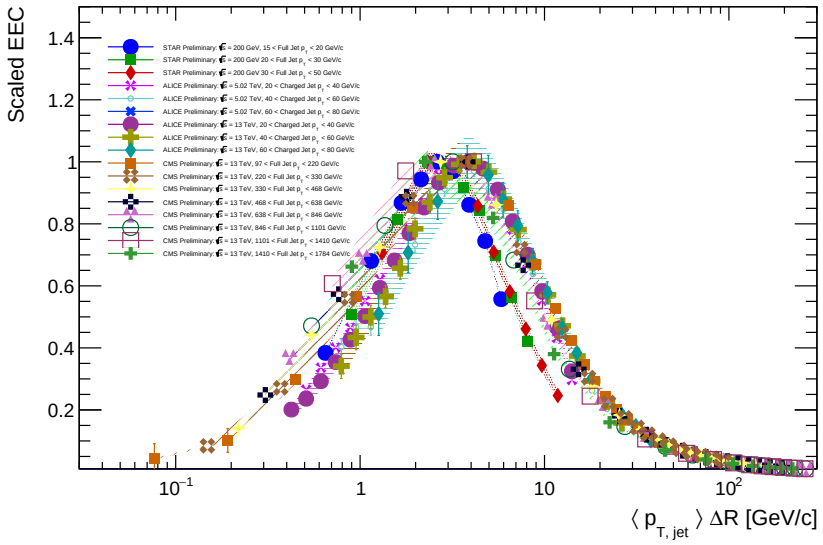


Figure 9.1: Summary of measurements of the two-point Energy Correlator across LHC and RHIC experiments. The peak position appears relatively consistent across datasets, with observed differences potentially arising from variations in the underlying jet populations being studied. Figure credit: Andrew Tamis.

A key ingredient in enabling such precision extractions is the incorporation of *track functions*, as discussed in Sec. 3.6.1. These functions allow perturbative QCD calculations to be extended to track-based observables. Since the renormalization group evolution of track functions is well understood [253], they offer a theoretically robust path to generating reliable predictions for measurements using charged jets (instead of full jets) in the ALICE kinematic regime.

Another promising direction is the study of the E3C/EEC ratio as a function of center-of-mass energy, $\sqrt{s}$. Because the anomalous dimensions of ENC operators are sensitive to the underlying quark and gluon fractions, comparing measurements across different energies could reveal these differences. However, such an analysis would require careful treatment of correlated statistical and systematic uncertainties (since the EEC and E3C are measured on the same dataset). If observed, these variations could provide new insights into the partonic composition of jets and their evolution with energy.

**Open Questions.** While this thesis has added to our understanding of ENC observables in jets, several important questions remain:

- The peak position of the ENC distribution is characterized by a scale $\Lambda$, yet its precise interpretation remains unclear. While STAR and ALICE measurements yield roughly similar values for this scale, they are based on full and charged jets, respectively. Moreover, the peak position has been shown to vary depending on the jet flavor (quark vs. gluon) [254]. How can we disentangle these effects and construct a unified framework to interpret $\Lambda$?

- Given that ENC ratios encode the anomalous dimensions of the corresponding QCD operators—thereby probing fundamental quantum interactions—can these observables serve as reliable tools for quark–gluon discrimination?

- What insights into hadronization mechanisms can be gained by comparing ENCs for different hadron species, such as baryons versus mesons? These can complement studies of the charge correlation ratio, $r_c$, that probes different hadronization mechanisms [255].

Addressing these questions will not only deepen our understanding of jet substructure and QCD dynamics but may also expand the applicability of ENCs as tools for jet substructure measurements in heavy-ion collisions.

### Opportunities for the ENC Measurement: Pb-Pb Collisions

Projected correlators in heavy-ion collisions offer a promising avenue for addressing selection bias—an inherent and unresolved challenge in nearly all jet measurements in such environments [243], as discussed in Sec. 3.6.2. While existing measurements of EECs in heavy-ion collisions have yet to provide a definitive separation between various medium response mechanisms, future measurements spanning a broader kinematic phase space hold the potential to place meaningful constraints on jet–medium

interactions. The work presented in this thesis contributes directly to advancing this goal by developing the tools and methodologies needed to perform such measurements.

Moreover, extending projected correlators to include higher-point functions may enhance their discriminating power. Recent studies suggest that such extensions could enable a clearer differentiation between competing medium response effects [256], providing a more detailed understanding of how jets are modified as they traverse the QGP.

## 9.3 Future Directions

Run 3 of the LHC has delivered unprecedented statistics, ushering in a new era for multi-differential jet substructure analyses. For the first time, it is now feasible to study heavy-flavor jets—both mesonic and baryonic—without being statistically limited. This advancement paves the way for detailed investigations of flavor and mass effects in QCD, offering new insights into the scale dependence of the theory. Moreover, the ability to explore collisions in small systems, such as oxygen–oxygen (O–O) or neon–neon (Ne–Ne), presents a unique opportunity to probe the origins of collective behavior. These studies have the potential to deepen our understanding of QGP formation in systems that lie at the boundary between proton–proton and heavy-ion collisions. Together, these developments mark a significant step forward in our ability to test QCD across a broad range of physical conditions.

# Appendix A

# pp Measurements

## A.1 Preliminary Results for ENC at $\sqrt{s} = 13$ TeV

Preliminary results for the ENC measurement presented in Chapter 6 employed an alternative correction technique known as the bin-by-bin method. The corresponding correction factor is defined as

$$f_{\text{corr}}(R_{\text{L}}^{\text{det}}, p_{\text{T,jet}}^{\text{det}}) = \frac{\text{ENC}_{\text{det}}}{\text{ENC}_{\text{true}}}, \tag{A.1}$$

where $\text{ENC}_{\text{det}} = \text{ENC}(R_{\text{L}}^{\text{det}}, p_{\text{T,jet}}^{\text{det}})$ and $\text{ENC}_{\text{true}} = \text{ENC}(R_{\text{L}}^{\text{true}}, p_{\text{T,jet}}^{\text{true}})$. Both the detector-level and truth-level ENC distributions were area-normalized prior to taking the ratio, and the resulting correction factor $f_{\text{corr}}$ was then applied to the raw data.[1] The corrected data are then area and bin-width normalized.

The detector-level ENC distribution was constructed using the full ALICE simulation framework, which integrates event generation via PYTHIA 8 (Monash Tune) and detector response modeling through GEANT, as described in Chapter 6.

1. This procedure is applied to 1D distributions, obtained by projecting the 2D distribution of jet $p_{\text{T}}$ and $R_{\text{L}}$ onto the $R_{\text{L}}$ axis within specific jet $p_{\text{T}}$ intervals. The weight is unbinned in this case.

### A.1.1 Systematic Uncertainties

A few sources of systematic uncertainties were considered. They are listed below:

1. **Tracking Efficiency Uncertainty:** For our hybrid track selection, the tracking efficiency uncertainty is estimated to be 3% [257]. To evaluate the impact on the ENC observable, we degrade the detector-level PYTHIA events by randomly removing an additional 3% of tracks. The correction factors are then recalculated using the modified sample. The difference from the nominal is taken as a systematic. The errors are symmetrized about this difference.

2. **Pair Efficiency:** To quantify the uncertainty associated with pair-efficiency cuts, we follow the methodology used in the ALICE EEC measurement at 5.02 TeV [215]. We vary the pair selection by ignoring all pairs with $\Delta\eta < 0.008$. We evaluate the sensitivity of the ENC observable to these variations within each jet $p_{\mathrm{T}}$ bin and use the corresponding differences in the correction factors as a source of systematic uncertainty.

3. **Generator Dependence:** Since detector effects are corrected using PYTHIA-based simulations, it is important to assess the dependence of our results on the choice of Monte Carlo generator. A study comparing corrections derived from alternative generators will be necessary to quantify this uncertainty. We do this using the HERWIG fast simulation described in Chapter 6.

4. **Jet $p_{\mathrm{T}}$ Migration:** To account for residual effects of jet $p_{\mathrm{T}}$ migration not fully corrected by the bin-by-bin method, we include an additional systematic. This is estimated by artificially shifting the detector-level jet $p_{\mathrm{T}}$ values as $p_{\mathrm{T,jet}}^{\mathrm{det}} \rightarrow p_{\mathrm{T,jet}}^{\mathrm{det}}/0.85$, thereby aligning them more closely with the truth-level spectrum. This procedure isolates migration effects from those due to pair efficiency.

The relative systematic uncertainties are plotted in Fig. A.1 for the EEC and in

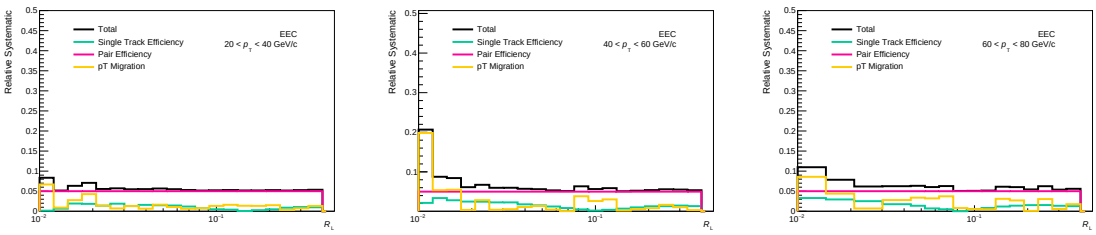


Figure A.1: Summary of systematic uncertainties for EEC.

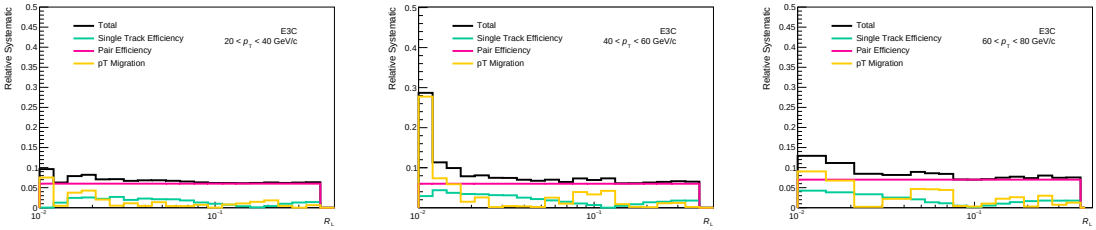


Figure A.2: Summary of systematic uncertainties for E3C.

Fig. A.2 for the E3C. All systematic uncertainties are propagated via standard error propagation. To compute the E3C/EEC ratio, the errors are treated as uncorrelated and added in quadrature.

### A.1.2 Results

Preliminary results using the bin-by-bin correction method are shown in Fig. A.3 for the EEC, E3C, and E3C/EEC ratio.

### A.1.3 Model Comparisons

The corrected distributions are compared to two MC Event Generators - PYTHIA8 [221] and HERWIG7 [123], which employ different hadronization models (Lund-String and Cluster hadronization, respectively) as described in Sec. 3.2.1.

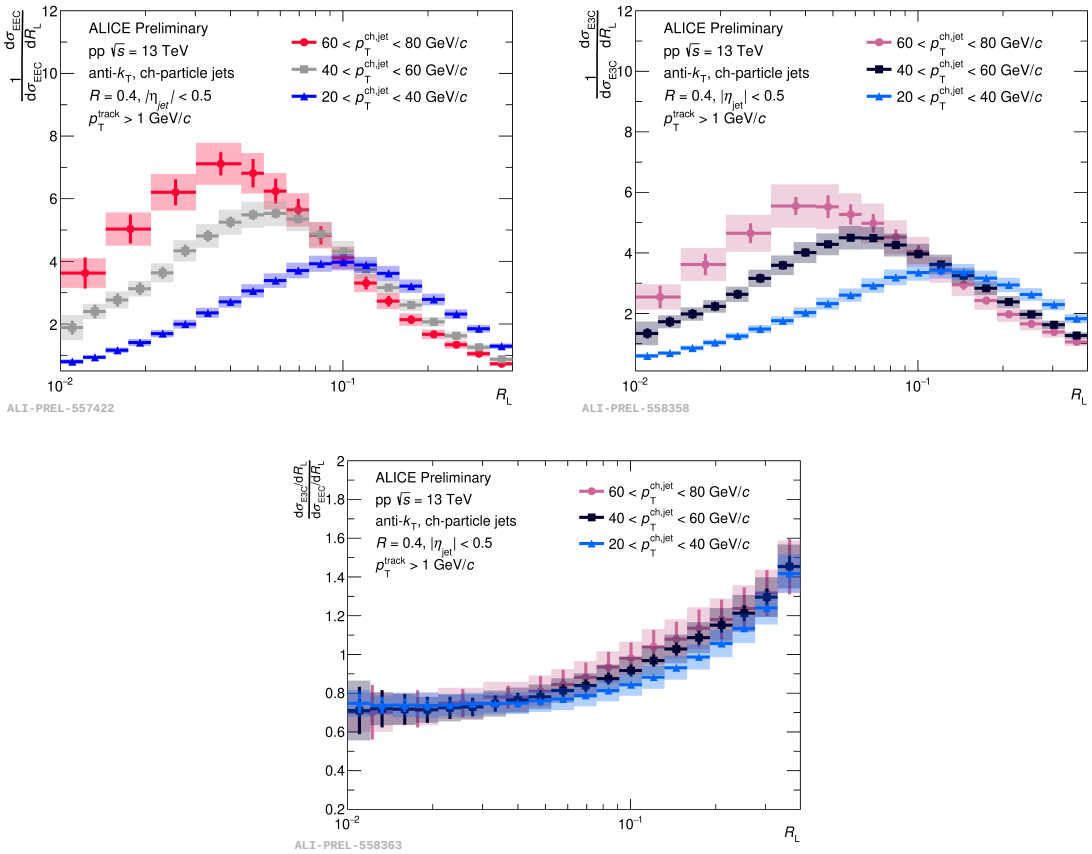


Figure A.3: Fully corrected, area and bin-width normalized ENC distributions for pp collisions at $\sqrt{s} = 13$ TeV. Top Left: EEC. Top Right: E3C. Bottom: E3C/EEC.

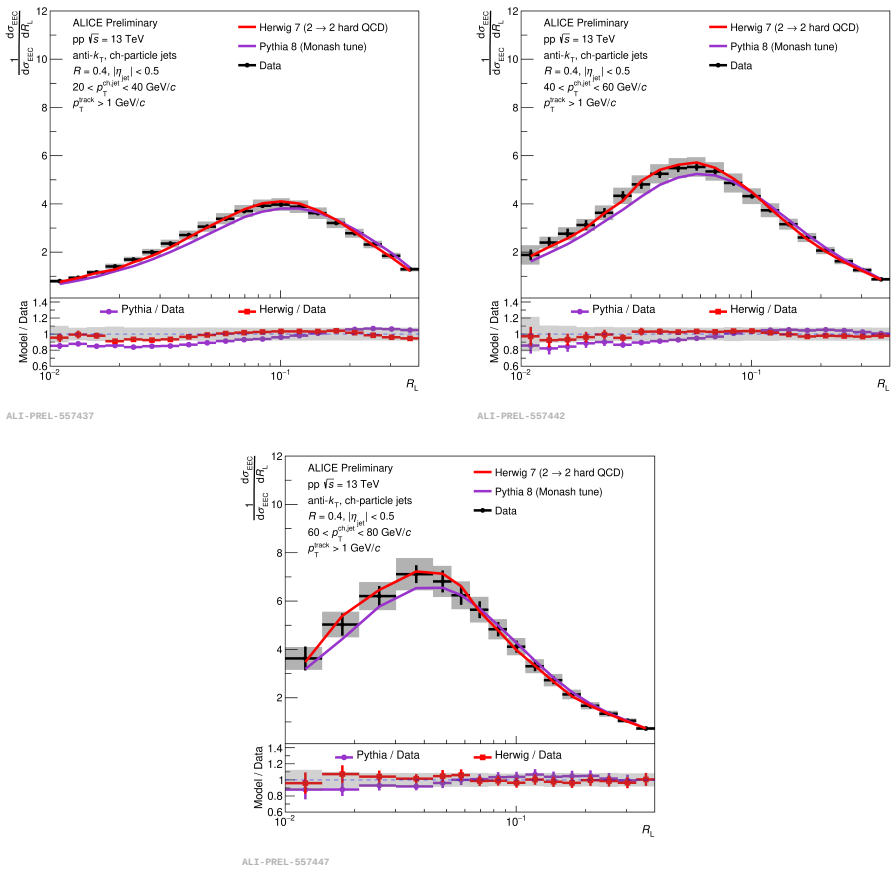


Figure A.4: Comparison of the corrected EEC with MC generators.

### EEC and E3C

The comparisons of the corrected EEC and E3C distributions are shown in Fig. A.4 and Fig. A.5, respectively. We see that HERWIG generally agrees better with the data, while PYTHIA underestimates the width of the peak. This trend has also been observed in other EEC measurements [22, 215].

### E3C/EEC

The fully corrected E3C and EEC distributions are compared to models as shown in Fig. A.6. Both models show agreement with the measured ratio, suggesting that non-perturbative effects largely cancel. The absence of a significant discrepancy between PYTHIA and HERWIG further supports this cancellation, indicating that the

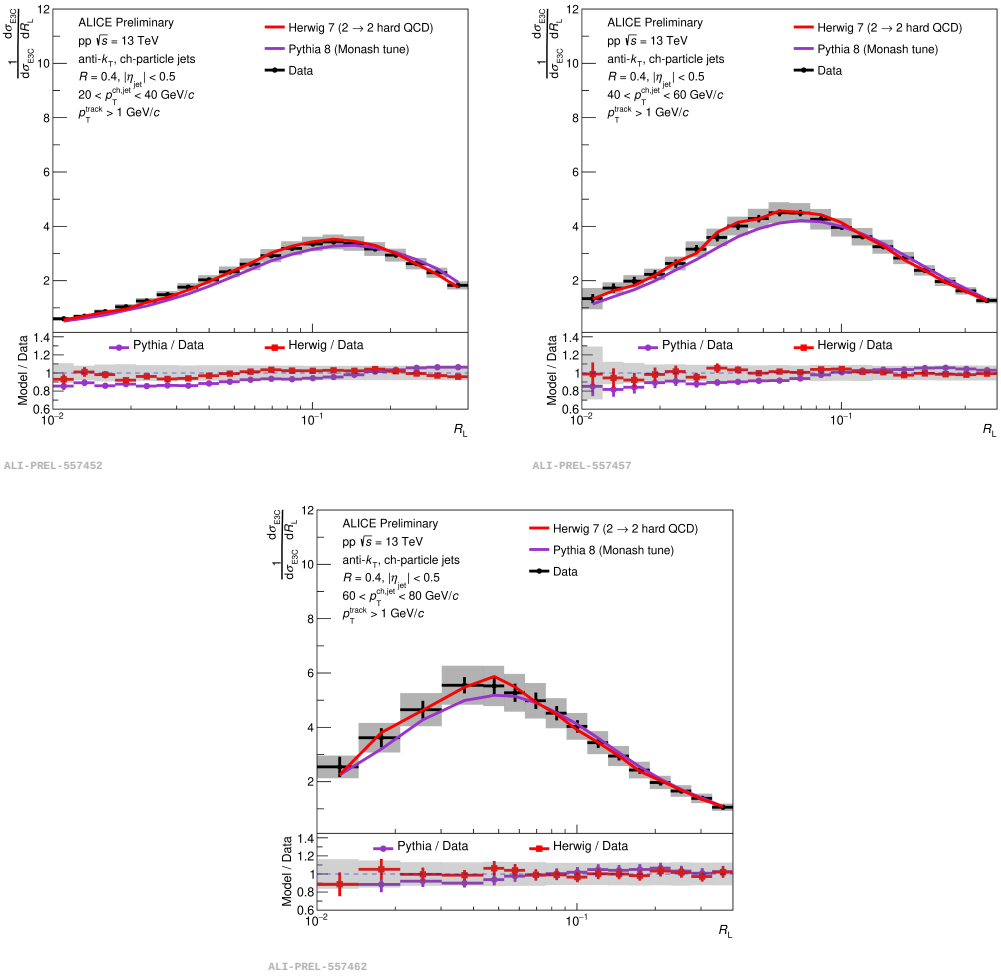


Figure A.5: Comparison of the corrected E3C MC generators.

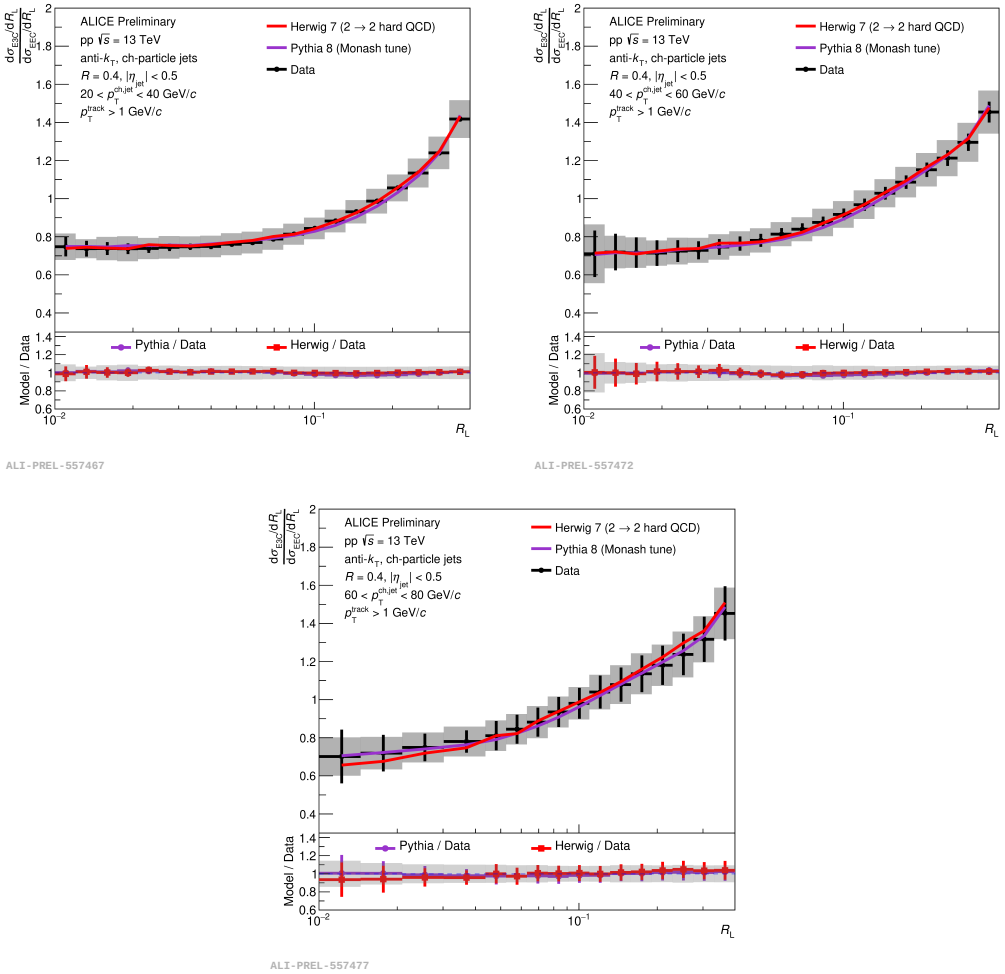


Figure A.6: Comparison of the corrected E3C/EEC ratio with MC generators.

observable is primarily sensitive to perturbative physics [15].[2]

2. Recent work has shown that these observables are still sensitive to non-perturbative effects of hadronization [218]. See Sec. 9.2 for further discussion.

## A.2 Updated ENC Measurement at $\sqrt{s} = 13$ TeV

This section contains supplemental plots for the ENC pp analysis at $\sqrt{s} = 13$ TeV.

### A.2.1 Unfolding Performance for $\sqrt{s} = 13$ TeV Analysis

This section contains plots of unfolding performance for the ENC across the entire phase space, i.e., for jet $p_{\mathrm{T}}$ bins 20-40, 40-60, 60-80 GeV/$c$.

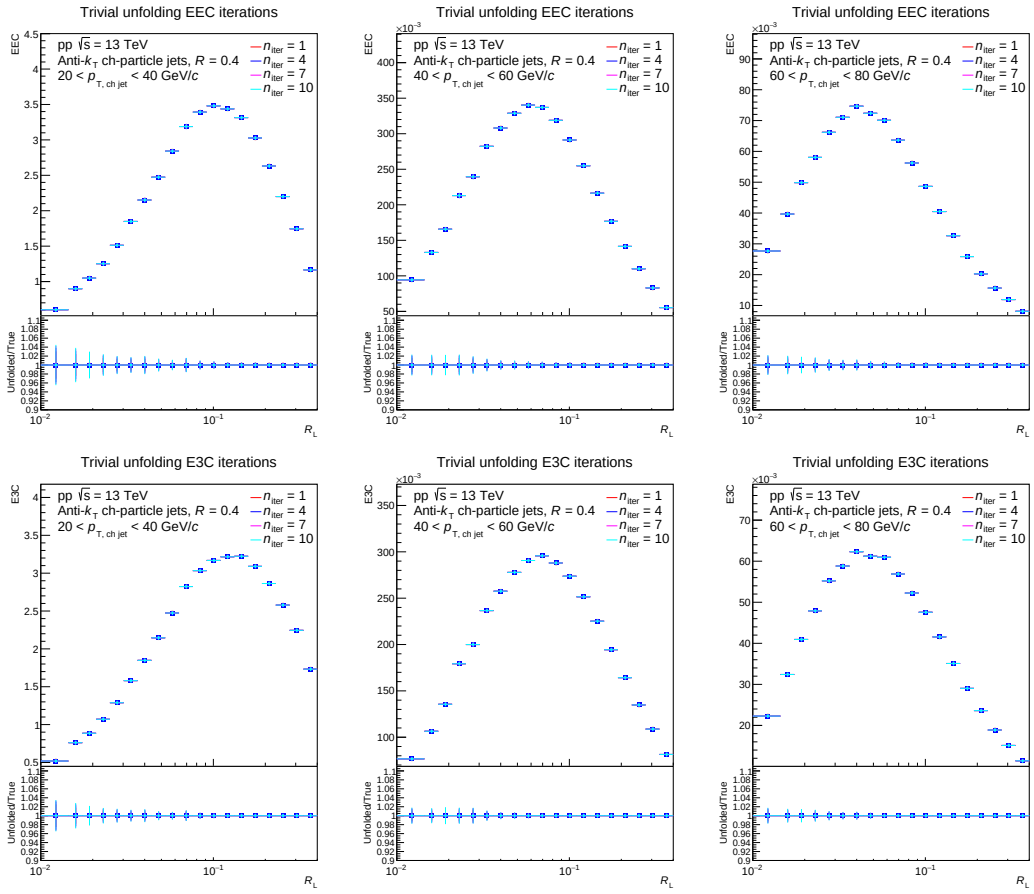


Figure A.7: Trivial closure in the measured jet $p_{\mathrm{T}}$ bins. Top: EEC. Bottom: E3C.

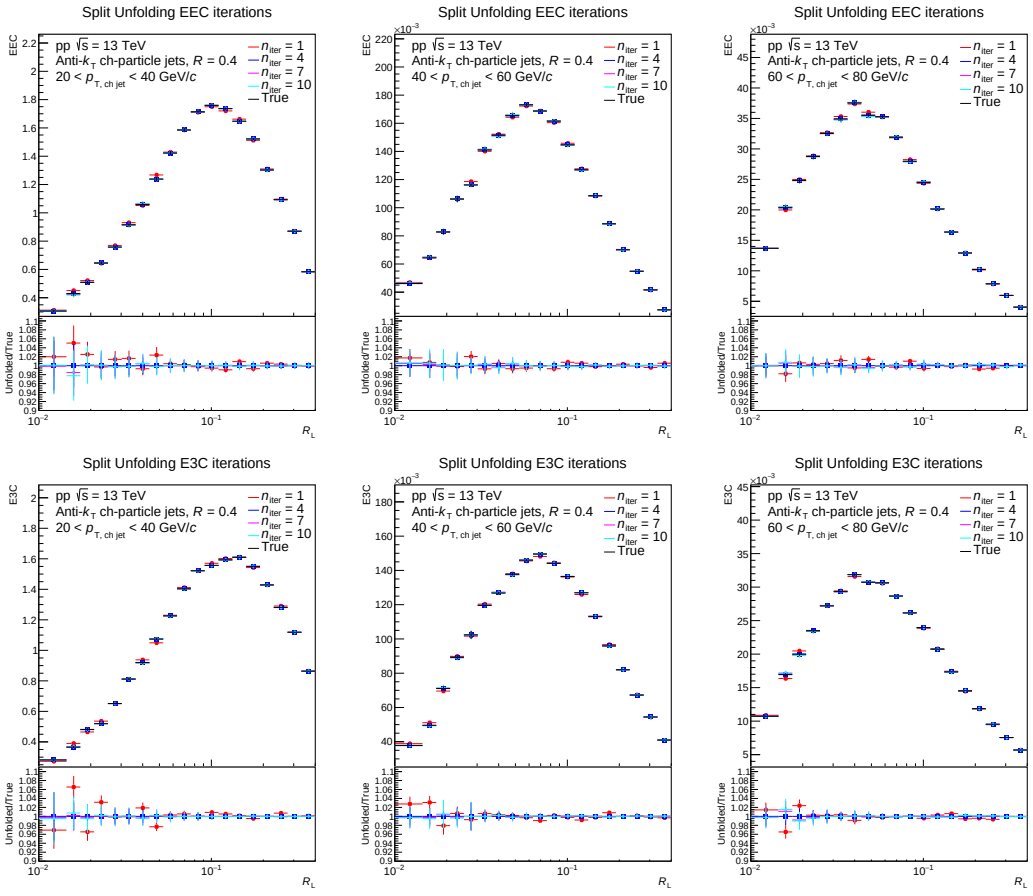


Figure A.8: Split closure in the measured jet $p_{\mathrm{T}}$ bins. Top: EEC. Bottom: E3C.

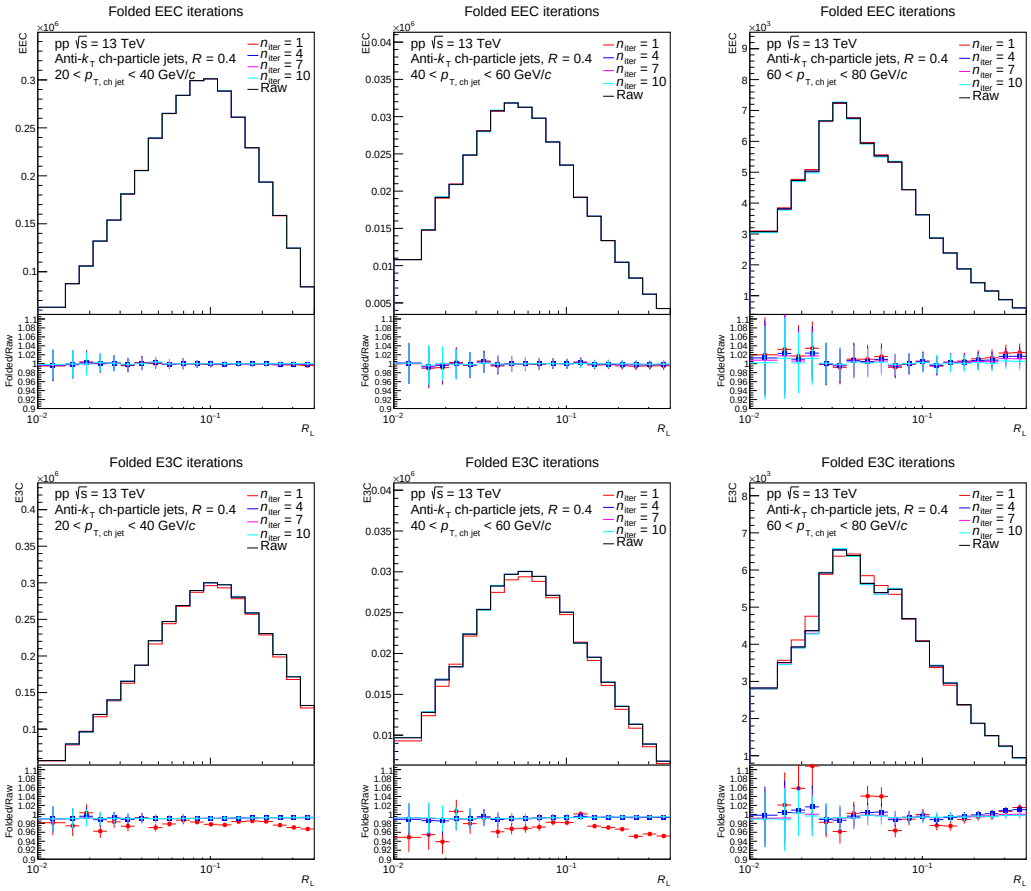


Figure A.9: Folding closure in the measured jet $p_{\mathrm{T}}$ bins at $\sqrt{s} = 13$ TeV. Top: EEC. Bottom: E3C.

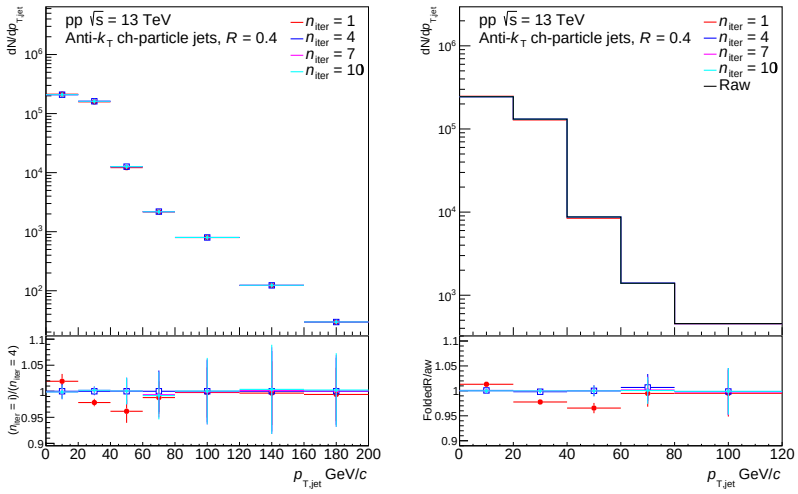


Figure A.10: Left: Unfolding convergence. Right: Refolding test for jet $p_{\mathrm{T}}$ at $\sqrt{s} = 13$ TeV.

### A.2.2 Systematics for $\sqrt{s} = 13$ TeV Analysis

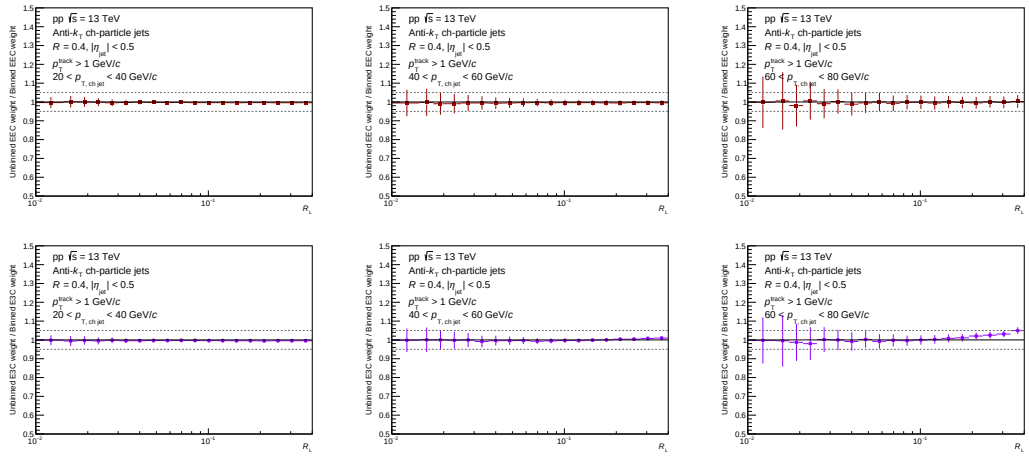


Figure A.11: Ratio of unbinned weight to the binned weight. Top: EEC. Bottom: E3C. The dotted lines are at ±5% from unity.

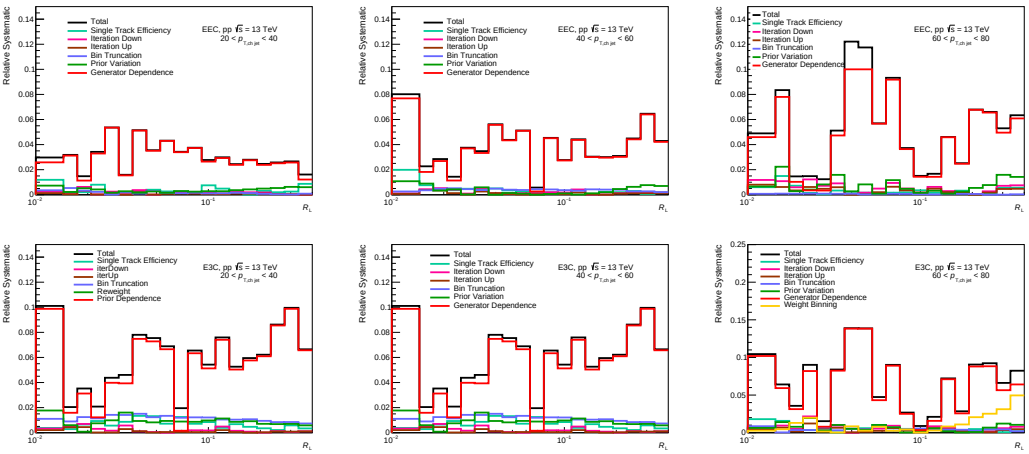


Figure A.12: Relative systematic uncertainties for across all measured jet $p_{\mathrm{T}}$ bins at $\sqrt{s} = 13$ TeV. Top: EEC. Bottom: E3C.

## A.3 Comparison of Unfolded and Bin-by-Bin Corrected Results at $\sqrt{s} = 13$ TeV

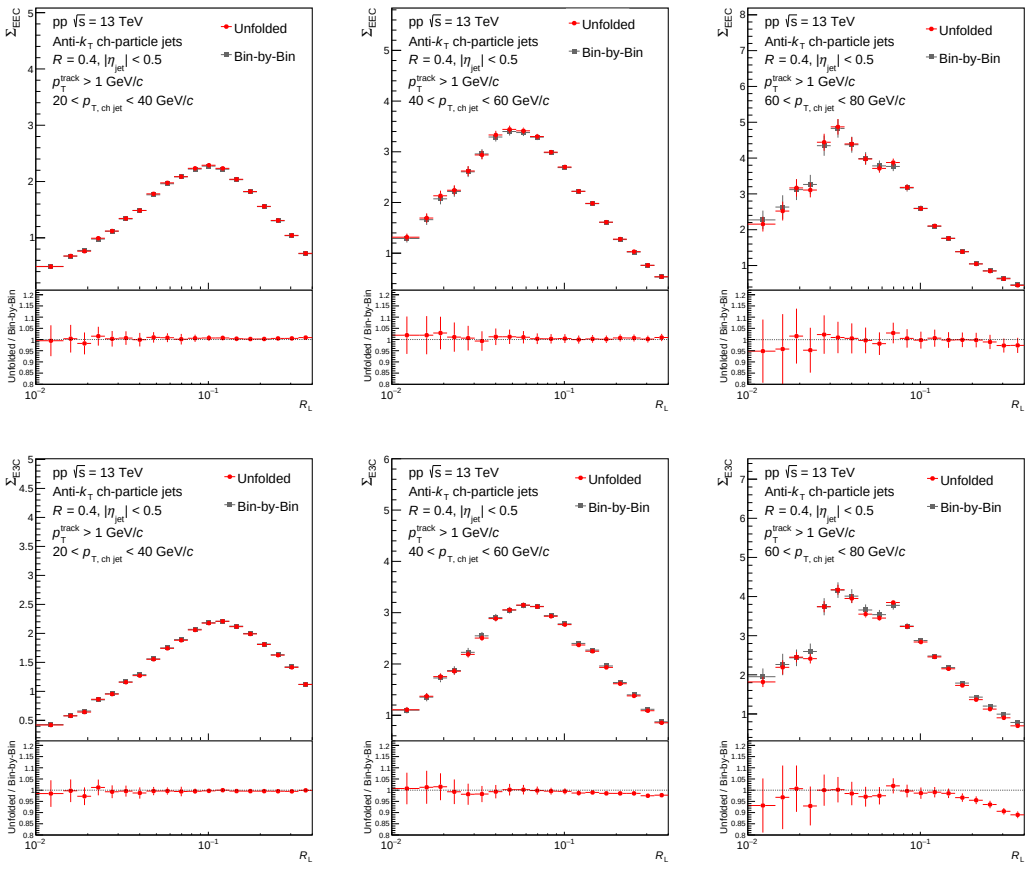


Figure A.13: Unfolded vs. Bin-by-Bin corrected results across all measured jet $p_T$ bins at $\sqrt{s} = 13$ TeV. Top: EEC. Bottom: E3C.

## A.4 ENC Analysis at $\sqrt{s} = 5.02$ TeV

This section contains supplemental plots for the ENC pp analysis at $\sqrt{s} = 5.02$ TeV.

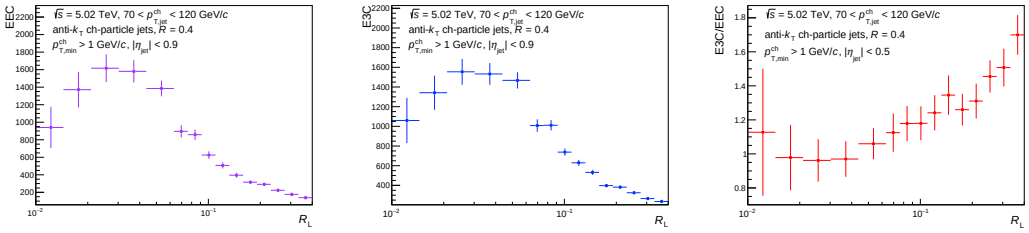


Figure A.14: Raw distributions normalized by the bin-width at $\sqrt{s} = 5.02$ TeV. Left: EEC. Middle: E3C. Right: E3C/EEC.

### A.4.1 Unfolding Performance for $\sqrt{s} = 5.02$ TeV analysis

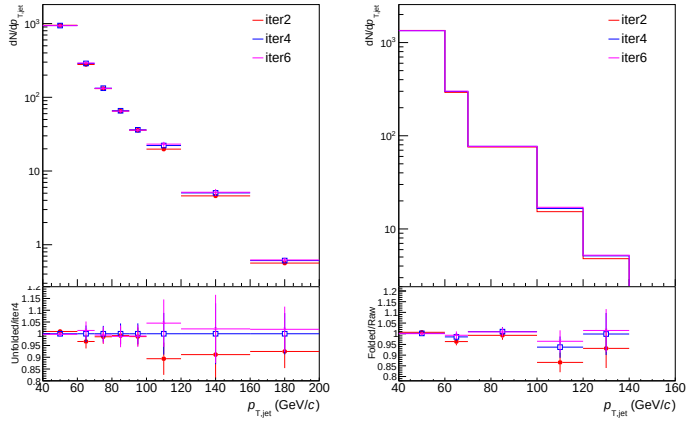


Figure A.15: Left: Unfolding convergence. Right: Refolding test for jet $p_T$ in pp collisions at $\sqrt{s} = 5.02$ TeV.

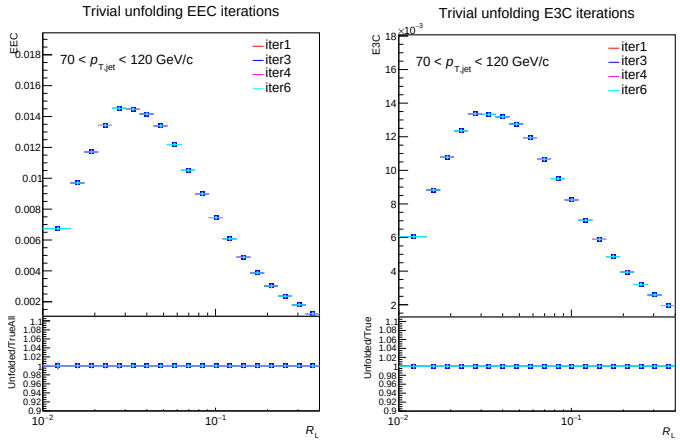


Figure A.16: Trivial closure at $\sqrt{s} = 5.02$ TeV. Left: EEC. Right: E3C.

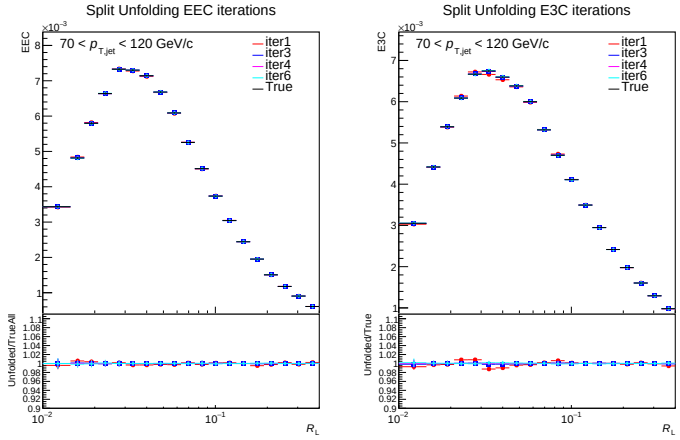


Figure A.17: Split closure at $\sqrt{s} = 5.02$ TeV. Left: EEC. Right: E3C.

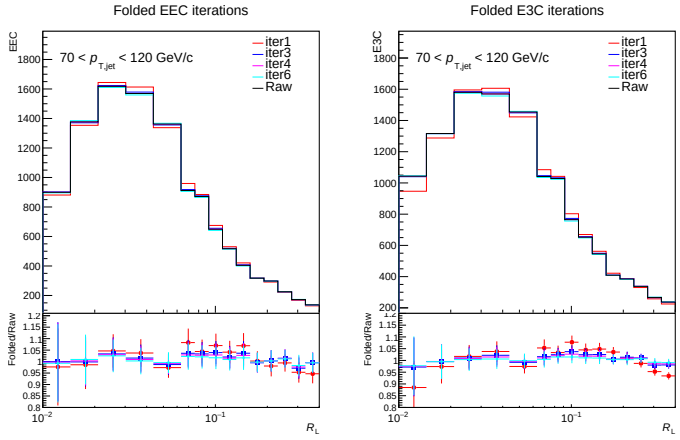


Figure A.18: Refolding test at $\sqrt{s} = 5.02$ TeV. Left: EEC. Right: E3C.

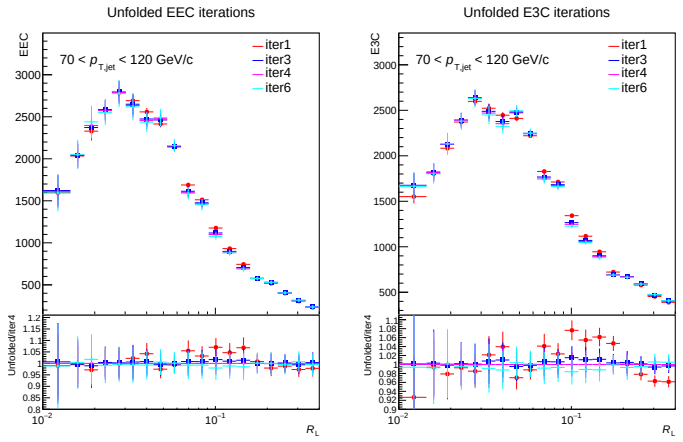


Figure A.19: Unfolding convergence at $\sqrt{s} = 5.02$ TeV. Left: EEC. Right: E3C.

### A.4.2 Systematics for $\sqrt{s} = 5.02$ TeV Analysis

The systematic uncertainties for the $\sqrt{s} = 5.02$ TeV analysis are the same as those described in Sec. 6.5. They are listed below for completeness, but the reader is referred to Chapter 6 for a complete description.

- Tracking Efficiency Systematic - same as described in 6.5.
- Choice of weight binning - same as described in 6.5.
- Unfolding Systematics - same as described in 6.5.

A summary of the systematic uncertainties for the EEC, E3C and E3C/EEC is presented in Fig. A.20.

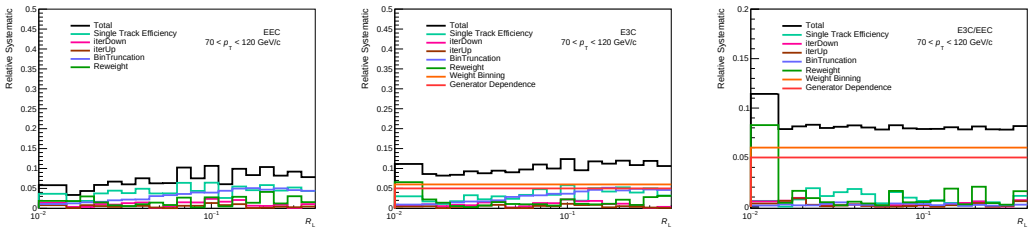


Figure A.20: Summary of systematic uncertainties for the measurement in pp collisions at $\sqrt{s} = 5.02$ TeV. Left: EEC. Middle: E3C. Right: E3C/EEC.

# Appendix B

# Studying Wake Effects with EEECs

## B.1 Coordinate Artifacts and Motivation for $(x, y)$ Coordinate System

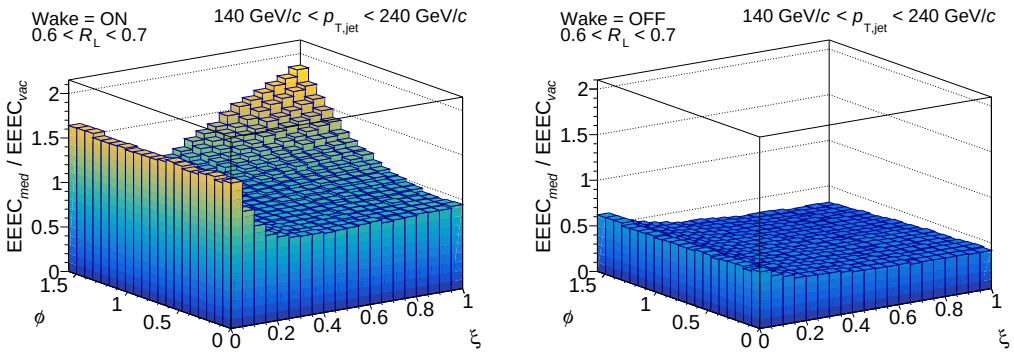


Figure B.1: The ratio of the shape-dependent EEEC in medium to the EEEC vacuum in $\xi$-$\phi$ coordinates. Left: With wake. Right: Without wake. This figure should be compared to Fig. 7.7, where the same ratios are plotted in $x$-$y$ coordinates. Noting that here the equilateral region is $(\xi, \phi) \sim (1, \pi/2)$, we see that here, as in Fig. 7.7, the wake shows up in the left plot as an enhancement in the equilateral region.

As shown in Fig. B.1, the enhancement of the EEEC in the equilateral region appears consistently in both coordinate systems. The figure shows the ratio of the EEEC for jets in medium—with and without the wake—to that in vacuum, using

the $\xi$–$\phi$ coordinates. Consistent with the $x$–$y$ results in Fig. 7.7, turning off wake hadrons yields a flat ratio below unity, reflecting parton energy loss. Including the wake introduces a clear enhancement in the equilateral region, confirming that the main physical conclusions from the ratio are coordinate-independent, as the Jacobian cancels. The $x$–$y$ coordinate system, introduced in Sec. 7.4, offers a flat Jacobian that simplifies the interpretation of unnormalized EEECs.

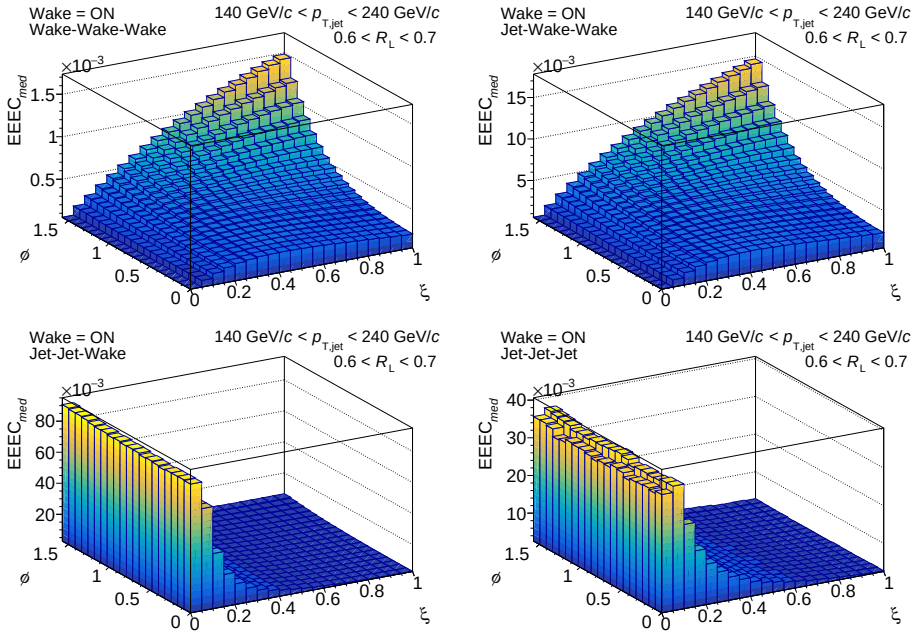


Figure B.2: Various contributions to the EEEC for jets in heavy-ion collisions in the $(\xi, \phi)$ coordinates. We see that the correlation in the equilateral region is dominated by correlations involving two or more hadrons originating from jet wakes.

Fig. B.2 breaks down EEEC contributions by particle-triplet type in the $\xi$–$\phi$ system. "Jet" particles come from the parton shower, while "wake" particles originate from the wake but are reconstructed as part of the jet. As shown in Fig. B.2, correlations involving multiple wake particles dominate near $(\xi, \phi) \sim (1, \pi/2)$. However, the sharp peak for equilateral triangles in this coordinate system is unphysical, given the uniform angular distribution of wake hadrons. This artifact arises from the coordinate Jacobian, not from the physics of the wake.

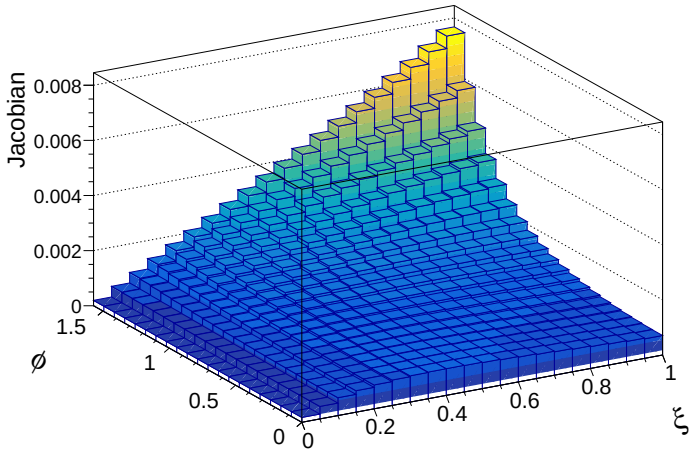


Figure B.3: The Jacobian in $\xi$-$\phi$ coordinates. It has a sharp peak at the equilateral triangle point $(\xi, \phi) = (1, \pi/2)$.

Sec. 7.4 defines the $x$–$y$ system with fixed particles at $(0, 0)$ and $(1, 0)$, and the third at $(x, y)$. A uniform distribution in $(x, y)$ maps to non-uniform bin areas in $(\xi, \phi)$ space, visualized as the Jacobian in Fig. B.3. As shown in Fig. B.3, the Jacobian is sharply peaked for equilateral configurations, mirroring the pattern in Fig. B.2 and confirming that the observed enhancement is geometric rather than physical. For more details, see [17].

## B.2 Cross-checks of Wake Effects

Within the Hybrid Model framework, particles can be tagged according to their origin, distinguishing those produced by parton fragmentation from soft hadrons generated by the wake. This tagging facilitates a separation of the various contributions to the EEEC. The different contributions to the EEEC are shown in Fig. B.4. The figure illustrates that triplets containing at least two wake hadrons contribute significantly to both the equilateral and collinear regions. Due to the sparse population of parton shower hadrons in the equilateral regime, correlations induced by wakes become the

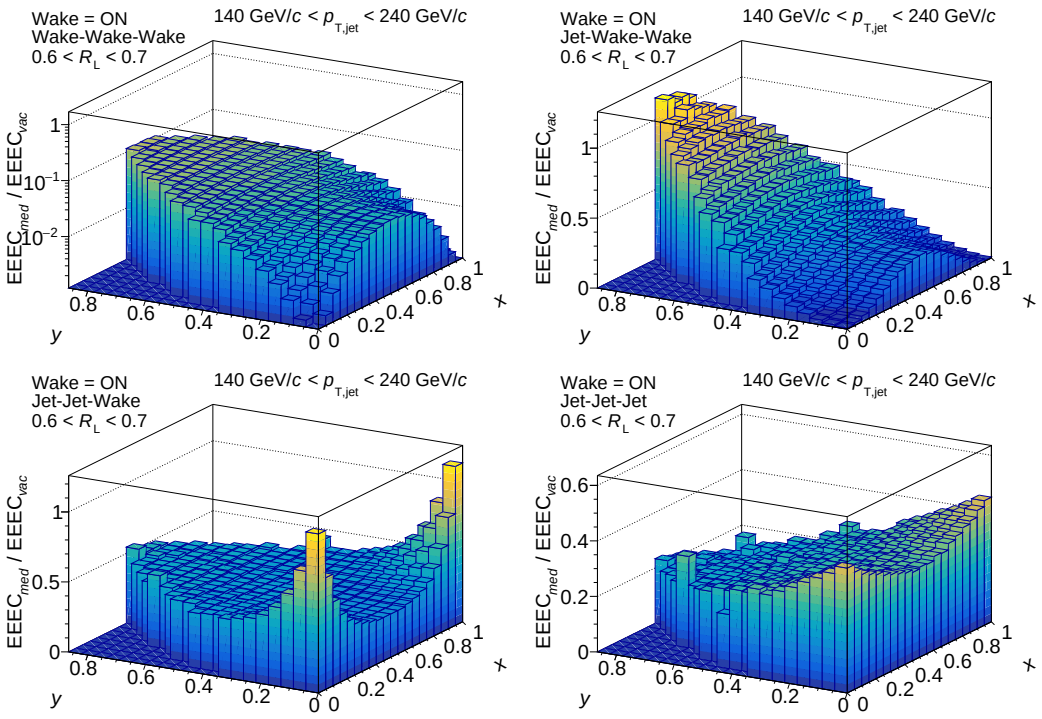


Figure B.4: Ratios of various contributions to the EEEC for jets in heavy-ion collisions with wakes to the EEEC for jets in vacuum, in $x$-$y$ coordinates. Note that the vertical axis scales are different in each plot in order to make the key features of the plot visible.

dominant contribution to the EEEC in that region.

## B.3 Effects of Negative Wake

Within the Hybrid Model framework, "negative wakes" correspond to regions of depleted soft particle density that arise opposite to the wake [258] generated by jet-medium interactions. These negative wake particles, characterized by negative energy, must be carefully subtracted in order to accurately construct the energy correlator observables discussed in Chapter 7. The subtraction procedure employed follows the method outlined in [17]. While the detailed methodology of subtraction is not the focus of this section, the emphasis here is on how negative wakes manifest in the EEEC and how they may enable direct experimental access to negative wake

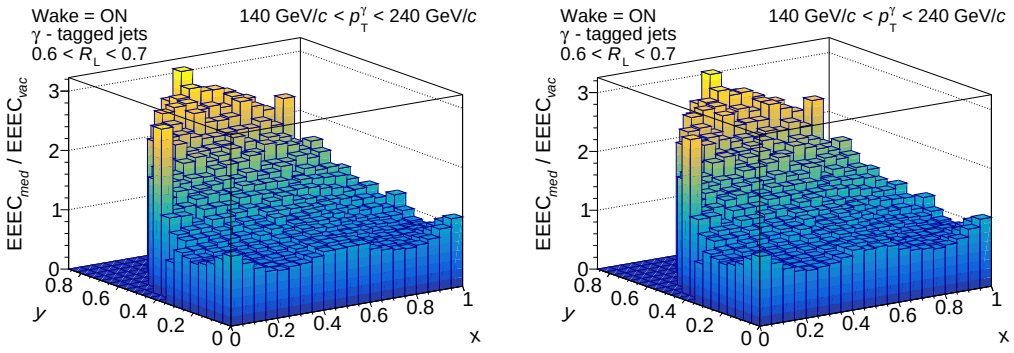


Figure B.5: Ratio of EEECs for jets in medium with wake to EEECs for jets in vacuum in $x$-$y$ coordinates for $R = 0.8$ $\gamma$-tagged jets. Left: Ignoring negative wake particles. Right: After subtracting negative wake particles.

phenomena, complementing the discussion in Sec. 3.6.2.

In dijet events, the negative wake produced by the near-side jet is often filled by the wake created by the away-side jet, complicating the observable's interpretation. In contrast, $\gamma$-tagged jet events offer a cleaner environment: the leading structure azimuthally opposite to the jet is constrained to be an isolated photon, and while additional away-side jets can occasionally appear, their occurrence is rare. Due to the long mean free path of photons relative to the size of the QGP, as discussed in Sec. 2.5.2, photons traverse the medium without generating wakes. Consequently, $\gamma$-tagged jets experience significantly fewer overlapping negative wake contributions compared to inclusive jets.

This expectation is confirmed in Fig. B.5, where the in-medium to vacuum EEEC ratio for $\gamma$-tagged jets remains essentially unchanged regardless of whether negative wake particles are subtracted, indicating their negligible presence. These observations collectively suggest that negative wakes can significantly distort the full shape-dependent EEEC when superimposed wakes from other jets overlap with the selected jet's wake. In principle, a comparative analysis of inclusive jet and $\gamma$-tagged jet EEECs could serve as a novel method to identify and characterize negative wakes in the QGP. A systematic exploration of this possibility is reserved for future work.

# Appendix C

# Background Subtraction for ENCs in Heavy-Ion Collisions

*The tests shown here are performed on 1D distributions of ENCs unless otherwise specified.*

### Construction of Thermal Toy

As an initial step in validating the analysis strategy, a study is conducted within a simplified toy model framework. In this setup, PYTHIA events are embedded into a thermal toy background that emulates the charged-particle multiplicity observed by ALICE in Pb-Pb collisions at $\sqrt{s_{\mathrm{NN}}} = 5.02$ TeV in the 0–5% centrality class, as reported in [259]. The toy background assumes a uniform distribution in pseudorapidity within the range $|\eta| < 0.9$. This background consists solely of uncorrelated particles and does not incorporate medium-related effects such as collective flow or expansion. This simplification is intentional: the goal is to isolate and subtract the uncorrelated background component from the observable to better probe the medium response associated with correlated background effects. anti-$k_{\mathrm{T}}$ jets of radius $R = 0.4$

are reconstructed. A pedestal subtraction is performed on the jets, and they are subsequently matched to the truth PYTHIA jet. For this study, an even lower track $p_{\mathrm{T}}$ cut of 0.7 GeV/c is applied for ENC construction after jet finding. The EEC and E3C distributions are shown in the left and right panels of Fig. C.1, respectively.

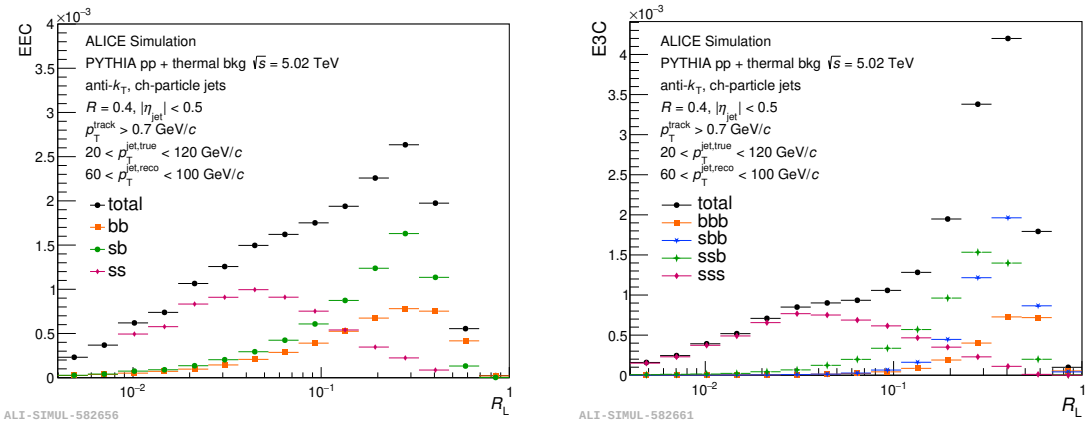


Figure C.1: Distribution for matched jets showing different contributions. Left: EEC. Right: E3C.

### Accounting for Differences in Underlying Event Density: c-factors

The number of background tracks within the jet cone and the random cone may differ due to the explicit jet $p_{\mathrm{T}}$ threshold imposed by the jet-finding algorithm. This effect is illustrated in the toy model study presented below. In the first scenario, shown in Fig. C.2, the same number of background tracks is added to both the jet cone and the random cone. In contrast, the second scenario introduces fewer background tracks into the random cone compared to the jet cone. As demonstrated in Fig. C.3, this mismatch causes the correction procedure to fail, resulting in a rising trend in the ratio at large $R_{\mathrm{L}}$. To illustrate what the c-factors might look like, these are plotted in Fig. C.4.

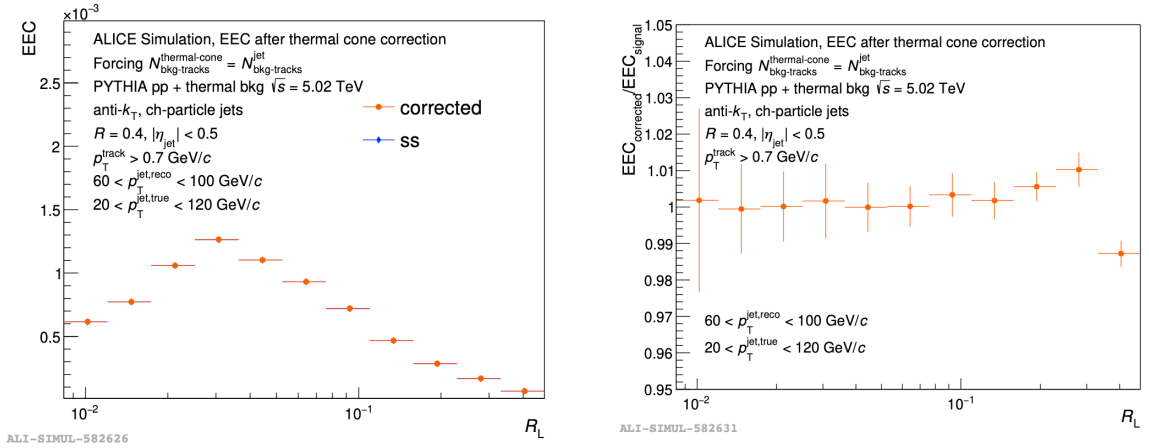


Figure C.2: Validity of correction method when the same number of background particles are present in the jet cone and in the random cone.

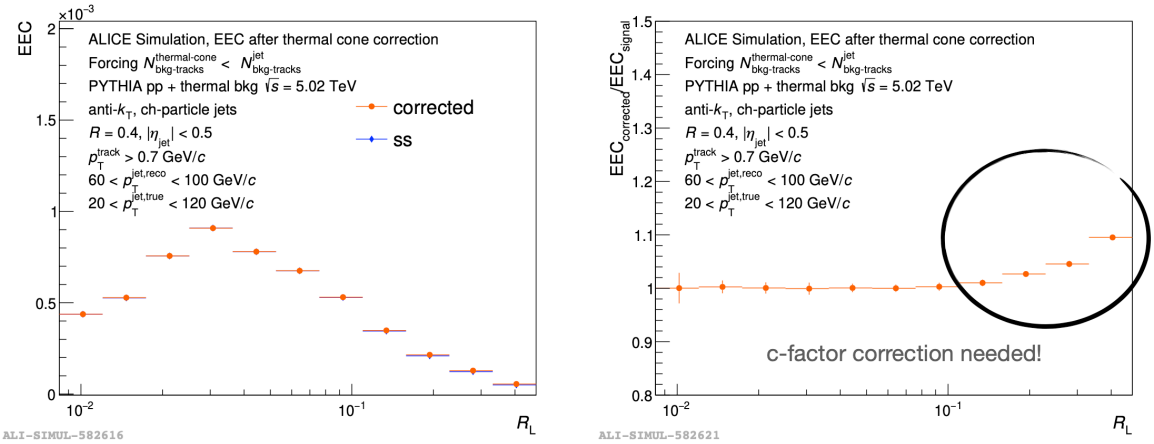


Figure C.3: Figure depicting the discrepancy in the correction method when the number of background particles in the jet cone is greater than the number of particles in the random cone.

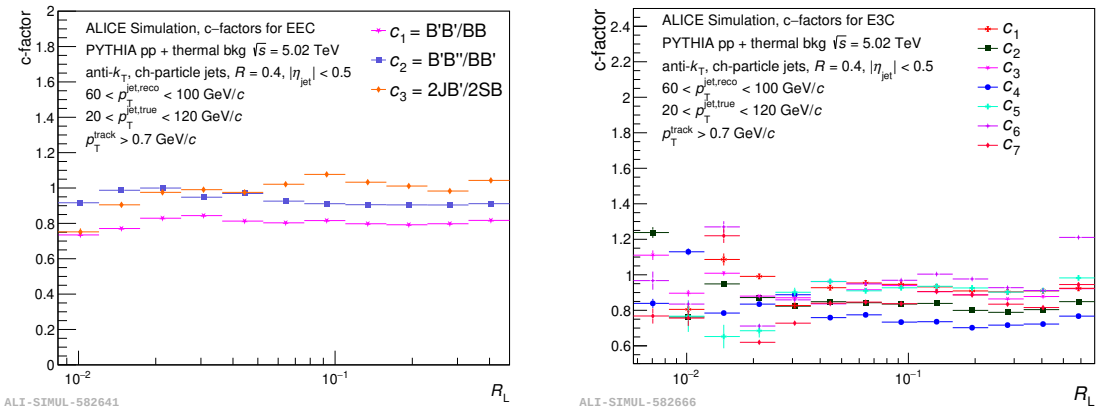


Figure C.4: c-factor distributions. Left: EEC. Right: E3C. The legend for c-factors for E3C is tabulated in Table C.1.

| **c-factor** | **Definition** |
|---|---|
| $c_1$ | $c_{BB'\tilde{B}} = (B'B''\tilde{B})/BB'B''$ |
| $c_2$ | $c_{BBB'} = (B'B'B'')/BBB'$ |
| $c_3$ | $c_{BB'B'} = (B'B''B'')/BB'B'$ |
| $c_4$ | $c_{B^3} = (B')^3/B^3$ |
| $c_5$ | $c_{SBB'} = (SB'B'')/SBB'$ |
| $c_6$ | $c_{SBB} = (SB'B')/SBB$ |
| $c_7$ | $c_{SSB} = (SSB')/SSB$ |

Table C.1: Table depicting how c-factors are constructed for E3C.

### Validation of Subtraction Procedure for EEC and E3C

The subtraction procedure described in Sec. 8.2.5 is applied both to the EEC and E3C in the toy model. Fig. C.5, shows the background subtraction. Left: With c-factor. Right: Without c-factor for the EEC (Top) and the E3C (Bottom), respectively.

### Validation of Analysis Methodology for EEC

*The tests shown here are largely performed for the EEC, but these can be extended to the E3C as well, since apart from the subtraction procedure, the rest of the analysis*

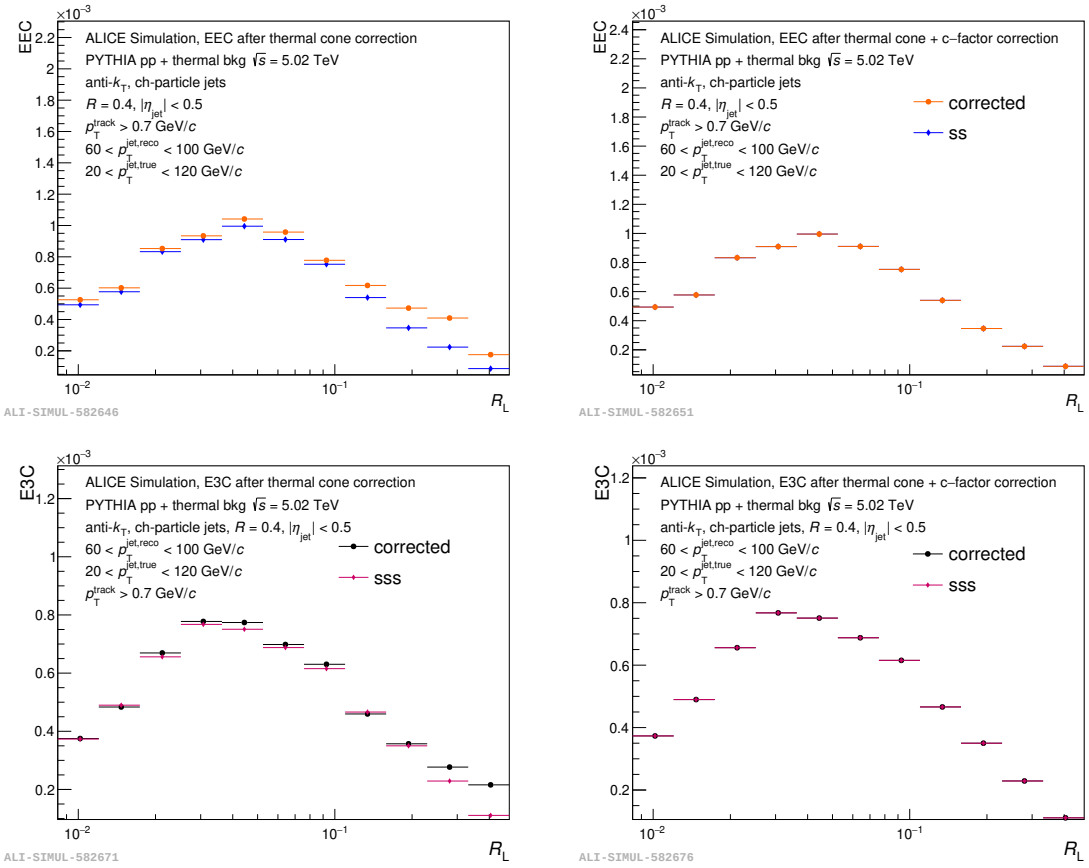


Figure C.5: ENC distributions before c-factor correction (Left) and after c-factor correction (Right). Top: EEC. Bottom: E3C.

*remains the same.*

In this stage of the analysis, the full three-dimensional distributions are considered, and the c-factor scaled background subtraction is performed in 3D space. This approach aligns with the methodology used in the pp analysis and enables subsequent application of 3D unfolding techniques. For matched jets, the resulting EEC distribution is shown in the left panel of Fig. C.1. The structure of this distribution is consistent with physical expectations: signal–background correlations, which correspond to hard–soft interactions, contribute more prominently than background–background correlations, which involve only soft–soft pairs. Additionally, the influence of uncorrelated background becomes apparent at large $R_{\mathrm{L}}$, reflecting the geometrical characteristics of a uniform distribution, which naturally peaks at large pairwise separations.

The signal–signal component in this context corresponds purely to the PYTHIA simulation.

***Case 1.1: Jet $p_{\mathrm{T}}$ smearing***

In this scenario, jet $p_{\mathrm{T}}$ smearing arises due to the re-clustering of jets following background subtraction. Despite this additional source of uncertainty, the unfolding performance remains robust, as anticipated. The comparison to the truth-level EEC distribution—accessible in this case due to the controlled nature of the toy model—is shown here. The results indicate good agreement, with deviations remaining within 5%, demonstrating the effectiveness of the unfolding procedure under these conditions. This is shown in Fig. C.8.

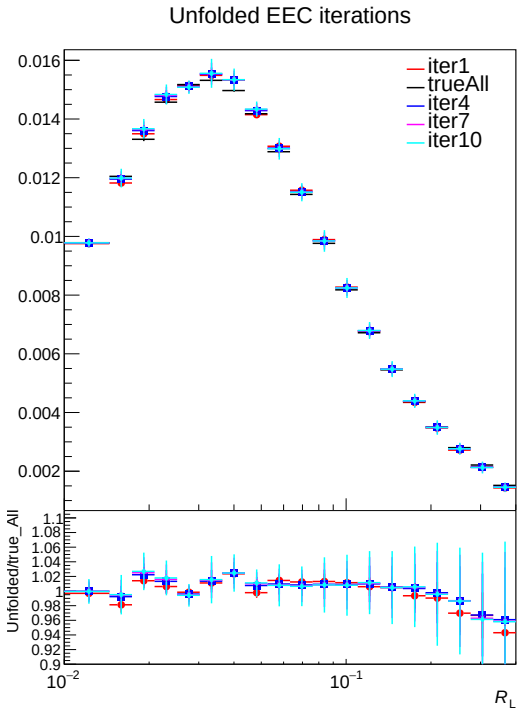


Figure C.6: Unfolding closure after applying a jet $p_{\mathrm{T}}$ smearing.

***Case 1.2: Jet and track $p_{\mathrm{T}}$ smearing***

In this scenario, track-level $p_{\mathrm{T}}$ smearing is introduced in addition to jet-level effects. The $p_{\mathrm{T}}$-dependent smearing is modeled according to the track momentum resolution

extracted from the ALICE detector simulation at $\sqrt{s} = 5.02$ TeV. Specifically, tracks are first smeared according to this efficiency model to generate detector-level jets, which are then embedded into a thermal background. Following embedding, jets are re-clustered, the underlying event density ($\rho$) is subtracted, and the resulting jets are matched to the original PYTHIA-level jets. The smearing profile is illustrated in Fig. C.7, where the shaded bands denote two different track selection thresholds—0.7 GeV/$c$ and 1 GeV/$c$—that may be applied during ENC construction.

The comparison between the unfolded and truth-level EEC distributions is shown in

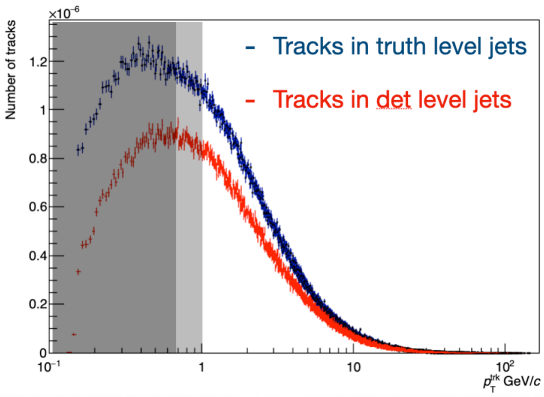


Figure C.7: $p_{\mathrm{T}}$ dependent track smearing applied to tracks. The shaded regions represent two choices of track cuts (at 0.7 GeV/$c$ and 1 GeV/$c$) that can be applied in ENC construction.

Fig. C.8, leveraging the fact that the truth-level information is accessible in this toy model. The unfolding performance is generally satisfactory, with deviations remaining within 5%. A slight downward trend is observed at large $R_{\mathrm{L}}$, which warrants further investigation.

### *Case 1.3: Finding c-factors from a different set of events*

In the analysis of real data, the c-factors will be computed using embedded samples. At the ensemble level, these c-factors are expected to account for differences in underlying event (UE) densities. However, discrepancies may still arise due to differences in the jet populations used for computing and applying the corrections. To study

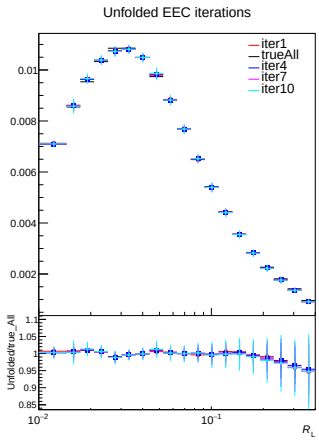


Figure C.8: Unfolding closure after applying a $p_{\mathrm{T}}$ dependent track smearing so that we have both jet $p_{\mathrm{T}}$ and track $p_{\mathrm{T}}$ smearing.

this effect within the toy model, two independent ensembles of events are generated using different random seeds. The $c$-factors are derived from jets in one ensemble and then applied to correct jets in the other. The resulting unfolded EEC distribution is shown in Fig. C.9. The closure achieved in this test remains within 10%, indicating reasonable stability of the correction procedure under these conditions.

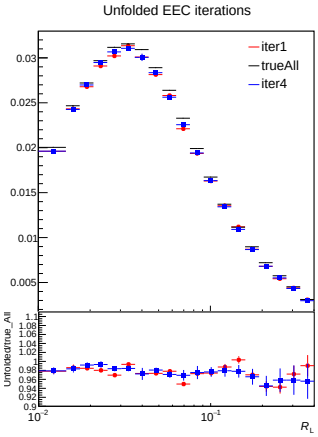


Figure C.9: Unfolding closure after applying c-factors obtained from different sets of jets to mimic the c-factor correction we will perform in data.

# Bibliography


[1] A. Deur, S. J. Brodsky, and G. F. de Teramond, *The QCD Running Coupling*, *Nucl. Phys.* **90** (2016) 1, [arXiv:1604.08082]. xiv, 9, 42

[2] **HotQCD** Collaboration, A. Bazavov et al., *Equation of state in ( 2+1 )-flavor QCD*, *Phys. Rev. D* **90** (2014) 094503, [arXiv:1407.6387]. xiv, 12

[3] A. D. (Maky), "Polytope24 - own work based on: Ads3 (new).png." https://commons.wikimedia.org/w/index.php?curid=38781800, 2023. CC BY-SA 3.0 license. xiv, 12

[4] M. Arslandok et al., *Hot QCD White Paper*, arXiv:2303.17254. xiv, 14, 16

[5] C. Beattie, *Pathlength-dependent jet quenching in the quark–gluon plasma at ALICE*. PhD thesis, Yale U., 3, 2023. xiv, 19

[6] J.-F. Paquet, *Electromagnetic probes in heavy-ion collisions: progress and open questions*, *PoS* **HardProbes2023** (2024) 009, [arXiv:2307.09967]. xiv, 23

[7] B. Muller, *Parton Energy Loss in Strongly Coupled AdS/CFT*, *Nucl. Phys. A* **855** (2011) 74–82, [arXiv:1010.4258]. xv, 27, 28, 39

[8] **CMS** Collaboration, A. Hayrapetyan et al., *Measurement of the primary Lund jet plane density in proton-proton collisions at* $\sqrt{s}$ *= 13 TeV*, *JHEP* **05** (2024) 116, [arXiv:2312.16343]. xv, 32

[9] R. K. Ellis and W. J. Stirling *et al.*, *QCD and Collider Physics*. Cambridge Monographs on Particle Physics, Nuclear Physics and Cosmology. Cambridge University Press, 1996. xv, 20, 34, 54

[10] D. S. Cerci, "Jet quenching results with cms." Presentation at Large Hadron Collider Physics (LHCP) 2017, 2017. Accessed: 2025-04-29. xv, 35

[11] **OPAL** Collaboration, G. Abbiendi et al., *Determination of alpha(s) using jet rates at LEP with the OPAL detector*, *Eur. Phys. J. C* **45** (2006) 547–568, [hep-ex/0507047]. xv, 42

[12] **ATLAS** Collaboration, *Measurement of Track Functions in ATLAS Run 2 Data*, . xv, 43

[13] **CMS** Collaboration, A. Hayrapetyan et al., *Girth and groomed radius of jets recoiling against isolated photons in lead-lead and proton-proton collisions at* $\sqrt{s_{\mathrm{NN}}}$ *= 5.02 TeV*, arXiv:2405.02737. xvi, 44, 45

[14] Z. Yang, T. Luo, W. Chen, L. Pang, and X.-N. Wang, *3d structure of jet-induced diffusion wake in an expanding quark-gluon plasma*, *Phys. Rev. Lett.* **130** (Feb, 2023) 052301. xvi, 46

[15] P. T. Komiske, I. Moult, J. Thaler, and H. X. Zhu, *Analyzing N-Point Energy Correlators inside Jets with CMS Open Data*, *Phys. Rev. Lett.* **130** (2023), no. 5 051901, [arXiv:2201.07800]. xvi, xvii, 52, 53, 55, 56, 57, 92, 96, 105, 130, 140

[16] K. Lee and B. Meçaj *et al.*, *Conformal Colliders Meet the LHC*, arXiv:2205.03414. xvi, 53, 55, 95

[17] H. Bossi, A. S. Kudinoor, I. Moult, D. Pablos, A. Rai, and K. Rajagopal, *Imaging the wakes of jets with energy-energy-energy correlators*, *JHEP* **12** (2024) 073, [arXiv:2407.13818]. xvii, 55, 57, 100, 129, 152, 153

[18] E. Lopienska, *The CERN accelerator complex, layout in 2022. Complexe des accélérateurs du CERN en janvier 2022*, . General Photo. xvii, 59

[19] A. Lopes and M. L. Perrey, "FAQ-LHC The guide." 2022. xvii, 61

[20] **ALICE** Collaboration, B. B. e. Abelev, *Performance of the ALICE Experiment at the CERN LHC*, *Int. J. Mod. Phys. A* **29** (2014) 1430044, [arXiv:1402.4476]. xvii, xxvi, 63, 64, 65, 76

[21] I. Belikov, "Alice vertexing performance in run 2 and prospects for run 3." https://indico.cern.ch/event/710050/contributions/3161650/attachments/1740133/2815485/15_15_belikov_vertex_2018.pdf, 2018. Presented at: 8th Annual Large Hadron Collider Physics Conference (LHCP 2018), Bologna, Italy. xvii, 67

[22] **STAR** Collaboration, *Measurement of Two-Point Energy Correlators Within Jets in p+p Collisions at* $\sqrt{s} = 200$ *GeV*, arXiv:2502.15925. xvii, 69, 70, 92, 138

[23] **CMS** Collaboration, A. Hayrapetyan et al., *Measurement of energy correlators inside jets and determination of the strong coupling* $\alpha_S(m_Z)$, arXiv:2402.13864. xvii, 69, 70, 92, 130

[24] C. Andres, F. Dominguez, R. Kunnawalkam Elayavalli, J. Holguin, C. Marquet, and I. Moult, *Resolving the scales of the quark-gluon plasma with energy correlators*, arXiv:2209.11236. xix, 55, 98, 99, 106

[25] Z. Yang, Y. He, I. Moult, and X.-N. Wang, *Probing the Short-Distance Structure of the Quark-Gluon Plasma with Energy Correlators*, arXiv:2310.01500. xix, 55, 98, 99, 106

[26] W. Busza and K. e. Rajagopal, *Heavy Ion Collisions: The Big Picture, and the Big Questions*, *Ann. Rev. Nucl. Part. Sci.* **68** (2018) 339–376, [arXiv:1802.04801]. xxi, 14, 113

[27] **ALICE** Collaboration, *The ALICE experiment – A journey through QCD*, arXiv:2211.04384. xxi, 15, 114

[28] **ALICE** Collaboration, *Centrality determination in heavy ion collisions*, . xxi, 114

[29] D. d'Enterria, *Jet quenching*, *Landolt-Bornstein* **23** (2010) 471, [arXiv:0902.2011]. xxvi, 24, 38, 39

[30] A. Pais, *Inward Bound: Of Matter and Forces in the Physical World*. Oxford University Press, New York, 1986. 1

[31] M. E. Peskin and D. V. Schroeder, *An Introduction to Quantum Field Theory*. Westview Press, 1995. Reading, USA: Addison-Wesley (1995) 842 p. 5, 6, 7, 31, 51

[32] P. A. M. Dirac, *The quantum theory of the emission and absorption of radiation*, *Proceedings of the Royal Society of London. Series A, Containing Papers of a Mathematical and Physical Character* **114** (1927), no. 767 243–265. 5

[33] J. A. Wheeler, *On the mathematical description of light nuclei by the method of resonating group structure*, *Phys. Rev.* **52** (Dec, 1937) 1107–1122. 5

[34] K. G. Wilson, *The renormalization group and critical phenomena*, *Rev. Mod. Phys.* **55** (Jul, 1983) 583–600. 5

[35] A. A. Migdal, *Zh. eksp. teor. fiz.*, *Zh. Eksp. Teor. Fiz.* **69** (1975) 1457. 5

[36] A. A. Migdal, *Zh. eksp. teor. fiz.*, *Zh. Eksp. Teor. Fiz.* **69** (1975) 810. 5

[37] L. P. Kadanoff, *Ann. phys. (n.y.)*, *Ann. Phys. (N.Y.)* **100** (1976) 359. 5

[38] A. V. Manohar and M. B. Wise, *Heavy quark physics*, vol. 10. 2000. 6

[39] S. Scherer, *Introduction to chiral perturbation theory*, *Adv. Nucl. Phys.* **27** (2003) 277, [hep-ph/0210398]. 6

[40] T. Becher, A. Broggio, and A. Ferroglia, *Introduction to Soft-Collinear Effective Theory*, vol. 896. Springer, 2015. 6

[41] A. V. Manohar, *Effective field theories*, *Lect. Notes Phys.* **479** (1997) 311–362, [hep-ph/9606222]. 6

[42] D. J. Gross and F. Wilczek, *Ultraviolet behavior of non-abelian gauge theories*, *Phys. Rev. Lett.* **30** (Jun, 1973) 1343–1346. 8

[43] C. Bender and S. Orszag, *Advanced Mathematical Methods for Scientists and Engineers: Asymptotic Methods and Perturbation Theory*, vol. 1. 01, 1999. 9

[44] A. J. Larkoski, *Improving the Understanding of Jet Grooming in Perturbation Theory*, arXiv:2006.14680. 10, 34

[45] S. Marzani, G. Soyez, and M. Spannowsky, *Looking inside jets: an introduction to jet substructure and boosted-object phenomenology*, vol. 958. Springer, 2019. 10

[46] J. C. Collins and D. E. Soper, *Parton Distribution and Decay Functions*, *Nucl. Phys. B* **194** (1982) 445–492. 10

[47] G. F. Sterman, *Perturbative quantum field theory*, *Int. J. Mod. Phys. A* **16** (2001) 3041–3066, [hep-ph/0012237]. 10

[48] P. Skands, *Introduction to QCD*, in *Theoretical Advanced Study Institute in Elementary Particle Physics: Searching for New Physics at Small and Large Scales*, pp. 341–420, 2013. arXiv:1207.2389. 11

[49] J. J. Ethier and E. R. Nocera, *Parton Distributions in Nucleons and Nuclei*, *Ann. Rev. Nucl. Part. Sci.* **70** (2020) 43–76, [arXiv:2001.07722]. 11

[50] A. Metz and A. Vossen, *Parton Fragmentation Functions*, *Prog. Part. Nucl. Phys.* **91** (2016) 136–202, [arXiv:1607.02521]. 11

[51] **ALICE** Collaboration, S. Acharya et al., *Measurement of the fraction of jet longitudinal momentum carried by $\Lambda c+$ baryons in pp collisions*, *Phys. Rev. D* **109** (2024), no. 7 072005, [arXiv:2301.13798]. 11, 24

[52] G. Altarelli and G. Parisi, *Asymptotic Freedom in Parton Language*, *Nucl. Phys. B* **126** (1977) 298–318. 11, 29

[53] V. N. Gribov and L. N. Lipatov, *Deep inelastic e p scattering in perturbation theory*, *Sov. J. Nucl. Phys.* **15** (1972) 438–450. 11, 29

[54] Y. L. Dokshitzer, *Calculation of the Structure Functions for Deep Inelastic Scattering and e+ e- Annihilation by Perturbation Theory in Quantum Chromodynamics.*, *Sov. Phys. JETP* **46** (1977) 641–653. 11, 29

[55] K. G. Wilson, *Confinement of quarks*, *Phys. Rev. D* **10** (Oct, 1974) 2445–2459. 11

[56] B. M. McCoy, *The Connection between statistical mechanics and quantum field theory*, in *7th Physics Summer School on Statistical Mechanics and Field Theory*, pp. 26–128, 3, 1994. hep-th/9403084. 12

[57] R. Gupta, *Introduction to lattice QCD: Course*, in *Les Houches Summer School in Theoretical Physics, Session 68: Probing the Standard Model of Particle Interactions*, pp. 83–219, 7, 1997. hep-lat/9807028. 12, 14

[58] J. M. Maldacena, *The Large N limit of superconformal field theories and supergravity*, *Adv. Theor. Math. Phys.* **2** (1998) 231–252, [hep-th/9711200]. 12, 41, 100

[59] J. Casalderrey-Solana, H. Liu, D. Mateos, K. Rajagopal, and U. A. Wiedemann, *Gauge/String Duality, Hot QCD and Heavy Ion Collisions*. Cambridge University Press, 2014. 13

[60] J. C. Collins and M. J. Perry, *Superdense matter: Neutrons or asymptotically free quarks?*, *Phys. Rev. Lett.* **34** (May, 1975) 1353–1356. 14

[61] **PHENIX** Collaboration, K. Adcox et al., *Formation of dense partonic matter in relativistic nucleus-nucleus collisions at RHIC: Experimental evaluation by the PHENIX collaboration*, *Nucl. Phys. A* **757** (2005) 184–283, [nucl-ex/0410003]. 14

[62] **BRAHMS** Collaboration, I. Arsene et al., *Quark gluon plasma and color glass condensate at RHIC? The Perspective from the BRAHMS experiment*, *Nucl. Phys. A* **757** (2005) 1–27, [nucl-ex/0410020]. 14

[63] **PHOBOS** Collaboration, B. B. Back et al., *The PHOBOS perspective on discoveries at RHIC*, *Nucl. Phys. A* **757** (2005) 28–101, [nucl-ex/0410022]. 14

[64] **STAR** Collaboration, J. Adams et al., *Experimental and theoretical challenges in the search for the quark gluon plasma: The STAR Collaboration's critical assessment of the evidence from RHIC collisions*, *Nucl. Phys. A* **757** (2005) 102–183, [nucl-ex/0501009]. 14

[65] M. Gyulassy and L. McLerran, *New forms of QCD matter discovered at RHIC*, *Nucl. Phys. A* **750** (2005) 30–63, [nucl-th/0405013]. 14

[66] P. Koch and B. Muller, *Strangeness in Relativistic Heavy Ion Collisions*, *Phys. Rept.* **142** (1986) 167–262. 15

[67] A. Collaboration, *Enhanced production of multi-strange hadrons in high-multiplicity proton–proton collisions*, *Nature Physics* **13** (2017), no. 6 535–539. 15

[68] T. Matsui and H. Satz, *J/psi suppression by quark-gluon plasma formation*, *Phys. Lett. B* **178** (1986), no. 4 416–422. 15

[69] J. D. Bjorken, *Energy Loss of Energetic Partons in Quark - Gluon Plasma: Possible Extinction of High p(t) Jets in Hadron - Hadron Collisions*, . 15, 38, 39

[70] J. W. Harris and B. Müller, *"QGP Signatures" Revisited*, arXiv:2308.05743. 15

[71] A. Bialas, M. Bleszynski, and W. Czyz, *Relation Between the Glauber Model and Classical Probability Calculus*, *Acta Phys. Polon. B* **8** (1977) 389–392. 16

[72] M. L. Miller, K. Reygers, S. J. Sanders, and P. Steinberg, *Glauber modeling in high energy nuclear collisions*, *Annual Review of Nuclear and Particle Science* **57** (2007) 205–243. 16, 114

[73] E. Iancu and R. Venugopalan, *The Color glass condensate and high-energy scattering in QCD*, pp. 249–3363. 3, 2003. hep-ph/0303204. 16

[74] A. Kurkela, A. Mazeliauskas, J.-F. Paquet, S. Schlichting, and D. Teaney, *Effective kinetic description of event-by-event pre-equilibrium dynamics in*

*high-energy heavy-ion collisions*, *Phys. Rev. C* **99** (2019), no. 3 034910, [arXiv:1805.00961]. 17

[75] B. Schenke, P. Tribedy, and R. Venugopalan, *Fluctuating glasma initial conditions and flow in heavy ion collisions*, *Phys. Rev. Lett.* **108** (Jun, 2012) 252301. 17

[76] W. Florkowski, M. P. Heller, and M. Spaliński, *New theories of relativistic hydrodynamics in the lhc era*, *Reports on Progress in Physics* **81** (feb, 2018) 046001. 17

[77] P. Romatschke, *Relativistic fluid dynamics far from local equilibrium*, *Phys. Rev. Lett.* **120** (Jan, 2018) 012301. 17

[78] P. Romatschke, *Do nuclear collisions create a locally equilibrated quark–gluon plasma?*, *The European Physical Journal C* **77** (2017) 21. 17

[79] B. Schenke, S. Jeon, and C. Gale, *Elliptic and triangular flow in event-by-event (3+1)D viscous hydrodynamics*, *Phys. Rev. Lett.* **106** (2011) 042301, [arXiv:1009.3244]. 17

[80] C. Shen, Z. Qiu, H. Song, J. Bernhard, S. Bass, and U. Heinz, *The iEBE-VISHNU code package for relativistic heavy-ion collisions*, *Comput. Phys. Commun.* **199** (2016) 61–85, [arXiv:1409.8164]. 17, 100

[81] L.-G. Pang, H. Petersen, and X.-N. Wang, *Pseudorapidity distribution and decorrelation of anisotropic flow within the open-computing-language implementation CLVisc hydrodynamics*, *Phys. Rev. C* **97** (2018), no. 6 064918, [arXiv:1802.04449]. 17

[82] Z.-W. Lin, C. M. Ko, B.-A. Li, B. Zhang, and S. Pal, *A Multi-phase transport model for relativistic heavy ion collisions*, *Phys. Rev. C* **72** (2005) 064901, [nucl-th/0411110]. 17

[83] Z. Xu and C. Greiner, *Thermalization of gluons in ultrarelativistic heavy ion collisions by including three-body interactions in a parton cascade*, *Phys. Rev. C* **71** (Jun, 2005) 064901. 17

[84] Z.-W. Lin, C. M. Ko, B.-A. Li, B. Zhang, and S. Pal, *Multiphase transport model for relativistic heavy ion collisions*, *Phys. Rev. C* **72** (Dec, 2005) 064901. 17

[85] W. Cassing and E. Bratkovskaya, *Parton–hadron–string dynamics: An off-shell transport approach for relativistic energies*, *Nuclear Physics A* **831** (2009), no. 3 215–242. 17

[86] F. Cooper and G. Frye, *Single-particle distribution in the hydrodynamic and statistical thermodynamic models of multiparticle production*, *Phys. Rev. D* **10** (Jul, 1974) 186–189. 18

[87] A. Andronic, P. Braun-Munzinger, K. Redlich, et al., *Decoding the phase structure of qcd via particle production at high energy*, *Nature* **561** (2018), no. 7723 321–330. 18

[88] E. Fermi, *High-energy nuclear events*, *Prog. Theor. Phys.* **5** (1950) 570–583. 18

[89] S. Z. Belenkij and L. D. Landau, *Hydrodynamic theory of multiple production of particles*, *Usp. Fiz. Nauk* **56** (1955) 309. 18

[90] R. Hagedorn, *Statistical thermodynamics of strong interactions at high-energies*, *Nuovo Cim. Suppl.* **3** (1965) 147–186. 18

[91] R. Sharma, F. A. Flor, S. Behera, C. Jena, and H. Caines, *Flavour-Dependent Chemical Freeze-Out of Light Nuclei in Relativistic Heavy-Ion Collisions*, arXiv:2412.20517. 18

[92] S. Voloshin and Y. Zhang, *Flow study in relativistic nuclear collisions by Fourier expansion of Azimuthal particle distributions*, *Z. Phys. C* **70** (1996) 665–672, [hep-ph/9407282]. 21

[93] R. Snellings, *Elliptic Flow: A Brief Review*, *New J. Phys.* **13** (2011) 055008, [arXiv:1102.3010]. 21

[94] J. F. Grosse-Oetringhaus and U. A. Wiedemann, *A Decade of Collectivity in Small Systems*, arXiv:2407.07484. 22

[95] J. L. Nagle and W. A. Zajc, *Small System Collectivity in Relativistic Hadronic and Nuclear Collisions*, *Ann. Rev. Nucl. Part. Sci.* **68** (2018) 211–235, [arXiv:1801.03477]. 22

[96] U. Heinz and R. Snellings, *Collective flow and viscosity in relativistic heavy-ion collisions*, *Ann. Rev. Nucl. Part. Sci.* **63** (2013) 123–151, [arXiv:1301.2826]. 22

[97] **PHOBOS** Collaboration, B. Alver et al., *System size dependence of cluster properties from two-particle angular correlations in Cu+Cu and Au+Au collisions at s(NN)**(1/2) = 200-GeV*, *Phys. Rev. C* **81** (2010) 024904, [arXiv:0812.1172]. 22

[98] M. Asakawa and M. Kitazawa, *Fluctuations of conserved charges in relativistic heavy ion collisions: An introduction*, *Prog. Part. Nucl. Phys.* **90** (2016) 299–342, [arXiv:1512.05038]. 22

[99] **ALICE** Collaboration, S. Acharya et al., *Underlying Event properties in pp collisions at $\sqrt{s}$ = 13 TeV*, *JHEP* **04** (2020) 192, [arXiv:1910.14400]. 22

[100] **STAR** Collaboration, J. Adam et al., *Underlying event measurements in $p+p$ collisions at $\sqrt{s}$ = 200 GeV at RHIC*, *Phys. Rev. D* **101** (2020), no. 5 052004, [arXiv:1912.08187]. 22

[101] F. Geurts and R.-A. Tripolt, *Electromagnetic probes: Theory and experiment*, *Prog. Part. Nucl. Phys.* **128** (2023) 104004, [arXiv:2210.01622]. 23

[102] **CMS** Collaboration, A. M. Sirunyan et al., *Observation of nuclear modifications in $W^{\pm}$ boson production in pPb collisions at $\sqrt{s_{\mathrm{NN}}}$ = 8.16 TeV*, *Phys. Lett. B* **800** (2020) 135048, [arXiv:1905.01486]. 23

[103] R. Rapp and H. van Hees, *Heavy Quarks in the Quark-Gluon Plasma*, pp. 111–206, 2010. arXiv:0903.1096. 24

[104] B. Svetitsky, *Diffusion of charmed quarks in the quark-gluon plasma*, *Phys. Rev. D* **37** (May, 1988) 2484–2491. 24

[105] M. He, H. van Hees, and R. Rapp, *Heavy-quark diffusion in the quark–gluon plasma*, *Progress in Particle and Nuclear Physics* **130** (2023) 104020. 24

[106] A. Andronic et al., *Heavy-flavour and quarkonium production in the LHC era: from proton–proton to heavy-ion collisions*, *Eur. Phys. J. C* **76** (2016), no. 3 107, [arXiv:1506.03981]. 24

[107] **CMS** Collaboration, A. M. Sirunyan et al., *Measurement of nuclear modification factors of $\Upsilon$(1S), $\Upsilon$(2S), and $\Upsilon$(3S) mesons in PbPb collisions at $\sqrt{s_{\mathrm{NN}}}$ = 5.02 TeV*, *Phys. Lett. B* **790** (2019) 270–293, [arXiv:1805.09215]. 24

[108] L. Apolinário, Y.-J. Lee, and M. Winn, *Heavy quarks and jets as probes of the QGP*, arXiv:2203.16352. 24

[109] **H1** Collaboration, V. Andreev et al., *Measurement of Jet Production Cross Sections in Deep-inelastic ep Scattering at HERA*, *Eur. Phys. J. C* **77** (2017), no. 4 215, [arXiv:1611.03421]. [Erratum: Eur.Phys.J.C 81, 739 (2021)]. 27

[110] **CMS** Collaboration, *Measurement and QCD analysis of double-differential inclusive jet cross sections in pp collisions at* $\sqrt{s} = 13$TeV, tech. rep., CERN, Geneva, 2021. 27

[111] **ATLAS** Collaboration, M. Aaboud et al., *Measurement of inclusive jet and dijet cross-sections in proton-proton collisions at* $\sqrt{s} = 13$ *TeV with the ATLAS detector*, *JHEP* **05** (2018) 195, [arXiv:1711.02692]. 27

[112] J. Campbell, J. Huston, and F. Krauss, *The Black Book of Quantum Chromodynamics : a Primer for the LHC Era*. Oxford University Press, 2018. 28

[113] J. C. Collins, D. E. Soper, and G. F. Sterman, *Factorization of Hard Processes in QCD*, *Adv. Ser. Direct. High Energy Phys.* **5** (1989) 1–91, [hep-ph/0409313]. 29

[114] J. Campbell and E. Glover, *Double unresolved approximations to multiparton scattering amplitudes*, *Nuclear Physics B* **527** (Aug., 1998) 264–288. 29

[115] S. Catani and M. Grazzini, *Infrared factorization of tree-level qcd amplitudes at the next-to-next-to-leading order and beyond*, *Nuclear Physics B* **570** (Mar., 2000) 287–325. 29

[116] F. A. Dreyer, G. P. Salam, and G. Soyez, *The Lund Jet Plane*, *JHEP* **12** (2018) 064, [arXiv:1807.04758]. 31

[117] G. P. Salam, *Towards Jetography*, *Eur. Phys. J. C* **67** (2010) 637–686, [arXiv:0906.1833]. 31, 35, 36

[118] A. Lifson, G. P. Salam, and G. Soyez, *Calculating the primary Lund Jet Plane density*, arXiv:2007.06578. 31

[119] **ALICE** Collaboration, *Physics Preliminary Summary: Measurement of the primary Lund plane density in pp collisions at $\sqrt{s} = 13$ TeV with ALICE*, . 31

[120] **ATLAS** Collaboration, G. Aad et al., *Measurement of the Lund Jet Plane Using Charged Particles in 13 TeV Proton-Proton Collisions with the ATLAS Detector*, *Phys. Rev. Lett.* **124** (2020), no. 22 222002, [arXiv:2004.03540]. 32

[121] S. Höche, *Introduction to parton-shower event generators*, in *Theoretical Advanced Study Institute in Elementary Particle Physics: Journeys Through the Precision Frontier: Amplitudes for Colliders*, pp. 235–295, 2015. arXiv:1411.4085. 33

[122] T. Sjostrand, S. Mrenna, and P. Z. Skands, *A Brief Introduction to PYTHIA 8.1*, *Comput. Phys. Commun.* **178** (2008) 852–867, [arXiv:0710.3820]. 33, 100

[123] M. Bahr et al., *Herwig++ Physics and Manual*, *Eur. Phys. J. C* **58** (2008) 639–707, [arXiv:0803.0883]. 33, 136

[124] P. Bartalini et al., *Multi-Parton Interactions at the LHC*, 11, 2011. arXiv:1111.0469. 34

[125] H.-M. Chang, M. Procura, J. Thaler, and W. J. Waalewijn, *Calculating Track-Based Observables for the LHC*, *Phys. Rev. Lett.* **111** (2013) 102002, [arXiv:1303.6637]. 35

[126] M. Cacciari and G. P. Salam *et al.*, *Dispelling the $N^3$ myth for the $k_t$ jet-finder*, *Phys. Lett. B* **641** (2006) 57–61, [hep-ph/0512210]. 36

[127] M. Cacciari and G. P. Salam *et al.*, *The anti-$k_t$ jet clustering algorithm*, *JHEP* **04** (2008) 063, [arXiv:0802.1189]. 36

[128] S. Chekanov, *Jet algorithms: A mini-review*, in *Hadron Collider Physics 2002* (M. Erdmann and T. Müller, eds.). Springer, Berlin, Heidelberg, 2003. 36

[129] M. Cacciari and G. P. Salam *et al.*, *FastJet User Manual*, *Eur. Phys. J. C* **72** (2012) 1896, [arXiv:1111.6097]. 36, 74, 115, 116

[130] M. Dasgupta, L. Magnea, and G. P. Salam, *Non-perturbative QCD effects in jets at hadron colliders*, *JHEP* **02** (2008) 055, [arXiv:0712.3014]. 37

[131] A. Banfi, *Hadronic Jets: An Introduction*, . 37

[132] **CMS** Collaboration, A. M. Sirunyan et al., *Dependence of inclusive jet production on the anti-$k_T$ distance parameter in pp collisions at $\sqrt{s}$ = 13 TeV*, *JHEP* **12** (2020) 082, [arXiv:2005.05159]. 38

[133] T. C. Collaboration, V. Khachatryan, A. M. Sirunyan, et al., *Measurement of transverse momentum relative to dijet systems in pbpb and pp collisions at $\sqrt{s_{\mathrm{NN}}} = 5.02$ tev*, *J. High Energ. Phys.* **2016** (2016), no. 6 6. Received: 30 September 2015, Accepted: 16 December 2015, Published: 04 January 2016. 38

[134] **CMS** Collaboration, A. M. Sirunyan et al., *Using Z Boson Events to Study Parton-Medium Interactions in Pb-Pb Collisions*, *Phys. Rev. Lett.* **128** (2022), no. 12 122301, [arXiv:2103.04377]. 38

[135] L. Cunqueiro and A. M. Sickles, *Studying the QGP with Jets at the LHC and RHIC*, *Prog. Part. Nucl. Phys.* **124** (2022) 103940, [arXiv:2110.14490]. 39

[136] M. Connors, C. Nattrass, R. Reed, and S. Salur, *Jet measurements in heavy ion physics*, *Rev. Mod. Phys.* **90** (2018) 025005, [arXiv:1705.01974]. 39

[137] R. Baier, Y. L. Dokshitzer, A. H. Mueller, S. Peigne, and D. Schiff, *Radiative energy loss of high-energy quarks and gluons in a finite volume quark - gluon plasma*, *Nucl. Phys. B* **483** (1997) 291–320, [hep-ph/9607355]. 40

[138] B. G. Zakharov, *Fully quantum treatment of the Landau-Pomeranchuk-Migdal effect in QED and QCD*, *JETP Lett.* **63** (1996) 952–957, [hep-ph/9607440]. 40

[139] M. Gyulassy, P. Levai, and I. Vitev, *NonAbelian energy loss at finite opacity*, *Phys. Rev. Lett.* **85** (2000) 5535–5538, [nucl-th/0005032]. 40

[140] N. Armesto, C. A. Salgado, and U. A. Wiedemann, *Medium induced gluon radiation off massive quarks fills the dead cone*, *Phys. Rev. D* **69** (2004) 114003, [hep-ph/0312106]. 40

[141] P. B. Arnold, G. D. Moore, and L. G. Yaffe, *Photon emission from ultrarelativistic plasmas*, *JHEP* **11** (2001) 057, [hep-ph/0109064]. 40

[142] X.-N. Wang and X.-f. Guo, *Multiple parton scattering in nuclei: Parton energy loss*, *Nucl. Phys. A* **696** (2001) 788–832, [hep-ph/0102230]. 40

[143] J. Casalderrey-Solana, D. C. Gulhan, J. G. Milhano, D. Pablos, and K. Rajagopal, *A Hybrid Strong/Weak Coupling Approach to Jet Quenching*, *JHEP* **10** (2014) 019, [arXiv:1405.3864]. [Erratum: JHEP 09, 175 (2015)]. 40, 41, 100, 108

[144] **STAR** Collaboration, J. Adam et al., *Measurement of inclusive charged-particle jet production in Au + Au collisions at* $\sqrt{s_{NN}}$ *=200 GeV*, *Phys. Rev. C* **102** (2020), no. 5 054913, [arXiv:2006.00582]. 40

[145] **ALICE** Collaboration, S. Acharya et al., *Measurements of inclusive jet spectra in pp and central Pb-Pb collisions at* $\sqrt{s_{\rm NN}}$ *= 5.02 TeV*, *Phys. Rev. C* **101** (2020), no. 3 034911, [arXiv:1909.09718]. 40

[146] **ATLAS** Collaboration, M. Aaboud et al., *Measurement of the nuclear modification factor for inclusive jets in Pb+Pb collisions at* $\sqrt{s_{\rm NN}} = 5.02$ *TeV with the ATLAS detector*, *Phys. Lett. B* **790** (2019) 108–128, [arXiv:1805.05635]. 40

[147] **CMS** Collaboration, V. Khachatryan et al., *Measurement of inclusive jet cross sections in pp and PbPb collisions at* $\sqrt{s_{NN}}$ *= 2.76 TeV*, *Phys. Rev. C* **96** (2017), no. 1 015202, [arXiv:1609.05383]. 40

[148] **ATLAS** Collaboration, G. Aad et al., *Measurements of the Nuclear Modification Factor for Jets in Pb+Pb Collisions at* $\sqrt{s_{\rm NN}} = 2.76$ *TeV with the ATLAS Detector*, *Phys. Rev. Lett.* **114** (2015), no. 7 072302, [arXiv:1411.2357]. 40

[149] **ALICE** Collaboration, J. Adam et al., *Measurement of jet suppression in central Pb-Pb collisions at* $\sqrt{s_{\rm NN}}$ *= 2.76 TeV*, *Phys. Lett. B* **746** (2015) 1–14, [arXiv:1502.01689]. 40

[150] **ALICE** Collaboration, S. Acharya et al., *Measurement of the radius dependence of charged-particle jet suppression in Pb–Pb collisions at sNN=5.02TeV*, *Phys. Lett. B* **849** (2024) 138412, [arXiv:2303.00592]. 40

[151] F. D'Eramo, K. Rajagopal, and Y. Yin, *Molière scattering in quark-gluon plasma: finding point-like scatterers in a liquid*, *JHEP* **01** (2019) 172, [arXiv:1808.03250]. 40

[152] J. a. Barata, Y. Mehtar-Tani, A. Soto-Ontoso, and K. Tywoniuk, *Revisiting transverse momentum broadening in dense QCD media*, *Phys. Rev. D* **104** (2021), no. 5 054047, [arXiv:2009.13667]. 40

[153] **STAR** Collaboration, D. Anderson, *Measurement of Medium-induced Modification of Jet Yield and Acoplanarity Using Semi-inclusive $\gamma_{\rm dir}$+jet and $\pi^0$+jet Distributions in $p+p$ and Central Au+Au Collisions at $\sqrt{s_{NN}} = 200$ GeV by STAR*, *Acta Phys. Polon. Supp.* **16** (2023), no. 1 1–A55, [arXiv:2212.09202]. 40

[154] **ALICE** Collaboration, S. Acharya et al., *Observation of Medium-Induced Yield Enhancement and Acoplanarity Broadening of Low-pT Jets from Measurements in pp and Central Pb-Pb Collisions at sNN=5.02 TeV*, *Phys. Rev. Lett.* **133** (2024), no. 2 022301, [arXiv:2308.16131]. 40

[155] F. D'Eramo, M. Lekaveckas, H. Liu, and K. Rajagopal, *Momentum Broadening in Weakly Coupled Quark-Gluon Plasma (with a view to finding the quasiparticles within liquid quark-gluon plasma)*, *JHEP* **05** (2013) 031, [arXiv:1211.1922]. 40

[156] J. Casalderrey-Solana, Y. Mehtar-Tani, C. A. Salgado, and K. Tywoniuk, *New picture of jet quenching dictated by color coherence*, *Phys. Lett. B* **725** (2013) 357–360, [arXiv:1210.7765]. 41

[157] K. C. Zapp, *JEWEL 2.0.0: directions for use*, *Eur. Phys. J. C* **74** (2014), no. 2 2762, [arXiv:1311.0048]. 41

[158] K. C. Zapp, F. Krauss, and U. A. Wiedemann, *A perturbative framework for jet quenching*, *JHEP* **03** (2013) 080, [arXiv:1212.1599]. 41

[159] J. H. Putschke et al., *The JETSCAPE framework*, arXiv:1903.07706. 41

[160] Y. He, T. Luo, X.-N. Wang, and Y. Zhu, *Linear Boltzmann Transport for Jet Propagation in the Quark-Gluon Plasma: Elastic Processes and Medium Recoil*, *Phys. Rev. C* **91** (2015) 054908, [arXiv:1503.03313]. [Erratum: Phys.Rev.C 97, 019902 (2018)]. 41

[161] **H1** Collaboration, T. Ahmed et al., *Determination of the strong coupling constant from jet rates in deep inelastic scattering*, *Phys. Lett. B* **346** (1995) 415–425. 42

[162] H.-M. Chang, M. Procura, J. Thaler, and W. J. Waalewijn, *Calculating track-based observables for the lhc*, *Phys. Rev. Lett.* **111** (Sep, 2013) 102002. 43

[163] H. Chen, I. Moult, X. Zhang, and H. X. Zhu, *Rethinking jets with energy correlators: Tracks, resummation, and analytic continuation*, *Phys. Rev. D* **102** (Sep, 2020) 054012. 43

[164] M. Jaarsma, Y. Li, I. Moult, et al., *Renormalization group flows for track function moments*, *J. High Energ. Phys.* **2022** (2022) 139. 43

[165] T. Renk, *Biased showers: A common conceptual framework for the interpretation of high-$P_T$ observables in heavy-ion collisions*, *Phys. Rev. C* **88** (Nov, 2013) 054902. 44

[166] J. Brewer, Q. Brodsky, and K. Rajagopal, *Disentangling jet modification in jet simulations and in z+jet data*, *J. High Energ. Phys.* **2022** (2022) 175. 44

[167] M. Dasgupta, A. Fregoso, S. Marzani, and G. P. Salam, *Towards an understanding of jet substructure*, *JHEP* **09** (2013) 029, [arXiv:1307.0007]. 44

[168] A. J. Larkoski, S. Marzani, G. Soyez, and J. Thaler, *Soft Drop*, *JHEP* **05** (2014) 146, [arXiv:1402.2657]. 44

[169] Y. Mehtar-Tani, A. Soto-Ontoso, and K. Tywoniuk, *Dynamical grooming of QCD jets*, *Phys. Rev. D* **101** (2020), no. 3 034004, [arXiv:1911.00375]. 44

[170] **ATLAS** Collaboration, G. Aad et al., *Search for the jet-induced diffusion wake in the quark-gluon plasma via measurements of jet-track correlations in photon-jet events in Pb+Pb collisions at* $\sqrt{s_{NN}}$ *= 5.02 TeV with the ATLAS detector*, arXiv:2408.08599. 45

[171] **CMS** Collaboration, *Evidence of the medium response with Z-hadron correlations in PbPb and pp collisions at sqrt(sNN) = 5.02 TeV*, . 46

[172] N. Sveshnikov and F. Tkachov, *Jets and quantum field theory*, *Phys. Lett. B* **382** (1996) 403–408, [hep-ph/9512370]. 48

[173] F. V. Tkachov, *Measuring multi - jet structure of hadronic energy flow or What is a jet?*, *Int. J. Mod. Phys. A* **12** (1997) 5411–5529, [hep-ph/9601308]. 48

[174] G. P. Korchemsky and G. F. Sterman, *Power corrections to event shapes and factorization*, *Nucl. Phys. B* **555** (1999) 335–351, [hep-ph/9902341]. 48

[175] C. W. Bauer, S. P. Fleming, C. Lee, and G. F. Sterman, *Factorization of e+e- Event Shape Distributions with Hadronic Final States in Soft Collinear Effective Theory*, *Phys. Rev. D* **78** (2008) 034027, [arXiv:0801.4569]. 48

[176] D. M. Hofman and J. Maldacena, *Conformal collider physics: Energy and charge correlations*, *JHEP* **05** (2008) 012, [arXiv:0803.1467]. 48, 50

[177] A. Belitsky, S. Hohenegger, G. Korchemsky, E. Sokatchev, and A. Zhiboedov, *From correlation functions to event shapes*, *Nucl. Phys. B* **884** (2014) 305–343, [arXiv:1309.0769]. 48

[178] A. Belitsky, S. Hohenegger, G. Korchemsky, E. Sokatchev, and A. Zhiboedov, *Event shapes in $\mathcal{N} = 4$ super-Yang-Mills theory*, *Nucl. Phys. B* **884** (2014) 206–256, [arXiv:1309.1424]. 48

[179] P. Kravchuk and D. Simmons-Duffin, *Light-ray operators in conformal field theory*, *JHEP* **11** (2018) 102, [arXiv:1805.00098]. 48, 49

[180] C. Basham, L. S. Brown, S. D. Ellis, and S. T. Love, *Energy Correlations in electron - Positron Annihilation: Testing QCD*, *Phys. Rev. Lett.* **41** (1978) 1585. 48

[181] C. L. Basham, L. S. Brown, S. D. Ellis, and S. T. Love, *Electron - Positron Annihilation Energy Pattern in Quantum Chromodynamics: Asymptotically Free Perturbation Theory*, *Phys. Rev. D* **17** (1978) 2298. 48

[182] R. K. Ellis, H. Georgi, M. Machacek, H. D. Politzer, and G. G. Ross, *Perturbation Theory and the Parton Model in QCD*, *Nucl. Phys. B* **152** (1979) 285–329. 48

[183] C. L. Basham, L. S. Brown, S. D. Ellis, and S. T. Love, *Energy Correlations in Perturbative Quantum Chromodynamics: A Conjecture for All Orders*, *Phys. Lett. B* **85** (1979) 297–299. 48

[184] C. Basham, L. Brown, S. Ellis, and S. Love, *Energy Correlations in electron-Positron Annihilation in Quantum Chromodynamics: Asymptotically Free Perturbation Theory*, *Phys. Rev. D* **19** (1979) 2018. 48

[185] M. Kologlu and P. Kravchuk *et al.*, *The light-ray OPE and conformal colliders*, *JHEP* **01** (2021) 128, [arXiv:1905.01311]. 49

[186] S. A. Larin, P. Nogueira, T. van Ritbergen, and J. A. M. Vermaseren, *The Three loop QCD calculation of the moments of deep inelastic structure functions*, *Nucl. Phys. B* **492** (1997) 338–378, [hep-ph/9605317]. 51

[187] A. D. Martin, *Proton structure, Partons, QCD, DGLAP and beyond*, *Acta Phys. Polon. B* **39** (2008) 2025–2062, [arXiv:0802.0161]. 51

[188] H. Chen, I. Moult, X. Zhang, and H. X. Zhu, *Rethinking jets with energy correlators: Tracks, resummation, and analytic continuation*, *Phys. Rev. D* **102** (2020), no. 5 054012, [arXiv:2004.11381]. 52, 54, 95

[189] L. J. Dixon, M.-X. Luo, V. Shtabovenko, T.-Z. Yang, and H. X. Zhu, *Analytical Computation of Energy-Energy Correlation at Next-to-Leading Order in QCD*, *Phys. Rev. Lett.* **120** (2018), no. 10 102001, [arXiv:1801.03219]. 52

[190] M.-X. Luo, V. Shtabovenko, T.-Z. Yang, and H. X. Zhu, *Analytic Next-To-Leading Order Calculation of Energy-Energy Correlation in Gluon-Initiated Higgs Decays*, *JHEP* **06** (2019) 037, [arXiv:1903.07277]. 52

[191] A. Belitsky, S. Hohenegger, G. Korchemsky, E. Sokatchev, and A. Zhiboedov, *Energy-Energy Correlations in N=4 Supersymmetric Yang-Mills Theory*, *Phys. Rev. Lett.* **112** (2014), no. 7 071601, [arXiv:1311.6800]. 52

[192] J. Henn, E. Sokatchev, K. Yan, and A. Zhiboedov, *Energy-energy correlation in N=4 super Yang-Mills theory at next-to-next-to-leading order*, *Phys. Rev. D* **100** (2019), no. 3 036010, [arXiv:1903.05314]. 52

[193] H. Chen, M.-X. Luo, I. Moult, T.-Z. Yang, X. Zhang, and H. X. Zhu, *Three point energy correlators in the collinear limit: symmetries, dualities and analytic results*, *JHEP* **08** (2020), no. 08 028, [arXiv:1912.11050]. 52, 55

[194] K. Yan and X. Zhang, *Three-point energy correlator in $\mathcal{N} = 4$ super Yang-Mills Theory*, arXiv:2203.04349. 52

[195] T.-Z. Yang and X. Zhang, *Analytic Computation of three-point energy correlator in QCD*, *JHEP* **09** (2022) 006, [arXiv:2208.01051]. 52

[196] T.-Z. Yang and X. Zhang, *Three-point energy correlators in hadronic Higgs boson decays*, *Phys. Rev. D* **109** (2024), no. 11 114036, [arXiv:2402.05174]. 52

[197] K. Lee, B. Meçaj, and I. Moult, *Conformal collider physics meets LHC data*, *Phys. Rev. D* **111** (2025), no. 1 L011502, [arXiv:2205.03414]. 54

[198] K. Devereaux, W. Fan, W. Ke, K. Lee, and I. Moult, *Imaging Cold Nuclear Matter with Energy Correlators*, arXiv:2303.08143. 55

[199] X. Liu and H. X. Zhu, *Nucleon Energy Correlators*, *Phys. Rev. Lett.* **130** (2023), no. 9 091901, [arXiv:2209.02080]. 55

[200] K.-B. Chen, J.-P. Ma, and X.-B. Tong, *The connection between Nucleon Energy Correlators and Fracture Functions*, arXiv:2406.08559. 55

[201] H.-Y. Liu, X. Liu, J.-C. Pan, F. Yuan, and H. X. Zhu, *Nucleon Energy Correlators for the Color Glass Condensate*, *Phys. Rev. Lett.* **130** (2023), no. 18 181901, [arXiv:2301.01788]. 55

[202] C. Andres, F. Dominguez, J. Holguin, C. Marquet, and I. Moult, *A coherent view of the quark-gluon plasma from energy correlators*, *JHEP* **09** (2023) 088, [arXiv:2303.03413]. 55, 98, 106

[203] C. Andres, F. Dominguez, J. Holguin, C. Marquet, and I. Moult, *Towards an Interpretation of the First Measurements of Energy Correlators in the Quark-Gluon Plasma*, arXiv:2407.07936. 55, 98, 106

[204] C. Andres, F. Dominguez, J. Holguin, C. Marquet, and I. Moult, *Seeing beauty in the quark-gluon plasma with energy correlators*, *Phys. Rev. D* **110** (2024), no. 3 L031503, [arXiv:2307.15110]. 55, 98, 106

[205] E. Craft, K. Lee, B. Meçaj, and I. Moult, *Beautiful and Charming Energy Correlators*, arXiv:2210.09311. 55

[206] K. Lee and I. Moult, *Energy Correlators Taking Charge*, arXiv:2308.00746. 55, 69

[207] **CMS** Collaboration, V. Chekhovsky et al., *Observation of nuclear modification of energy-energy correlators inside jets in heavy ion collisions*, arXiv:2503.19993. 55, 99

[208] G. Apollinari, O. Brüning, T. Nakamoto, and L. Rossi, *High Luminosity Large Hadron Collider HL-LHC*, *CERN Yellow Rep.* (2015), no. 5 1–19, [arXiv:1705.08830]. 60

[209] S. van der Meer, *Calibration of the effective beam height in the ISR*, tech. rep., CERN, Geneva, 1968. 62

[210] CERN, *Lhc report: Protons on a mission accomplished*, 2024. Accessed: 2025-04-28. 62

[211] W. H. Trzaska, *New alice detectors for run 3 and 4 at the cern lhc*, *Nuclear Instruments and Methods in Physics Research Section A: Accelerators, Spectrometers, Detectors and Associated Equipment* **958** (2020) 162116. Proceedings of the Vienna Conference on Instrumentation 2019. 62

[212] **ALICE** Collaboration, K. e. Aamodt, *The ALICE experiment at the CERN LHC*, *JINST* **3** (2008) S08002. 63

[213] J. D. Cockcroft, *Experimental nuclear physics*, *Nature* **175** (1955) 53–54. 66

[214] **ALICE** Collaboration, Y. Belikov, K. Safarík, and B. Batyunya, *Kalman Filtering Application for Track Recognition and Reconstruction in ALICE Tracking System*, . 67

[215] **ALICE** Collaboration, S. Acharya et al., *Exposing the parton-hadron transition within jets with energy-energy correlators in pp collisions at* $\sqrt{s} = 5.02$ *TeV*, arXiv:2409.12687. 69, 76, 92, 135, 138

[216] **ALICE** Collaboration, S. Acharya et al., *Energy-energy correlators in charm-tagged jets in proton-proton collisions at* $\sqrt{\mathbf{s}} = \mathbf{13}$ *TeV*, arXiv:2504.03431. 69

[217] ALICE Collaboration, "Measurement of the charged-particle Energy-Energy Correlator in pp collisions at $\sqrt{s} = 13$ TeV." Poster presented at Quark Matter 2025, 2025. Quark Matter 2025, Boston, USA. 69

[218] K. Lee, A. Pathak, I. W. Stewart, and Z. Sun, *Nonperturbative Effects in Energy Correlators: From Characterizing Confinement Transition to Improving $\alpha s$ Extraction*, *Phys. Rev. Lett.* **133** (2024), no. 23 231902, [arXiv:2405.19396]. 70, 130, 140

[219] **ALICE** Collaboration, *ALICE 2016-2017-2018 luminosity determination for pp collisions at* $\sqrt{s} = 13$ *TeV*, . 71

[220] **ALICE** Collaboration, *ALICE 2017 luminosity determination for pp collisions at* $\sqrt{s} = 5$ *TeV*, . 71

[221] T. Sjöstrand, S. Ask, J. R. Christiansen, R. Corke, N. Desai, P. Ilten, S. Mrenna, S. Prestel, C. O. Rasmussen, and P. Z. Skands, *An introduction to PYTHIA 8.2*, *Comput. Phys. Commun.* **191** (2015) 159–177, [arXiv:1410.3012]. 73, 80, 95, 124, 136

[222] R. Brun, F. Bruyant, M. Maire, A. C. McPherson, and P. Zanarini, *GEANT 3: user's guide Geant 3.10, Geant 3.11; rev. version*. CERN, Geneva, 1987. 73, 80, 124

[223] T. A. Collaboration, K. Aamodt, A. A. Quintana, R. Achenbach, S. Acounis, D. Adamová, C. Adler, M. Aggarwal, F. Agnese, and G. A. Rinella, *The alice experiment at the cern lhc*, *Journal of Instrumentation* **3** (2008), no. 08 S08002. 76

[224] **ALICE** Collaboration, K. Aamodt et al., *Two-pion Bose-Einstein correlations in central Pb-Pb collisions at $\sqrt{s_{NN}} = 2.76$ TeV*, *Phys. Lett. B* **696** (2011) 328–337, [arXiv:1012.4035]. 76

[225] G. D'Agostini, *A Multidimensional unfolding method based on Bayes' theorem*, *Nucl. Instrum. Meth. A* **362** (1995) 487–498. 79

[226] A. Hocker and V. Kartvelishvili, *SVD approach to data unfolding*, *Nucl. Instrum. Meth. A* **372** (1996) 469–481, [hep-ph/9509307]. 79

[227] A. Andreassen, P. T. Komiske, E. M. Metodiev, B. Nachman, and J. Thaler, *OmniFold: A Method to Simultaneously Unfold All Observables*, *Phys. Rev. Lett.* **124** (2020), no. 18 182001, [arXiv:1911.09107]. 79

[228] **ATLAS** Collaboration, G. Aad et al., *Simultaneous Unbinned Differential Cross-Section Measurement of Twenty-Four Z+jets Kinematic Observables with the ATLAS Detector*, *Phys. Rev. Lett.* **133** (2024), no. 26 261803, [arXiv:2405.20041]. 79

[229] T. Adye, *Unfolding algorithms and tests using RooUnfold*, in *PHYSTAT 2011*, (Geneva), pp. 313–318, CERN, 2011. arXiv:1105.1160. 81

[230] B. Efron, *The Jackknife, the Bootstrap, and Other Resampling Plans*. Society for Industrial and Applied Mathematics, Philadelphia, 1982. 85

[231] B. Efron and R. J. Tibshirani, *An Introduction to the Bootstrap*. Chapman and Hall, New York, 1993. 85

[232] J. Shao and D. Tu, *The Jackknife and Bootstrap*. Springer, New York, 1996. 85

[233] **ATLAS** Collaboration, *Evaluating statistical uncertainties and correlations using the bootstrap method*, . 85

[234] A. collaboration, *Bootstrapgenerator (1.11.2)*, 2021. 85

[235] **ALICE Collaboration** Collaboration, S. e. a. Acharya, *Measurements of inclusive jet spectra in pp and central pb-pb collisions at* $\sqrt{s_{NN}} = 5.02\,\text{TeV}$, *Phys. Rev. C* **101** (Mar, 2020) 034911. 88

[236] Y. L. Dokshitzer, V. A. Khoze, A. H. Mueller, and S. I. Troian, *Basics of perturbative QCD*. 1991. 92

[237] O. Nachtmann, *A New Tool for the Study of Fundamental Interactions: Parity Odd Correlations in Quark Fragmentation*, *Nucl. Phys. B* **127** (1977) 314–330. 94

[238] J. a. Barata and Y. Mehtar-Tani, *Energy loss effects in EECs at LO*, in *11th International Conference on Hard and Electromagnetic Probes of High-Energy Nuclear Collisions: Hard Probes 2023*, 7, 2023. arXiv:2307.08943. 98, 106

[239] J. a. Barata, J. G. Milhano, and A. V. Sadofyev, *Picturing QCD jets in anisotropic matter: from jet shapes to Energy Energy Correlators*, arXiv:2308.01294. 98, 106

[240] J. Barata, P. Caucal, A. Soto-Ontoso, and R. Szafron, *Advancing the understanding of energy-energy correlators in heavy-ion collisions*, arXiv:2312.12527. 98, 106

[241] J. a. Barata and R. Szafron, *Leading order track functions in a hot and dense QGP*, arXiv:2401.04164. 98, 106

[242] **ALICE** Collaboration, S. Acharya et al., *Measurement of isolated photon-hadron correlations in $\sqrt{s_{\rm NN}}$ = 5.02 TeV pp and p-Pb collisions*, *Phys. Rev. C* **102** (2020), no. 4 044908, [arXiv:2005.14637]. 104

[243] C. Andres, J. Holguin, R. Kunnawalkam Elayavalli, and J. Viinikainen, *Minimizing selection bias in inclusive jets in heavy-ion collisions with energy correlators*, arXiv:2409.07514. 105, 132

[244] A. S. Kudinoor, D. Pablos, and K. Rajagopal, *Visualizing How the Structure of Large-Radius Jets Shapes Their Wakes*, arXiv:2501.18683. 107

[245] J. a. Barata, I. Moult, A. V. Sadofyev, and J. a. M. Silva, *Dissecting Jet Modification in the QGP with Multi-Point Energy Correlators*, arXiv:2503.13603. 111

[246] **ATLAS** Collaboration, G. Aad et al., *Correlations between flow and transverse momentum in Xe+Xe and Pb+Pb collisions at the LHC with the ATLAS detector: A probe of the heavy-ion initial state and nuclear deformation*, *Phys. Rev. C* **107** (2023), no. 5 054910, [arXiv:2205.00039]. 113

[247] X. Luo, J. Xu, B. Mohanty, and N. Xu, *Volume fluctuation and auto-correlation effects in the moment analysis of net-proton multiplicity distributions in heavy-ion collisions*, *J. Phys. G* **40** (2013) 105104, [arXiv:1302.2332]. 113

[248] V. Skokov, B. Friman, and K. Redlich, *Volume Fluctuations and Higher Order Cumulants of the Net Baryon Number*, *Phys. Rev. C* **88** (2013) 034911, [arXiv:1205.4756]. 113

[249] C. A. Bertulani, S. R. Klein, and J. Nystrand, *Physics of ultra-peripheral nuclear collisions*, *Ann. Rev. Nucl. Part. Sci.* **55** (2005) 271–310, [nucl-ex/0502005]. 114

[250] **ALICE** Collaboration, B. Abelev et al., *Measurement of charged jet suppression in Pb-Pb collisions at* $\sqrt{s_{NN}}$ *= 2.76 TeV*, *JHEP* **03** (2014) 013, [arXiv:1311.0633]. 115

[251] **ALICE** Collaboration, B. Abelev et al., *Measurement of Event Background Fluctuations for Charged Particle Jet Reconstruction in Pb-Pb collisions at* $\sqrt{s_{NN}} = 2.76$ *TeV*, *JHEP* **03** (2012) 053, [arXiv:1201.2423]. 116, 117

[252] **CMS** Collaboration, *Energy-energy correlators from PbPb and pp collisions at 5.02 TeV, CMS-PAS-HIN-23-004*, tech. rep., CERN, Geneva, 2023. 119

[253] M. Jaarsma, Y. Li, I. Moult, W. Waalewijn, and H. X. Zhu, *Renormalization group flows for track function moments*, *JHEP* **06** (2022) 139, [arXiv:2201.05166]. 131

[254] L. Apolinário, R. Kunnawalkam Elayavalli, N. O. Madureira, J.-X. Sheng, X.-N. Wang, and Z. Yang, *Flavor dependence of Energy-energy correlators*, arXiv:2502.11406. 132

[255] Y.-T. Chien, A. Deshpande, M. M. Mondal, and G. Sterman, *Probing hadronization with flavor correlations of leading particles in jets*, *Phys. Rev. D* **105** (Mar, 2022) L051502. 132

[256] A. Kudinoor, "Energy correlators in pp and pb-pb collisions with alice." Talk presented at Quark Matter 2025, Boston, USA, Apr., 2025. 133

[257] **ALICE** Collaboration, S. Acharya et al., *Measurement of charged jet cross section in pp collisions at* $\sqrt{s} = 5.02$ *TeV*, *Phys. Rev. D* **100** (2019), no. 9 092004, [arXiv:1905.02536]. 135

[258] J. Casalderrey-Solana, D. Gulhan, G. Milhano, D. Pablos, and K. Rajagopal, *Angular Structure of Jet Quenching Within a Hybrid Strong/Weak Coupling Model*, *JHEP* **03** (2017) 135, [arXiv:1609.05842]. 153

[259] **ALICE** Collaboration, S. Acharya et al., *Transverse momentum spectra and nuclear modification factors of charged particles in pp, p-Pb and Pb-Pb collisions at the LHC*, *JHEP* **11** (2018) 013, [arXiv:1802.09145]. 155